THE CENTRAL LASER FACILITY AT THE PIERRE AUGER OBSERVATORY. STUDIES OF THE ATMOSPHERIC VERTICAL AEROSOL OPTICAL DEPTH AND OTHER APPLICATIONS TO COSMIC RAY MEASUREMENTS

by

Carlos Francisco Medina Hernandez

© **Copyright by Carlos Francisco Medina Hernandez, 2017**

All Rights Reserved

A thesis submitted to the Faculty and the Board of Trustees of the Colorado School of Mines in partial fulfillment of the requirements for the degree of Doctor of Philosophy (Applied Physics).

Golden, Colorado

Date _____

Signed: _____
Carlos Francisco Medina Hernandez

Signed: _____
Dr. Lawrence Wiencke
Thesis Advisor

Golden, Colorado

Date _____

Signed: _____
Dr. Jeff Squier
Professor and Head of physics department
Department of Physics

ABSTRACT

The two largest observatories in the world dedicated to the study of Ultra High Energy Cosmic Rays (UHECR) are the Pierre Auger Observatory (Auger) in Mendoza, Argentina and the Telescope Array (TA) in Utah, USA. The measurements of the cosmic ray flux by Auger and TA present a discrepancy at the highest part of the energy spectrum. In this thesis, I study if this discrepancy can be attributed to instrumental effects related to the measurements of the atmospheric aerosol contents in Auger. The Auger Fluorescence Detector (FD) measures the scattered light from laser tracks generated by the Central Laser Facility (CLF) and the eXtreme Laser Facility (XLF) located near the center of Auger, to estimate the vertical aerosol optical depth (τ(z,t)). A good knowledge of τ(z,t) is needed to obtain unbiased and reliable FD measurements of the energy of the UHECR primary particle. The CLF was upgraded substantially in 2013 to improve laser reliability. A substantial part of my Ph.D work is dedicated to building, maintaining and analyzing data from this upgraded facility. The upgraded CLF includes a backscatter Raman LIDAR which independently measures τ(z,t). For the first time in a cosmic ray experiment, two years of measurements of τ(z,t) obtained with the Raman LIDAR are compared with the measurements obtained with the FD. Based on these comparisons, an alternative atmospheric database was created to study its effects on the measurements of the flux as a function of energy. The resulting energy spectrum plot is found to be more compatible with the energy spectrum plot released by TA.

TABLE OF CONTENTS

ABSTRACT iii

LIST OF FIGURES viii

LIST OF TABLES xx

ACKNOWLEDGMENTS xxii

CHAPTER 1 INTRODUCTION 1

CHAPTER 2 INTRODUCTION TO COSMIC RAYS 6

2.1 A Brief History 6

2.2 Flux and Energy Spectrum 8

2.3 GZK 9

2.4 Cosmic Rays Sources 10

2.5 Phenomenology 12

2.5.1 Electromagnetic Shower 13

2.5.2 Hadronic Shower 15

2.6 Mass Composition 16

CHAPTER 3 THE PIERRE AUGER OBSERVATORY 20

3.1 The Surface Detector (SD) 21

3.2 The Fluorescence Detector (FD) 23

3.3 Other Extensions to the Observatory 26

3.4 Atmospheric Monitoring 27

3.4.1 HAM and FRAM 27

3.4.2 APF 28
3.4.3 Cloud Cameras 28
3.4.4 Elastic LIDARs 28
3.4.5 Raman LIDAR 29
3.4.6 The CLF and the XLF 29
3.5 Fluorescence Detection at Auger 31
3.5.1 Light Propagation 31
3.5.2 Rayleigh and Mie Scattering 33
3.5.3 Phase Function 35
3.5.4 Atmospheric Effects on the Fluorescence Detection 36
3.6 The Offline Software Framework 38
3.7 FD Reconstruction 39
3.8 SD Reconstruction 42
CHAPTER 4 THE UPGRADE OF THE CENTRAL LASER FACILITY 46
4.1 Upgrade Summary 46
4.2 Intercontinental Travel 47
4.3 The Laser 49
4.4 SBC and GPS 50
4.5 Optical Components 52
4.6 The Energy + Polarization Calibration System 54
4.7 The Steering System 55
4.8 Power System 61
4.9 Insulation and Temperature Stability 64

4.10 The Raman LIDAR 66

4.10.1 Raman vs Elastic 67

4.10.2 Instrument Setup and Operations 68

4.10.3 Raman Output 70

4.11 CLF Operations 72

CHAPTER 5 LASER BEAM CHARACTERIZATION 74

5.1 Absolute and Relative Energy Measurements 74

5.2 The Calibration Factors 78

5.3 Cross-calibration 80

5.4 Laser Alignment 81

5.5 Linearity Studies 83

5.6 Polarization Measurements 86

5.7 Beam Divergence 88

5.8 Energy Equivalence Between Laser and Cosmic Events 89

CHAPTER 6 AEROSOL MEASUREMENTS AND THE DATA NORMALIZED ANALYSIS 97

6.1 Detection of Laser Light by the FD 97

6.2 The Data Normalized Analysis Formulation 102

6.3 The Reference Profiles 104

6.4 Building a $\tau(z)$ Profile 107

6.5 The Laser Simulation Analysis 109

6.6 Post Upgrade Results 111

6.6.1 Comparison Between Laser Facilities 113

6.6.2 Comparison Between FD Telescopes 116

6.6.3 Comparison Between Analyses 118

6.7 Comparison to the Raman LIDAR 124

6.8 Summary of τ(z=3 km) Differences 128

CHAPTER 7 EFFECTS OF DIFFERENT AEROSOL DATABASES ON THE UHECR SPECTRUM 131

7.1 Alternative Aerosol Databases 131

7.1.1 Bi-modality Corrections 131

7.1.2 Aerosol Scattering and Multiple Scattering 132

7.1.3 Raman LIDAR 133

7.1.4 Raman Biased DN Database 134

7.2 The FD-SD Energy Fit 138

7.3 The Energy Spectrum 141

CHAPTER 8 SUMMARY AND CONCLUSIONS 147

APPENDIX A - THE AUTOLOGS FILES 151

APPENDIX B - CLF CONNECTION SUMMARY 153

REFERENCES CITED 154

LIST OF FIGURES

Figure 1.1 The flux exhibits a power law with a spectral index (γ) of approximately 3 . A power law rather than a black body spectrum indicates that cosmic rays are not products of thermal sources. Some important spectrum features (the knees and the ankle) are indicated in the plot and they will be discussed in Chapter 2. 1

Figure 1.2 Two energy spectrum measurements by HIRES (in two different modes)and AGASA disagree at the highest region of the spectrum . The flux is multiplied by E^3. 2

Figure 1.3 Recent measurements of the cosmic ray spectrum for the Pierre Auger experiment and TA present disagreements. To help visualized the differences, only the highest part of the spectrum is shown and the fluxes have been scaled by E^3 3

Figure 2.1 The combined energy spectrum of cosmic rays for different experiments . Some values of the integral flux are shown. The flux has been scaled by $E^{2.5}$ to better visualize spectral features 9

Figure 2.2 Energy of three protons with different initial energy as a function of propagation distance through the cosmic microwave background . For large propagation distances, each proton reaches an identical energy. . . . 11

Figure 2.3 Possible candidate sources for cosmic ray primaries are placed on this Hillas plot according to their size and magnetic field 12

Figure 2.4 A simplified schematic of a vertical EAS in the atmosphere showing the secondary particles created in the electromagnetic, hadronic and muonic component 13

Figure 2.5 The development of an electromagnetic shower according to the Heitler model 14

Figure 2.6 A simulation of the number of particles as a function of slant depth and altitude for the muonic component (green line), the EM component (red line for $e^{\pm}$ and blue line for photons) and hadronic component (black line) of an EAS . The electromagnetic component dominates at all altitudes relative to the hadronic component. 16

Figure 2.7 Left: Different Xmax distribution for simulated showers with a proton primary compared to a real profile measured by the Pierre Auger Collaboration . Right: The relatively smaller Xmax fluctuations of the iron primaries allows the use the RMS Xmax to identify primaries. 17

Figure 2.8 Elongation plot for Xmax (left) and RMS Xmax (right). The red and blue lines represent simulation, using different models and primaries. Dots represent the measured number of events in each bin . the number of events used to find Xmax average is below the data. A mix composition of primary particles with a heavier component toward higher energies is visible. 18

Figure 2.9 Xmax measurements by TA . The color and black lines represent fit to the simulation and data respectively. TA results are compatible with Auger. 19

Figure 3.1 Layout of the Pierre Auger Observatory . The city of Malargë, the FD sites and the atmospheric instruments including the CLF and XLF are observed. The approximate locations of the SD stations are represented with black dots. A larger concentration of dots near the Coihueco site represents the SD infill. The FD field of view is illustrated with blue lines. 21

Figure 3.2 A deployed SD station in the field and its main components. 22

Figure 3.3 The hybrid concept of the observatory including a view of Los Leones FD building and a SD station. 23

Figure 3.4 Left: Schematic aerial view of one FD site building containing 6 telescopes for a 180° field of view in azimuth. Right: An schematic side view of one FD telescope and its components. 24

Figure 3.5 Left: Some PMTs and light collectors are mounted on the camera metallic structure . Right: The camera with all PMTs and light collectors mounted 25

Figure 3.6 Fundamental types of pattern searches for the Second Level Trigger 26

Figure 3.7 Left: A picture of the CLF, near the Celeste SD station. Right: A picture of the XLF, near the Ramiro SD station. 29

Figure 3.8 The second positive fluorescence spectrum of the N_2 molecule measured by the AIRFLY collaboration with an electron beam of 3 MeV 32

Figure 3.9 Two aerosol samples taken at the observatory in 2008 under an electron microscope reveal the size of the aerosol particles . Left: Sample taken during a low aerosol content period. Right: Sample taken during a high aerosol content period. 34

Figure 3.10 A Calculated profile of τ_{mol} (dots), is compared with three profiles of measured τ_{aer} under high, average, and low aerosols concentration (blue solid lines). 35

Figure 3.11 A comparison of the scattering phase function between Rayleigh (red) and Mie scattering (blue) 36

Figure 3.12 Left: Difference in the energy (left) and Xmax (right) reconstructed values using the aerosol measurements from the CLF and the assumption of purely molecular transmission 37

Figure 3.13 Left: Difference in the energy (left)and Xmax (right) reconstructed values when the multiple scattering effects are taken into account 37

Figure 3.14 Left: A hybrid event successfully reconstructed by the 4 FD telescopes triggers some SD stations (represented by color). All other SD stations can be seen as black dots. Colored lines represent the fluorescence light seen by the telescopes. Right top: Pixels trigered by this event spread over three adjecent bays in FD Los Leones. They are represented by hexagons color coded acording to the time of light detection. Right bootom: The photon trace produced in Los Leones by this event. 39

Figure 3.15 A representation of the shower detector plane from a cosmic ray as it travels in front of the field of view of one FD telescope. 40

Figure 3.16 Left: Example of the FD reconstruction of one event. Left: Light at aperture for different light components. Right: Energy deposition as a function of slant depth, X_{max} can be found after this profile is fitted with a GHF 41

Figure 3.17 An EAS modeled as a spherical wave moving toward the SD. 43

Figure 3.18 Attenuation curve is described by a third order polynomial function, a dashed line is drawn at 38° 44

Figure 3.19 Correlation between S_{38} and E_{FD} . The red line represents the best fit. . 45

Figure 4.1 The design of the upgraded CLF as originally proposed. The actual instrument has a similar layout. 47

Figure 4.2 The inside of the CLF after completion of the upgrade (April 2013). From left to right: Eric Mayotte, Carlos Medina, Jorge Rodriguez. 48

Figure 4.3 Left: October 2012, the container is shipped from CSM. Center: the CLF trip. Right: March 2013, the container at the Pierre Auger Observatory. 49

Figure 4.4 Left: Laser head and the laser controller before installation (courtesy of Quantel laser). Right: The laser head as mounted on the optical table in the CLF next to some optical components (they will be described in the following sections). 50

Figure 4.5 The SBC with the GPSY engine unit mounted, the additional serial-port cards. A protective case was added later 51

Figure 4.6 Diagram of the elements found on the optical tables in the CLF. 53

Figure 4.7 The CLF calibration system in optical box. A white box has been drawn around the system. The calibration system parts are labeled with black fonts. Other important elements are labeled using a white font. . . 55

Figure 4.8 The steering head and cover box is located on top of the CLF container. . 56

Figure 4.9 A close up of the steering head, the axis of the rotational stages are represented with dash lines 57

Figure 4.10 The steering head vertical reference was set using a self leveling laser and a target 8 m away from it. 58

Figure 4.11 Comparison of a very inclined steered shot towards Los Leones and a fixed vertical one as seen by Los Leones FD camera 60

Figure 4.12 Red points represent the reconstructed inclination angles of AGNs included laser shots. The AGN inclined laser shots (plot courtesy of Levy Patterson) are represented with green dots. 61

Figure 4.13 Left: solar panels are arranged next to each other, a metallic fence prevents wildlife from breaking the panels. Right: 18 high capacity batteries. 62

Figure 4.14 Top: Battery bank 1 voltage measurements during 2010, before the upgrade. Lower voltage values in May June and July indicate that the batteries were not fully charged. Data is taken every 5 minutes. Bottom: Battery bank 1 voltage measurements in 2014. Issues with the battery charge are solved. Data is taken every 5 minutes. 63

Figure 4.15 Outside temperatures at the CLF location during a full year, one measurement is taken every 5 minutes. 64

Figure 4.16 Left: Laser room has been covered using fiberglass insulation pads. Right: Laser room after installation of the drywalls. The structures for the water reservoir and the Raman LIDAR optics can be seen on the back. 65

Figure 4.17 Top: Laser room temperatures for a year before the upgrade, the data is taken every 5 minutes. Bottom: Laser room temperatures become noticeably more stable after the upgrade. Abrupt changes in temperatures (September and November 2015) are due to temporary changes in the thermostat setting. 66

Figure 4.18 Elastic LIDARs have an additional assumption on the relationship between the amount of backscattering coming from nitrogen molecules and aerosols. This is not the case with the Raman technique since the N2 Raman backscattering is very well defined 68

Figure 4.19 The Raman receiver is separated into the telescope mirror and the optics, they are connected via WLS optical cable. Both compartments are observed. An oscilloscope has been temporally placed to test the PMTs signal. 69

Figure 4.20 The arrangement of the Raman LIDAR optics that measures the amount of light in 3 separate bands. 70

Figure 4.21 Examples of hourly τ(z,t) during a clear and a typical night with aerosols. The red line represents the electronic signal. 71

Figure 5.1 Top: Absolute laser energy measurements at the maximum energy setting after the CLF upgrade. The average maximum energy of the laser in the fixed vertical mode is 4.7 mJ. Center: Relative measurements and histogram by the monitoring probe. Green lines represent the $\pm$10% deviation from average. Bottom: The ratio of these two quantities presents a better stability. Vertical dashed lines mark changes to the hardware or optics (see text). 75

Figure 5.2 The correlation between the calibration and monitoring probe for the three different periods between 2014 and 2015. The percentage of light received by the monitoring probe has been found using a linear fit (red line). 76

Figure 5.3 Top and center: The energy measurements in the XLF are presented in similar fashion as for the CLF in Figure 5.1 from 2009 to 2015. The aging of the laser can be easily observed. The vertical dashed line represents a change in the system (see text). Bottom: The ratio of these two quantities is not sensitive to the laser variations on energy. Before November 2013 the ratio is contained within the two green lines representing a ± 15% deviation from the average. After that date the data is within ± 15% away from the average value. 77

Figure 5.4 A year (2015) of energy measurements provided by the monitoring probe for atmospheric laser shots during the duration of FD shifts. Top: The CLF measurements remain within ±5% from the average. A gap in laser shots is visible in the second half of 4h UTC, this is due to the Raman operations. Bottom: The XLF laser is older and it presents slightly lower stability than the CLF. XLF measurements remain within 7% from the average 78

Figure 5.5 Left, pre-upgrade CF are shown in circles. Black and red lines represent fit functions including corrections. Blue lines represent epochs. (Right, post-upgrade) CF are measured every day. Calibration functions, fits or epochs are no longer required. Blue lines represent hardware changes. . 79

Figure 5.6 Simplified schematic of the laser alignment setup inside the CLF container. 82

Figure 5.7 The trigger signal seen by the oscilloscope for 6 E_{SET}, the offset time between the raising edge of the Qswitch IN signal and the raising edge of the Diode IN signal is proportional to the laser energy. 83

Figure 5.8 The CLF internal linearity has been tested with three energy probes. The data was fitted to a straight line. 84

Figure 5.9 Left: Light profiles for laser shots (200 laser shots) fired with 5 different energy setting (in mJ): A:4.93, B:3.89, C:2.82, D:1.77, E:0.89. Right: The integrals of the traces are plotted vs the laser energy (average of 200 shots) and fitted to a straight line. 85

Figure 5.10 Schematic of the polarization cube mounted on the rotatory stage and the incoming laser beam. 86

Figure 5.11 Left: Example of one daily polarization monitoring run fitted to a 3 parameter ellipse for the CLF. Right: The same method is applied to the XLF. Three different parameters are found in each fit. 87

Figure 5.12 Chronological factors (deviation from circular) for both laser facilities. Blue dots represent the daily deviation factor. Green lines represent the average value. Dashed red lines indicate the maximum percentage deviation. Top and bottom plots have different time scales 88

Figure 5.13 Schematic of the beam divergence measurement performed on the CLF and XLF container roof. 89

Figure 5.14 The ground core location of the 10 shower events passing the criteria relative to the location of the 3 FD eyes and the 2 laser facilities. Events marked with a circle are selected for further analysis. 91

Figure 5.15 A 3D representation of the geometry of the shower events. The colors in the FD rays and SD tanks represent time of detection and signal strength, respectively. 92

Figure 5.16 The energy development of the shower as function of the slant depth for event 140601-072450 and event 131206-053107. The red line is a Gaisser-Hillas fit. 92

Figure 5.17 Top: Pixels triggered in FD LL camera for events 140601-072450 (left) and 131206-053107 (right). The pixels with a gray color are noisy pixels. Bottom: Sum of photon traces for the same event. 93

Figure 5.18 The superimposed FD traces of the shower and laser for event 140601-072450 (left) and 131206-053107 (right). The shower light profile is inverted and translated in time. The laser light profile with a spike in intensity indicates a cloud presence over the CLF. Regions of interest are between the dashed lines. 94

Figure 5.19 Left: The integral of the selected shower events next to the integral of the truncated laser profile. Right: The ratio of the integrals. 95

Figure 5.20 The ratio of the integral vs shower energy. A line has been drawn to indicate a possible linear behavior, although more statistics will be needed to determined if this linearity is real. 96

Figure 6.1 Left: A representation of a CLF laser event recorded by 4 FD sites. The lines represent the scattered light traveling towards the cameras, they are color coded to represent time of detection. Right: The light track produced in each FD camera. The pixels are color coded to represent time of detection (purple is earlier time and red is later time). . 97

Figure 6.2 Left: A laser track detected in FD LL. The track can be identified to be produced by the CLF due to is 250 ms offset (GPS nanosecond signature). The pixels are color coded to represent time of detection. Right: The ADC counts vs time, of several pixels (marked with a dot) from this laser track are superimposed. Negative counts are the product of a noise pedestal subtraction. 98

Figure 6.3 Left: The light profile obtained by the FD from the side scattered light from 50 laser shots (nominal for a quarter of hour) from the CLF. Right: The light profile for the same quarter hour period when normalized by the laser energy. The repeating peaks and valleys of intensity are an effect of spot sweeping across the small gaps between pixels in the camera. 100

Figure 6.4 Left: Three hourly light profiles seen by the FD Los Morados during 2015 for three different aerosol attenuation levels: high (04/10 at 01 UTC), average (05/16 at 00 UTC) and low(06/16/ at 23 UTC). Right: A cloud above the laser (08/21 at 09 UTC) and cloud between the laser and the FD (05/27 at 04 UTC) affect the amount of laser light reaching the detector. 101

Figure 6.5 Layout of the laser-FD geometry, where D is the distance between the laser and the FD site, Z is the scattering point altitude (a.g.l) and θ is the elevation angle of the scattered light detected by the FD. T_M, T_A, S_M and S_A are the atmospheric, aerosol transmission and scattering factors. The backscattered light is only detected by the Raman LIDAR. 102

Figure 6.6 The reference light profiles used found from 2012 to 2015 in all FD sites. The light profiles obtained with the FD site LL, LM and CO use the CLF, while the profile from FD site LA uses the XLF. The intensity of each FD site light profile varies accordingly to its distance to the laser. Differences in the profiles up to 10% suggest that not all yearly reference profile are of a purely molecular nature and free of aerosols. . 105

Figure 6.7 The reference light profiles used found from 2012 to 2015 in all FD sites. 106

Figure 6.8 Left: Example of the light profiles for an hour with typical aerosol content at the FD Los Leones. The green line represents the reference profile and the red line represents the observed profile. Right: Corresponding $\tau(z)$ profiles after being proceeded with the DN analysis. The black traces represent τ_{meas} and its uncertainties (correlated and uncorrelated). The red traces represents the fitted profiles (τ_{fit}). 109

Figure 6.9 Left: a comparison between a real (blue) and a simulated (red) light profile. Right: the simulated profile presented has been selected among a group of profiles simulated under different atmospheric conditions to be the most similar in shape and in scale to the real profile. 110

Figure 6.10 Average monthly τ measurements using the CLF after the upgrade (June 2013) shows a seasonal dependency. The yearly average (represented with the gray horizontal line) is consistent with the historical averages. 112

Figure 6.11 Average yearly τ profiles after the CLF upgrade. The FD site CO presents consistently lower values (see text). 113

Figure 6.12 Average τ profiles after the CLF upgrade for all FD sites and laser facilities. All profiles agree within the uncertainties. The two FD eyes (LL and LA) that are not nearly equidistant to the laser sources presents the largest profile differences. 114

Figure 6.13 τ at z=1.4 km (left), z=3.0 km (center), and z=4.5 km (right) a.g.l, correlations between the CLF and XLF using the DN analysis data available after the CLF upgrade. The red dashed line represents a linear fit passing by the origin. The black line is the unitary line. The total number of common hours found is presented in the top right corner of each plot. 115

Figure 6.14 τ(z=3 km) normalized differences for common XLF-CLF hours. LL presents the highest differences ($\sim$ 10%) , while LA and CO presents $\sim$ 5% and a $\sim$ 1% average difference for LM 116

Figure 6.15 τ(z=3 km) correlations between FD sites looking at the CLF. The dashed red line represent a linear fit passing by the origin. The solid black line is the unitary line. 117

Figure 6.16 τ(z=3 km) difference normalized to the average between different combinations of two FD sites using the CLF as a light source. The widths of the distribution increased compared to the ones in Figure 6.14 which may suggest a large non-uniformity in the atmosphere aerosol concentration. 118

Figure 6.17 τ(z=3 km) correlations between the LS and the DN analysis for the CLF data after the upgrade. Both analysis are consistent within the uncertainties. 119

Figure 6.18 τ(z=3 km) correlations between the LS and the DN analysis for the XLF data after the upgrade. Both analysis are consistent within the uncertainties. 120

Figure 6.19 Common measurements of τ(z=3 km) between the LS and the DN analysis for the CLF from 2013 to 2015. Red dashed lines are lines are linear fit passing through the origin. The number of common hours found are presented on the top right corner. One outlier in LM has been marked with a red circle an its $\tau(z)$ profile is presented in Figure 6.21. . 121

Figure 6.20 Common measurements of τ(z=3 km) between the LS and the DN analysis for the XLF from 2013 to 2015. Red dashed lines are linear fit passing through the origin. The number of common hours found are presented on the top right corner. 122

Figure 6.21 Left: $\tau(z)$ profile for the measurement marked in red in Figure 6.13. Right: The light profile in the camera revels a cloud presence near 3km a.g.l 123

Figure 6.22 τ(z=3 km) difference normalized to the average for the data points presented in Figure 6.19. The RMS are comparable to those from Figure 6.16 exept for LM where a clear offset is observable. 124

Figure 6.23 τ(z=3 km) correlations between the Raman and the DN analysis. Red dashed lines are linear fits 125

Figure 6.24 τ(z=3 km) normalized difference to the average for the data points presented in Figure 6.23. The scale of the X axis was increased to illustrate the larger RMS values. 126

Figure 6.25 τ profile comparison between the Raman and the DB analyses. All the FD site τ values presented here were measured using the CLF and they were averaged. 127

Figure 6.26 τ(z=3 km) average monthly. The DN values for all FD sites have been included in the average. The green dashed line represents the average difference. 128

Figure 6.27 A summary of the τ(z=3 km) differences (Normalized to average) for the different analyses described in this chapter (see text for labeling description). 129

Figure 7.1 Left: A Bi-modality behavior was noticed in the scattered plots of the DN analysis vs the LS analysis. The τ profiles corresponding to the point circled in red are presented on the right. Right: This hour presents a clear discrepancy between the two analyses. 132

Figure 7.2 Scatter plots of τ(z=3 km) for two FD eyes between a compromised version of the DN (DN.v0) and a later version (DN.v1) that corrects for effects of the bug discovered. The bi-modality behavior is evident. . . . 133

Figure 7.3 Difference on the τ(z) profiles (2014 and 2015 average) due to the introduction of aerosol scattering and multiple scattering effects. 134

Figure 7.4 Left: Average τ(z) profiles for the 34 hours found in Table 7.1 as seen for the Raman analysis and the DN analysis Right: The difference between the two profiles was simplified to a linear function. 136

Figure 7.5 The inverted transmission function based in the difference for selected hour between the DN and the Raman analysis. This function is used to scale the reference light profiles used in the DN database to create a "DN(Raman biased)" database. 137

Figure 7.6 Left: A comparison between the DN(Raman biased) and the original DN databases for the averaged τ(z) profiles using only the selected days from Table 7.1. Right: The difference between the two profiles presented on the left (black dots) agrees with the linear function presented in Figure 7.4 (right). 138

Figure 7.7 A comparison of the average τ(z) profiles of the DN(Raman biased) and the original DN databases using all the average produced in all FD eyes. The DN(Raman biased) presents differences larger than 0.02 after 3 km a.g.l. 139

Figure 7.8 Different energy fits are found when using four alternative aerosol databases. 140

Figure 7.9 Left: The FD-SD energy calibration functions using alternative aerosol databases are superimpose to illustrate the change on the relationship between E_{FD} and S_{38}. Right: The use of different aerosol databases affects the reconstructed FD energies; therefore, the number of events passing the lower energy cut changes. 141

Figure 7.10 Left: spectrum plots created with the toolkit (ICRC 2015) reproduced the results published in Right: To enhance the spectral features, each point is scaled by a factor of E^3. 142

Figure 7.11 The particle flux achieved using different aerosol databases. Each plot includes the flux as measured and the correction due to migration effects (unfolded spectrum). 143

Figure 7.12 Relative differences in the number of entries per energy bin between the flux obtained with different aerosol databases and the flux reported in the ICRC 2015. 144

Figure 7.13 Energy Spectrum for different aerosol databases features an increase in the scaled flux for databases with average larger values of τ(z). 145

Figure 8.1 The cosmic ray spectrum measured by TA is compared with the spectrum obtained using the DN(Raman biased) database. The discrepancies (particularly at high energies) are reduced compared to those in Figure 1.3. The comparison reveals that the fluxes are within the uncertainty bars at the highest part of the spectrum. 149

Figure B.1 CLF hardware integration. 153

LIST OF TABLES

Table 3.1 UTM coordinates (Zone 19H) of the FD buildings and the laser facilities according to GPS survey 30

Table 3.2 Distances (in km) from the laser facilities to the FD sites. 30

Table 3.3 Angles are measured counterclockwise from the east. The angle vertex is located on the FD eye 30

Table 4.1 List of the SBC communication ports connections 51

Table 4.2 Summary of optical components on the optical table 53

Table 4.3 56

Table 4.4 Summary angles 59

Table 4.5 Reference of major powers system components 63

Table 4.6 An example of the operations and laser shots executed at the CLF during an FD shift. Each type of shot is expained in the text. 72

Table 5.1 The information inside the CF files 80

Table 5.2 Cross calibration measurements using a standard (Std) probe and a reference (Ref) probe. 81

Table 5.3 Summary of the shower candidates passing the selection criteria. 90

Table 5.4 Summary of the light profile integrals and ratio for the 10 candidate shower and laser events. 95

Table 6.1 Summary of the pixels columns and bays used in the DN analysis. 99

Table 6.2 Dates when the reference hours were found for each FD site, year and laser facility. 104

Table 6.3 Number of hourly profiles obtained using the DN analysis after the CLF upgrade 111

Table 6.4 Number of LS hourly profiles available 118

Table 6.5 Summary of the linear fit of the scattered plots presented in Figure 6.23. 126

Table 7.1 List of dates and hours identified as a clean hour according to the DN analysis. 135

Table 7.2 list of hours produced in the DN (Raman biased) aerosol database 137

Table 7.3 The FD-SD calibration parameters for each aerosol databases used. . . . 140

Table A.1 This table describes the information in any line of the autologs that stars with the Prefix DATA:FIRE: 151

ACKNOWLEDGMENTS

I would like to acknowledgments my adviser Dr Lawrence Wiencke for his continuous support and efforts to built a scientific horizon in me. He managed to sharpen my strong interest for science into a new standard of excellence. Thanks to my good friends Johannes Eser and Eric Mayotte who helped me during difficult times during my PHD. Thank to my family members, my mom, dad, and brother who never stopped believing in me. I hope that the long time they had to wait to see this moment was worthy. To the Lab buddies and colleges that made this journey possible.

Quisiera agradecer de manera especial a mi profesor Dr Lawrence Wiencke por sus esfurezos constantes en crear un horizonte científico en mi. Lawrence logró mejorar mis fuerte inters por la ciencia y llevarlo a unos nuevos niveles de excelencia. A mis amigos Johannes Eses y Eric Mayotte quienes siempre me ayudaron durante los tiempos mas difíciles durante el doctorado. A los miembros de mi familia especialmente a mi mama, a mi papa y a mi hermano. Espero que el largo tiempo que ellos tuvieron que esperar para ver este momento halla valido la pena. A los chicos del laboratorio y dems colegas que hicieron posible este viaje.

CHAPTER 1

INTRODUCTION

Ultra High Energy Cosmic Rays (UHECRs) are subatomic particles of cosmological origin featuring energies that extend beyond the reach of the Large Hadron Collider (LHC). Their energy ranges from 10^{17} eV to 10^{20} eV. Their origin, sources and composition are still an open topic in astrophysics. The measurement of UHECRs is challenging due their extreme low flux. For example, at the highest energies, the expected flux is less than one particle per square kilometer per century making direct detection impractical. Instead, indirect observation of secondary particles (air shower measurements) is carried out by large ground-based experiments.

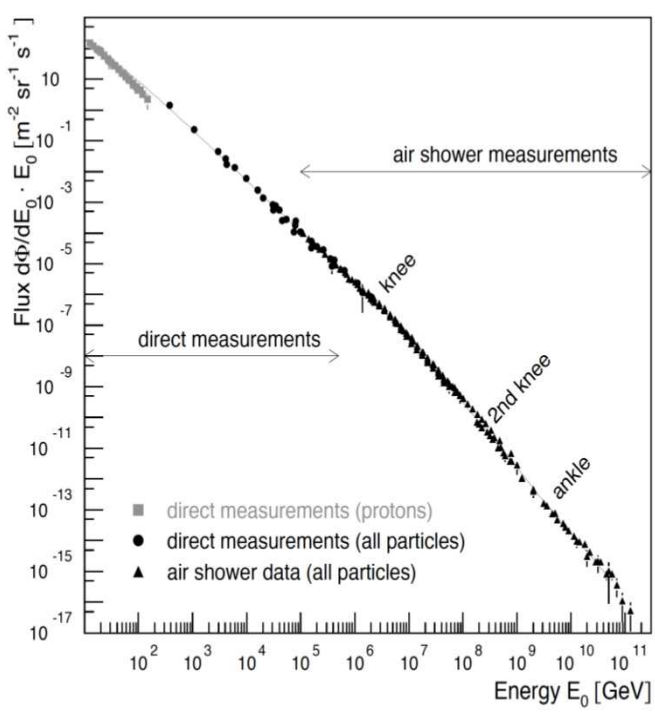

Figure 1.1: The flux exhibits a power law with a spectral index (γ) of approximately 3 [1]. A power law rather than a black body spectrum indicates that cosmic rays are not products of thermal sources. Some important spectrum features (the knees and the ankle) are indicated in the plot and they will be discussed in Chapter 2.

The knowledge of the cosmic ray flux at the highest energies is relevant to the understanding of particle acceleration mechanisms, element abundance and the identification of sources. The flux exhibits a power law with a spectral index (γ) of approximately 3 (Figure 1.1). A power law rather than a black body spectrum indicates that the cosmic rays are not exclusively produced by thermal processes.

Previous measurements of the high energy cosmic ray flux disagreed significantly. A well known case occurred between the HIRES experiment, that used a fluorescence detection technique in the air and a contemporary experiment (AGASA) that samples secondary particles on the ground (Figure 1.2). Although it was clear the energy scales of the two experiments were not consistent, the controversy focused on the shape of the measured spectrum above $10^{19.5}$ eV. Therefore a controversy arose regarding weather or not a limit to the spectrum has been found.

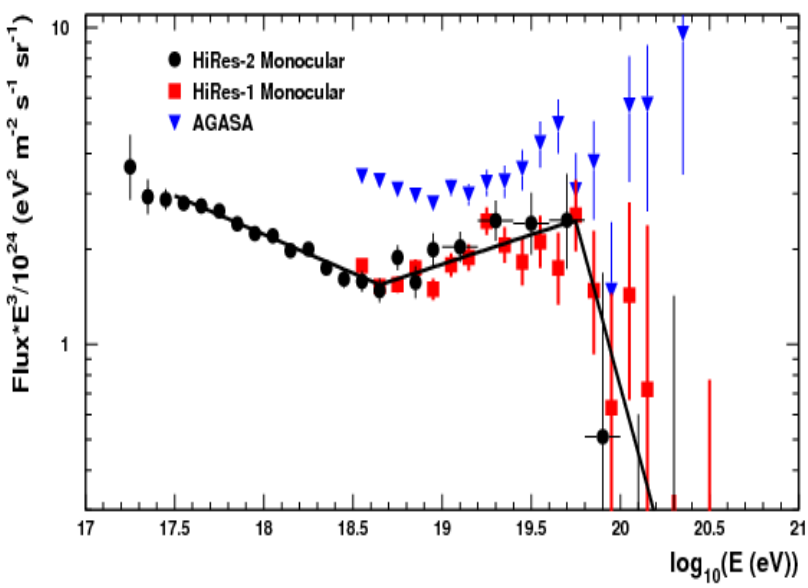

Figure 1.2: Two energy spectrum measurements by HIRES (in two different modes)and AGASA disagree at the highest region of the spectrum [2]. The flux is multiplied by E^3.

Motivated in part by this disagreement and by the need for a larger detector able to detect more cosmic rays, the Pierre Auger Observatory was built in Malargüe, Argentina.

It is the largest cosmic ray observatory in the world, with an area of 3000 km^2 (30 times larger than AGASA). The observatory results confirmed the HIRES observations using a hybrid technique that combines a Fluorescence Detector (FD) and a Surface Detector(SD) [3]. More recently, the Telescope Array (TA) was completed in the northern hemisphere in Delta, Utah. Although TA is nearly one third in size of Pierre Auger, it also uses the hybrid technique. Both observatories measured the high energy spectrum. While the shapes of the spectrum are similar, statistical significant differences persist at the highest energies (Figure 1.3). It has not yet been determined if these differences are the result of instrumental effects, or if they are due to the differences between the northern and southern sky.

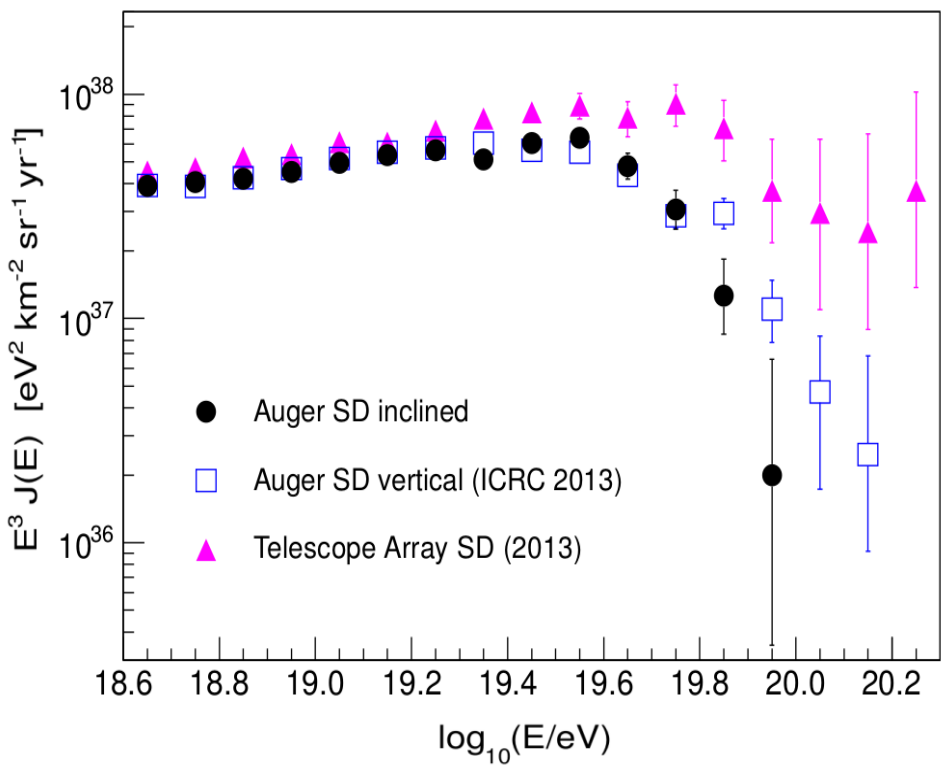

Figure 1.3: Recent measurements of the cosmic ray spectrum for the Pierre Auger experiment and TA present disagreements. To help visualized the differences, only the highest part of the spectrum is shown and the fluxes have been scaled by E^3 [4].

While the shape of the spectrum is sensitive to physical phenomena such as propagation mechanisms, anisotropy of the sources or the physical limits of the acceleration mechanisms,

There are also instrumental effects that can contribute to changes in the spectrum shape such as systematic errors in the calibration of the detectors.

This thesis is dedicated to the measurement and the impact of challenging source of potential systematic errors. These are the measurement of the atmospheric clarity and the aerosol contents. To realize this study, an upgrade to a critical instrument in the Pierre Auger observatory known as the Central Laser Facility (CLF) was performed. The CLF and its "twin brother", the eXtreme Laser Facility (XLF) are located near the center of the observatory. The laser beams generated in these facilities are used by the FD to measure the vertical aerosol optical depth (τ(z,t)), an important quantity used in all physics analysis, including the spectrum. The upgrade allows the comparison (for the first time) of τ(z,t) measurements taken with the FD and a Raman LIDAR installed in the CLF. Raman LIDARs are the standard instrument used in the atmospheric scientific community to measure τ(z,t). At the Observatory, the Raman LIDAR measures τ(z,t) independently.

The thesis is organized as follows:

- A brief introduction to cosmic rays will be provided in Chapter 2.
- The Pierre Auger Observatory, including, the FD, the SD, the CLF, the XLF and other atmospheric instruments are described in Chapter 3. A description of the physics involved in FD detection is also included.
- My participation in the upgrade of the CLF is one of my key contributions. It will be described in detailed in Chapter 4.
- The laser beam characterization and a study comparing laser and cosmic ray traces are presented in Chapter 5 .
- Two methods to measure τ(z,t) are the Data Normalized (DN) and the Laser Simulation (LS). They will be presented in Chapter 6. This chapter also includes my contributions to the production and analysis of a τ(z,t) database with the DN anal-

ysis using the CLF and XLF. Comparisons between the DN, LS and Raman LIDAR measurements are presented.

- The official aerosol database used in physics analysis by the observatory is obtained using the DN and LS analysis. Alternative databases were created by the atmospheric group based on the new measurements of the CLF and the Raman LIDAR. A study of how these databases change the measurements of the flux as a function of energy will be presented on Chapter 7.

CHAPTER 2

INTRODUCTION TO COSMIC RAYS

This chapter briefly reviews the research carried out on cosmic rays with primary energies above 10^{17} eV .

2.1 A Brief History

The study of cosmic rays began over 100 years ago with Victor Hess and his famous balloon flights. Following the discovery of radioactivity, originated in ores by Becquerel and the Curies, it was a popular assumption that all sources of radiation originated from the inside of the Earth. In 1912, Hess demonstrated that ionization effects increase dramatically with altitude [5]. He justified these results by claiming that the origin of the ionization may be extraterrestrial. He believed that the ionization effects were of pure electromagnetic nature, which explain the name "cosmic rays". He was awarded the Nobel Prize in Physics in 1936 for this discovery. Some important contributions to the understanding of the physics of cosmic rays after Hess' balloon flights include:.

- The term "cosmic rays" was coined in the 1920's by Robert Millican (USA)[6].
- In 1923, Arthur Compton (USA) demonstrated that the cosmic ray flux is latitude dependent [7].
- In 1927, Dimitri Skobelzin (USSR) observed cosmic ray traces for the first time using a cloud chamber [8].
- In 1937, Pierre Auger (France) proved the existence of Extensive Air Showers (EAS). He set many Geiger counters at different positions and observed simultaneous triggers among them. In this way he demonstrated that a cosmic ray particle may induce large showers of secondary particles [9].

- In 1949 Enrico Fermi (Italy/USA) proposed a model explaining the acceleration of cosmic rays.
- In 1954, Walter Heitler (Germany) formulated the first theoretical description of the development of an EAS [10].
- In 1965, Arno Penzias (USA) and Robert Wilson (USA) discovered cosmic microwave radiation at the Bell Telephone Laboratories in New Jersey [11].
- In 1966 Kenneth Greisen (USA), Vadim Kuzmin (URSS) and Georgiy Zatsepin (USSR) predicted a suppression in the flux of cosmic rays due to interactions with the cosmic microwave background. This suppression is known as the GZK cut-off [12].

More recently, cosmic rays have been measured by several experiments at different energy ranges and parts of the Earth. For example, in 1960 at the Volcano Ranch experiment, using a detector array, John Linsley (USA) observed a shower with an energy of 1×10^{20} for the first time [13]. Another experimental array known as the Haverah Park experiment was built near North-Yorkshire (England) by the University of Leeds. The Haverah Park experiment used water Cherenkov detector stations over an area of 12 km^2. During its lifetime of nearly 20 years, the Haverah Park experiment recorded more than 1000 EAS, including four with energies larger than 1×10^{20} eV [14].

In 1967, at Cornell University, Kenneth Graissen (USA) and Bruno Rossi (Italy/USA) built a particle detector using a novel idea involving fluorescence detection in the atmosphere [15] [16]. This instrument served as an inspiration to the construction of the Fly's Eye experiments in Utah in 1991. Fly's Eye reported a cosmic ray of energy close to 3×10^{20} eV [17]. Some years later, using a ground detection technique, the Akeno Giant Air Shower Array (AGASA) in Japan reported 6 events with energies larger than 3×10^{20}eV over 10 years of operation [18]. Their observations suggested that the energy spectrum extended beyond the GZK cut-off energy. But these results were challenged by the HIRES experiment (High Resolution Flys Eye), a successor of the Fly's Eye experiment, also located in Utah.

HIRES used a next generation fluorescence technique and they reported strong evidence of the flux suppression. The comparison of both results was discussed in Chapter 1.

Resolving contradictory results was one of the motivations behind the construction of the Pierre Auger Observatory in Malargüe, Argentina. And although the Pierre Auger Observatory (Auger) has found evidence supporting the flux suppression results, many other questions remain unsolved concerning the origin and composition of cosmic rays at the highest energies.

2.2 Flux and Energy Spectrum

The flux of cosmic rays has been measured by several experiments at different energy ranges. The flux spreads over 11 decades of energy and several orders of magnitude in flux. The combined results present three interesting features (Figure 2.1):

- At 10^{15} eV a steepening in the flux is observed in a region of the spectrum known as the "knee". Most of the flux below and around the knee is believed to originate from inside of our galaxy. Measurements with the KASCADE experiment indicate a reduction of lighter particles such as proton and Helium nuclei [19] at 10^{15} eV. This phenomena may be due to the limited capability of the galaxy to accelerate heavier particles and the lack of a strong magnetic field to contain them.

- An increase in the spectral index in a region known as the "ankle" at about 5×10^{18} eV. This feature has been commonly interpreted as the region where a transition from galactic to extra-galactic cosmic rays occurs [20].

- A strong flux suppression above $5\text{x}10^{19}$ has been observed. It is not clear yet, if the flux suppression is due to the GZK cut-off or simply because this is the point where cosmological sources reach the energy ejection limit to accelerate particles to higher energies. Observations on the flux suppression region by TA [21] and Auger [22] were presented in Chapter 1.

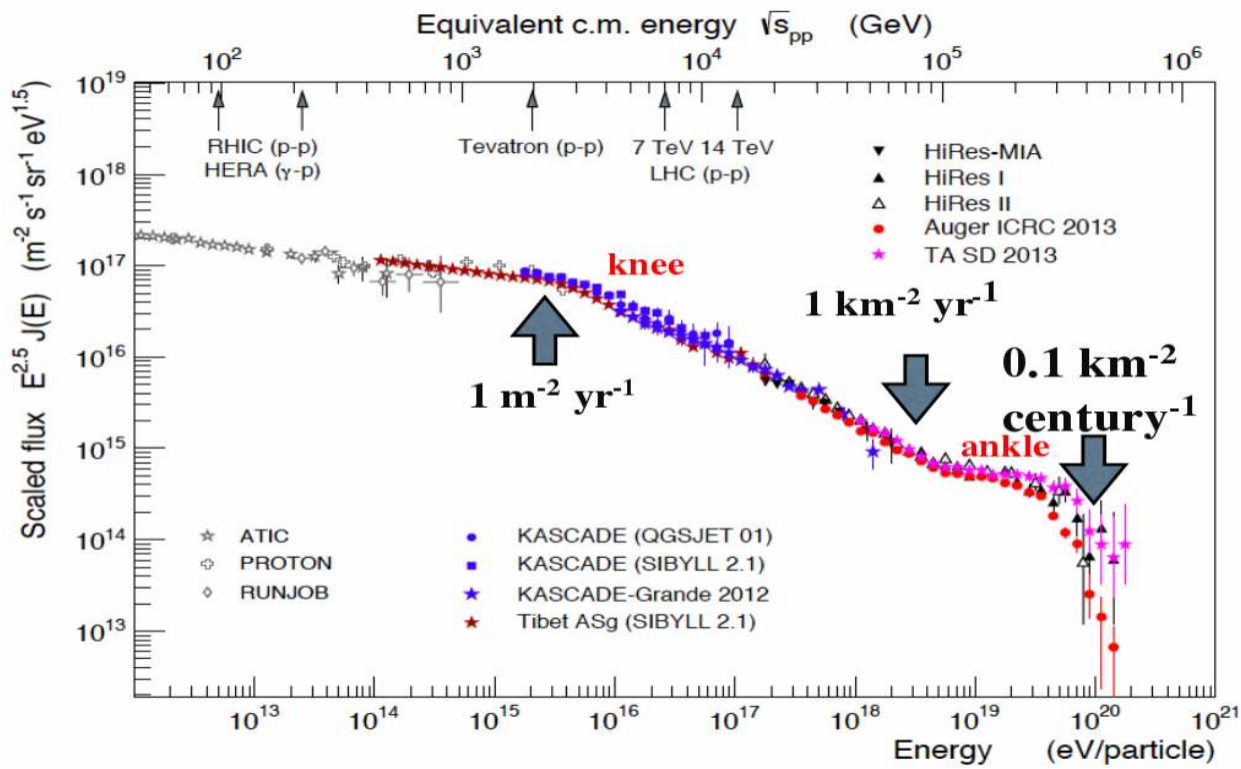

Figure 2.1: The combined energy spectrum of cosmic rays for different experiments [23]. Some values of the integral flux are shown. The flux has been scaled by $E^{2.5}$ to better visualize spectral features

The topics studied in this thesis aim to help understanding the Auger disagreement with TA in the highest part of the spectrum. This thesis explores if the disagreement is due to instrument calibration, specifically the effects of the aerosol database has on the energy reconstruction of the Auger events.

2.3 GZK

The GZK effect predicts that the highest energetic protons will interact with the cosmic microwave background (CMB), according to:

$$p + \gamma_{CMB} \longrightarrow p + \pi^0 \tag{2.1}$$

$$p + \gamma_{CMB} \longrightarrow n + \pi^+ \tag{2.2}$$

The center of mass energy is provided by:

$$s = \sqrt{m_p^2 + 2E_p\epsilon\,(1 - \beta cos\theta)} \tag{2.3}$$

where ϵ is the energy of the photon, β is the proton speed relative to the speed of light, and θ is the angle between the proton and the photon. The energy threshold (E_{th}) for this process is:

$$E_{th} = \frac{m_\pi}{4\epsilon}\,(2m_p + m_\pi) \tag{2.4}$$

where m_p and m_π are the rest frame masses of the proton and the pion. For an average photon energy ($\epsilon \sim 6 \cdot 10^{-4}$), this energy threshold is about 10^{20} eV, and at this energy the mean free path L can be estimated via:

$$L \sim (\sigma_{p\gamma}\rho)^{-1} \sim 8Mpc \tag{2.5}$$

where $\sigma_{p\gamma} \sim 10^{-28}cm^2$, is the photo-pion cross section at $E_{th} = 10^{20}$ eV [24], and ρ is the CMB photon energy density with a value of $400\gamma/cm^3$. The energy losses per interaction are near 20% making the proton energy fall below the E_{th} after just a few interactions. This sets a GZK horizon of nearly 100 Mpc for UHECR proton sources.

The energy development of three protons with different initial energies vs their propagation distance as they interact with the CMB is shown in Figure 2.2. Independent of the initial energy, all the protons reach the threshold energy after traveling around 100 Mpc.

2.4 Cosmic Rays Sources

Cosmic rays with Energies below 10^{15} eV are believed to be originated within the Milky Way and its trajectory contained to galaxy's magnetic field. Charged Particles are accelerated by stochastic scattering against the magnetic field of the source's moving plasma. This mechanism, first described by Enrico Fermi in 1949 [25] is known as Fermi acceleration. In it's simplest form:

$$E_{max} \sim \beta_S ZBL \tag{2.6}$$

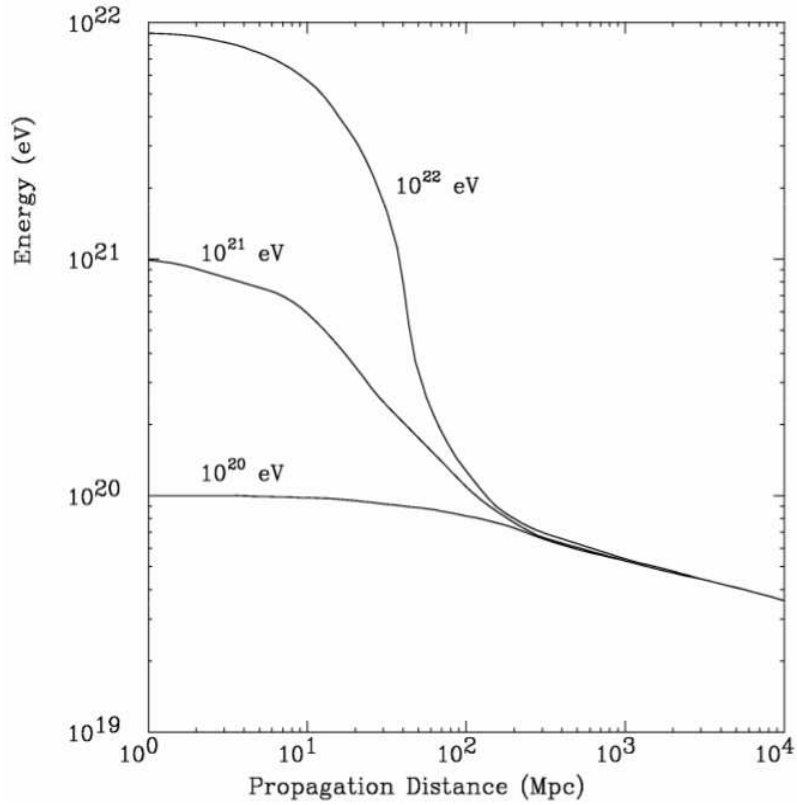

Figure 2.2: Energy of three protons with different initial energy as a function of propagation distance through the cosmic microwave background [12]. For large propagation distances, each proton reaches an identical energy.

where Z is the charge of the accelerated particle, B the accelerating magnetic field, β_s is the velocity of the shock wave and L is the size of the active region. The relationship between magnetic field and size for sources to be able to accelerate protons to 1 Zev, 100 Eev or iron to 100 EeV is presented in Figure 2.3, also known as a Hillas plot. For example, cosmic rays with energies up to 10^{17} eV can be accelerated by supernova explosions remnants (SNR) [26]. For energies larger than 10^{19} eV, there are no candidates within our galaxy. Some extra-galactic candidate sources are Active Galactic Nuclei (AGN), hot spots of radio galaxies or Gamma Ray Burst (GRB).

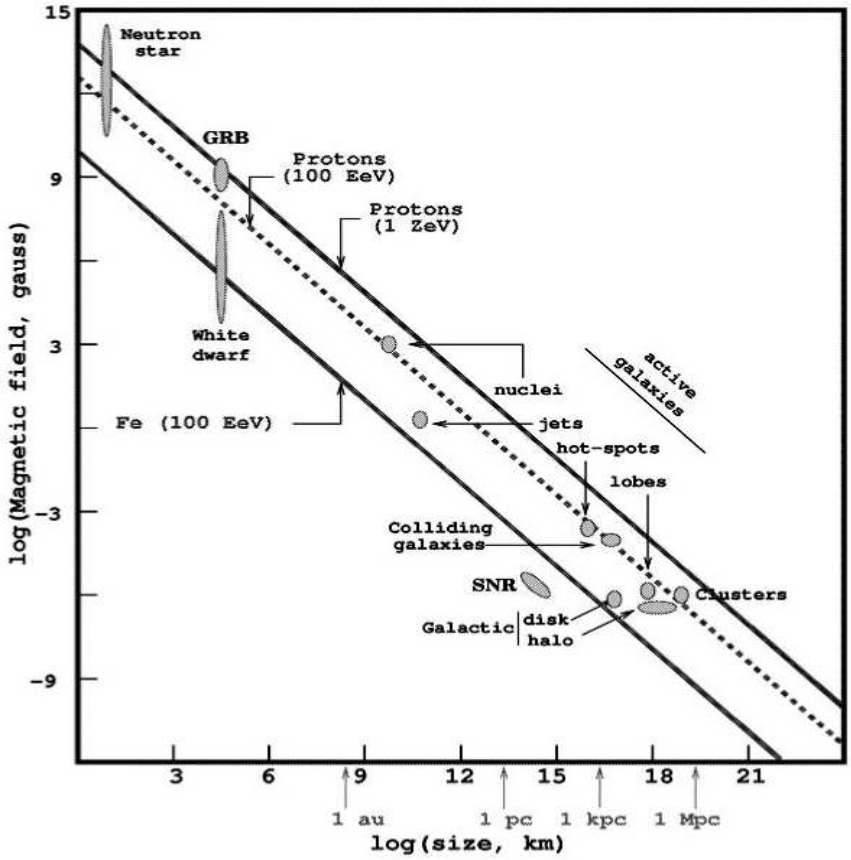

Figure 2.3: Possible candidate sources for cosmic ray primaries are placed on this Hillas plot according to their size and magnetic field [27]

.

2.5 Phenomenology

The measured flux of UHECRs is extremely low, making direct detection impractical. For example, at 5×10^{18} the flux is less than one particle per square kilometer per century. UHECRs are studied by observing secondary particles produced in extensive air showers (EAS). An EAS is created when a cosmic ray particle enters the Earth's atmosphere and it interacts with air molecules initiating a cascades of secondary particles Figure 2.4. An EAS contains millions of secondary particles that are generally categorized into three sub-showers groups, the electro-magnetic, muonic and hadronic components (Figure 2.4). The secondary particles continue traveling until they reach the ground covering a large area. For example, an EAS initiated by a 10^{20} eV cosmic ray may reach an area of 16 km^2 [28].

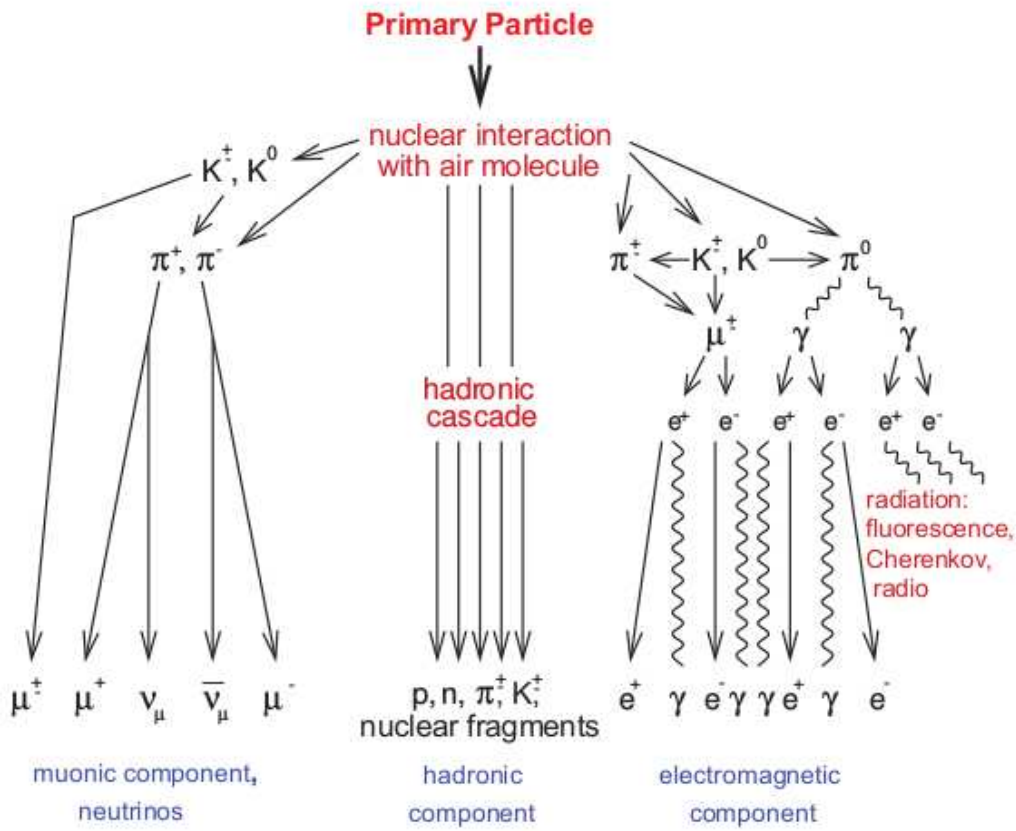

Figure 2.4: A simplified schematic of a vertical EAS in the atmosphere showing the secondary particles created in the electromagnetic, hadronic and muonic component [29].

The longitudinal development of an EAS depends on the energy, type of primary and atmospheric slant depth. Atmospheric slant depth (X) is defined as:

$$X_{slant}(h,\theta) = \frac{1}{cos\theta} \cdot \int_{h}^{\infty} \rho(h)dh \tag{2.7}$$

where "h" is the height, θ is the inclination angle and ρ is the atmospheric density.

2.5.1 Electromagnetic Shower

The electromagnetic component is made of electrons, positrons, and photons. It carries nearly 90% of the shower's energy. The development of its component is described by the Hietler Model [10]. Pair production and Bremsstrahlung radiation are the two dominant components (Figure 2.5).

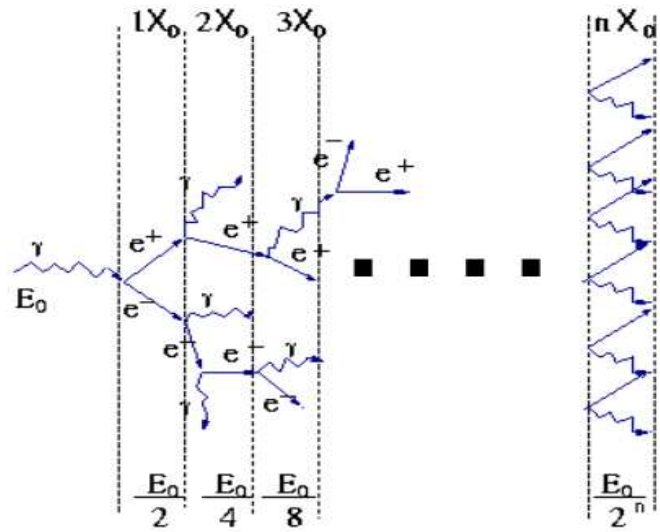

Figure 2.5: The development of an electromagnetic shower according to the Heitler model [30].

For example, a photon interacting with a nucleus in the atmosphere can create a e^+ e^- pair. The $e^\pm$ creates more photons via Bremsstrahlung radiation. These processes repeat until the energy of the photon falls below twice the electron mass (e^- mass $\sim$ 511 KeV). Using the Hietler Model, the number of particles at each step doubles and the energy is equally shared between the particles. After the E_C is reached, energy losses due to inelastic collisions dominate and the shower's intensity decreases. The number of particles (N) follow a geometrical growth according to

$$N(X) = 2^{X/X_0} \tag{2.8}$$

Where X is slant depth and X_0 the interaction length. The average energy of a particle in the shower as a function of the slant depth becomes:

$$E(X) = \frac{E_0}{N(X)} \tag{2.9}$$

where E_0 is the energy of the primary particle. The slant depth of maximum shower development is called X_{max}. The number of particles at X_{max} is:

$$N(X_{max}) = \frac{E_0}{E_C} \tag{2.10}$$

and from equation 2.8 X_{max} can be rewritten as:

$$X_{max} = \frac{ln\frac{E_0}{E_C} \cdot X_0}{ln2} \tag{2.11}$$

Although this simplified model is not completely accurate, (for example an $e^{\pm}$ will not always deposit exactly half of its energy to the Bremsstrahlung photon) it does provides an important relationship between the energy of the primary particle and Xmax, according to:

$$X_{max} \propto log(E_0). \tag{2.12}$$

2.5.2 Hadronic Shower

Hadronic interactions dominate the early development of the shower. When a hadron interacts with an atomic nucleus in the atmosphere, it mostly produces pions and kaons. Kaons decay into pions ($\pi^{\pm}, \pi^0$), muons and neutrinos. The neutral pions decay to a photon pair that contributes to the EM shower. The charged pions decay into muonic and neutrino components. After these decays the EM component quickly dominates the EAS. It can be shown [31] that Xmax is proportional to:

$$X_{max} \propto ln\frac{E_A}{A} \tag{2.13}$$

where A is the mass of the primary nucleus with energy E_A. The hadronic component has been modeled using Quantum Chromo-Dynamics (QCD). These models have been tuned to agree with accelerators at much lower energies, for example the Large Hadron Collider (LHC). These models must be extrapolated to higher energies for use in air shower physics.

Among the most recognized hadronic interaction models used for air shower simulations are: EPOS-QGSJET II [32], SIBYLL [33], and Corsika [34]. A simulation of an EAS created by a proton (energy of 10^{20} eV) is presented in Figure 2.6. The longitudinal profiles and

depth of shower maxima for different particle components are shown.

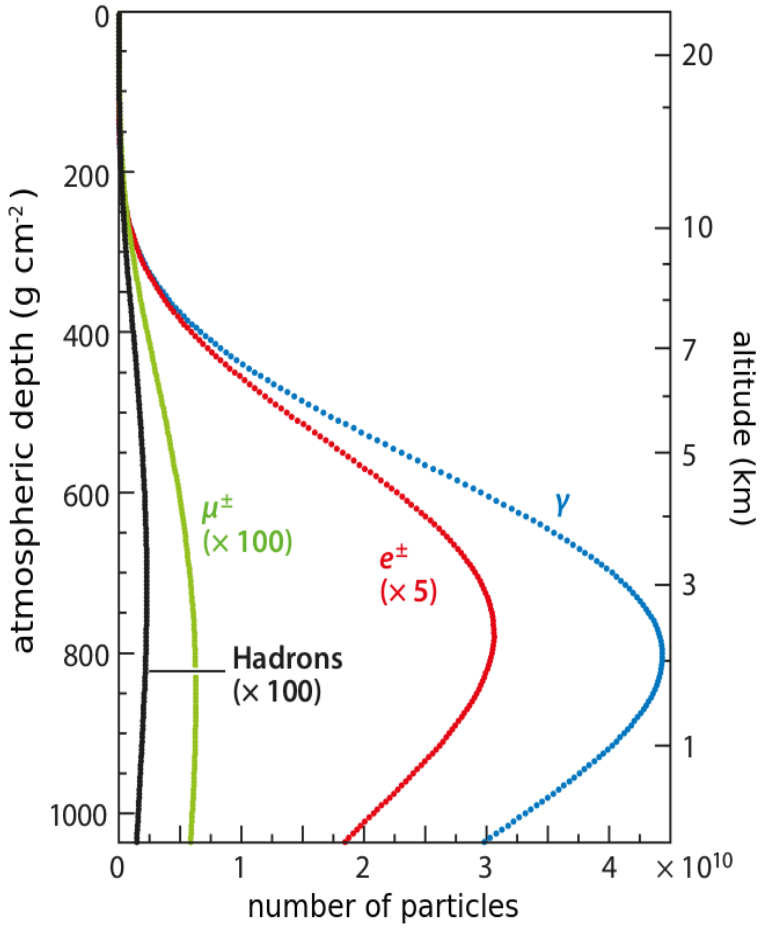

Figure 2.6: A simulation of the number of particles as a function of slant depth and altitude for the muonic component (green line), the EM component (red line for $e^{\pm}$ and blue line for photons) and hadronic component (black line) of an EAS [35]. The electromagnetic component dominates at all altitudes relative to the hadronic component.

2.6 Mass Composition

The determination of the composition is crucial for the understanding of acceleration mechanisms and propagation theories of UHECR primaries. Direct measurements of mass composition is possible for primary particles with energy lower than 10^{14} eV on an event by event basis. This is not the case of UHECR, where only a statistical and indirect estimation is possible. One method is based on the average of X_{max} over large sample of events and

compared to simulations. Auger can measure Xmax with a systematic uncertainty less than 15 g/cm^2. A comparison of shower longitudinal profiles is displayed in Figure 2.7(left) for different proton induced showers simulations and a measured profile by the Pierre Auger observatory. A similar plot using simulation of iron induced showers is displayed on the right.

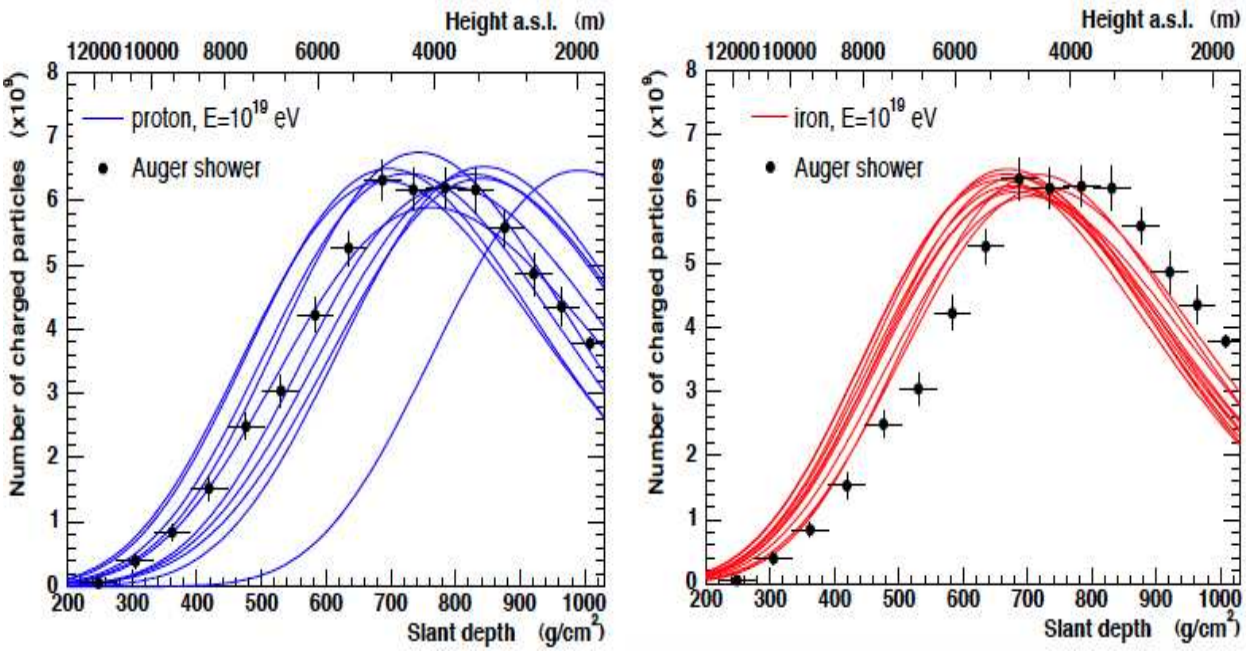

Figure 2.7: Left: Different Xmax distribution for simulated showers with a proton primary compared to a real profile measured by the Pierre Auger Collaboration [30]. Right: The relatively smaller Xmax fluctuations of the iron primaries allows the use the RMS Xmax to identify primaries.

At the same energy, heavier primaries (iron) are more likely to develop higher in the atmosphere than lighter ones (protons). Due to the statistical nature of the EAS process, the primary particle composition can not be determined on a shower by shower basis. Instead the Xmax average and RMS of large samples is calculated and correlated to primary mass. For example, the relative smaller fluctuation on Xmax of the iron primaries compare to proton primaries is used as an identification tool of the shower composition.

Elongation Rate (ER) plots have been used to study composition since the original Fly's Eyes experiment. The ER plots Xmax vs. log(E) (or RMS Xmax vs. log(E)) from data and

compares it to simulations. The latest ER plot from Auger is shown in Figure 2.8. The data and model suggest a mixed composition for the entire energy range. The red and blue lines indicate the mean value for pure proton and iron simulations respectively using post LHC models as EPOS-LCH, QGSJet and Sibyl [36].

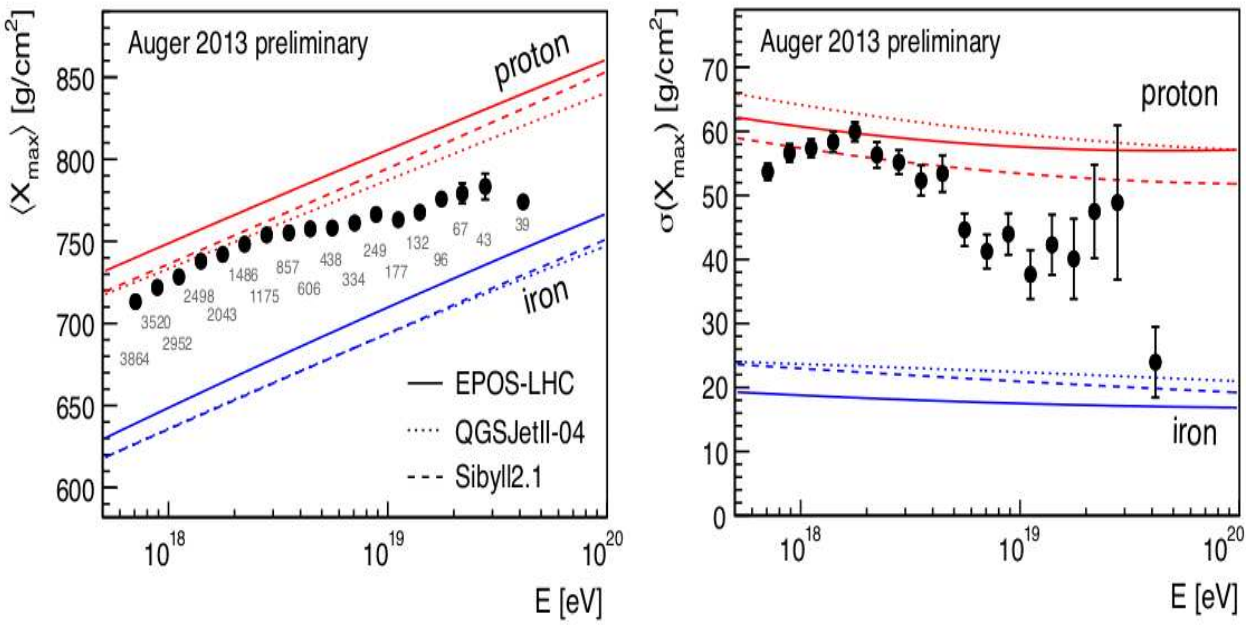

Figure 2.8: Elongation plot for Xmax (left) and RMS Xmax (right). The red and blue lines represent simulation, using different models and primaries. Dots represent the measured number of events in each bin [37]. the number of events used to find Xmax average is below the data. A mix composition of primary particles with a heavier component toward higher energies is visible.

The ER plots reveal a mixed scenario where proton composition dominate over iron composition for all energies. The number of events used to find the Xmax average is presented under the data. But a transition from lighter primaries to heavier is noticeable at higher energies, both in Xmax and RMS Xmax.

The results of mass composition delivered by TA are presented in the elongation plots in Figure 2.9. The data is superimposed with simulations similar to the one presented in the Auger elongation plots. Although TA results seem to favor lighter compositions of primary particles, both results agree within the systematic uncertainties and they allow the possibility

of a heavier composition at the highest energies [38].

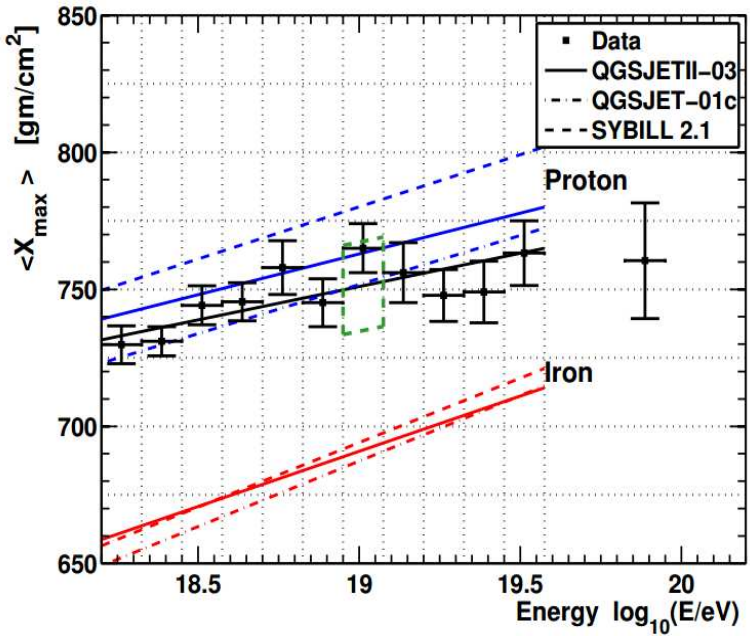

Figure 2.9: Xmax measurements by TA [39]. The color and black lines represent fit to the simulation and data respectively. TA results are compatible with Auger.

CHAPTER 3

THE PIERRE AUGER OBSERVATORY

The Pierre Auger Observatory is the largest cosmic ray detector in the world with an area of 3000 km^2. It is located in the Argentinian region of Mendoza, north of the city of Malargüe at an average altitude of 1400 m above sea level. The observatory measures Ultra High Energy Cosmic Rays (UHECR) with energies above 10^{18} eV [40]. The main scientific goal of the observatory is to answer the most fundamental unknowns about UHECRs, such as their arrival directions, their mass composition and the cosmic ray energy spectrum. Those are important topics that will improve the understanding of the acceleration mechanisms in Supernovae Remnants, Active Galactic Nuclei and Gamma Rays Bursts.

The observatory is named after French physicist Pierre Auger, who was the first to suggest the construction of an observatory of very large proportions [41]. The Auger project concept was born in a series of workshops held in Paris (1992), Adelaide (1993), Tokyo (1993), and Fermilab (Chicago,USA) in 1995 [42], where an international collaboration was established to assure the design and construction of the Observatory [43]. The construction was entirely finished (excluding some extensions) in 2008, with data collection ongoing since January 2004. Currently, the Pierre Auger collaboration is composed of over 500 members, representing institutions from 16 different countries [44]. The observatory includes a central campus headquarters building located in the city of Malargüe. Most of the observatory operations (maintenance and data collection) are controlled from this building.

The observatory uses a hybrid design concept that combines a Surface Detector (SD) and a Fluorescence Detector (FD) (Figure 3.1). The FD measures the EAS longitudinal profile using a calorimetric technique, while the SD samples the particles that reach the ground to measure the EAS lateral profile.

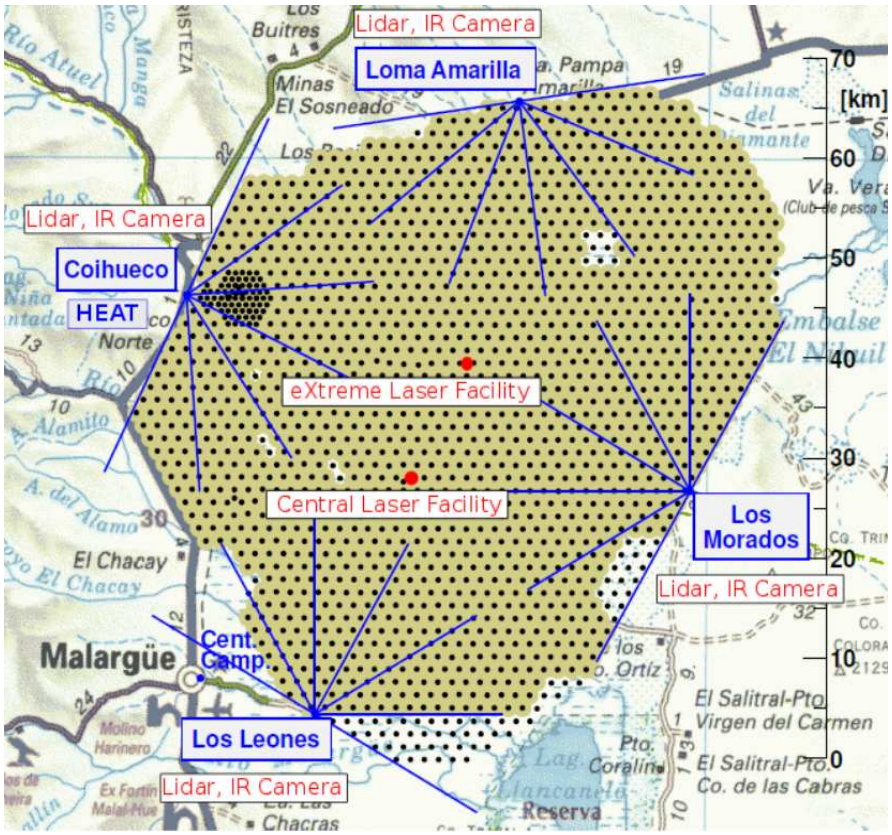

Figure 3.1: Layout of the Pierre Auger Observatory [1]. The city of Malargë, the FD sites and the atmospheric instruments including the CLF and XLF are observed. The approximate locations of the SD stations are represented with black dots. A larger concentration of dots near the Coihueco site represents the SD infill. The FD field of view is illustrated with blue lines.

3.1 The Surface Detector (SD)

The SD is an array of 1600 stations, placed in a triangular grid that extends over 3000 km^2 . The distance between adjacent stations is 1.5km. An SD station is equipped with a water-Cerenkov tank containing approximately 2000 liters of distilled water. Each tank is approximately 3.6 m in diameter and 1.2 m tall. Three downwards-facing PMTs, each with a 9 inch diameter, are located at the top of the tank. Cerenkov light is produced in the tank when relativistic charged particles from EAS pass through the water. This light is captured by the PMTs and recorded by the SD station electronics. The SD is the main statistical collector for the observatory since its duty circle is near 100%. The SD reaches

full trigger efficiency for an EAS above 3 EeV. Each station's electronics is fully powered by solar energy. It communicates with a Central Data Acquisition System (CDAS) in the headquarters building by radio link. the details of the SD design and operations can be found in [45]. A schematic overview of an SD station is shown in Figure 3.2.

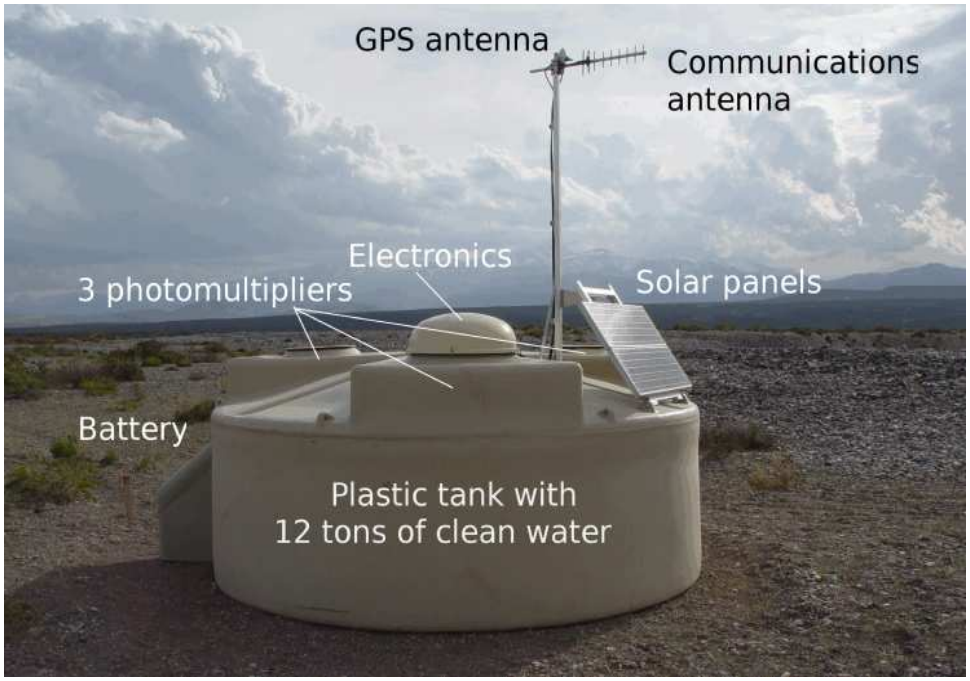

Figure 3.2: A deployed SD station in the field and its main components.

The amount of light collected by the photomultipliers in each SD station is calibrated in terms of 1 Vertical Equivalent Muon (VEM). 1 VEM is the signal recorded by the station electronics when an atmospheric muon passes through the tank vertically. The conversion from raw signals to VEM provides a common reference between stations. Each SD station is triggered when the photomultiplier average signal is larger than 1.7 VEM. This trigger is known as first level (T1) [40]. A second level trigger (T2) is generated if the signal remains above 0.2 VEM for longer than 300 ns. This reduces the rate of the T1 from 100 Hz to about 20 Hz. When a T2 has been activated in a station, its VEM signal and the ones from stations with simultaneous T1 (if any) are acquired as a physical events. All this information is sent to CDAS for storage and later analysis. The next level triggers are made off-line.

A third level trigger (T3) is applied only if neighboring stations were triggered as well. A high quality event (T4) occurs when a T2 station is surrounded by an hexagon of triggered stations. These events are of particular interest for the analysis of vertical showers. The SD is complemented with an infill array for the study of EAS above $3 \times 10^{17} eV$ [40]. This array is considerably smaller in size (23.5 km^2) and the distance between stations is smaller (750 m).

3.2 The Fluorescence Detector (FD)

The FD is composed of 27 telescopes along the perimeter of the SD array, designed to overlook the atmosphere above the SD array [1]. The telescopes are distributed in 4 FD sites.

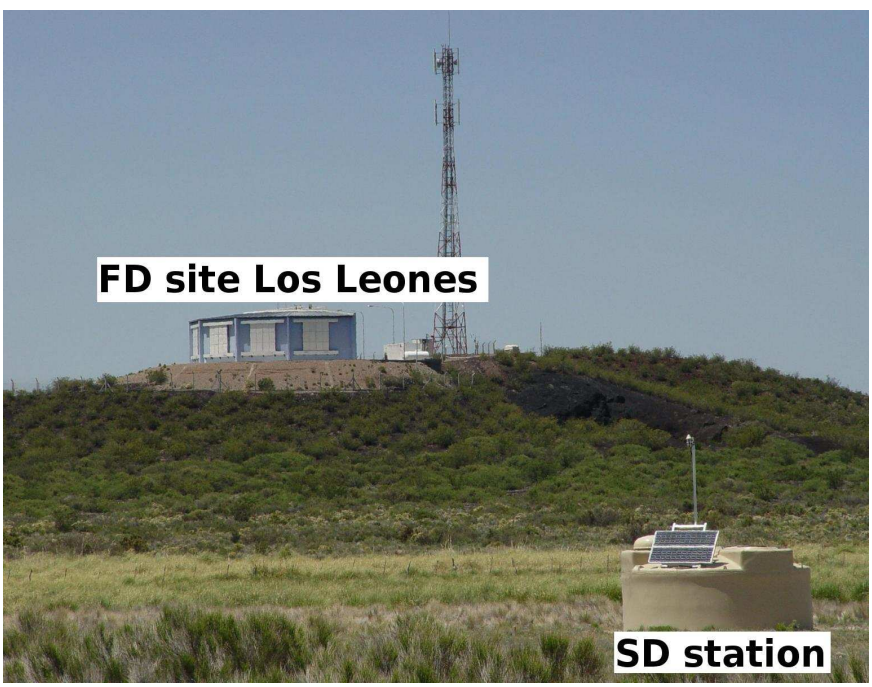

Figure 3.3: The hybrid concept of the observatory including a view of Los Leones FD building and a SD station.

The FD sites are named: "Los Leones" (LL) located in the south, "Los Morados" (LM) to the east, "Loma Amarilla" (LA) on the north and "Coihueco" (CO) to the east (see Figure 3.1). Each FD site has a building housing 6 telescopes (sometimes referred as bays)

with a field of view of 30° X 30° in azimuth and elevation. An additional group of 3 FD telescopes called "HEAT" is also located at the CO site. HEAT has a different field of view, from 30° to 60° in elevation, designed to study EAS developing at higher altitudes in the atmosphere. HEAT is not efficient at detecting the scattered light from the observatory laser facilities. A photo of one FD building next to one SD station is presented in Figure 3.3.

Detected light at a FD telescope from EAS passes through a 2.2 m diameter aperture, an UV filter and a correction ring and reaches the 3.4 m radius segmented spherical mirror. This mirror reflects the light back to the telescope camera. The camera is an array of 440 photomultipliers (PMTs). The telescope also has a protective shutter that opens and closes in cases of unwanted light or inclement weather. A schematic view of the FD telescope building and the telescope elements is shown in Figure 3.5.

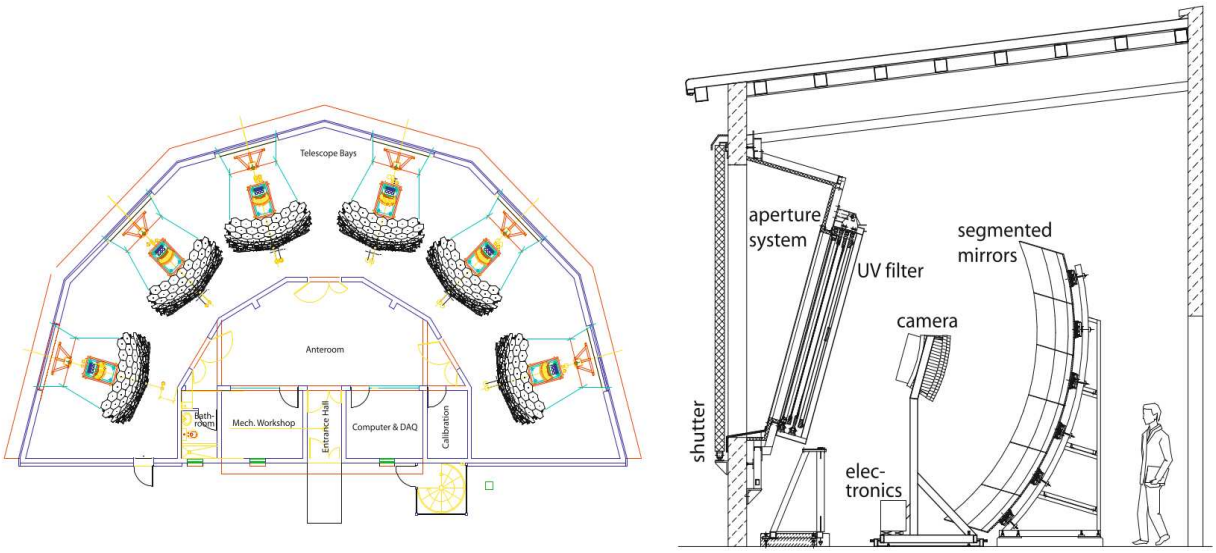

Figure 3.4: Left: Schematic aerial view of one FD site building containing 6 telescopes [46] for a 180° field of view in azimuth. Right: An schematic side view of one FD telescope [46] and its components.

Each PMT has a hexagonal shape with a 46.6 mm side length. They are arranged in a honeycomb array configuration of 20 columns by 22 rows. Each PMT constitutes a pixel in the camera with an individual field of view of 1.5° by 1.5°. Between each PMT a star shaped

light collector is installed to minimize any light lost between gaps. These plastic pieces are coated with aluminized "Mylar" foils.

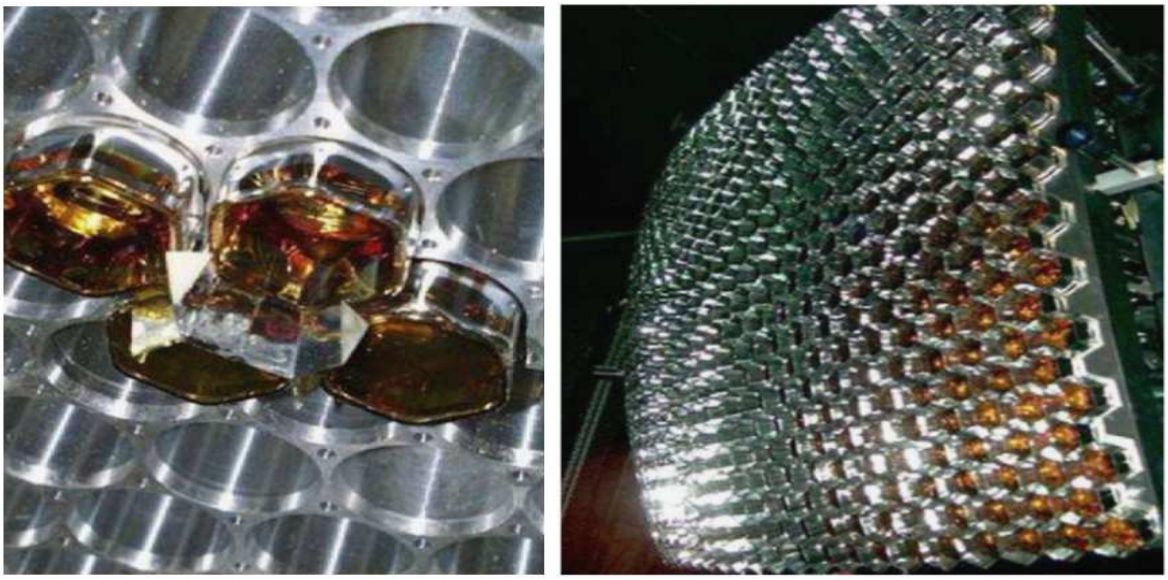

Figure 3.5: Left: Some PMTs and light collectors are mounted on the camera metallic structure [46]. Right: The camera with all PMTs and light collectors mounted [46].

The data acquisition system of a telescope is controlled by the front end electronics mounted on the camera rack and an associated mirror computer. Three trigger levels are implemented. The First Level Trigger (FLT) is performed by a circuit in the camera that digitizes the PMT output and identifies signals beyond a threshold value. The threshold value is dynamically adjusted to produce a rate of 100 Hz. The Second Level Trigger (SLT) is also a hardware trigger that collects its input from the FLT. It looks for chronological patterns in the camera which could possibly be the signature of an EAS. At least five adjacent triggered pixels are required by the SLT to pass the trigger as a possible even. Figure 3.6 provides examples of the five most common patterns.

Events passing the SLT are sent to the central computer in the FD building for Third Level Trigger (TLT) analysis. The TLT is a software trigger which discards events generated by background light or any other unwanted events (e.g. lightening, electronic noise, etc). Events passing TLT selection are sent to CDAS using a radio link.

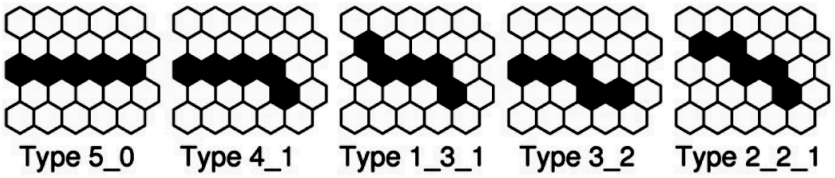

Figure 3.6: Fundamental types of pattern searches for the Second Level Trigger [47].

The FD data analysis of EAS tracks requires the calibration of the camera signal into units of "photons per aperture". The reference standard, described in [48], is known as "the Drum". The Drum is a 2.5 m diameter by 1.4 m deep drum shape light source which provides identical light flux to each pixel (an average of 5 photon per ADC bin). The same drum is carried to the different telescopes. An additional relative calibration is performed in the FD cameras before and after data acquisition [49]. This calibration tracks changes in the FD performance by uniformly flashing the same light from three different light sources mounted at different positions. The light sources are a 470 nm LED and a two xenon flash lamps [46]. The light arrives to the FD cameras via optical fiber and a diffuser in the center of the optical mirrors. A full description of the design and operations of the FD can be found in [46].

3.3 Other Extensions to the Observatory

The Pierre Auger Observatory science program includes the research and development of new detection techniques. The Auger Engineering Radio Array (AERA) studies a new technique to observe EAS by detecting a short radio signal with antennas in the 30 to 80 MHz range. The moving charged particles in an EAS emit radio signals which can be observed by 124 AERAs antennas which are distributed over a 6 km^2 area [50] . The AERA radio stations duty cycle is almost 100% since the antennas only need to be turned off during thunderstorms. This new technique can independently measure the energy and arrival direction of EAS.

Another extension to the observatory is the AMIGA (Auger Muon Infield Ground Array) project. The objective of the project is to extend the SD detection capabilities to lower energy particles (less than 10^{17} eV) by installing muon counters 2.5 m underground next to SD stations. The muon counters provide information used to better understand the muon contribution in EAS.

3.4 Atmospheric Monitoring

Altitude profiles of atmospheric state variables (e.g temperature, pressure, humidity) have been measured in detailed at the observatory. Air density and molecular optical depth can be derived from these variables. Several campaigns of meteorological balloon launches took place between 2002 and 2010 [51]. These measurements validated the use of the Global Data Assimilation System (GDAS) in the air shower reconstruction. Additionally, the observatory maintains a network of atmospheric systems, including a horizontal attenuation monitor, an aerosol phase function monitor, a network of cloud cameras, elastic and Raman LIDARs, and two laser facilities. These systems can be identified in Figure 3.1.

3.4.1 HAM and FRAM

The Horizontal Attenuation Monitor (HAM) is located at the Coihueco site. It is used to measure the dependence of the aerosol extinction coefficient (α) of the air with respect to the light wavelength. The system fires a horizontal collimated beam of light at five different wavelengths which is detected by a CCD (Charge-coupled device) camera at the LL site (about 45 km away). It also monitors the time dependence of the aerosol extinction by firing hourly during FD operation times.

The Photometric Robotic Atmospheric Monitor (FRAM) measures the integrated optical depth by comparing the light flux of some stars and their values from catalogs. FRAM has measured the Angstrom coefficient with a value of 0.1 ± 0.9, in good agreement with expected theoretical values for a desert-like region [52].

3.4.2 APF

There are two Aerosol Phase Function (APF) monitors located at the CO and LM site. An APF measures the differential scattering cross section σ/Ω. The measurements are achieved by firing a Xenon flash lamp of collimated light at wavelengths between 350 nm and 390 nm across the two FD sites. Then, the FD measures the amount of light registered as a function of the scattered angle. Analysis of this data suggests that the aerosol scattering follows the Henyey-Greenstein function (equation 3.11). Detailed information about the APF and the analysis can be found in [53].

3.4.3 Cloud Cameras

Infrared cameras have been installed on the roof of every FD building to detect clouds at night. Each camera has full coverage of the sky at a wavelength between 7 and 14 μm. They take a picture of the sky every 15 minutes. For the majority of the physics analysis, hybrid data is only used if the hourly cloud coverage is below 20% [54]. The cloud coverage is extracted from the cloud cameras and the LIDARs.

3.4.4 Elastic LIDARs

LIDARs (Light Detector and Ranging) are used in Auger to measure the cloud coverage above the detector [55]. They are also able to provide profiles of the backscatter coefficient or the extinction coefficient. Four elastic LIDARs are installed, one near each FD site. All LIDARs fire 300 Hz, 351 nm laser pulses with an energy of 0.1 mJ. The laser is fired in directions of the sky behind the field of view of the corresponding FD site telescopes. A telescope measures the elastic backs-scattered light by particles and molecules in the atmosphere. The LIDAR telescopes collect light with three 80 cm radius concave mirrors and a fourth 20 cm radius concave mirror. Each mirror reflects the light into a wavelength filter and then into a photomultiplier. The LIDARs are steerable and semi-automatic. They are controlled from the central campus during FD data taking.

3.4.5 Raman LIDAR

A Raman LIDAR was installed for the observatory atmospheric monitoring in 2013 at the CLF site as part of the CLF upgrade. Raman LIDARs are inelastic LIDARS. They detect back-scattered light with shorter wavelength than the light emitted. The primary measurement of the Raman LIDAR is the aerosol vertical optical depth profiles of the atmosphere above the CLF, but it can also provide vertical profiles of the water content, the elastic backscattering coefficient and the aerosol extinction. The installation was a team effort between two institutions: Colorado School of Mines and University of L'Aquila. A detailed description of the Raman LIDAR will be given in Chapter 4.

3.4.6 The CLF and the XLF

The Central Laser Facility (CLF) and the eXtreme Laser Facility (XLF) are the laser test beams for the Pierre Auger Observatory. These multipurpose facilities produce the light used by the FD to measure hourly profiles of the vertical aerosol optical depth (VAOD or τ) during FD data taking. The CLF and XLF are similar (but not identical) in design and operation. The outside of the laser facilities and a nearby SD station are shown in Figure 3.7.

Figure 3.7: Left: A picture of the CLF, near the Celeste SD station. Right: A picture of the XLF, near the Ramiro SD station.

The CLF and XLF location are designed to be nearly equidistant to three FD sites (see Figure 3.1). Table 3.1, Table 3.2 and Table 3.3 summarize the location, distances and angles between the FD and laser facilities.

Table 3.1: UTM coordinates (Zone 19H) of the FD buildings and the laser facilities according to GPS survey [56].

Building name	UMT EAST	UMT NORTH	Altitude (m.a.s.l)
Los Leones	459201	6071873	1421
Los Morados	498898	6094561	1423
Loma Amarilla	480734	6134057	1483
Coihieco	445347	6114147	1719
CLF	469378	6095769	1412
XLF	473873	6106126	1409

Table 3.2: Distances (in km) from the laser facilities to the FD sites.

Name	Los Leones	Los Morados	Loma Amarilla	Coihueco
CLF	26.56	28.11	39.53	31.40
XLF	37.25	27.57	28.76	29.62

Table 3.3: Angles are measured counterclockwise from the east. The angle vertex is located on the FD eye

Name	Los Leones	Los Morados	Loma Amarilla	Coihueco
CLF	67.03°	177.70°	-111.10°	-37.45°
XLF	66.84°	155.23°	-104.45°	-15.70°

Both systems fire 10 ns laser pulses with energies near 5 mJ and 355 nm wavelength. Every 15 minutes during FD operations, each laser facility fires 50 laser pulses at a 1Hz rate vertically towards the sky. The laser wavelength is near the prominent 357 nm band of ultraviolet fluorescence, (see Figure 3.8). This is important because the laser light scattered by air molecules and aerosols produce tracks in the FD that appear similar to EAS tracks. A photometric comparison of the FD detected laser scattered light with respect to a reference hour, clear of aerosols, is the basis for hourly τ measurements. The details of these measurements will be explained in Chapter 6.

Other uses for the laser facilities are:

- Geometrical reconstruction studies: Laser shots are directed toward astronomical objects of interest to check the FD geometrical reconstruction of events.
- FD inter-calibration: Laser steered with an accuracy of 0.2° can be directed toward any point between FD eyes to inter-calibrate the FD stereo performance.
- Timing offset studies: Some amount of laser light is diverged by beam splitter optics into a optic fiber and conducted into a nearby SD station in a hybrid event fashion.

The XLF was completed in 2007 but just a few weeks after completion, a terrible accident occurred and the XLF was destroyed by an explosion. The caused of the explosion is believed to be a small undetected internal gas leak in the heater system. The XLF was rebuilt and resumed operations in 2009. The CLF was originally built in 2003 [57], it was operational for nearly 10 years until it was significantly upgraded in 2013. This upgrade is one of the main topics of this thesis and it will be explained in detail in Chapter 4.

3.5 Fluorescence Detection at Auger

The fluorescence detection technique is based on the photo detection of UV light emitted by atmospheric N_2 molecules that are excited by the passage of an EAS. The lifetime of excitation is around 10 ns and then light is emitted isotropically. Most of these emissions range typically between 300 nm and 400 nm, with the more prominent peaks located at 337 and 357 nm (Figure 3.8).

3.5.1 Light Propagation

The relationship between the amount of fluorescence light emitted and the energy of the EAS is known as the fluorescence yield. The fluorescence yield depends on the gas mixture in the atmosphere and on atmospheric conditions. Several experiments have measured the fluorescence yield with a precision of about 14%. They estimate an emission of 4 to 5 fluorescence photons per meter, per charged particle [59]. The photons reaching the detector

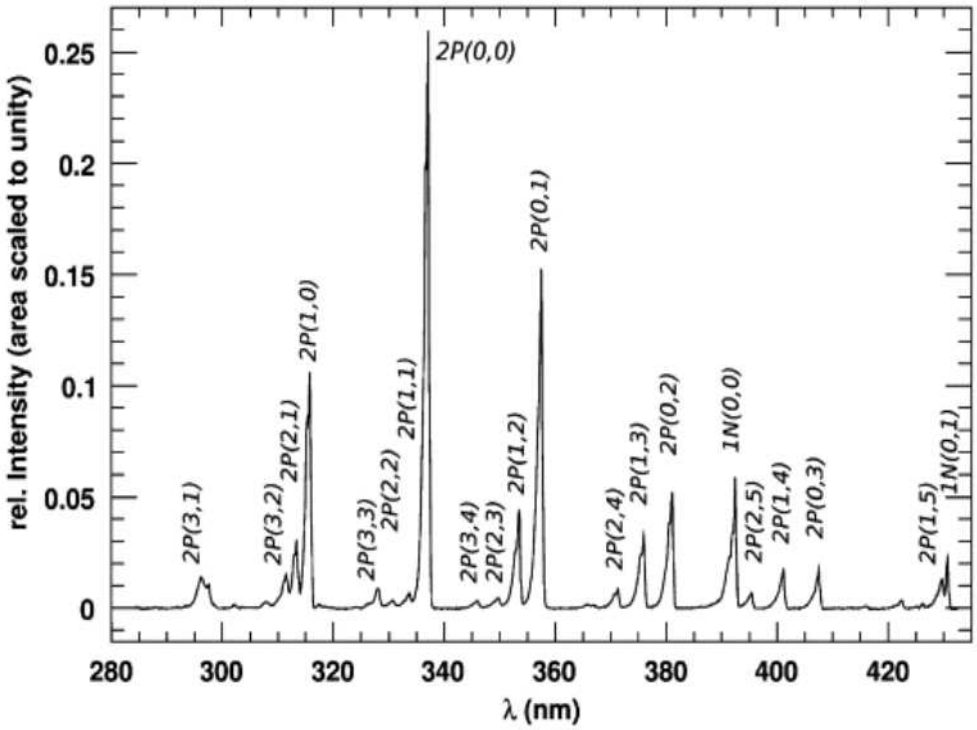

Figure 3.8: The second positive fluorescence spectrum of the N_2 molecule measured by the AIRFLY collaboration with an electron beam of 3 MeV [58].

from excited N_2 molecules must travel through different regions of the atmosphere. These distances typically range from 2 to 30 km. During this time, the light experiences attenuation processes due to absorption and scattering by molecules and aerosols. Consequently the knowledge of the atmospheric conditions at the time of detection becomes very important.

The attenuation of the light is characterized by the optical depth transition coefficient $T(H, \lambda)$ defined as:

$$T(H, \lambda) = \frac{I(\lambda)}{I_0(\lambda)} \tag{3.1}$$

where $I(\lambda)$ is the intensity of the light with wavelength λ after traveling through a layer of atmosphere H from a light source with intensity $I_0(\lambda)$. The "optical depth" $\tau(H, \lambda)$ can be defined in terms of $T(H, \lambda)$ using the BeerLambert-Bougers law:

$$T(H, \lambda) = e^{-\tau(H,\lambda)} = e^{-\int_0^H \alpha(r)dr} \tag{3.2}$$

where $\alpha(r)$ is the extinction coefficient and represents the probability per unit length, that a photon can be either scattered or absorbed. Assuming horizontal uniformity, the transmission coefficient for an elevation at an angle θ over the horizon can be expressed as:

$$T(h, \lambda, \theta) = e^{-\tau(h,\lambda)/sin(\theta)} \tag{3.3}$$

where h is the height above ground level.

The transmission factor from 3.2 (atmospheric transmission) can be separated into two components: $T_{molecular}(H, \lambda)$ due to Rayleigh scattering and $T_{aerosol}(H, \lambda)$ due to the aerosol component.

$$T = e^{(-\tau_M - \tau_A)} \tag{3.4}$$

3.5.2 Rayleigh and Mie Scattering

Rayleigh scattering is a well known electromagnetic process. Its contribution can be calculated using measurements of the vertical profiles of temperature and pressure. The molecular transmission as a function of the total Rayleigh cross section can be written as.

$$T_{mol}(H, \lambda) = e^{-\int_0^H \sigma_R(\lambda) N_{mol}(H) dH} \tag{3.5}$$

where

$$N_{mol}(H) = \frac{N_A}{R} \cdot \frac{p_h}{T(h)} \tag{3.6}$$

and,

$$\sigma_R(\lambda, p, T, e) = \frac{24\pi^3}{\lambda^4 N_{mol}^2} \cdot \left(\frac{n_{air}^2 - 1}{n_{air}^2 + 2}\right)^2 \cdot F_{air}(\lambda, T, p, e) \tag{3.7}$$

where N_A is Avogadro's number, n_{air} is the refractive index of the air and F_{air} is the "King" correction factor that accounts for anisotropic scattering introduced by the non-spherical scattering [60].

Aerosol scattering is more complicated. The concentration of the aerosol particles floating in the air changes rapidly with time and altitude. In addition, the shapes of the aerosol also affects the wave-dependence of the scattering. Types of aerosols include ice crystals, organic

particles, fog and clouds. Studies suggest several aerosol origins including ocean air mass transport, wind blown dust, urban pollution and biomass burning [61]. They have a wide range of sizes, from a few tens of nanometers to a few millimeters. Two aerosol samples collected at the observatory site under an electron microscope are presented in Figure 3.9.

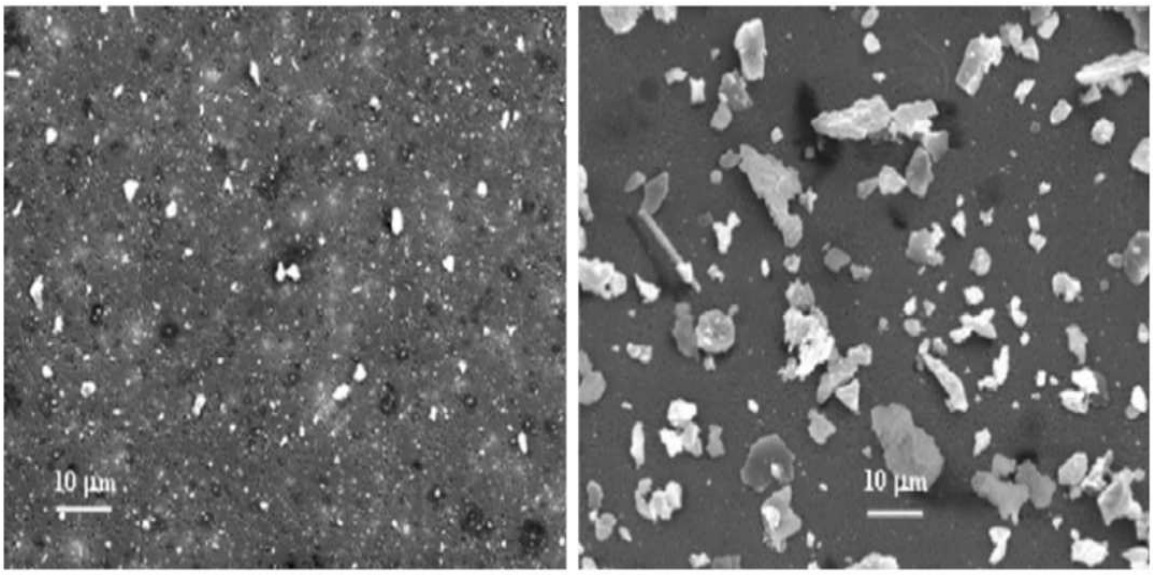

Figure 3.9: Two aerosol samples taken at the observatory in 2008 under an electron microscope reveal the size of the aerosol particles [62]. Left: Sample taken during a low aerosol content period. Right: Sample taken during a high aerosol content period.

Aerosol scattering can be approximated using Mie scattering theory. Under a horizontally uniform atmosphere the aerosol extinction coefficient can be expressed as:

$$\alpha_{aer}(h,\lambda) = \alpha_{aer}(h,\lambda_0) \cdot \left(\frac{\lambda_0}{\lambda}\right)^{\gamma} \tag{3.8}$$

where γ is the Armstrong coefficient.

From equation 3.3 the aerosol transmission can be expressed in terms of the optical depth (τ) in a similar way as in

$$T_{aer}(h,\lambda,\theta) = e^{-\tau_{aer}(h,\lambda)/sin(\theta)} \tag{3.9}$$

The vertical optical depth of the molecular τ_{mol}(Rayleigh) and representative aerosol profiles τ_{aer}(mie) are presented in Figure 3.10. The comparison is for UV light at 355 nm

wavelength under three different atmospheric aerosol conditions [51]. The profiles presented are monthly averages over a year of data at the Pierre Auger Observatory. The molecular profile increases with altitude but it is affected by the decreasing number density of nitrogen and oxygen. The τ_{aer} profiles typically flatten at altitudes of 8 km where the aerosol concentration becomes negligible.

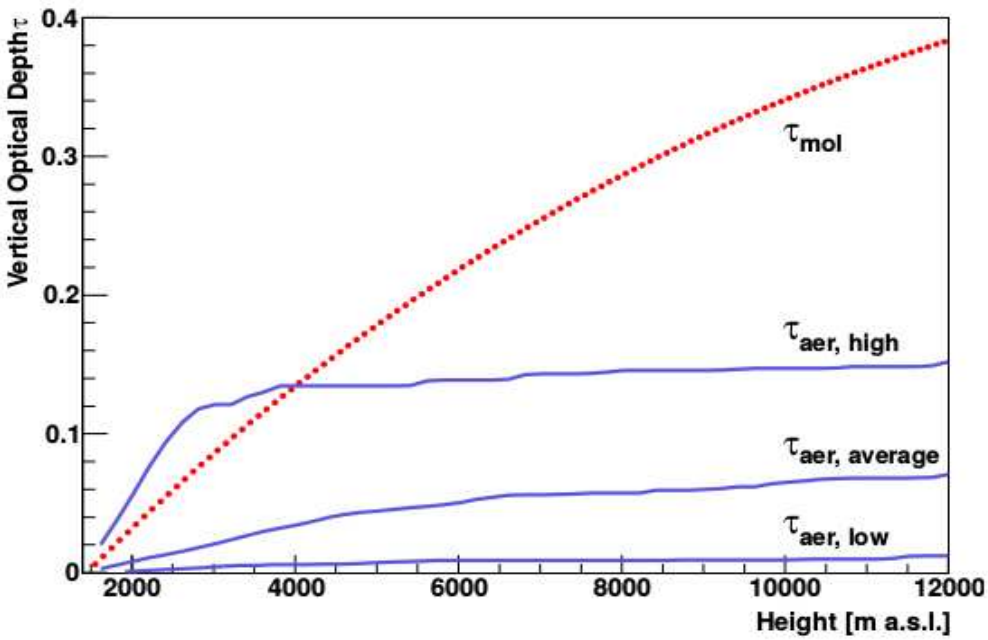

Figure 3.10: A Calculated profile of τ_{mol} (dots), is compared with three profiles of measured τ_{aer} under high, average, and low aerosols concentration (blue solid lines).

3.5.3 Phase Function

The amount of light scattered at different angles is characterized by the differential cross section also known as phase function. For Rayleigh scattering the phase function can be parameterized as:

$$P_{mol}(\theta) = \frac{3}{16\pi} \cdot \frac{1}{1+2\gamma} \cdot \big((1+3\gamma) + (1-\gamma)cos^2(\theta)\big) \tag{3.10}$$

where gamma is a polarization factor with a value near 0.01 [63]. The phase function provides larger values for angles closer to incoming direction of the light and smaller values for opposite

directions. The aerosol phase function does not have an exactly analytical solution but it has been parameterized according to the "Henyey-Greenstein" function [64]:

$$P_{aer}(\theta) = \frac{1-g^2}{4\pi} \cdot \left(\frac{1}{(1+g^2-2g \cdot cos\theta)^{3/2}} + f\frac{(3cos^2\theta - 1)}{2(1+g^2)^{3/2}} \right) \tag{3.11}$$

The first term accounts for the forward scattering while the second term describes a peak in the background scattering. The factor f is the strength between the two terms and g is a measurement for the asymmetry of the scattering. Both of these two parameter depend on the local aerosol conditions. A descriptive figure comparing the Rayleigh and Mie scattering is presented in Figure 3.11.

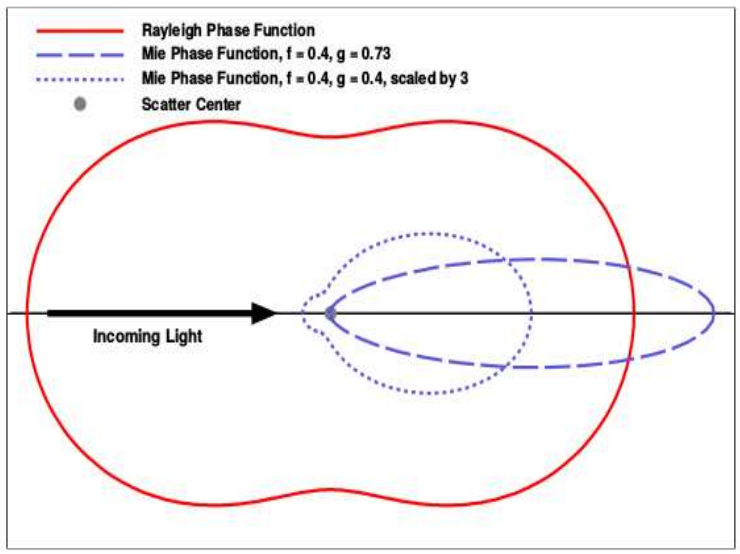

Figure 3.11: A comparison of the scattering phase function between Rayleigh (red) and Mie scattering (blue) [51].

3.5.4 Atmospheric Effects on the Fluorescence Detection

Aerosols increase the light attenuation and reduce the amount of photons reaching the cameras. Some studies by the Pierre Auger collaboration estimate that aerosol effects may bias the energy reconstruction of cosmic rays up to 25% and the Xmax reconstruction up to 8 g/cm^2 (Figure 3.13).

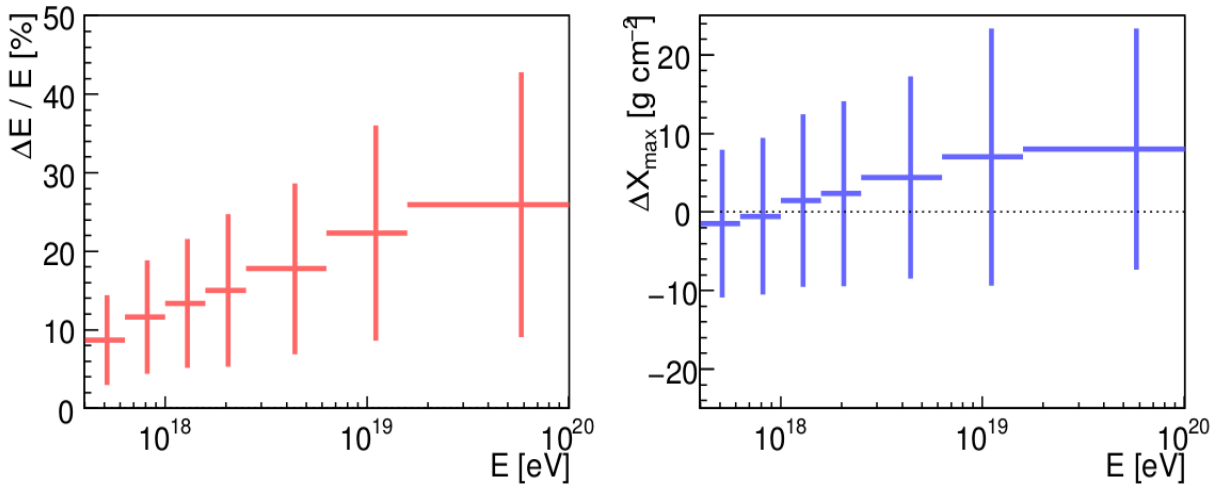

Figure 3.12: Left: Difference in the energy (left) and Xmax (right) reconstructed values using the aerosol measurements from the CLF and the assumption of purely molecular transmission [65].

The study included multiple-scattering effects(Figure 3.13). These effects bias the reconstruction of the energy between 2% and 5% and produce an increase on Xmax up to 2 g/cm^2.

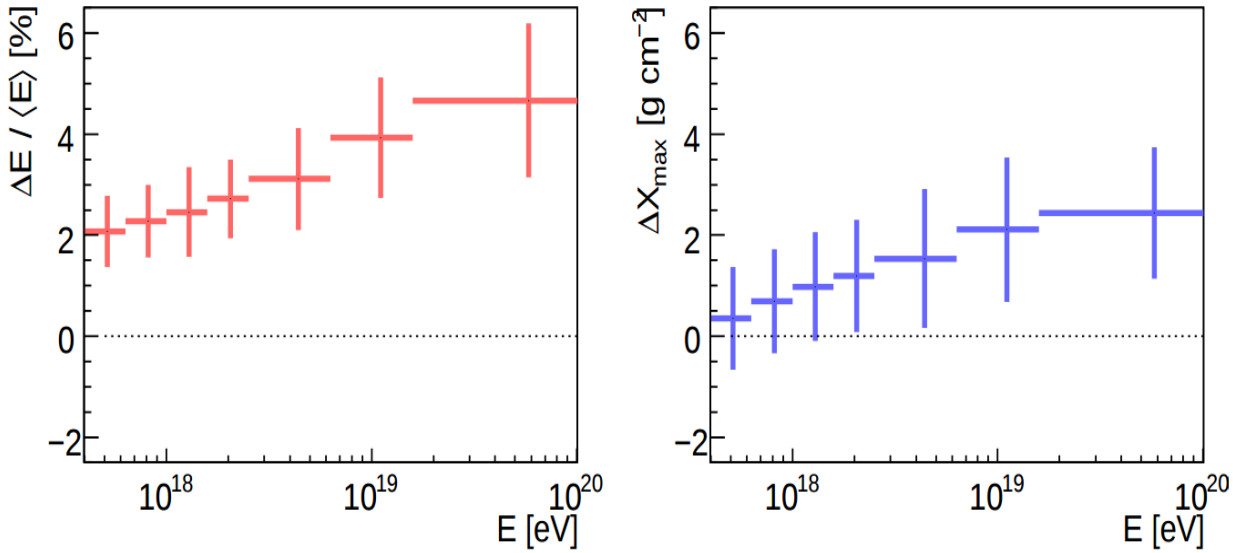

Figure 3.13: Left: Difference in the energy (left)and Xmax (right) reconstructed values when the multiple scattering effects are taken into account [65].

This bias in the reconstruction can be significant, making the monitoring of aerosols extremely important in any florescence observation. Aerosols must be measured continuously since aerosol contents may vary on hourly time scales. An effort to include multiple scattering corrections in these techniques will be addressed in Chapter 7.

3.6 The Offline Software Framework

The Pierre Auger Observatory uses a common software framework called $\overline{Off}\underline{line}$. A detailed description of the framework is found in [66]. This software is employed to manage all the physics analysis, including simulation and reconstruction of EAS and laser events. The most useful features of $\overline{Off}\underline{line}$ include:

- It is a modular platform, written entirely in C++ language.
- Uses XML cards to configure different modules without changing any source code.
- Full integration of a database system (MySQL software). Examples of the databases include: atmospheric, calibration and weather conditions.
- uses ROOT files for efficient data storage known as Advanced Data Summary Trees (ADSTs).
- A visualization tool called "EventBrowser" for reconstructed events.

A nice example of a shower event seen by all 4 FDs is presented in Figure 3.14 (left) using "EventBrowser". This tool also allows the visualization of the pixels triggered in the FD camera and the photon trace response (see Figure 3.14(right)).

The techniques used for event reconstruction vary depending if they are recorded on the FD, the SD, or both. This latter events are known as hybrid. The reconstruction is based on the signal of the triggered pixels and PMTs in the tanks for the FD and SD respectively. A brief description of these processes is provided in the next sections.

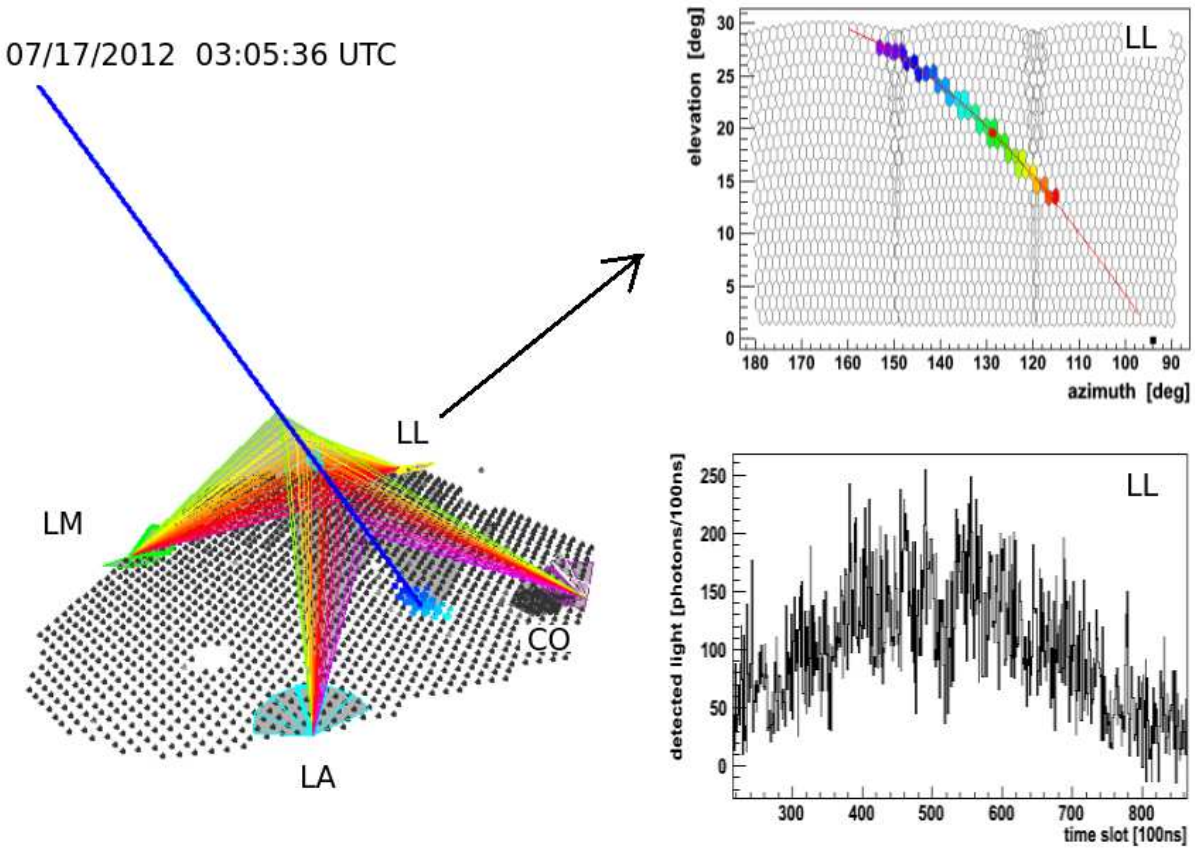

Figure 3.14: Left: A hybrid event successfully reconstructed by the 4 FD telescopes triggers some SD stations (represented by color). All other SD stations can be seen as black dots. Colored lines represent the fluorescence light seen by the telescopes. Right top: Pixels trigered by this event spread over three adjecent bays in FD Los Leones. They are represented by hexagons color coded acording to the time of light detection. Right bootom: The photon trace produced in Los Leones by this event.

3.7 FD Reconstruction

The FD reconstruction can be separated into two major parts, geometrical reconstruction and profile reconstruction. Geometrical reconstruction starts by determining the shower detector plane (SDP) defined as the plane that includes both the FD eye and the line that represents the shower axis (see Figure 3.15).

The calculation of the SDP involves a χ^2 minimization of the triggered pixel's field of view vector projected onto the normal vector of the SDP and weighted by the pixel signal.

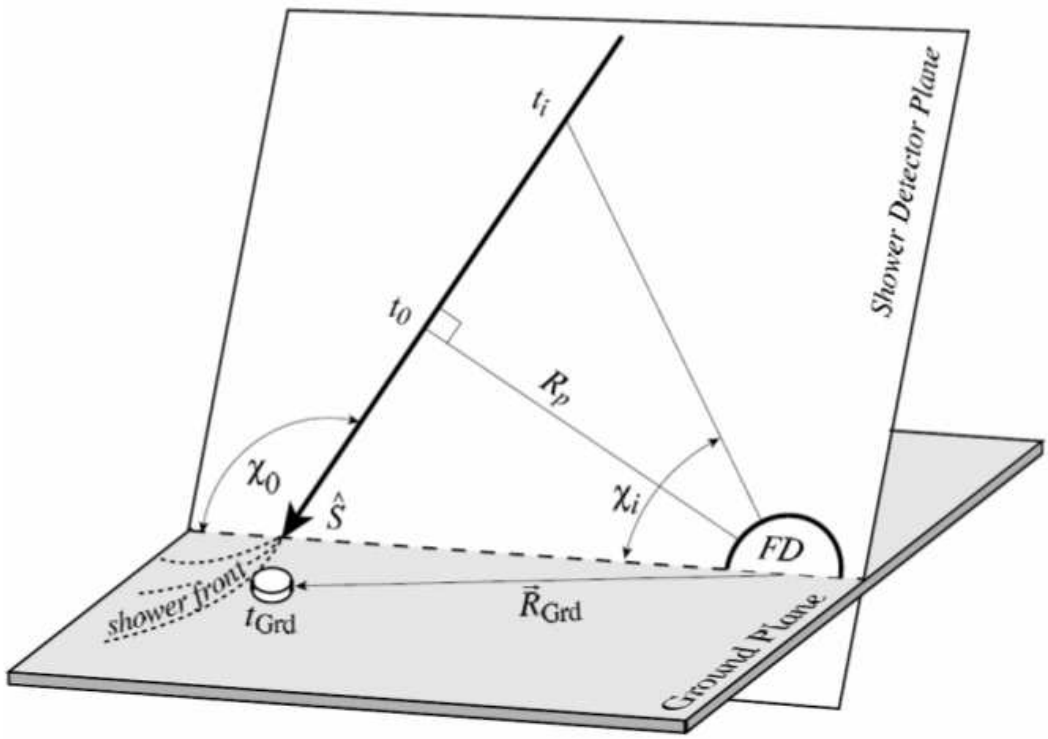

Figure 3.15: A representation of the shower detector plane from a cosmic ray as it travels in front of the field of view of one FD telescope.

Once the SDP has been determined, the shower axis is found by calculating three free parameters:

- R_p: the closest distance from the track to the eye.
- $\overrightarrow{\chi}_0$ is the angle between the track and the horizontal.
- t_0: time of emission at R_p.

The parameters are found minimizing (over all the triggered pixels)

$$\chi^2 = \sum \frac{(t_i - t(\chi_i))^2}{\sigma(t_i)^2} + \frac{(t_{SD} - t(\chi_{SD}))^2}{\sigma(t_{SD})^2} \tag{3.12}$$

where

$$t(\chi_i) = t_0 + \frac{R_p}{C} \cdot tan\left(\frac{\overrightarrow{\chi}_0 - \overrightarrow{\chi}_i}{2}\right) \tag{3.13}$$

and χ_i is the angle between the horizontal plane and each emission point. C is the speed of light. To obtain χ_0 with better accuracy the information associated with the SD is included. This "Hybrid reconstruction" uses the timing information (t_{SD}) from the SD stations closest to the shower core and the expected angle (χ_{SD}) at ground. σ_{SD} and $\sigma(t_i)$ are the associated uncertainties. The reconstruction uncertainties are validated using a known geometry, for example tracks from the CLF and the signals from its adjacent SD station produces a hybrid event (The CLF location and its axis angle are known). The geometry reconstruction has an accuracy of 50 m in the shower's core estimation, and a resolution 0.6° in the arrival direction [67].

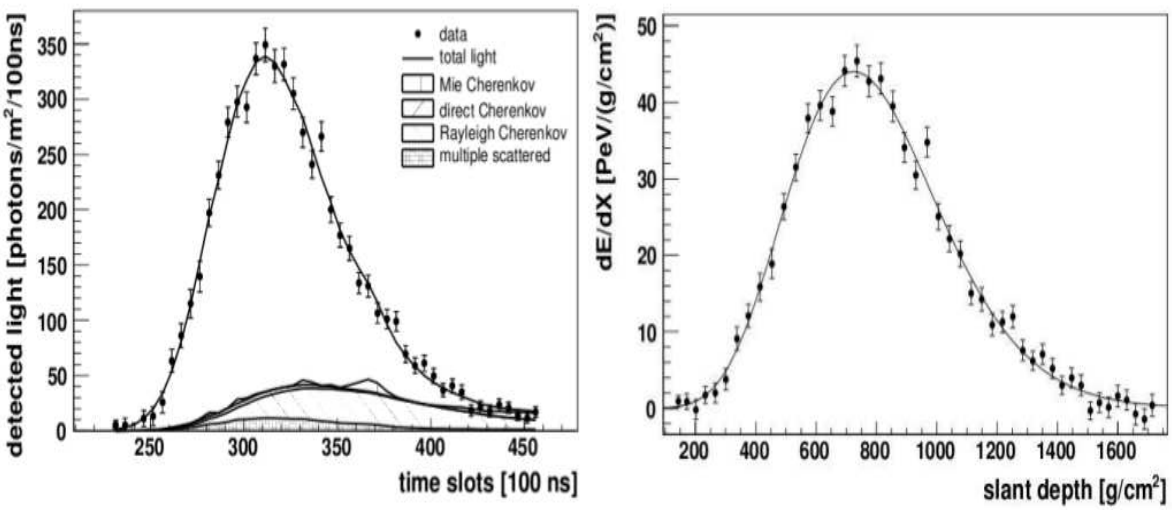

Figure 3.16: Left: Example of the FD reconstruction of one event. Left: Light at aperture for different light components. Right: Energy deposition as a function of slant depth, X_{max} can be found after this profile is fitted with a GHF [68].

After the shower geometry is reconstructed, the energy reconstruction can be implemented. The signal of the pixels (number of photons collected) as a function of time is used to calculate a shower profile as function of slant depth. To do this accurately, the light attenuation from the light source to the pixel due to the atmospheric conditions needs to be included [23], [69]. Light attenuation effects on the Cerenkov light and the fluorescence light produced by the shower and multiple scattering effects are taken into account. Finally, the

longitudinal energy profile is estimated by fitting to a Gaisser-Hillas function (GHF) [70]

$$f_{GH}(X) = \left(\frac{dE}{dX}\right)_{max} \cdot \left(\frac{\chi - \chi_0}{\chi_{max} - \chi_0}\right)^{(\chi_{max}-\chi_0)/\lambda} \cdot e^{(\chi_{max}-\chi_0/\lambda)} \tag{3.14}$$

Where X_{max} is the position of the shower maximum, $\left(\frac{dE}{dX}\right)_{max}$ is the maximum energy deposit, χ and χ_0 are two shape parameters. The final step is to correct for the invisible energy carryout by the neutrinos and high energy muons in the shower. This correction is based on Monte-Carlo simulations [46] and it is of the order of 10% for mixed composition [71]. An example of the light reconstructed at aperture vs time for different source components and the final energy profile reconstruction as a function of slant depth are shown in Figure 3.16.

3.8 SD Reconstruction

SD reconstruction is fundamentally different from the FD. Since the SD is incapable of measuring the longitudinal profile of the shower, assumptions are made based on the well defined lateral profile provided by the SD stations. The first step in the reconstruction is to calculate the shower axis. For a particular event, a spherical model is assumed if at least four stations have been triggered. A spherical wave-front traveling at the speed of light c is assumed to have a time evolution according to

$$c \cdot (t_i - t_0) = |\overrightarrow{x}_0 - \overrightarrow{x}_i| \tag{3.15}$$

where t_i is the time information and $\overrightarrow{x}_i$ the position at each station. t_0 and $\overrightarrow{x}_0$ are the time and position of a virtual shower origin (Figure 3.17).

After the shower arrival axis is estimated, a minimization is necessary to determine the lateral distribution function (LDF) of the shower. The SD only samples a small fraction of the total shower particles arriving to the ground. This makes the LDF unique to every experiment based on their detector configuration. The function to be minimized is called the Nishimura-Kamata-Greisen (NKG) [72] defined in 3.16. The NKG function takes into account the signal of the triggered stations, the probabilities of a non-triggered station or

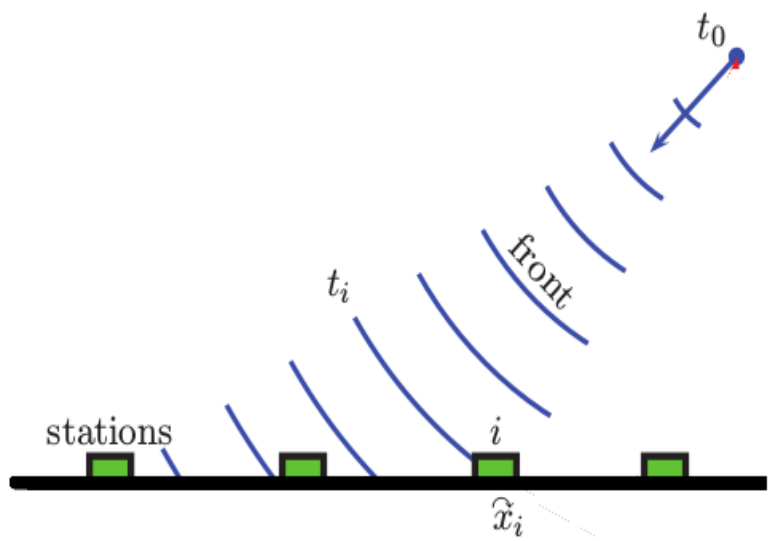

Figure 3.17: An EAS modeled as a spherical wave moving toward the SD.

saturated stations.

$$S(r) = S(r_{opt}) \left(\frac{r}{r_{opt}}\right)^{\beta} \cdot \left(\frac{r + r_1}{r_{opt} + r_1}\right)^{(\beta+\gamma)} \tag{3.16}$$

where r_{opt} is the optimal distance which depends on the space between stations and it can be found using simulations. β is a geometrical parameter that depends on the inclination of the shower. r_1 is the estimator for the transition between the lateral distribution of the muonic and electromagnetic components and it has been estimated to be 700 m [73]. $S(r_{opt})$ is an estimator of the shower size which is proportional to energy. For the 1500 meter array spacing, r_{opt} was found to be 1000 m. For the in-filled array (750 m spacing), r_{opt} is 450 m [73]. Therefore, the SD observable that is the best related to the energy of the shower is the signal size at 1000 m, known as S(1000). The conversion from SD signals to energy is performed either by simulations or by correlating the FD energy reconstructed with S(1000).

The estimator S(1000) changes depending on the inclination of the shower. As the inclination angles increases the SD signal decreases due to the shower traversing more of the atmosphere prior to reaching the ground. The angle 38° was chosen as a reference such that

$$S_{38} \equiv S(1000)/CIC(\theta) \tag{3.17}$$

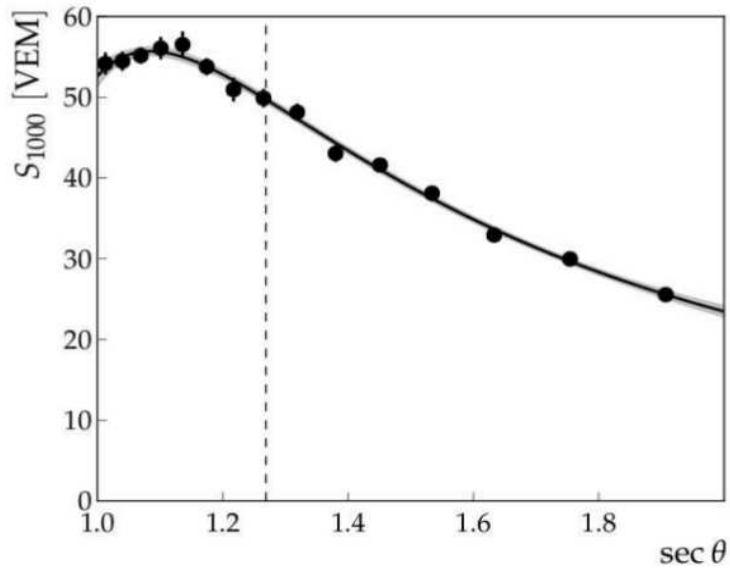

Figure 3.18: Attenuation curve is described by a third order polynomial function, a dashed line is drawn at 38° [74]

where CIC is defined as the Constant Intensity Cut and is a third order polynomial function. The CIC fits the attenuation curve dependency between theta and S(1000) [73], as shown in Figure 3.18.

For each high-quality hybrid reconstructed events S_{38} can be correlated with the FD reconstructed energy. The events selected must pass a high quality criteria:

- an accurate fit of the Gaissier Hillas profile
- X_{max} must be contained within the FD field of view
- the reconstruction must have an accuracy better than $40g \cdot cm^{-2}$
- the reconstructed FD energy should have an uncertainty less than 18%.

The relationship between FD energy and S_{38} follows a power-law function:

$$E_{FD} = A\,(S_{38})^B \tag{3.18}$$

where A and B are two parameters that are found by using a maximum likelihood minimization technique. There are several sets of parameters depending on the event inclination

(vertical or inclined) or the size of the array used (1500 or 700). For vertical events, the zenith angle must be less than 60°. Parameters A and B for vertical events have been calculated in [75] with data up to the end of 2013. The correlation plot and the parameters found are shown in Figure 3.19

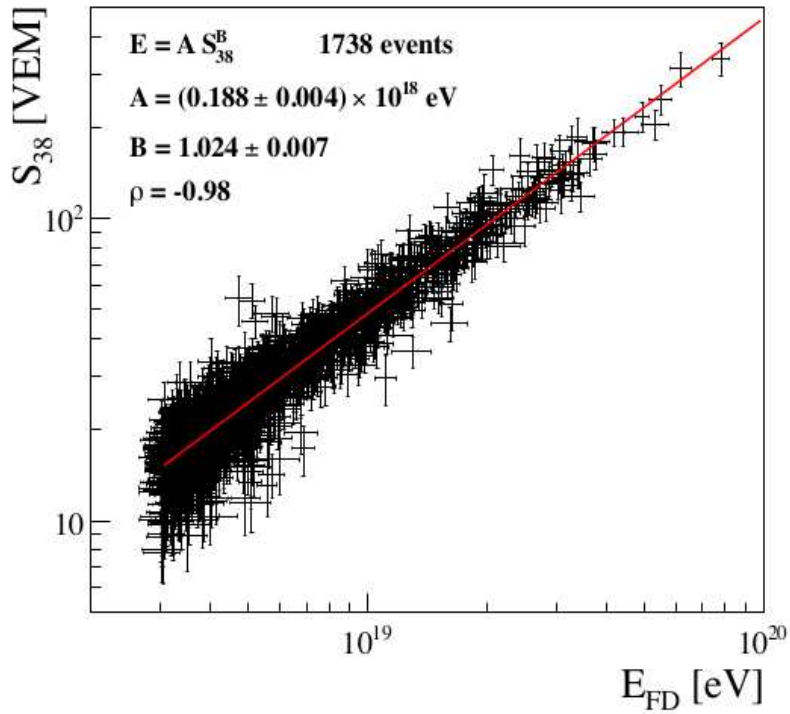

Figure 3.19: Correlation between S_{38} and E_{FD} [76]. The red line represents the best fit.

Chapter 7 discusses how different aerosol databases affect the S_{38} and E_{FD} energy fit parameters and the resulting energy spectrum.

CHAPTER 4

THE UPGRADE OF THE CENTRAL LASER FACILITY

The CLF upgrade was first proposed in 2011 [77]. It was very clear by then that because the original CLF was built rather quickly as a pioneering instrument, an upgrade would certainly allow room for many improvements and additions. After nearly a decade of service, the CLF was finally upgraded during the first half of 2013. The upgrade was performed by the Colorado School of Mines (CSM) group and the university of L'Aquila group. The design and initial construction took place at the CSM campus and it was completed in Argentina. This chapter explains the motivations, design and execution of the upgrade.

4.1 Upgrade Summary

The most important improvements and additions to the CLF include:

- A back-scatter Raman LIDAR receiver was installed to independently measure values of τ(z,t) .
- The original flash lamp pumped laser was replaced by a solid state laser.
- A newer GPS clock system improves the timing resolution from 100 to 20 ns.
- The original 20 ft shipping container was replaced by a newer 40 ft unit with tighter doors and better insulation. A 2000 liter thermal reservoir coupled with the optical table was added to reduce thermal variations.
- The better sealed container features a separate room for the laser system to reduce the dust accumulation. This is important because dust accumulation on optical components increases the systematic uncertainty of laser energy delivered into the sky.
- The number of solar panels and batteries in the bank was increased because an insufficient charge was noted in previous winters.

- The radio network was upgraded to higher speeds to provide better Internet connection between the CLF and the observatory.
- A robotic system for automatic energy and polarization calibrations was added.
- A newer Single Board Computer (SBC) was installed. The software was modified to better integrate and handle the new instruments and laser routines.

All of the elements described above are explained in detail later in this chapter. A diagram of the upgraded CLF instrument can be seen in Figure 4.1

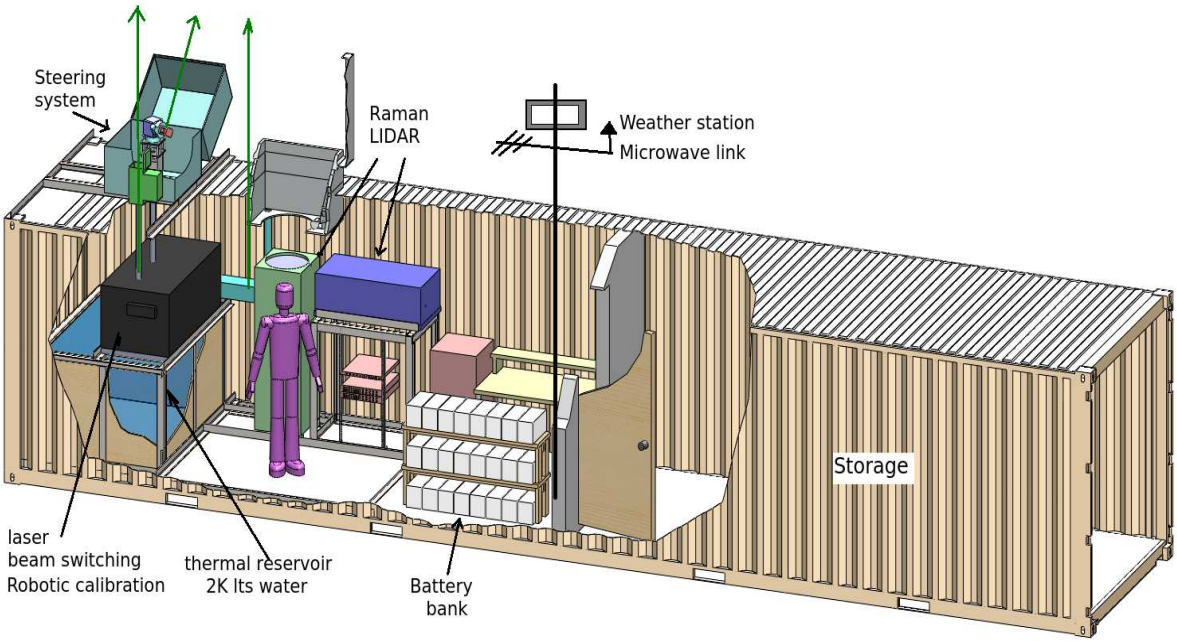

Figure 4.1: The design of the upgraded CLF as originally proposed. The actual instrument has a similar layout.

A photo of the CLF interior and some of the people involved in the upgrade is presented in Figure 4.2. The photo was taken after the completion of the upgrade.

4.2 Intercontinental Travel

Initial work on the new CLF structure started at CSM in Golden, Colorado. This work included the modification of a shipping container for the installation of optical tables. Other

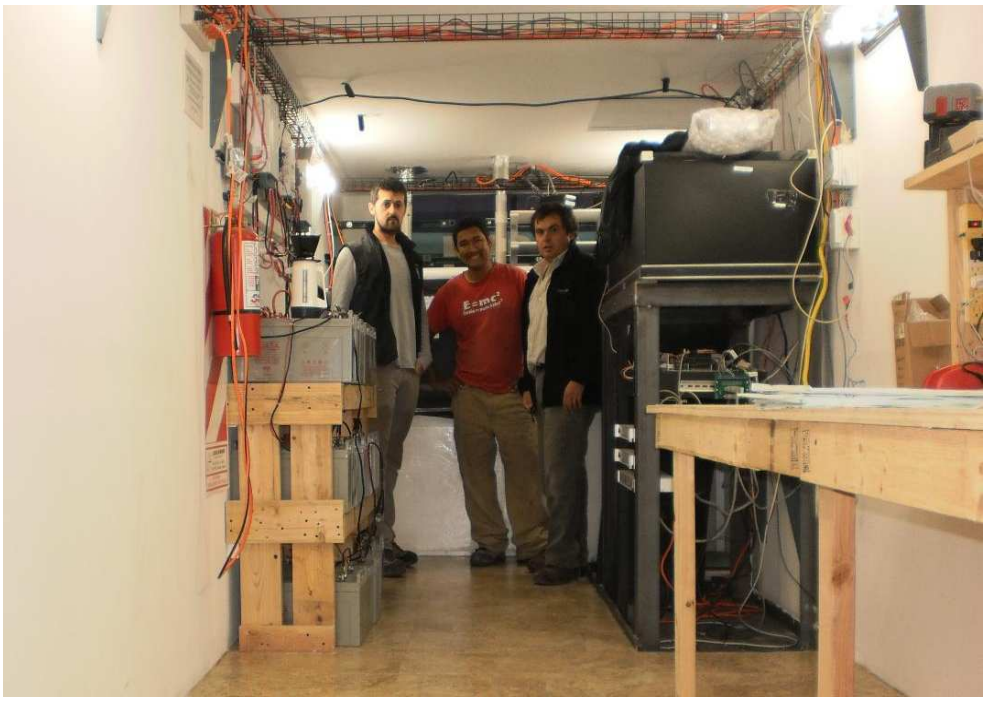

Figure 4.2: The inside of the CLF after completion of the upgrade (April 2013). From left to right: Eric Mayotte, Carlos Medina, Jorge Rodriguez.

work performed at CSM includes the installation of the wood structure for the insulation, a metal structure for a water reservoir and the installation of the floor support. Ideally, the full installation of the CLF would have been completed at CSM but due to international travel regulations, the container could not be modified prior to its shipping. It was decided that the remainder of materials and components should be packed inside the CLF container and shipped via train and later, cargo ship, to Buenos Aires, Argentina for final completion. A semi truck transported the container from Buenos Aires to the observatory's campus. The total trip from Golden to Malargüe took over 6 months. Figure 4.3 illustrates the process.

Once in the observatory, the remainder of the materials and components were installed. This includes the thermal insulation, the water reservoir installation, the optical table covers, ceiling and floors, and electrical connections. This work took about a month. The old CLF container was removed and transported to the Auger campus, freeing space on the concrete foundation pad for the new system. The CLF container was transported to its

Figure 4.3: Left: October 2012, the container is shipped from CSM. Center: the CLF trip. Right: March 2013, the container at the Pierre Auger Observatory.

final location for the installation of the following parts: the optical components, computers, cables, hardware controllers, sensors, solar panels and batteries. The final step of the CLF upgrade was the precise alignment of the optical components and the full system integration. This last step was the most time-consuming, taking nearly 4 months. The upgraded CLF was finally ready for operations in June 2013.

4.3 The Laser

The laser selected for the CLF upgrade is the "Centurion" model, manufactured by Quantel lasers (formerly big sky lasers). This laser is an air cooled, diode pumped Nd:YAG This laser replaced the water cooled "frequency tripled Nd:YAG lamp" laser at the former CLF. The Centurion laser includes the laser head and the laser controller as shown in Figure 4.4.

Among the advantages of the Centurion laser are that it requires very little maintenance, its long diode lifetime of about 1 billion shots and its simple configuration. The laser is configured to deliver 355 nm wavelength and laser pulses of 7 ns width with an energy range from nearly 0.5 mJ to nearly 5 mJ and two repetition rates, 1 Hz and 100 Hz. The laser wavelength emission falls near the center of the two largest peaks of the Nitrogen spectrum, which is near the wavelength of the FD EAS detection (see Figure 2.1). The laser characterization will be presented in Chapter 6.

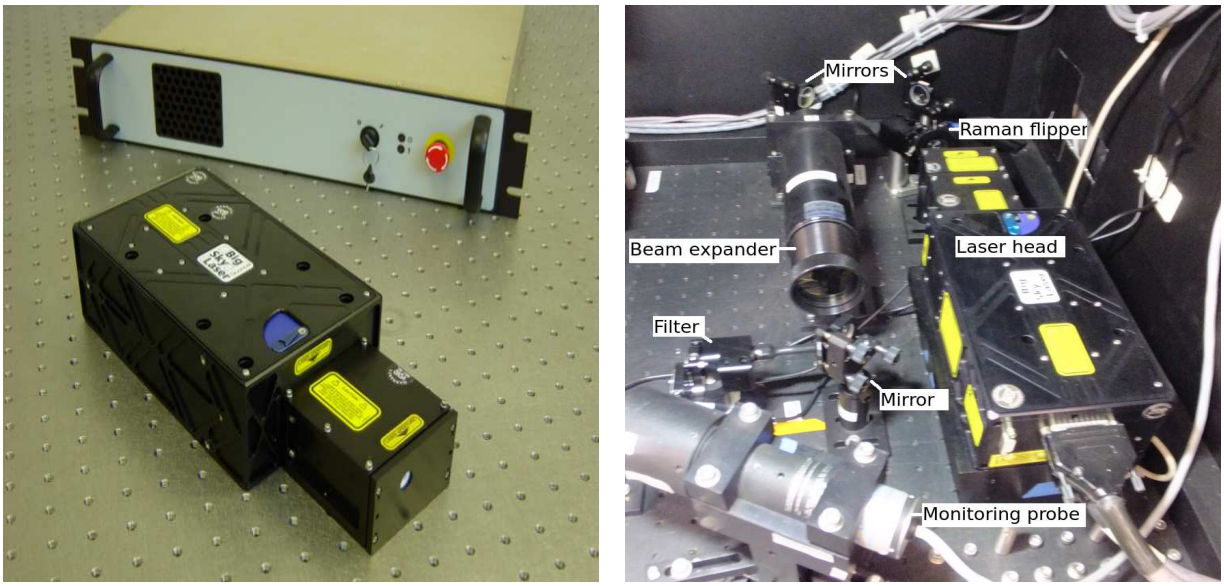

Figure 4.4: Left: Laser head and the laser controller before installation (courtesy of Quantel laser). Right: The laser head as mounted on the optical table in the CLF next to some optical components (they will be described in the following sections).

4.4 SBC and GPS

The Single Board Computer (SBC) controls all operations (except the Raman analysis) at the CLF. The SBC is a TS-5500 model, manufactured by "Technology Systems" (Figure 4.5). This computer futures an AMD ELAM520 processor at 133 MHz and it runs on a lite Linux version software (Red Hat Linux 7.1 2.96-98). The same model was used for the original CLF and it has demonstrated to be optimal for the laser system due to its extremely low power consumption close to 5W (regulated 5VDC at 900 mA). This computer has no keyboard, mouse or monitors, so all communications are either done via the SSH protocol or using RS-232 computer to computer serial port. The SBC has full Internet access using the observatory radio network and a link modem reference : TL-WA5210G Wireless G by TP-Link.

The SBC has no moving parts. The operating system and user data are stored in a 256 MB compact flash card. One additional feature is its flexibility to communicate with external devices via serial ports. The SBC comes with 3 built in serial ports; expandable to a total of 11 via the PC/104 expansion bus and 2 TS-SER4 cards. 38 additional digital

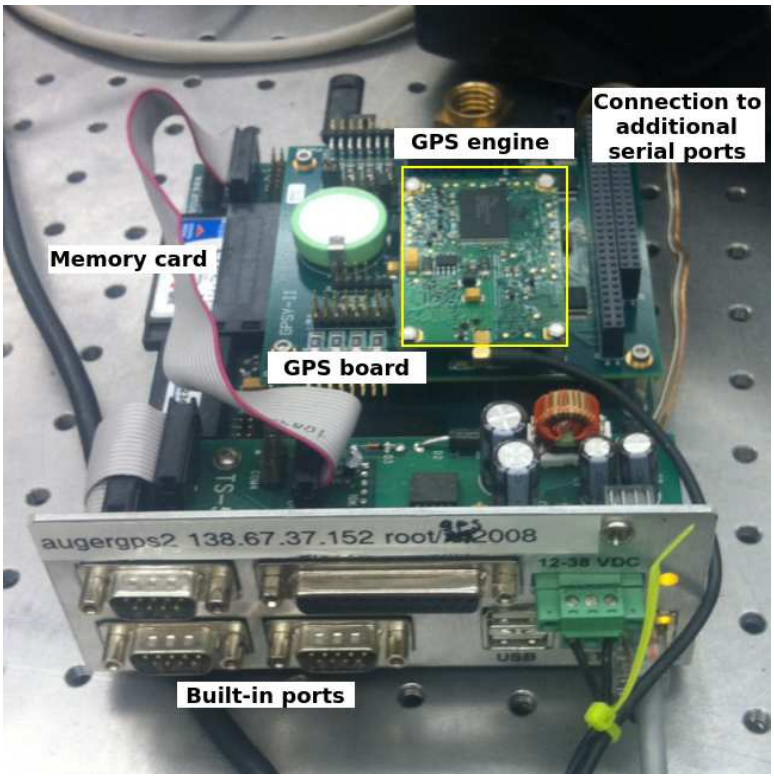

Figure 4.5: The SBC with the GPSY engine unit mounted, the additional serial-port cards. A protective case was added later

Input/Output (DIO) lines are available. Table 4.1 lists the communication ports used. Due to limitation of the SBC linux kernel, all of the programming code is written and compiled using external computers and the executable files are moved to the SBC. The programs are written in C or C++ language and compiled with the standard gcc protocol.

Table 4.1: List of the SBC communication ports connections

Port	connected to:	Port	connected to:
serial 1	Calibration stage controllers	serial 8	laser (J3 PC-com)
serial 2	(Com2) not used	serial 9	radiometer 2 (RS 232C)
serial 3	alternative PC-SBC comms	serial 10	cover box controller
serial 4	rain sensors	serial 11	DIO(flippers, temperature, rain)
serial 5	Radiometer 3 (RS 232)	serial 12	steering head controllers
serial 6	RPC 2 (EIA 323)	Ethernet	modem
serial 7	Radiometer 1 (RS 232C)	USB	not used
DIO	Termomethers, rain sensor	DIO	flipper mirror control

The SBC is used to control the trigger signals that allow the laser to fire. The timing of the laser firing is of extreme importance since it is the only way that the FD electronics can distinguish and separate the laser events from cosmic events. To be correctly identified, the laser pulses needs to be fired in a time window which has a center with exact offsets after the second. The time offsets are centered at 250 ms, and 500 ms 350 and 700 ms. This precision is achieved using an integrated programmable GPS module mounted directly in the SBC (see Figure 4.5). This module, which was developed by the HIRES collaboration, is called the "GPSY" [78].

4.5 Optical Components

The laser and most of the optical components are mounted on the main optical table in the CLF. This optical table is mounted over a metallic frame which is welded to the container structure and also supports the water reservoir. This makes the optical table very stable to support the laser and the optical components. The laser heat sink is connected to the water reservoir using copper rods. An additional optical table was set up next to the main table to accommodate additional optics that deliver the beam for the Raman receiver. Both tables are covered by a metallic frame with sliding metallic windows to protect from dust accumulation but also to allow easy access when the optics need to be serviced.

The optical components listed in Table 4.2 and illustrated in Figure 4.6 will be described as they are positioned downstream of the laser.

An iris diaphragm is located right after the laser head beam exit, to prevent halo spots in the beam. Once the beam passes the iris, it encounters a computer controlled flipper mirror (flipper #1) which has two positions: up and down. In the "up" position the mirror is out of the beam line while in the "down" position it reflects the beam towards the Raman optical table, and specifically a mirror, a 10X beam expander and finally another mirror which reflects the light in the upper vertical direction. This provides the vertical beam for the Raman receiver and it is near and parallel to the Raman telescope receiver. The specifics of the Raman receiver will be explained later in this chapter. Flipper #1 is important

Table 4.2: Summary of optical components on the optical table

Quantity	Part name	Part number	Manufacturer
1	UV Laser	Centurion	Quantel
2	Harmonic separators	BSR-31/*-1025	CVI Laser
1	355 nm mirrors	Y3-1025-P	CVI Laser
2	Depolarizer	DPL-10-355	CVI Laser
1	AR coated window	W2-PW1-1025-UV	CVI Laser
2	Charge controller	C35-12V	CVI Laser
2	355/633 mirror	EH-353/*-45UNP	CVI Laser
1	Pick-off splitter	PW1-1025-UV	CVI Laser
3	Motorized flipper	8892-K	New Foucus
various	Mounts and post	various	Thor Labs

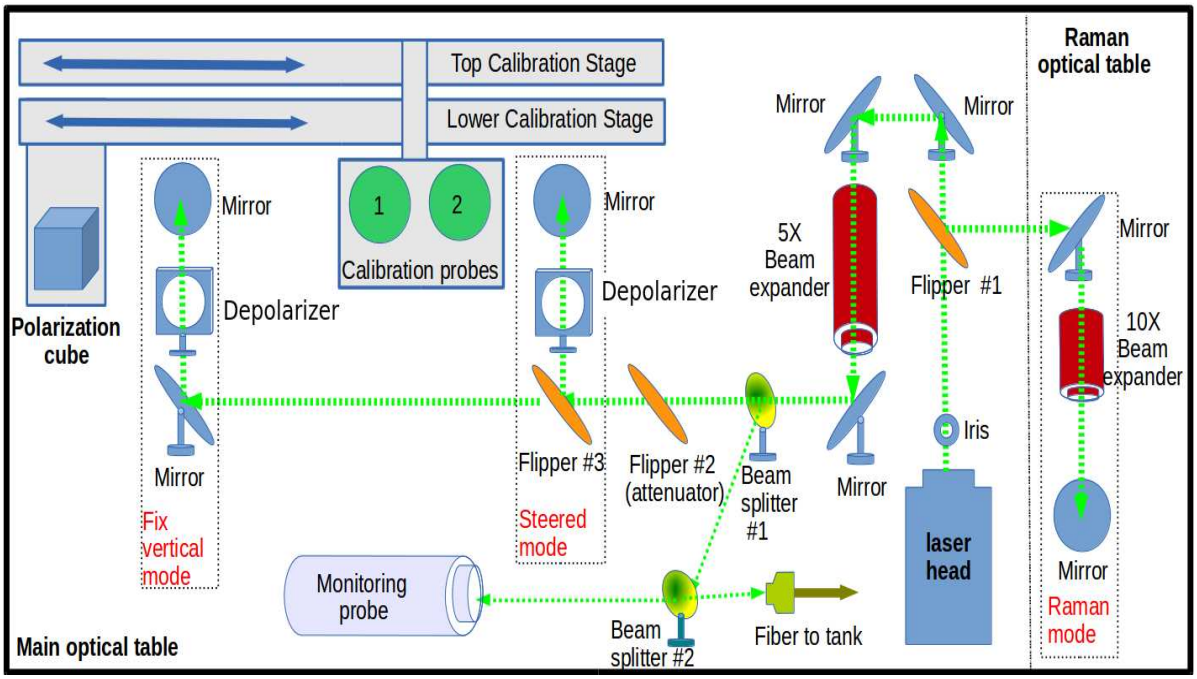

Figure 4.6: Diagram of the elements found on the optical tables in the CLF.

because its state selects between CLF and Raman modes. To improve spectral purity, two harmonic separator mirrors are located downstream the beam line to reflect only the 355 nm wavelength and transmits infrared 1064 nm and visible 532 nm wavelengths. The beam later passes through a 5X beam expander which decreases energy density and prevents damage to the energy probes. After the beam expander, the beam gets reflected 90° by another mirror towards other optical components. A beam splitter (#1) reflects a fraction of the light (8%)

in the beam into another splitter (#2), the largest fraction the light out of the beam splitter #2 goes to a "monitoring probe" for energy measurements. The smallest fraction of light out of splitter #2 goes to a light collector and it is transmitted using 20 m of fiber optical cable towards the nearest SD station named "Celeste". The larger fraction of the light that did not get reflected from beam splitter #1 continues along the original beam path. The next element found is another flipper mirror (flipper #2). This flipper is equipped with an AR coated window that significantly reduces the energy of the beam when its set in the beam path (down position). The AR coated window is only used for shots that require very low intensity, such as the ones directed very close towards the FD. One more flipper mirror (flipper #3) selects between fixed vertical mode or steering mode. When flipper #3 is in the beam path (down position) the beam is in steering mode. In this mode the flipper mirror reflects the light 90° towards a depolarizer element, and a vertical mirror that directs the light toward a steering system mounted on the roof of the facility. The steering system will be explained in the following section. If the flipper is out of the beam path (up position), the beam is in "fixed vertical mode". In this mode, the light continues towards another mirror that reflects the light 90° toward another set of a depolarizer element plus vertical mirror which conducts the light out of the container.

4.6 The Energy + Polarization Calibration System

The amount light arriving to the FD cameras depends on the energy and polarization of the laser beam. The methods used to monitor the atmosphere transparency (it will be explained in Chapter 6) require periodic measurements of the absolute laser energy and polarization. For this purpose, the CLF and XLF have a robotic energy and polarization calibration system. The calibration system uses three computer controlled linear actuators and a rotary table. Two of the linear actuators move two energy probes over (or away from) the laser beam. The third linear actuator has a polarization splitter cube mounted on the rotary table that also can be move over (or away) the beam. The arrangement is illustrated in Figure 4.7.

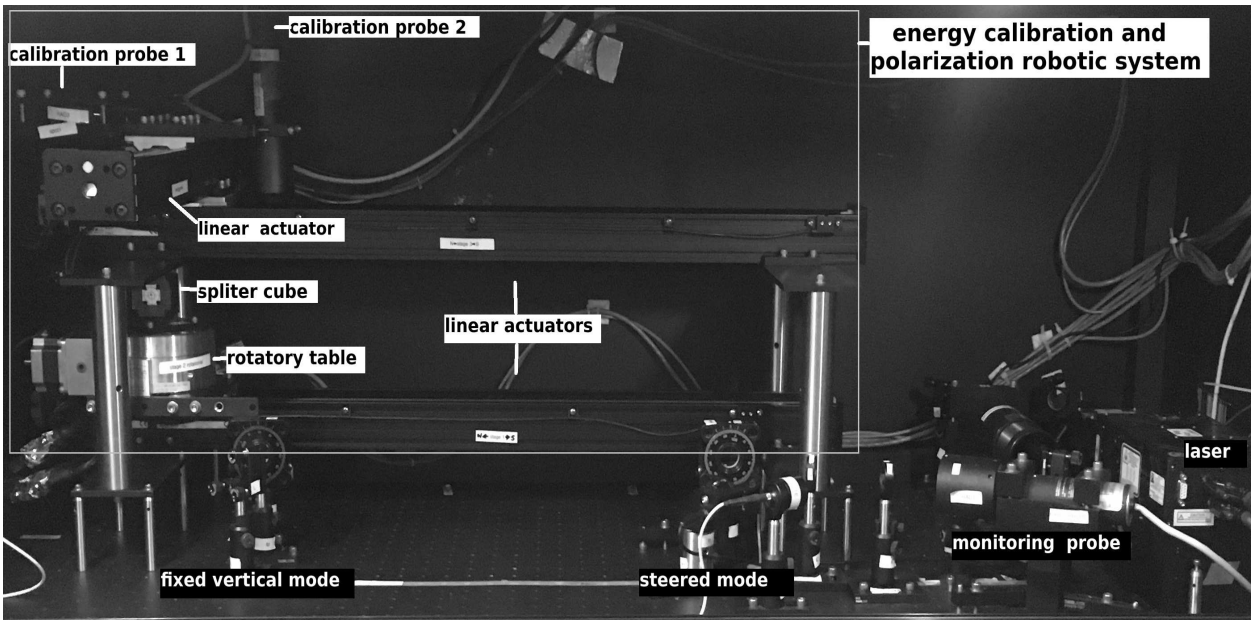

Figure 4.7: The CLF calibration system in optical box. A white box has been drawn around the system. The calibration system parts are labeled with black fonts. Other important elements are labeled using a white font.

The upper part of the system has two linear actuators which are set orthogonality and accommodate two energy probes. One pyro-electric probe (probe 1) measures the absolute energy of the laser ($E_{calibration}$) at the highest energy settings. A pyro-electric energy probe (probe 2) measures the laser energy at lower intensities. During normal laser operations, these two probes remain in their home position, away from the laser beam. The energy probes are used to calibrate the monitoring probe in terms of absolute beam energy. All energy probes are connected to radiometers. The lower part of the system has a polarizing-cube beam-splitter sitting on a rotational table that is moved by a lower linear actuator. The polarization and energy calibration routines are explained in Chapter 5. The components of the calibration system are listed in Table 4.3.

4.7 The Steering System

The steering system allows the CLF to fire inclined shots at any point above the horizon. The laser steering system was taken from the original system and mounted on the roof of

Table 4.3

Component	ID	Manufacturer	Comments
Monitoring probe	PE-25BB-574733	Laser Probe	0-1.4 mJ range
Calibration Probe 1	PY 221377 PE25BB-V2	OPHIR	1-20 mJ range
Radiometer 1	NV-2 519767	NOVA2	connected to probe 1
Calibration Probe 2	PE-25BB-221377	Standard probe.	0-1.4 mJ range
Radiometer 2	RM370	Laser Probe IN	connected to probe
Radiometer 3	RM370	Laser Probe IN	connected to monitoring probe
Polarizing cube	PC26U035	Rocky Mtn insts	
Linear actuators	BiSlide Series M	VELMEX inc	3 units
rotary table	B48 Series	VELMEX inc	
Step motor controller	VMX-3	VELMEX inc	2 controllers (4 step motors)

the new container that houses the upgraded CLF. The steering system includes a steering head, a protective cover box and a wind sensor.

Figure 4.8: The steering head and cover box is located on top of the CLF container.

The steering head is protected by an aluminum cover box from the harsh weather conditions. A step motor opens the cover box leaving the steering head exposed for steering operations. The cover box is designed to operate with winds up to 40 Km/h. If the winds

overpass this value, the cover box will not open or closed as a security measurement. A picture of the steering head inside the cover box on top of the container is presented in Figure 4.8.

The steering head features two orthogonal rotational stages, one azimuth and one vertical. Each rotational stage has mounted two 45° tilted UV mirrors which are aligned to allow motion on a 360° azimuth range and a 180° vertical range. The stages are powered by step motors. The number of steps to move one rotational stage by one degree is 80 steps, providing a steering precision of 0.0125 degrees. Each stage has a reference limit switch that needs to be triggered to find a reference to move to the desired angle. The stages and the cover box are remotely and autonomously operated via computer control. A photo of the steering head is presented in Figure 4.9.

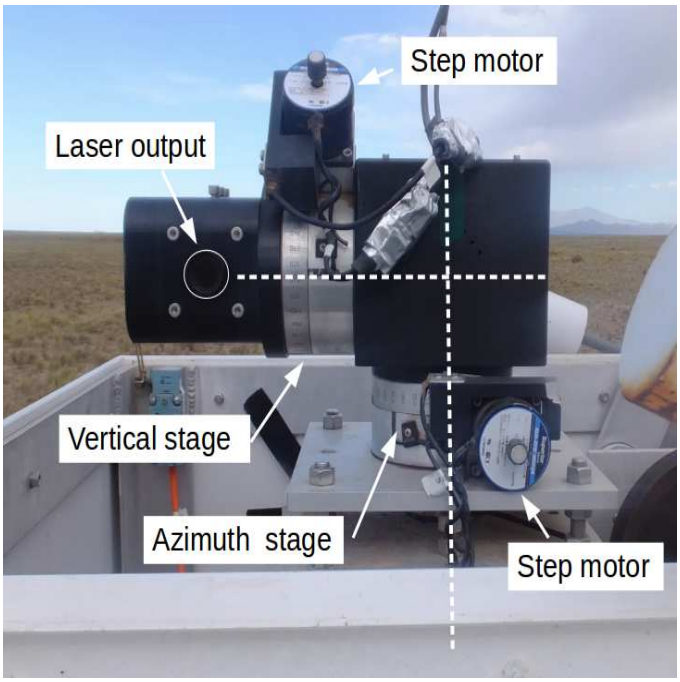

Figure 4.9: A close up of the steering head, the axis of the rotational stages are represented with dash lines

The correct alignment of the steering head is very important to assure the correct firing of the laser towards the points of interest (e.g. the FD telescopes). The vertical reference was found using a using a GPL3 self leveling laser devise with an accuracy of 1/4800 and a

fabricated target installed on the opposite end of the container roof away from the steering head (8 mts away). A diagram of the steering head and the target is presented in Figure 4.10

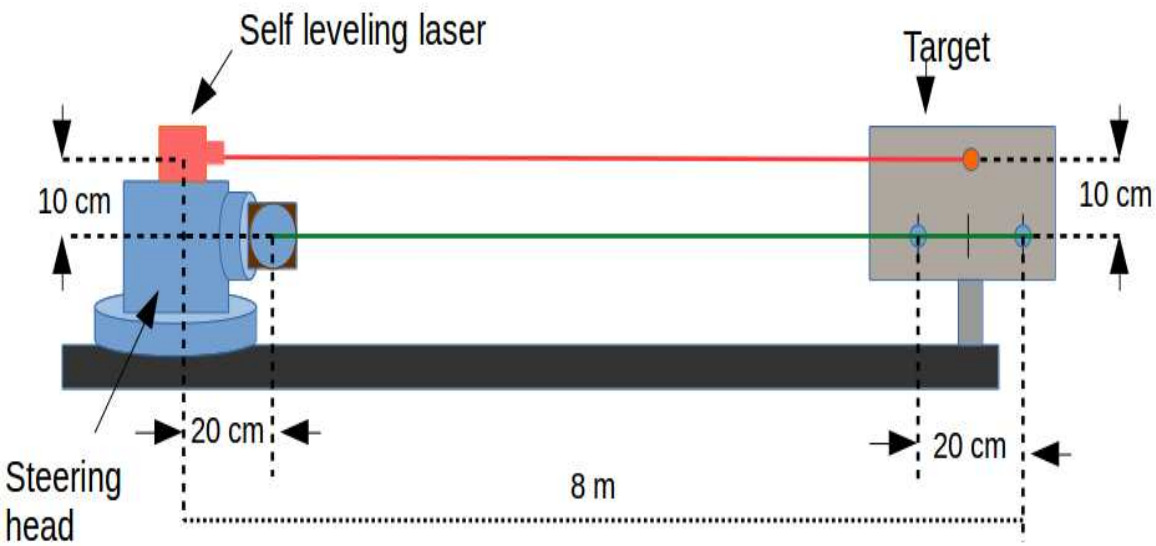

Figure 4.10: The steering head vertical reference was set using a self leveling laser and a target 8 m away from it.

The GPL3 was set on top of the steering head as shown in Figure 4.10. The steering head has internal mirrors with alignment knobs. This knobs were fine tune until the CLF laser beam the GPL3 laser beam were parallel. This alignment is double checked by measuring the vertical distance between the two laser spots at the target and near the steering head (10 cm as measured). When both of the rotary stages are moved by exactly 180° the steering head output is in a position separated 40 cm away from the initial position. The difference between the initial and final position is twice the distance between the vertical axis and the steering head output as shown in Figure 4.10. To avoid a cross-eye the horizontal distance between the two spots created by the CLF laser on the target must be also equal as the initial-final position of the steering head output (40 cm). This alignment also requires that the middle point between the two spots is at the same horizontal position as the GPL3 spot on the target. Once all of the previous conditions are realized, the two CLF laser spots on the target are noted.

The angles necessary to rotate the steering head and hit the two marked spots are shown in Table 4.4. These angles are monitored for consistency during the facility's scheduled monthly service to the facility.

Table 4.4: Summary angles

	Azimuthal	Elevation
Right target	78.113	0
Left target	258.103	180

The azimuth reference is more complicated to establish because no azimuth equivalent laser level device exists. The following strategy was developed to find an absolute azimuth reference with respect to the geographical north:

1. Each eye (LL,LM,LA and CO) is used as a target. Using the steering head, the laser is aimed to a very low angle such that the beam passes slightly above the FD camera.

2. Under this condition the light trace recorded by the FD will start looking like the trace of a fixed vertical laser shot (see Figure 4.11).

3. The attenuation filter on the CLF optical table is used for these kind of laser shots to avoid PMT saturation.

4. The laser beam is fired multiple times (changing the steering angles) until the laser trace look perfectly vertical.

5. When this condition is achieved the number of motor steps from the limit switch is noted as a temporary reference.

6. The positions of the CLF and the FD are known via GPS survey [56]. The angle between the FD and the geographical north using the CLF as the vertex, is calculated.

7. The last step is a conversion from motor steps to the absolute azimuthal reference angle (in degrees) using the information from the previous line.

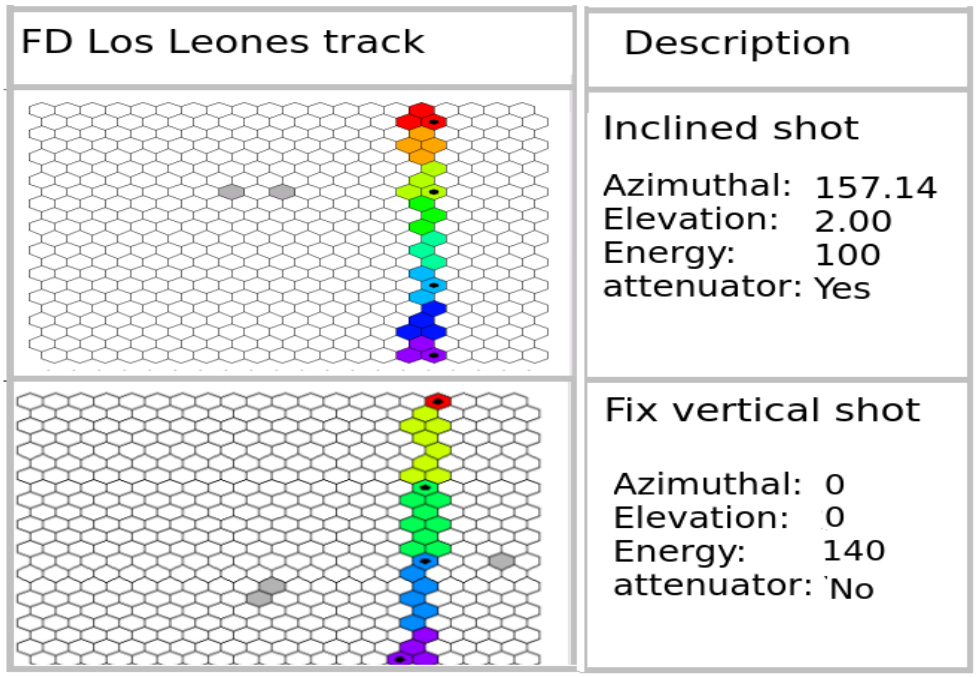

Figure 4.11: Comparison of a very inclined steered shot towards Los Leones and a fixed vertical one as seen by Los Leones FD camera

The CLF and XLF are programmed to fire inclined shots to celestial points of interest using the steering system during some periods of FD data acquisition. A short list of AGS coordinates are calculated by the SBC and the steering system is set to fire at them. Currently these shots are programmed to be fired once per FD night, to 10 different AGS, 3 times per AGN, at 3 Hz rate. They are fired during the 15 minute gap between atmospheric shots. The reconstructed arrival directions of the FD laser traces created by these inclined shots can be compared to the actual AGN positions. This tests the accuracy of the angular reconstruction algorithms used by the FD and the absolute timing of the FD eyes. The reconstructed arrival directions (for all FD sites) of a group of inclined laser shots fired towards some AGN's positions is presented in Figure 4.12.

This previous strategy proved to be efficient, as similar angles were found with the traditional use of a theodolite. but it presents the advantage of remote execution.

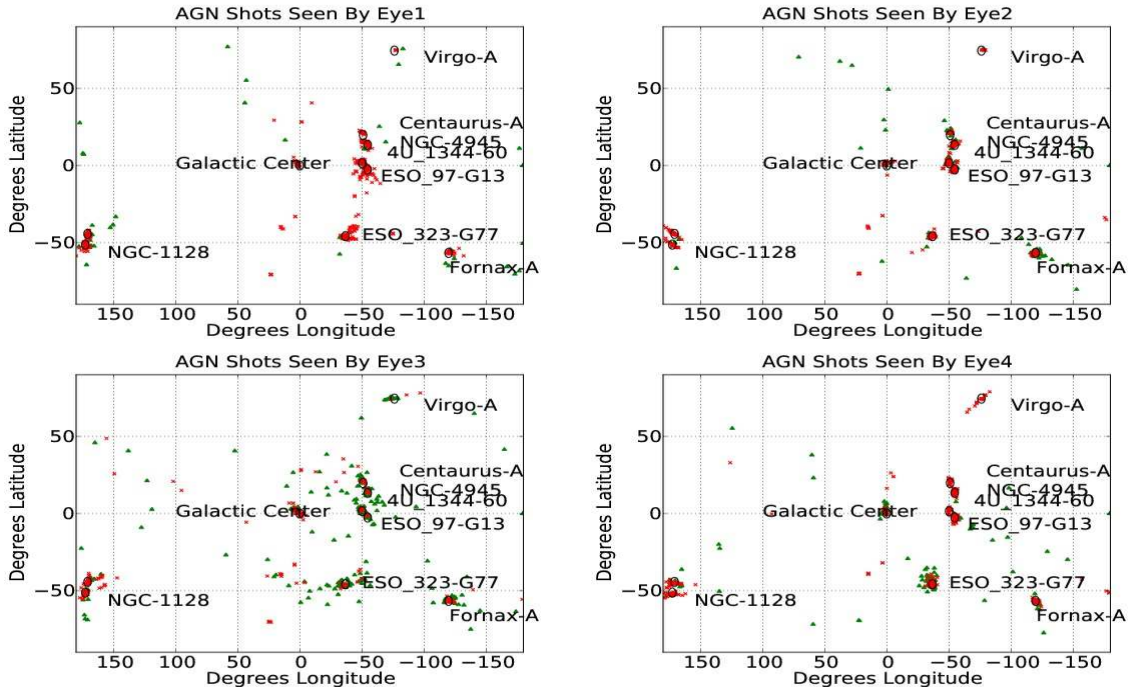

Figure 4.12: Red points represent the reconstructed inclination angles of AGNs included laser shots. The AGN inclined laser shots (plot courtesy of Levy Patterson) are represented with green dots.

4.8 Power System

The CLF instruments are powered by solar energy because electricity services are not available. 14 photo-voltaic solar panels with a combined power of 945W charge 18 batteries (100 amp-hour) through a standard charge controller. Figure 4.13 presents a picture of the arrangement of the solar panels and the batteries.

While the computers are directly powered to the batteries, the remainder of the components are connected to an AC inverter powered by the batteries that provide 110V AC (also used for lights and outlets). As a redundancy measure, the batteries are separated into 2 banks of 9 batteries each and interconnected by two diodes to prevent one bank from drawing the charge from the other bank. Bank 1 feeds the lights and electric outlets. Bank 2 feeds two remote power controllers connected to the equipment. The first remote power control has 6 outlets and is connected to:

Figure 4.13: Left: solar panels are arranged next to each other, a metallic fence prevents wildlife from breaking the panels. Right: 18 high capacity batteries.

1. Laser power control
2. Raman LIDAR high voltage control
3. Radiometers (some include a 9V DC converter)
4. Vertical hatch motor (vertical laser output)
5. Step motor controllers (calibration stages, steering system)
6. LIDAR hatch motor.

The RPC3 controls two gas heaters and it can be accessed remotely. Table 4.5 provides specifics of the power components.

All of the solar panels already installed at the old CLF (12 in total) were installed in the upgraded system. Two additional solar panels were added for a total of 14 panels. The additional panels were added to provide the expected additional power demand coming for the Raman LIDAR and to avoid possible power deficiencies during winter time. The historical measurements of the battery bank voltages for a year before the upgrade are

Table 4.5: Reference of major powers system components

Quantity	Part name	Part number	Manufacturer
8	Solar Panel 1	SP75,SQ75	Shell Solar
6	Solar Panel 2	SMSX-56	Solarex
1	Remote power control	RPC2	BayTech
1	Remote power control	RPC3	BayTech
18	Batteries	UHX12-100	Yuasa
2	Charge controller	C35-12V	Xandrex/Trace

plotted in Figure 4.14 (top). 2010 is presented as an example. Years before the upgrade have similar behavior.

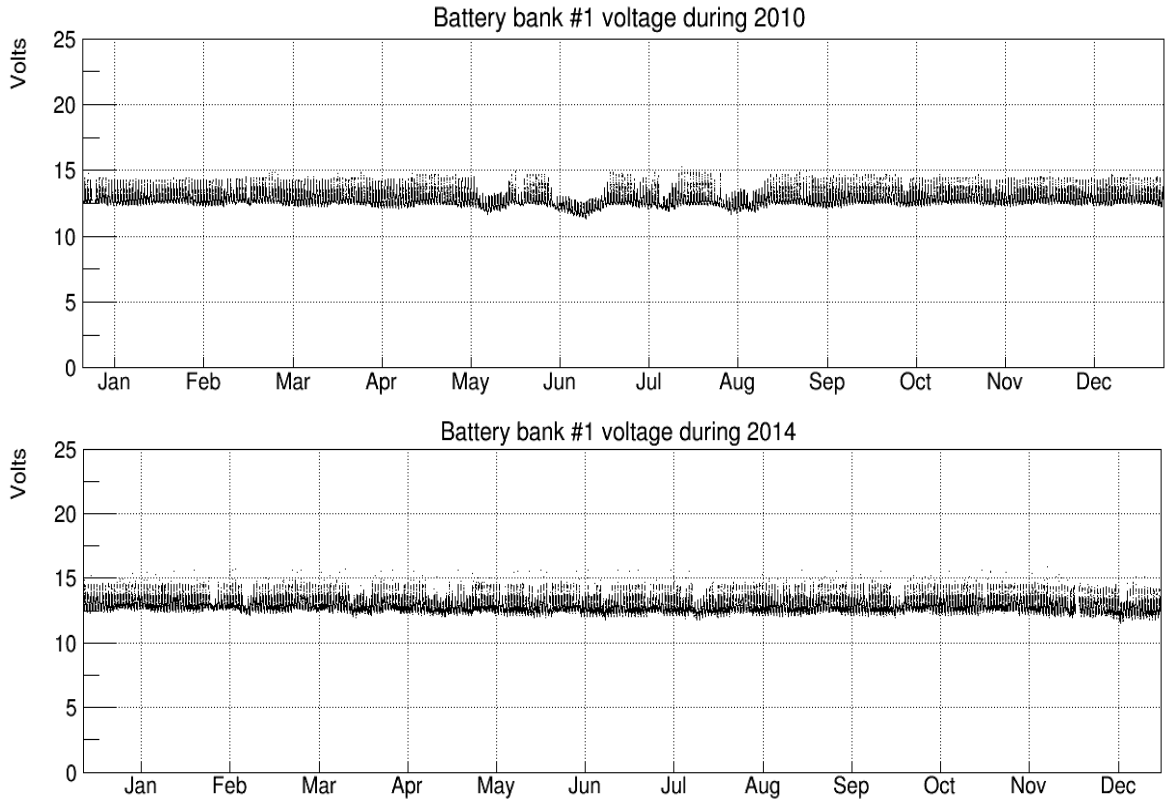

Figure 4.14: Top: Battery bank 1 voltage measurements during 2010, before the upgrade. Lower voltage values in May June and July indicate that the batteries were not fully charged. Data is taken every 5 minutes. Bottom: Battery bank 1 voltage measurements in 2014. Issues with the battery charge are solved. Data is taken every 5 minutes.

A lower voltage value during the winter period suggests that the batteries were not fully charged. This can be explained by a combination of shorter periods of daylight and weather

conditions. Although a fully charged battery is preferred, the lower charge did not bring a problem in the CLF operations at the time. If the battery bank voltage is below 11 Volts or higher than 14 Volts the system protects itself by disconnecting from the power bank. Figure 4.14 (bottom) presents the same measurements for a year after the upgrade (2015 is presented as an example but all other years have a similar behavior). The battery charge issue has been solved.

4.9 Insulation and Temperature Stability

Figure 4.15 presents the temperatures measured in 2015 by a thermometer located outside the CLF. It can be observed that the daily temperature fluctuations at the CLF location may reach values as high as 30 C°. A poorly insulated laser housing affects the stability of the laser system including the power delivered.

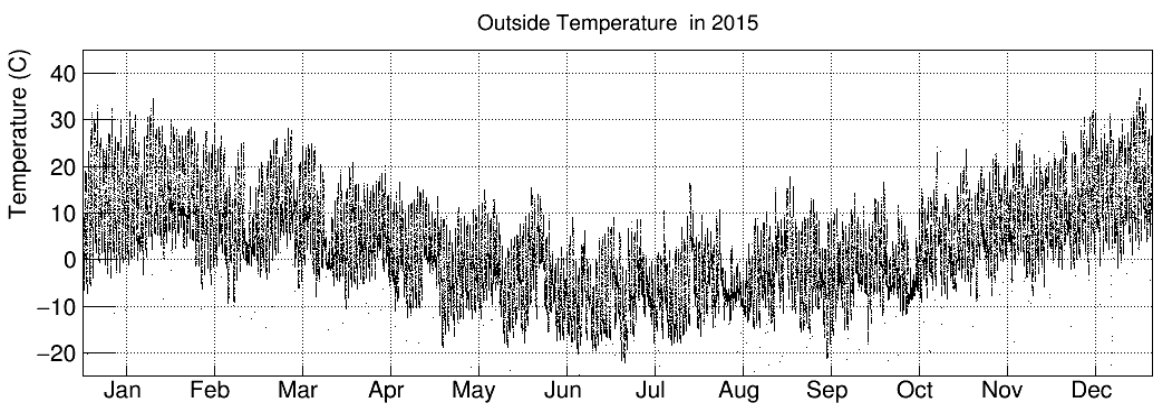

Figure 4.15: Outside temperatures at the CLF location during a full year, one measurement is taken every 5 minutes.

.

The new CLF container was separated into two rooms. The laser room includes thermal insulating materials in all walls, the ceiling and the floor. Fiberglass isolation pads were placed against the container metallic wall and covered with drywall (see Figure 4.16). Cable pipes exiting the container were filled with a spray foam insulating material. A 2000 liter water reservoir rests under the optical table.

Figure 4.16: Left: Laser room has been covered using fiberglass insulation pads. Right: Laser room after installation of the drywalls. The structures for the water reservoir and the Raman LIDAR optics can be seen on the back.

To increase thermal stability of the laser, the laser room is maintained at nearly 20 degrees Celsius using propane gas heaters controlled by a thermostat. The propane tank capacity is 1600 liters with an expected life span of 10 years.

Three thermometers monitor the temperature each 5 minutes, one in the laser room, one near the equipment, and one for the outside temperature. The newer and better insulation also reduces dust contamination which is a problem in the semi-arid region where the CLF is located. Dust accumulating on the optical components will scatter light and reduce the efficiency of the delivered laser light, which forces the inclusion of scheduled services to clean the optics. The cleaning carries some potential risk of affecting the optics alignment.

Plots of the temperatures in the laser room in 2010, before the upgrade and in 2015, after the upgrade are shown in Figure 4.17. The plots demonstrate the improvement in the thermal stability of the CLF after the upgrade.

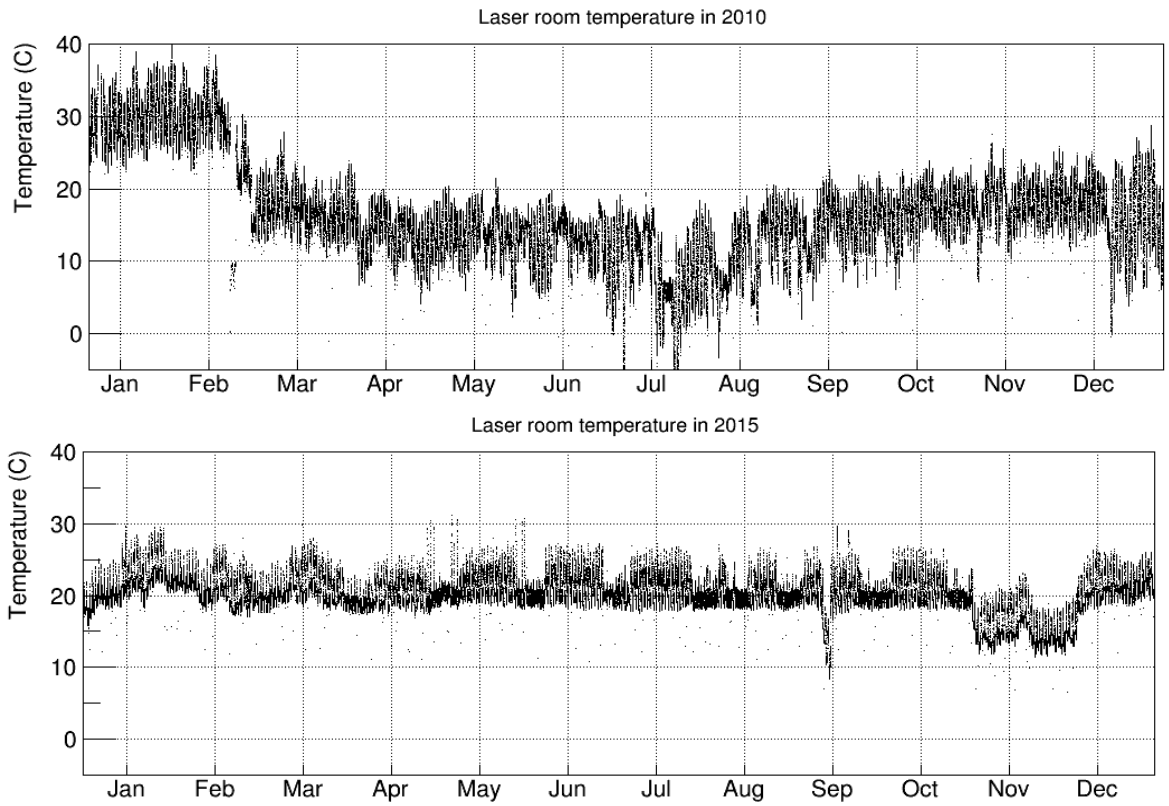

Figure 4.17: Top: Laser room temperatures for a year before the upgrade, the data is taken every 5 minutes. Bottom: Laser room temperatures become noticeably more stable after the upgrade. Abrupt changes in temperatures (September and November 2015) are due to temporary changes in the thermostat setting.

.

4.10 The Raman LIDAR

The Raman LIDAR is an important addition to the upgraded CLF because it measures τ(z,t) independently [79]. It was designed and built in the University of L'Aquila (Italy) and installed at the CLF at the time of the upgrade. An independent measurement of τ(z,t) can be used to check the side scattered method. Additionally the Raman LIDAR can identify the hours with the lowest levels of aerosols. This is the first time that a Raman LIDAR is used in a high energy cosmic ray experiment.

4.10.1 Raman vs Elastic

The measurement of the τ(z,t) using an elastic LIDAR requires knowledge of the fraction of light arriving to and from the scattering point. It also requires the fraction of light scattered in the backwards direction. The first two terms can be combined. The back scattering fraction has a molecular component and an aerosol component. The first one can be determined from molecular scattering theory, but the aerosol components cannot be modeled easily due to the irregularities of the aerosol particles whose shape typically changes with altitude and time. This imposes an inherent problem for elastic LIDARS which carry an assumption about the aerosol backscattering fraction.

The Raman LIDAR is a proven and widely used technique for atmospheric measurements of τ(z,t). The Raman LIDAR method presents significant advantages over the traditional elastic LIDARs.

- The Raman scattering does not depend on the aerosol content since the fraction of back-scattered light only depends on the number of N_2 atoms along the beam path.
- The N_2 density profiles can be obtained from radiosonde studies or from databases such as GDAS.
- The N_2 Raman cross-section is well known, making it possible to calculate the fraction of light scattered out of the beam, therefore leaving the aerosol attenuation as the only unknown that it can be measured.
- The same Raman LIDAR has been tested previously in Lamar, Colorado as R&D [51].
- The aerosol extinction and the aerosol back scattered coefficient [79] can also be measured.

Figure 4.18 illustrates how the Raman LIDAR avoids the assumption made on the elastic LIDAR technique about the relationship between the aerosol scattering and the aerosol extinction.

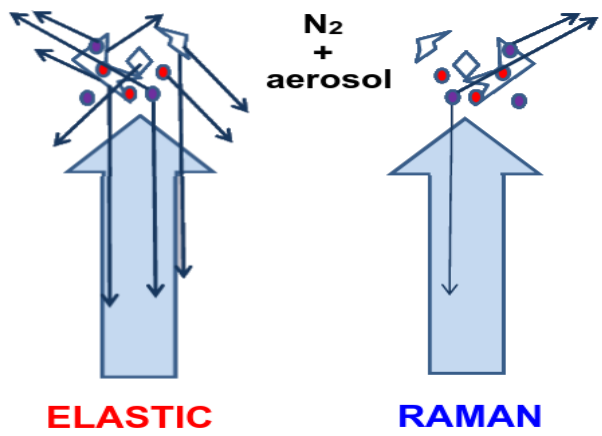

Figure 4.18: Elastic LIDARs have an additional assumption on the relationship between the amount of backscattering coming from nitrogen molecules and aerosols. This is not the case with the Raman technique since the N2 Raman backscattering is very well defined

One of the disadvantages of the Raman LIDAR is its extended acquisition time because the Raman backscatter cross section is nearly three orders of magnitude less than that of the cross section of its Rayleigh counterpart. Another disadvantage is that the system will interfere with the cosmic ray observation if it is run simultaneously at times of FD operations (FD shift).

4.10.2 Instrument Setup and Operations

The outside of the Raman receiver can be seen in Figure 4.19. It includes a structure housing the light collector telescope mirror and another one housing the optics and electronics.

The parabolic mirror has a 50 cm diameter and it reflects the light into a collector connected to an optical cable. The mirror and the light collector are also inside the second compartment. The optical cable carries the light to the optical component located into the third compartment. The optical components are a combination of dichroic beam splitters, interference filters and photo-multipliers. The light is filtered out into three different channels (Figure 4.20):

Figure 4.19: The Raman receiver is separated into the telescope mirror and the optics, they are connected via WLS optical cable. Both compartments are observed. An oscilloscope has been temporally placed to test the PMTs signal.

- 355 nm channel for elastic scattering.
- 386.7 nm inelastic channel for N_2 Raman backscattering.
- 407.5 nm for Raman H_2O backscattering (water vapor)

Directly above the Raman telescope, a 2 m X 1 m aluminum sliding hatch is mounted on the roof. It opens automatically when the Raman beam is ready to be fired. The hatch has been designed to resist harsh weather and operates with winds up to 100 km/h. When the hatch is opened, a UV transmitting window protects the interior from dust or rain exposure. This window also allows the pass of backscattered light back into the container into the second compartment where the Raman receiver is located.

During Raman operations, the CLF laser is set in the Raman mode. This mode allows the laser to fire pulses at full energy and a repetition rate of 100 Hz. Under this mode it is very important to direct the laser pulses only toward the Raman output in order to prevent any possibility for the beam to damage an energy probe. This condition is achieved

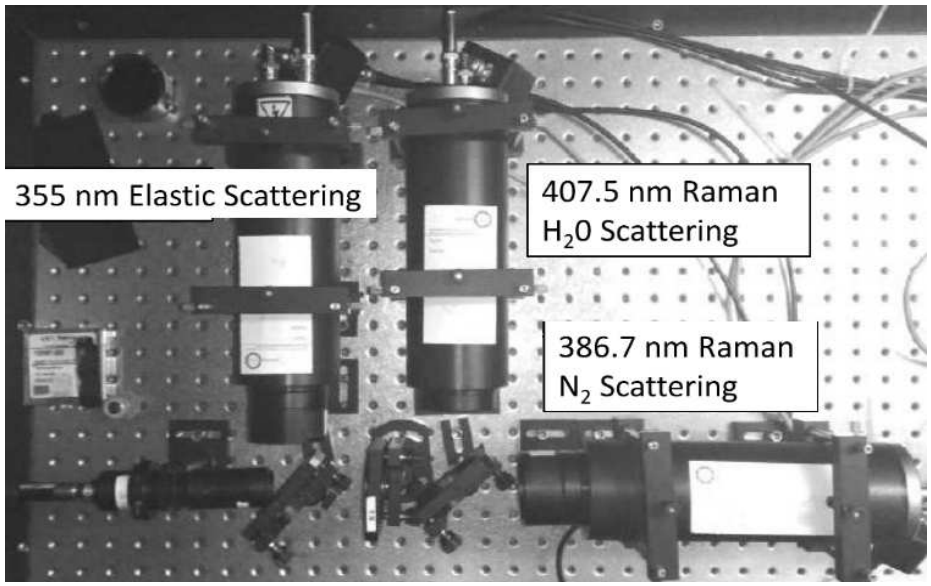

Figure 4.20: The arrangement of the Raman LIDAR optics that measures the amount of light in 3 separate bands.

by ensuring that the flipper mirror #1 is in Raman mode (down position). The SBC then opens the Raman hatch and communicates the start of the Raman analysis to the Raman SBC. The laser continues firing until the end of the Raman run (typically 24 minutes). The SBC continuously monitors the weather so in case of rain the hatch is closed automatically. After the Raman run is over the hatch is closed and the system returns to CLF mode.

During the fist year of operation, two Raman runs were performed 30 minutes before and 30 minutes after every FD shift. The Raman LIDAR runs are typically about 24 minutes but shorter or longer runs can also be programmed if needed. Since November 2014, an additional (24 minutes) run was added near the middle of the FD shift at a fixed time of 04:30 UTC. During this additional Raman run, the FD bays overlooking the CLF are closed to avoid saturation of the FD photo-multipliers. The fixed time simplifies the FD scheduling.

4.10.3 Raman Output

The Raman LIDAR provides vertical profiles of τ(z,t) with a resolution of 40 m for altitudes in the 800 m to 6000 m range, above ground. Below 800 m the LIDAR's measurements

are affected by the optical overlap function [79]. τ measurements above 6000 m are available but not considered, due to the high uncertainty bars and very low aerosol contributions. in addition, most EAS's X_max measurements are found below that altitude. The technical discussion of the calculation of the VAOD using the Raman LIDAR is explained in [79].

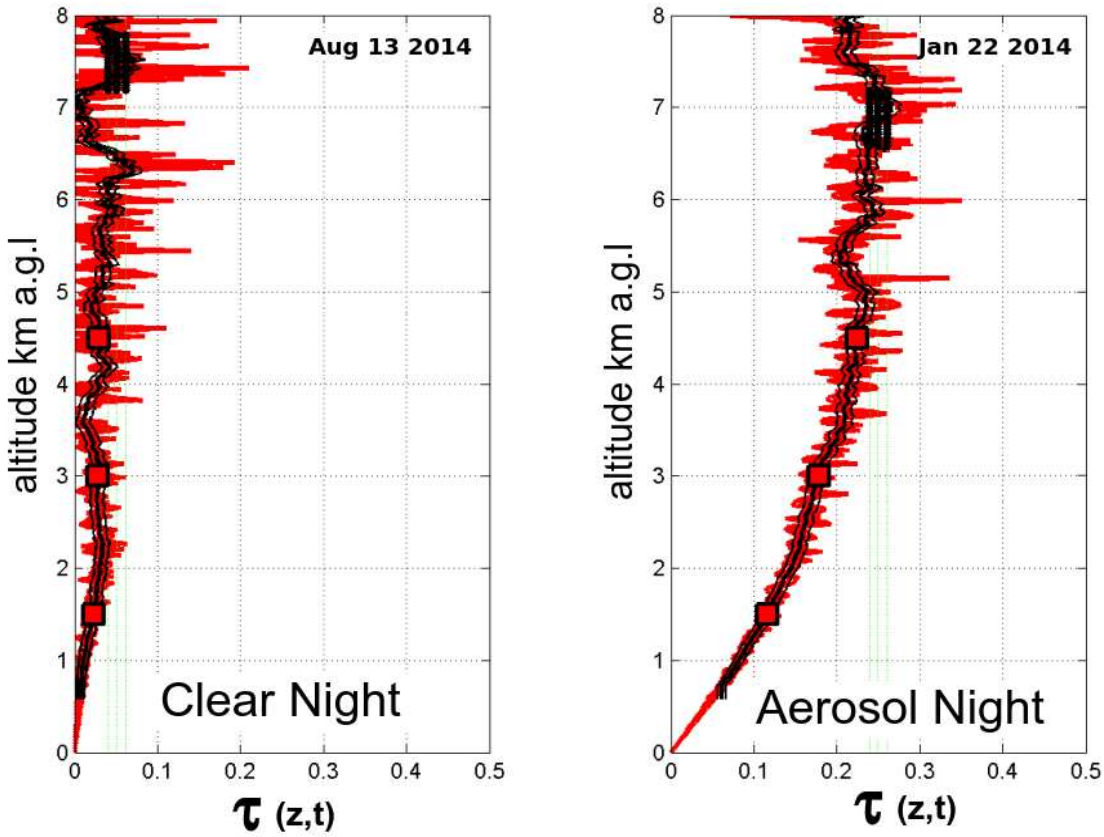

Figure 4.21: Examples of hourly τ(z,t) during a clear and a typical night with aerosols. The red line represents the electronic signal.

An example of two measurements from Raman LIDAR as provided by the University of L'Aquila group are presented in Figure 4.21. The two measurements are taken during two hours exhibiting different levels of aerosol content. Each measurement corresponds to about 144000 laser shots (24 minutes at 100 Hz). Raman LIDAR measurements in 2014 and 2015 are used to create an alternative atmospheric database. Comparison between this aerosol and the standard Data Normalized (DN) side scattering measurements are one of the focus

of this research (see chapter 6).

4.11 CLF Operations

The FD shift calendar is calculated by the collaboration, it changes based on the astronomical twilight but is affected by the moon calendar[80]. For each night of FD operations, the CLF schedule is calculated based on the starting and the finishing time of FD shifts. The SBC accesses the FD shift calendar and creates a routine that includes atmospheric shots for every hour of FD shift. An example of the CLF schedule for the FD shift in July 20th 2015 is presented in Table 4.6.

Table 4.6: An example of the operations and laser shots executed at the CLF during an FD shift. Each type of shot is expained in the text.

UTC	**1st quarter hour**	**2nd quarter hour**	**3rd quarter hour**	**4th quarter hour**
23:00	power on and warm up	energy calibration	24 minutes Raman run	
00:00	FD shift starts			
00:00	hybrid, atmospheric	atmospheric	atmospheric	atmospheric
01:00	hybrid, atmospheric	atmospheric	atmospheric	atmospheric
02:00	hybrid, atmospheric, AGN	atmospheric, AGN	atmospheric, AGN	atmospheric, AGN
03:00	hybrid, atmospheric	atmospheric	atmospheric	atmospheric
04:00	hybrid, atmospheric	atmospheric	24 minutes Raman run	
05:00	hybrid, atmospheric, dimmed	atmospheric, dimmed	atmospheric, dimmed	atmospheric, dimmed
06:00	hybrid, atmospheric	atmospheric	atmospheric	atmospheric
07:00	hybrid, atmospheric, steered	atmospheric, steered	atmospheric, steered	atmospheric, steered
08:00	hybrid, atmospheric	atmospheric	atmospheric	atmospheric
09:00	hybrid, atmospheric	atmospheric	atmospheric	atmospheric
10:00	FD shift finished			
10:00	24 minutes Raman run		energy calibration	polarization run
11:00	steering head diagnosis and shutdown			

Atmospheric shots are sets of 50 laser shots, fired at a 1Hz at full energy in the fixed vertical mode. These shots are currently used to measured τ(z,t). This operation is repeated in 15 minute intervals, for a total of 200 shots per hour. 200 laser shots per hour allows for statistical significance, reducing the RMS by $\sqrt{200}$ while still being conservative in laser usage. The approximate 14 minute gap between atmospheric shots allows time to schedule steered and dimmed shots for other purposes (e.g.steered shots towards the FD or AGN shots). Additionally, at the start of each FD operational hour, 3 fixed vertical shots are fired in hybrid mode for FD/SD timing studies. Three 24-minute Raman runs are scheduled during the night:

- A first run before the FD shift.
- A second run nearly in the middle of the FD shift (at 4:30 UTC).
- A third run at the end of the FD shift.

During the second Raman run, the FD bays overlooking the CLF are closed by the FD shifter. The fixed starting time of this run facilitates the shifter responsibility. During days with no FD operation, the CLF runs routine operations such as energy calibrations, polarization measurements and steering head diagnosis.

CHAPTER 5
LASER BEAM CHARACTERIZATION

This chapter describes laser characterization measurements that were performed at the CLF and XLF using the calibration system described in Chapter 4. The measurements include absolute and relative laser energies, polarization measurements and stability. Additional sections describe alignments, linearity studies and laser divergence. The last section of this chapter compares the tracks seen by the FD produced by the laser with the tracks from EASs.

5.1 Absolute and Relative Energy Measurements

The absolute energy of the laser delivered to the sky ($E_{calibration}$) is measured by a pyro-electric probe (probe 1) placed on the top of the beam stream by the calibration system, as explained in Chapter 4. There is also a second pyro-electric energy probe (probe 2), placed near the first probe, that is used to measure the beam energy at a lower energy setting. This provides a redundancy in measurements in case of a malfunction of the main probe, plus cross-checks. During any laser operation, these two probes remain in their home position, away from the laser beam (Figure 4.7). Each day, an energy calibration routine is performed. The SBC is programmed to automatically move probe 1 carefully over the vertical beam, just before exiting the laser box and the container. Then, 13 laser shots are fired at the maximum energy setup, followed by another set of 13 shots at lower energy. Later, probe 2 is moved over the vertical beam and a set of 13 laser shots at lower energy is fired again. All the energy values measured by the probes are recorded in the autologs. An additional option for absolute energy measurements is also available for the steered mode beam. It is a similar procedure, but it has not yet been programmed into the daily operations. This option is generally performed during service visits. The choice of 13 shots is a compromise

between statistical significance and conservation of laser shots. The final ($E_{calibration}$) value is the average of the 13 (successful) measurements for each of the different energies.

The monitoring probe was described in Chapter 4. It measures a fraction of light delivered for every single laser shot fired in the fixed vertical and steering mode. The absolute energy measurements at the maximum energy setting and the corresponding relative energy measurements of the monitoring probe are plotted as a function of time in Figure 5.1 (top and center). The ratio of the two measurements is presented in Figure 5.1 (bottom).

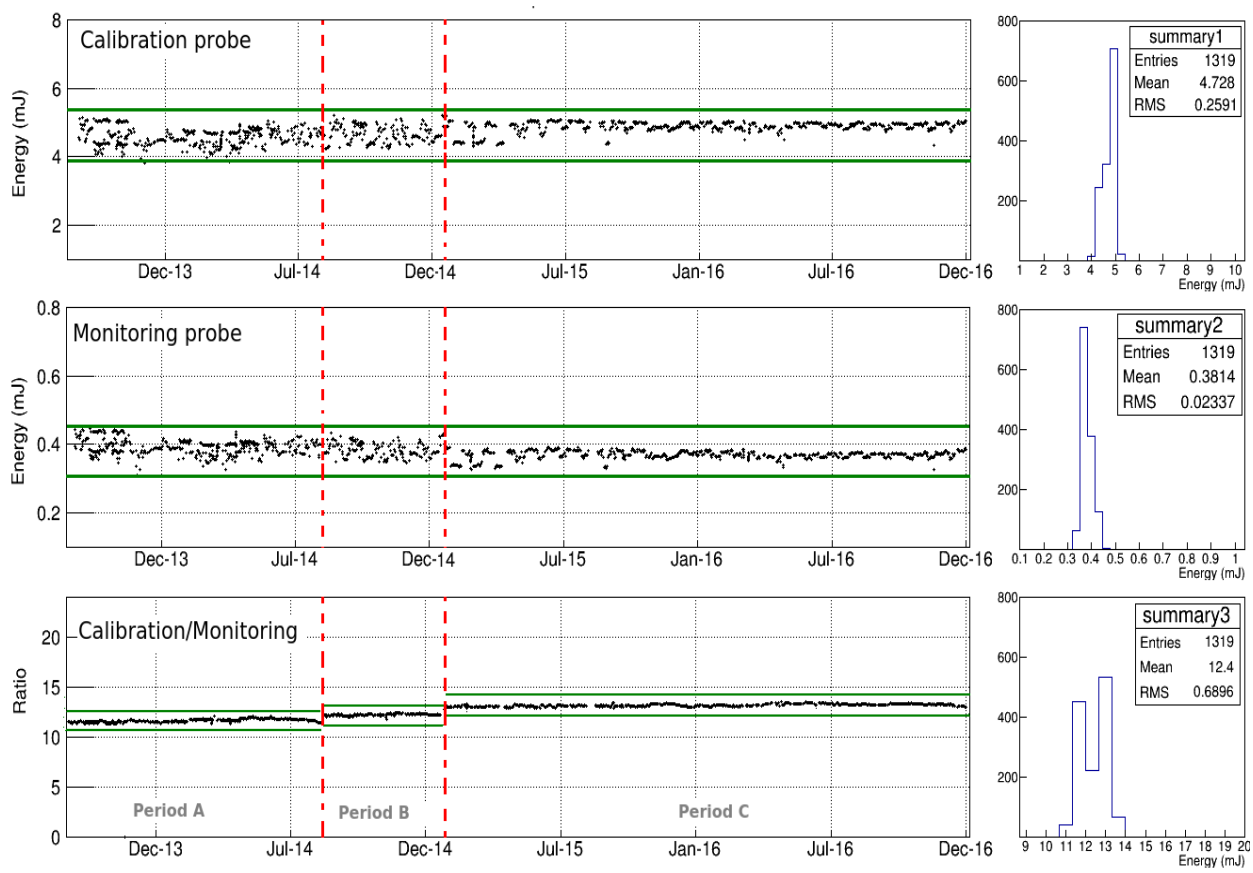

Figure 5.1: Top: Absolute laser energy measurements at the maximum energy setting after the CLF upgrade. The average maximum energy of the laser in the fixed vertical mode is 4.7 mJ. Center: Relative measurements and histogram by the monitoring probe. Green lines represent the ±10% deviation from average. Bottom: The ratio of these two quantities presents a better stability. Vertical dashed lines mark changes to the hardware or optics (see text).

The ratio of the two measurements is relatively stable and it is only affected by manipulation of the hardware. On Aug 14, 2014, the position of the calibration probe was fine-tuned to improve the alignment with the beam. On Jan 20, 2015, the CLF was serviced and the optical components were cleaned from dust. The alignment of the monitoring probe may have been slightly compromised. The effect of these two changes is visible in Figure 5.1. As a consequence of the changes, three distinct periods were created. A linear relationship between the monitoring probe and the calibration probe can be seen in Figure 5.2. This plot includes measurements during the three different periods. The slope of the linear fit represents the fraction of the total light captured by the monitoring probe. This fraction represents the average of the calibration factors (CF) explained in the next section.

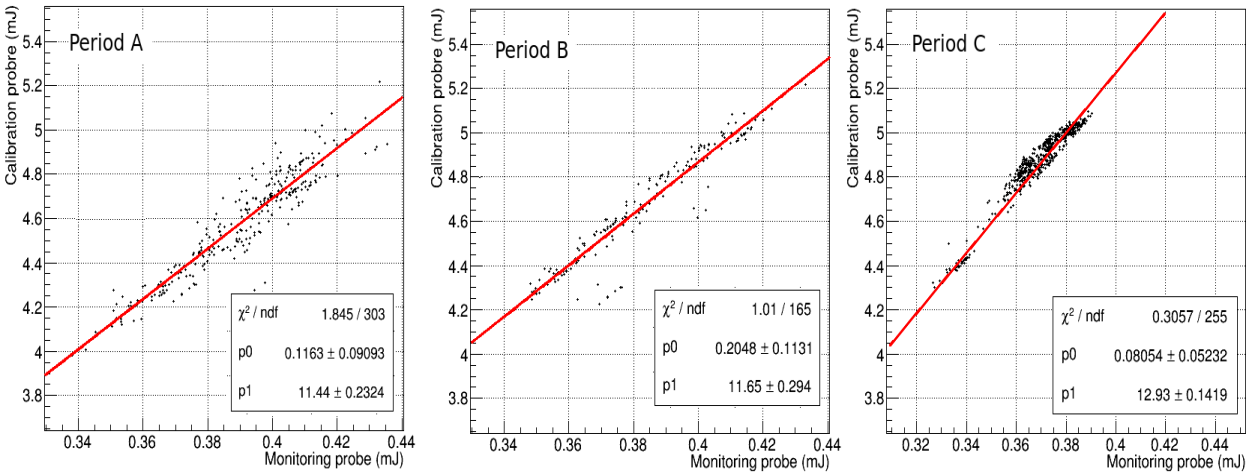

Figure 5.2: The correlation between the calibration and monitoring probe for the three different periods between 2014 and 2015. The percentage of light received by the monitoring probe has been found using a linear fit (red line).

The XLF laser energy measurements operates in a similar fashion as the CLF and they were described above. This plot presents 8 years of data because the XLF was operative before the upgrade of the CLF. From Figure 5.3 (top and center) it is easy to observe the aging of the laser. During November 2013, the XLF operations were updated to match those of the CLF including two energy calibrations per day, one before the start of the FD shift and the other immediately following the end of the FD shift. A systematic difference

between measurements can be observed between the measurement before after the FD shift. The lower energy measurement (after the FD shift) is due to the intense laser usage during the FD operation, affecting the maximum amount energy delivered in the beam. A lengthy cool down allows time for recovery. This systematic effect disappears when calculating the ratio of the two energies Figure 5.3 (bottom). Percentage lines are not drawn for the XLF of the slow decrease in energy in this larger period of time, except for the ratio plot which is not sensitive to the aging of the laser.

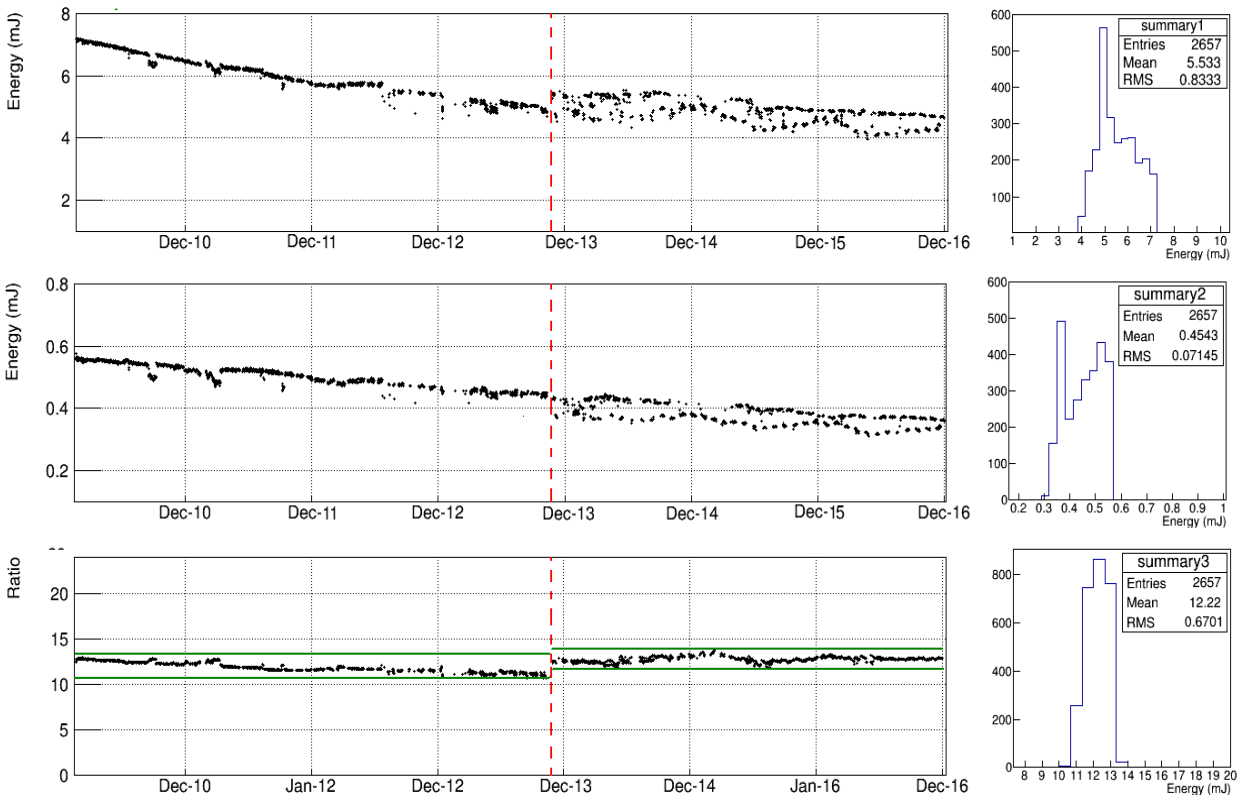

Figure 5.3: Top and center: The energy measurements in the XLF are presented in similar fashion as for the CLF in Figure 5.1 from 2009 to 2015. The aging of the laser can be easily observed. The vertical dashed line represents a change in the system (see text). Bottom: The ratio of these two quantities is not sensitive to the laser variations on energy. Before November 2013 the ratio is contained within the two green lines representing a $\pm$ 15% deviation from the average. After that date the data is within $\pm$ 15% away from the average value.

The stability of the CLF and XLF laser during a night of operation is presented in Figure 5.4 and presents the energy measurements by the monitoring for all the atmospheric laser shots vs the time lapse of an FD shifts. The plot superimposes the data from all the FD shifts in 2015.

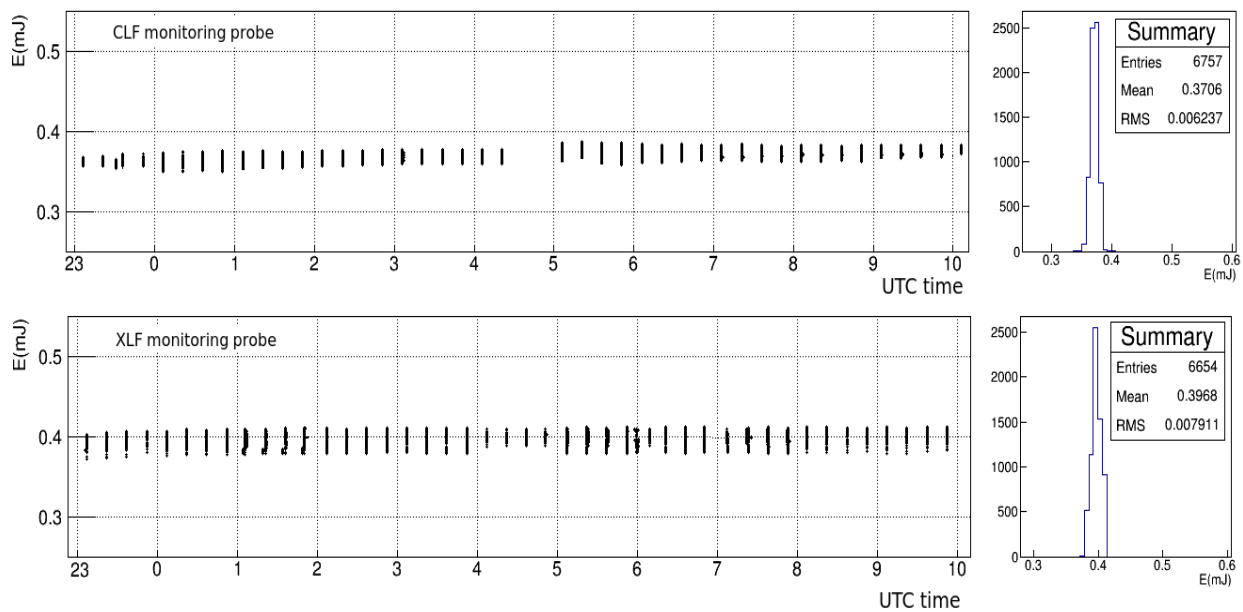

Figure 5.4: A year (2015) of energy measurements provided by the monitoring probe for atmospheric laser shots during the duration of FD shifts. Top: The CLF measurements remain within ±5% from the average. A gap in laser shots is visible in the second half of 4h UTC, this is due to the Raman operations. Bottom: The XLF laser is older and it presents slightly lower stability than the CLF. XLF measurements remain within 7% from the average

5.2 The Calibration Factors

A Calibration Factor (CF) is the average of the ratio between the energy measured by the calibration probe and the monitoring probe during a daily energy calibration routine (13 shots at the highest energy setting in the vertical mode).

$$CF = \frac{1}{13} \cdot \sum_{i=1}^{13} \left(\frac{E_{calibration}}{E_{monitoring}} \right). \tag{5.1}$$

Generally, one CF is calculated daily, but additional CFs can be calculated as frequently as needed for both vertical and steered mode (Figure 4.7). The CF is important, because

when multiplied by the relative energy (monitoring probe), it provides a good estimation of the absolute energy on every single laser shot.

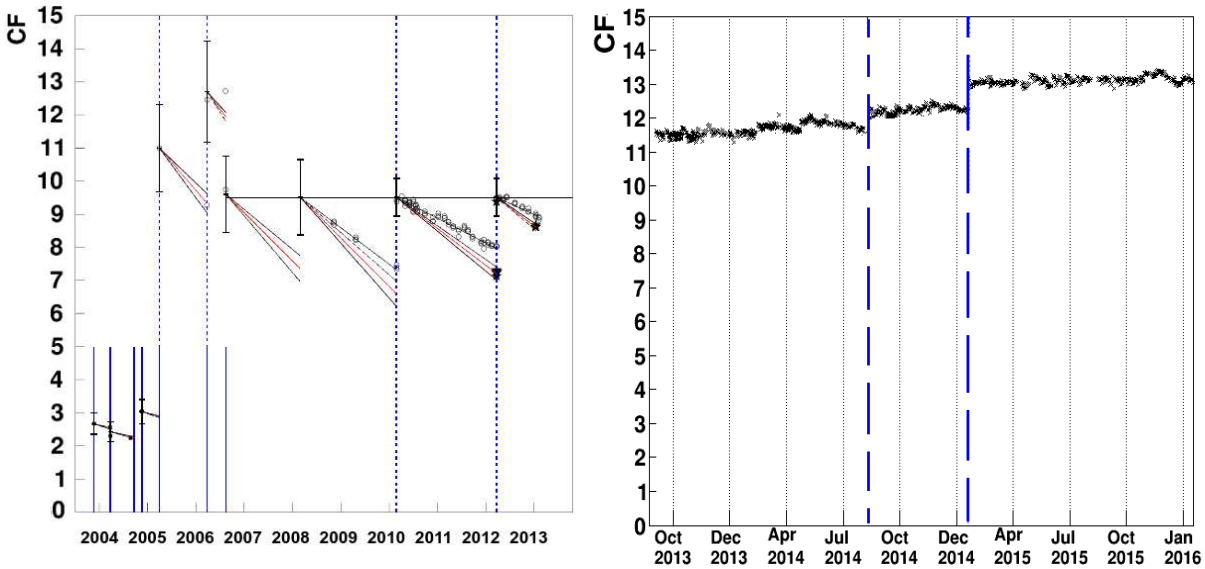

Figure 5.5: Left, pre-upgrade CF are shown in circles. Black and red lines represent fit functions including corrections. Blue lines represent epochs. (Right, post-upgrade) CF are measured every day. Calibration functions, fits or epochs are no longer required. Blue lines represent hardware changes.

Before the upgrade the process to obtain CFs was not simple nor accurate. Absolute energy measurements were performed manually at time intervals that ranged from a couple of months to one year. The available data was linearly fitted to provide a calibration function for different epochs. The epochs described a range of dates when the hardware was changed or the optics were cleaned. The calibration function has additional uncertainties, for example, it was corrected to account for the amount of light expected to scatter out of the beam due to the accumulated dust on the tilted mirror. The CF distributions before and after the upgrade are presented in Figure 5.5. This plot demonstrates the improvement in the stability of the laser energy delivered to the sky and the frequency of the CF measurements. After the CLF upgrade epochs are no longer required. The vertical dashed blue lines in Figure 5.5 (right) represent two modifications to the optics.

The sources of systematic errors that now dominate the calculation of the CF are the uncertainty in the measurements of the calibration energy probe (3%), the relative energy measurements (3%) and the uncertainty on the absolute polarization of the beam (3% to 5% dependent on the directions). Polarization measurements will be addressed in a later section. Rarely (less than 1%), the system fails to perform the energy calibration routine. For these cases (based on the stability of the system), the CF value is assigned to the last available measurement and its uncertainty error is increased to 10%.

Table 5.1: The information inside the CF files

Column	name	description
1	prefix	Number of shots in the set.
2,3,4	date	(2)year, (3)month and (4)day of the laser shot.
5	gps second	GPS second of laser shots
6	gps nanosecond	250, 500 for the CLF (350 and 700 for the XLF)
7	e_monitoring	Energy reading from the monitor (pick up) probe.
8	e_delivered	$CF * E_{monitoring}$
9,10	error	Energy errors
11	mode	Energy setting
12	azi	Azimuth angle (0° for vertical shots).
13	elv	Elevation angle (90° for vertical shots)

A binary file with the CF and some additional information is saved for future aerosol analysis (Table 5.1). These are used to match the shot by shot monitor measurements with each laser shot observed by the FDs. There is one CF file per month and per laser facility. Chapter 6 describes how these CF files are used in the calculation of the vertical aerosol optical depth.

5.3 Cross-calibration

Additional measurements of the CF are performed at least once per year using a reference energy probe on the CLF and XLF. The standard probe (probe 3) which normally is on the calibration stage during operations, is replaced with an standard probe brought from CSM. The standard probe ID is 221377 for the CLF and 5055291 for the XLF, the reference probe

ID is 718183. When the reference probe is placed on the calibration stage it must be aligned with the laser beam. Then absolute energy measurements are taken and CFs are calculated according to equation 5.1. A summary of the measurements is presented Table 5.2.

Table 5.2: Cross calibration measurements using a standard (Std) probe and a reference (Ref) probe.

Date	Location	CF (Std probe)	CF (Ref probe)	% Difference
03-18-14	CLF	11.91	11.26	5.5
01-24-15	CLF	13.14	12.47	5.0
09-21-15	CLF	13.12	12.44	5.1
03-03-16	CLF	13.27	12.56	5.3
03-13-17	CLF	13.09	12.41	5.1
03-16-14	XLF	12.36	11.83	4.2
01-23-15	XLF	13.12	12.34	5.9
09-21-15	XLF	12.64	11.61	8.1
03-09-16	XLF	12.95	12.01	7.2
03-12-17	XLF	12.87	11.75	8.7

The results present percentage differences that are less than 5.5% for the CLF. These difference variations remain less that 0.5% during all the measurements. Neither the reference probe or the standard probes have been factory calibrated recently. The XLF presents larger differences (up to 8.7%) with variation that seem increasing with time. This may suggest an aging of either the calibration or monitoring standard probes. This problem should be addressed in the near future. The reference probe (ID:718183) has been returned to CSM to go under a factory re-calibration.

5.4 Laser Alignment

The alignment was performed using a "3-point self-leveling laser level" (REF: Bosch Model # GPL3). The manufacturer claims an accuracy of ±0.25 inches at 100 feet. A vertical laser alignment in-situ is very challenging since setting up a reference point directly above the laser output at a considerable vertical distance is impractical. Instead the alignment is performed inside the container as illustrated in Figure 5.6.

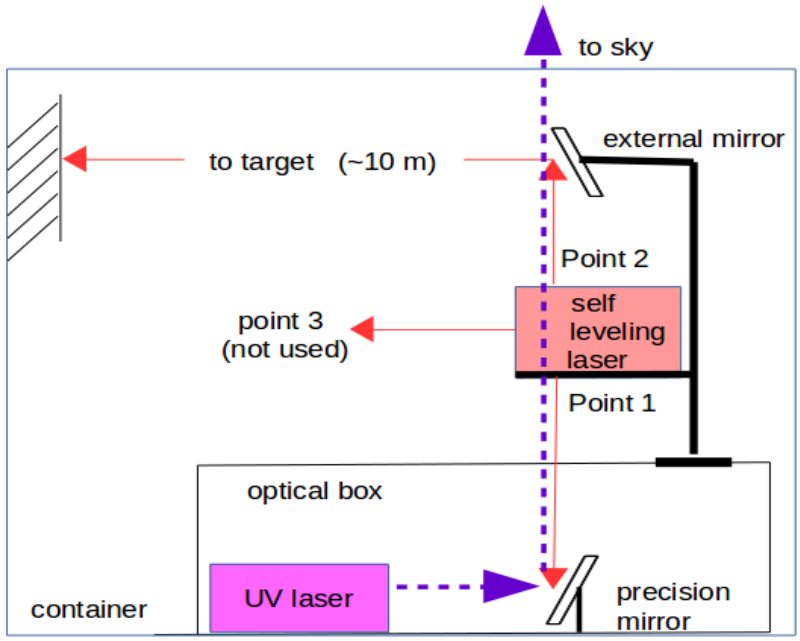

Figure 5.6: Simplified schematic of the laser alignment setup inside the CLF container.

The self-leveling laser is placed on a special platform over the UV laser exit in such a way that the beam pointing down (point 1) from the leveling laser is collocated over the UV beam path. The special platform includes an external mirror 45° above the leveling laser. The upside end of the leveling laser (point 2) is deflected by the external mirror towards a target placed in the inside of the container, about 10 m away. The leveling laser is then rotated in steps of 30° degrees and the new position over the target is marked. This process is repeated until completing a full circle. The marked positions form a circle with a radius less than 1 cm. Later on, the leveling laser is removed and the UV laser is turned on (placement and use of the external mirror is maintained). The knobs on the precision mirrors, located on the optical table, are tuned until the UV laser lies over the center of the previously marked spots. The external mirror is removed to allow the now aligned UV laser to continue vertically towards the sky. This process may take several hours to be completed. The same procedure is applied to the steered mode beam with similar results. This process allows the delivery of a fixed vertical beam with a deviation from vertical below 1 ± 0.002

cm (the radius of the target plus leveler uncertainty) per 10m (or less than $0.001° \pm 0.0002$ from vertical).

5.5 Linearity Studies

The laser needs to be fired within a μs time precision controlled by the "GPSY" (see Chapter 4).

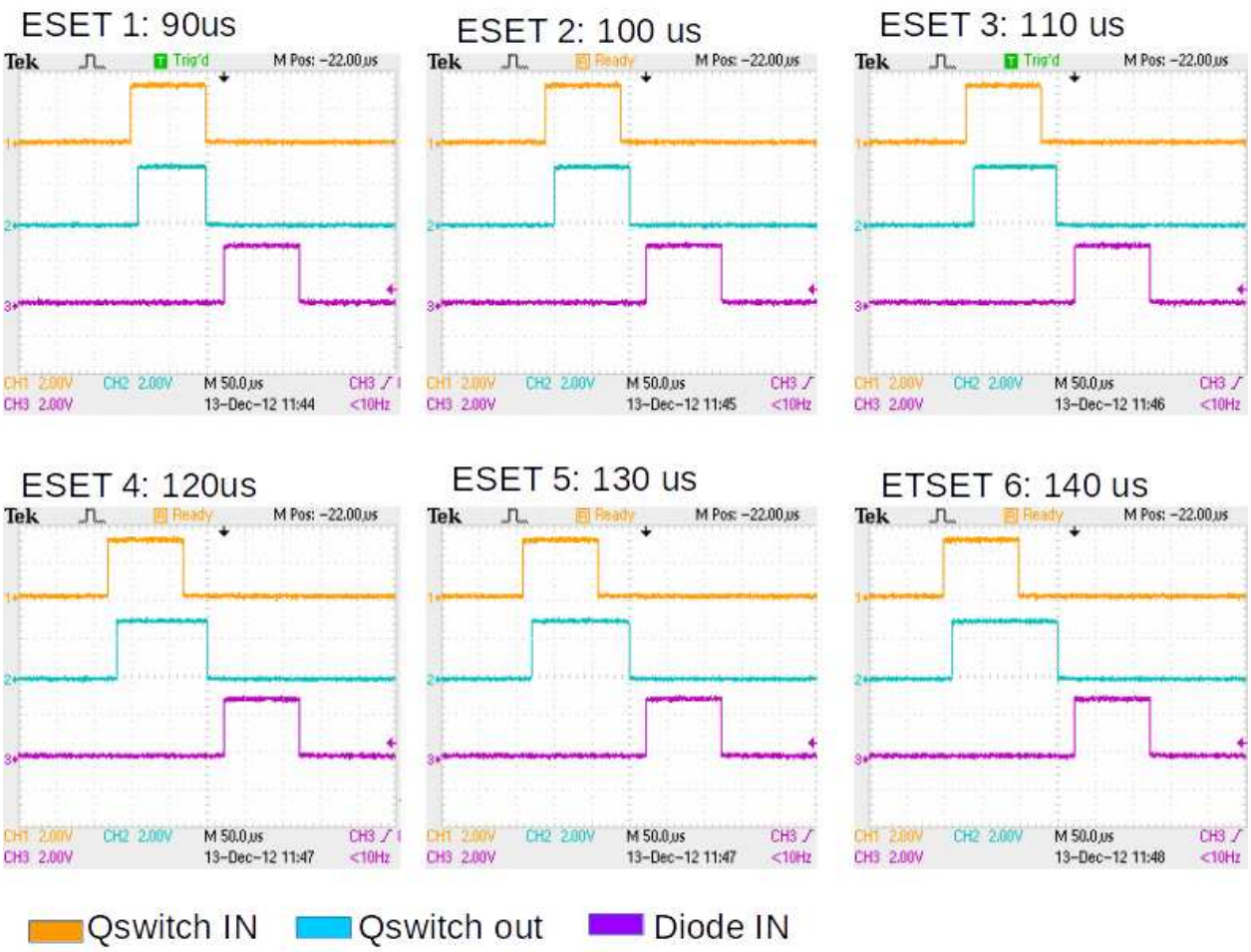

Figure 5.7: The trigger signal seen by the oscilloscope for 6 E_{SET}, the offset time between the raising edge of the Qswitch IN signal and the raising edge of the Diode IN signal is proportional to the laser energy.

The GPSY features a GPS engine (ref: Motorola m12+), one receiver, two trigger outputs and an outside antenna. Both GPSY outputs can be programmed in steps of 1 μs with an accuracy of $\pm 50ns$ [57]. Trigger output (1) is connected to the laser controller "Qswitch

IN". Trigger output (2) is connected to the laser "Diode IN". The Qswitch OUT signal is connected back to the SBC GPSY for feedback and to the laser probes controllers. This configuration allows to control the time of a laser shot, the duration of the laser pulse and the energy. The time difference between the rising edge of the Qswitch IN signal and the rising edge of the Diode IN signal is called the trigger offset.

The GPSY triggers (Figure 5.7) are configured in increments of 10 μs, such that a total of 6 different triggers offsets (90, 100, 110, 120, 130 and 140 μs) are available. Each trigger offset is proportional to the laser energy output and they are also referred as energy settings or E_{SET}. The programing of these variables was tested prior to the deployment of the CLF.

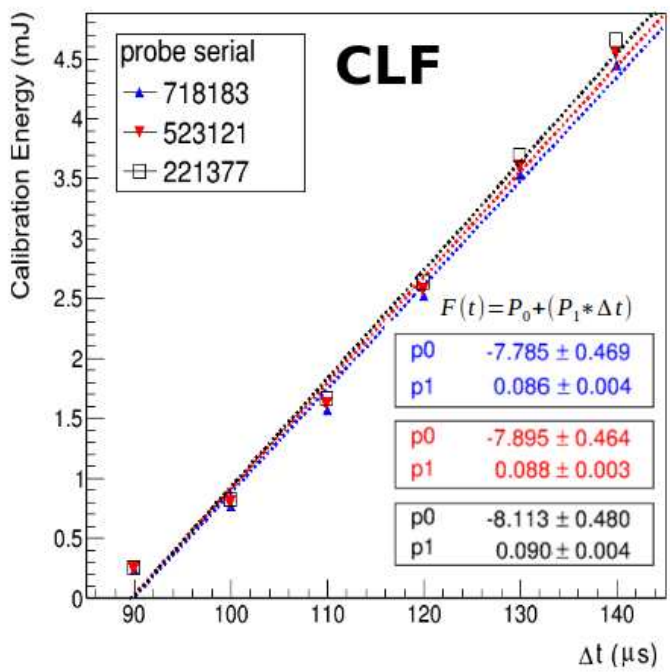

Figure 5.8: The CLF internal linearity has been tested with three energy probes. The data was fitted to a straight line.

For each of these E_{SET} the output energy, the laser was measured with 3 external probes (see Figure 5.8). The data fits a one degree polynomial function and the parameters are shown for each calibration probe.

A similar study was performed using the FD Los Leones to establish a relationship between the laser energy delivered to the sky and the number of photons from the laser arriving to the FD after being scattered in the air. Five sets of 200 laser shots with different energies (using the laser settings described before) were fired during an hour with the lowest levels of aerosol content in 2015 (Aug 18th at 5 UTC). The traces produced in the telescope by the laser are average for each set of 200 shots (see Figure 5.8 (left)). The method used to determine an hour free of aerosols and the calculation of the trace is explained in Chapter 6. The average for each of the five sets of 200 shots are as follows: A:4.93 mJ, B:3.89 mJ, C:2.82 mJ, D:1.77 mJ, and E:0.89mJ. The lowest energy setting available (E=0.20 mJ) was not included in this study, because the beam is too dim to systematically trigger the FD camera. A linear relationship was established between the averaged energy of the laser and the area under the curve of each trace in the camera (Figure 5.9 (right)).

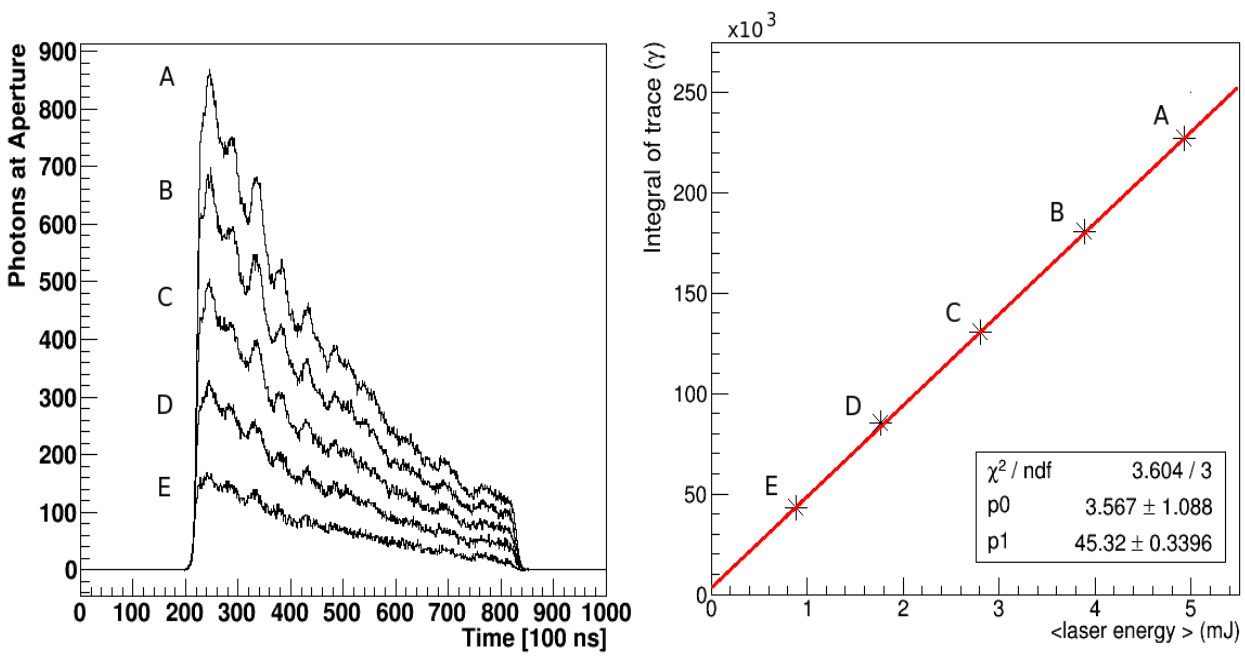

Figure 5.9: Left: Light profiles for laser shots (200 laser shots) fired with 5 different energy setting (in mJ): A:4.93, B:3.89, C:2.82, D:1.77, E:0.89. Right: The integrals of the traces are plotted vs the laser energy (average of 200 shots) and fitted to a straight line.

5.6 Polarization Measurements

A randomly polarized beam is preferred in order to assure that the light in the beam is equally scattered towards the FD buildings. Two depolarizing elements (one for each beam mode) produce a varying phase shift and randomizes the beam polarization (Table 4.2). The robotic calibration system includes a polarizing cube beam splitter, which separates the incident beam into vertical and horizontal polarization components (Figure 5.10).

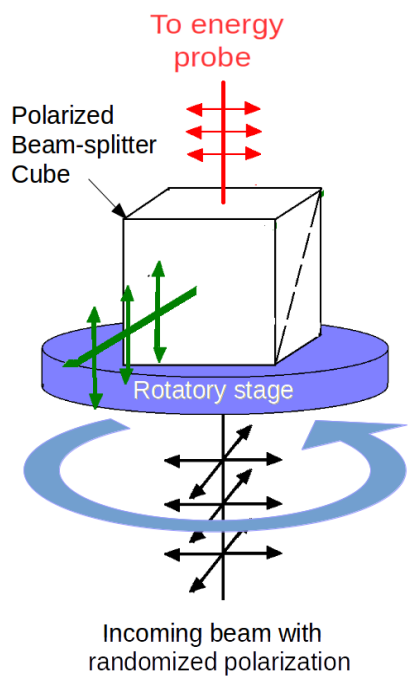

Figure 5.10: Schematic of the polarization cube mounted on the rotatory stage and the incoming laser beam.

The system was programmed to take polarized calibration measurements after each FD shift as follows:

- The lower stage is moved until the polarization cube is positioned over laser beam.
- Five laser shots at 1 Hz are fired at energies near 1 mJ. The laser energy is measured using probe 1.
- The averaged calibration factor (CF) for these 5 shots is recorded.

- The cube is incrementally rotated in steps of 45° and the process is repeated until full circle is completed.

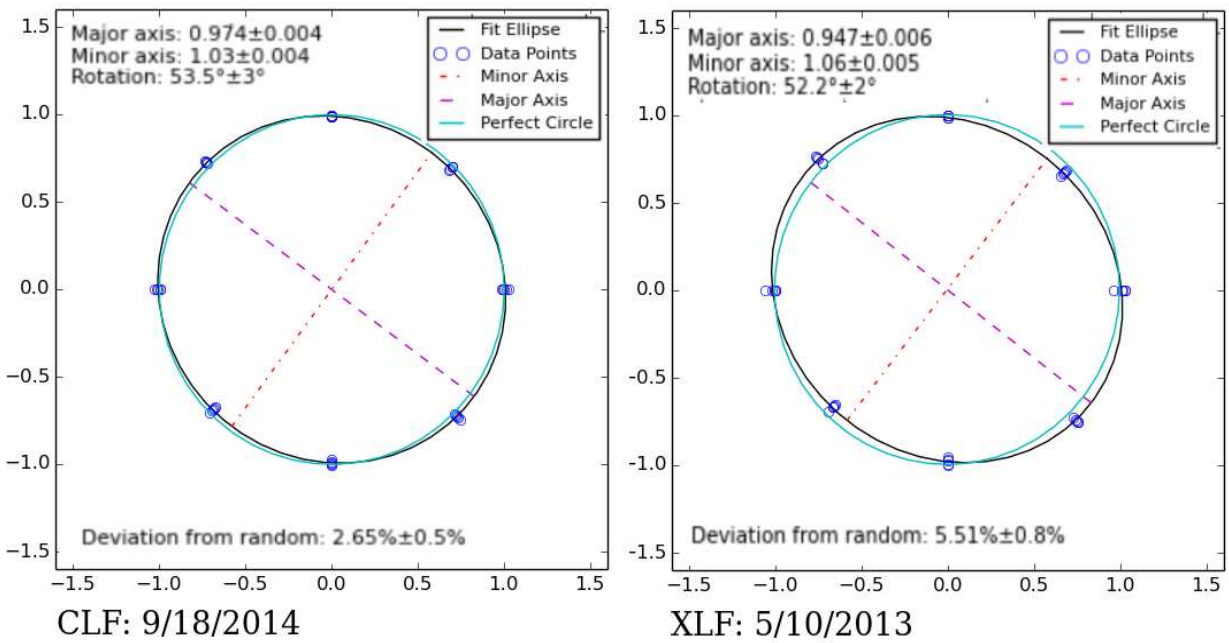

Figure 5.11: Left: Example of one daily polarization monitoring run fitted to a 3 parameter ellipse for the CLF. Right: The same method is applied to the XLF. Three different parameters are found in each fit.

A daily polarization calibration data includes 8 CF measurements with different P-cube rotation angles. The data for one polarization calibration in each laser facility can be displayed in polar coordinates as a function of the rotation angle (Figure 5.11), where the CF is normalized to an average of the 8 measurements. For a perfectly randomly polarized laser beam, the 8 data points should lie on a unitary circle. To assess the quality of the randomization, the data can be fitted to an ellipse using a least square minimization routine. A fitting program has been developed with the help of Michael Eustis and Jordan Diemer [81]. The parameters in the fit include the major axis, the minor axis and the rotation angle of the ellipse. A factor representing the percentage deviation from circular is defined as:

$$Deviation\ from\ circular = \frac{major\ axis - minor\ axis}{major\ axis + minor\ axis} \tag{5.2}$$

An example of the ellipse fit found for a calibration run in both laser facilities is shown in Figure 5.11. The two examples illustrated have exceptionally higher polarization parameters. They were selected to appreciate the deviation from circular.

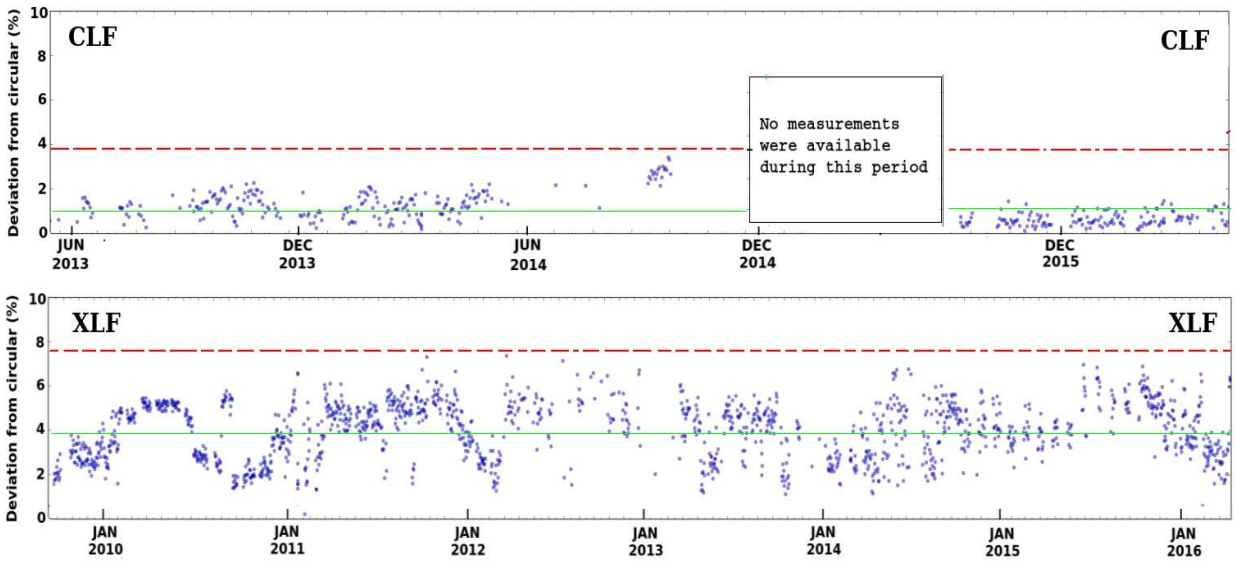

Figure 5.12: Chronological factors (deviation from circular) for both laser facilities. Blue dots represent the daily deviation factor. Green lines represent the average value. Dashed red lines indicate the maximum percentage deviation. Top and bottom plots have different time scales

The chronological values of the deviation from circular factors are plotted in Figure 5.12. The average percentage deviation from circular is 7% for the XLF and 3% for the CLF. The CLF has a lower average deviation since it is a newer and better understood laser. A large amount of the polarization data in 2014 is unfortunately not available but is expected to have similar values.

5.7 Beam Divergence

A small diverge in the vertical beam is preferred. If the beam spot diameter increases with altitude the scattered light at higher altitudes may arrive to additional pixel columns in the FD camera. This affects the scattered light FD measurements since the number of pixel columns used in the laser analysis is fixed.

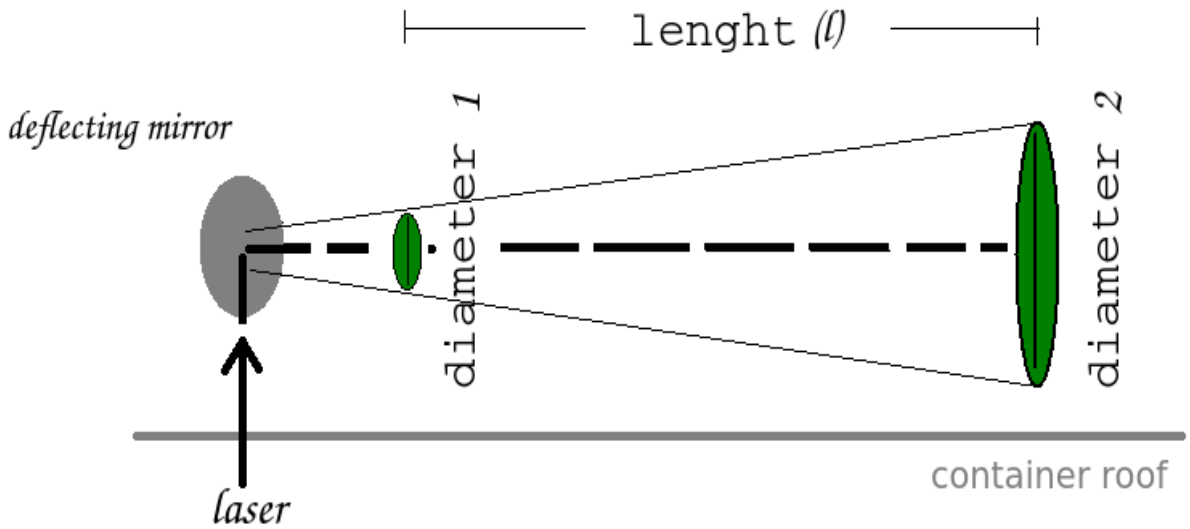

Figure 5.13: Schematic of the beam divergence measurement performed on the CLF and XLF container roof.

The divergence of the CLF laser beam in the fixed vertical mode was measured using the setup presented in Figure 5.13. The beam was deflected at the container roof exit towards a fixed target. The beam cross section diameter D_1 and D_2 were measured at two different points . Divergence is calculated as:

$$Divergence = arctan\left(\frac{D_2 - D_1}{l}\right) \tag{5.3}$$

D_1 was measured near the deflection point, D_2 at the end of the container wall. l is the distance to the fix target (11m). This same procedure was carried out using the laser output from the steering mode. The deflecting mirror is not necessary in this mode since the steering head can be used to point the beam towards the target. The beam divergences found are 0.8 mrad in the fixed vertical mode and 1.5 mrad in the steered mode.

5.8 Energy Equivalence Between Laser and Cosmic Events

Light scattered of a laser beam and fluorescence light emitted by an air shower is attenuated in the same way. Therefore, it is possible to compare the intrinsic brightness of EAS event and laser event, using the FD telescopes. To study this relationship, showers that have

geometrical properties similar to a CLF laser track have been identified. The EAS selected are nearly vertical and have similar distances from the FD as the CLF. The light profiles of these events are compared with the light profile of a CLF laser shot fired in the same hour. This time constraint is important to ensure that the reference laser events and EAS events of interest, were recorded by the FD under similar atmospheric conditions.

EAS events in this study, belonging to data sample known as the "Golden Hybrid", have been independently reconstructed by SD and FD[47] [82]. The initial study only considers events in the FD LL since it is the closest to the CLF, but the study can be extended to other eyes. The selection criteria are:

- Only shower events after the CLF upgrade are considered (2013-2015).
- The reconstructed FD energy (E) is larger that 10 EeV.
- The reconstructed inclination angle (θ) is less than 25° (near to vertical).
- The reconstructed distance between the FD and the shower event core at ground level, (D) is in a range of 26 ± 3km (The CLF-LL distance is nearly 26 km).
- The number of pixels triggered is larger or equal to 10.

Table 5.3: Summary of the shower candidates passing the selection criteria.

Event	YYMMDD-HHMMSS	E(EeV)	Theta	North(UTM)	EAST(UTM)	Dist(m)	Pixels
1	130603-002219	12.56	13.8	462188	6095137	23455	11
2	130827-014323	20.03	22.8	451713	6099080	28218	10
3	131206-053107	35.45	13.6	471988	6097766	28878	12
4	140203-013637	17.82	21.9	484164	6085788	28579	10
5	140601-072450	50.47	8.38	480791	6084302	24912	15
6	140726-012152	41.40	17.0	480501	6088442	26985	11
7	141022-055858	14.92	16.7	462419	6100259	28567	11
8	150417-032532	11.45	9.91	450248	6094219	24072	10
9	150612-053912	11.73	17.1	477783	6088602	25003	10
10	150721-085505	20.45	17.8	481081	6081861	24051	10

10 shower events passed the criteria selection (Table 5.4). The date is provided in a YYMMDD-HHMMSS format for identification purposes.

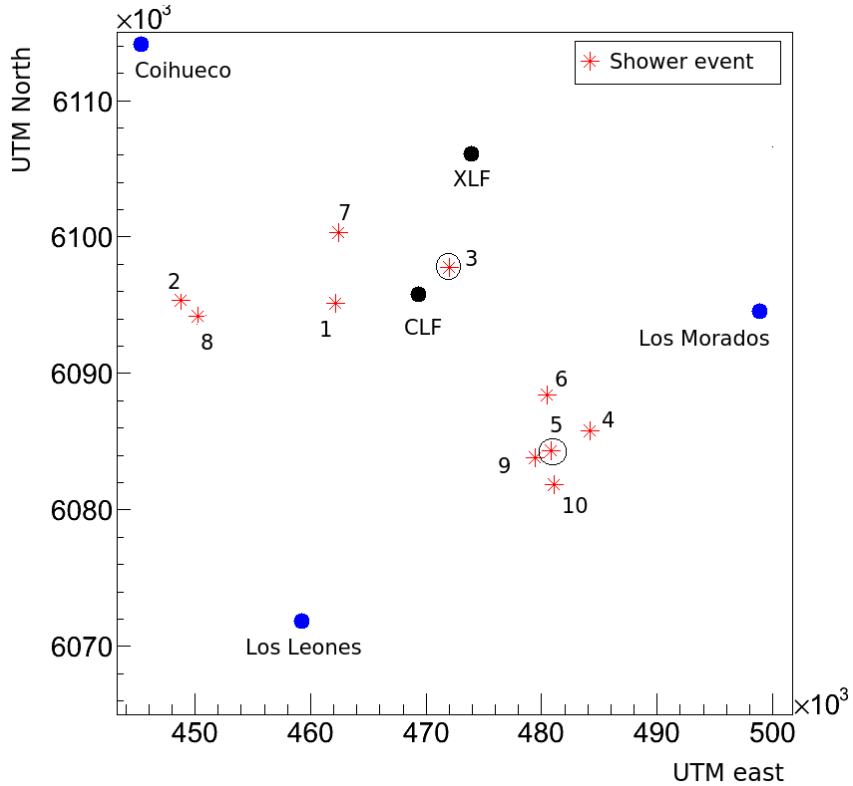

Figure 5.14: The ground core location of the 10 shower events passing the criteria relative to the location of the 3 FD eyes and the 2 laser facilities. Events marked with a circle are selected for further analysis.

Figure 5.14 presents the location of the 10 selected events relative to the location of the Pierre Auger facilities. Two stereo events are of particular interest and they are presented with a red circle on the map. Event 131206-053107 has the closest core distance from the CLF (therefore the light traveled nearly the same region of the atmosphere), and event 140601-072450 has the largest reconstructed energy (50.47 EeV) and the smallest vertical inclination (8.38°) . Both events are observed in stereo mode, which means that they are reconstructed by more than one FD site. A representation of the geometrical reconstruction (using $\overline{Offline}$) is presented in Figure 5.15.

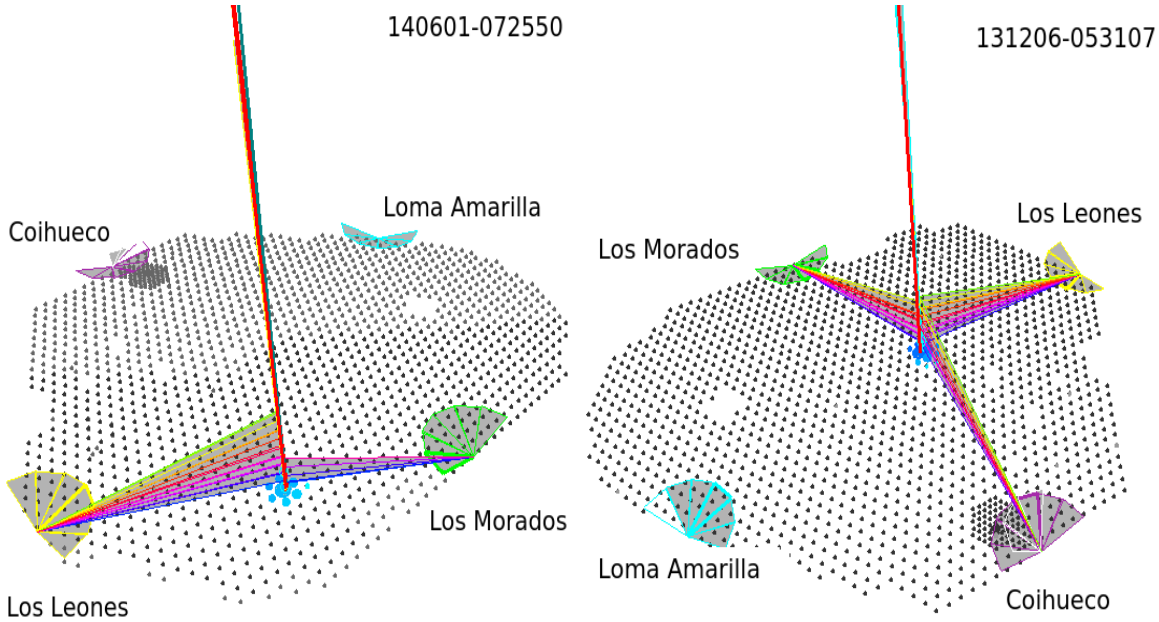

Figure 5.15: A 3D representation of the geometry of the shower events. The colors in the FD rays and SD tanks represent time of detection and signal strength, respectively.

Figure 5.16 compares the reconstructed energy deposition vs the slant depth for the same two events. The Xmax measured was $722 \pm 16 g/cm^2$ and $743 \pm 28 g/cm^2$ respectively.

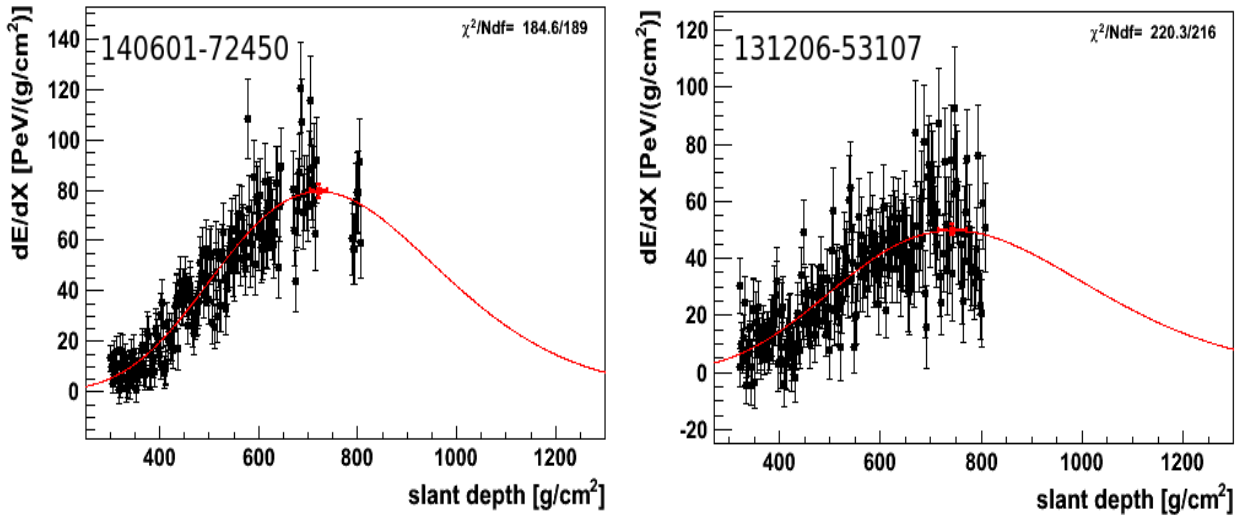

Figure 5.16: The energy development of the shower as function of the slant depth for event 140601-072450 and event 131206-053107. The red line is a Gaisser-Hillas fit.

The triggered camera pixels and the sum of pixel traces vs time bins (light profile) are presented in Figure 5.17. The two selected events were detected by different bays of FD LL. Event 140601-072450 was detected on bay 4 and event 131206-053107 was detected on bay 3. Each triggered pixel has a color code representing time of detection. The intensity of the light profiles is different but proportional to the energy of the shower event.

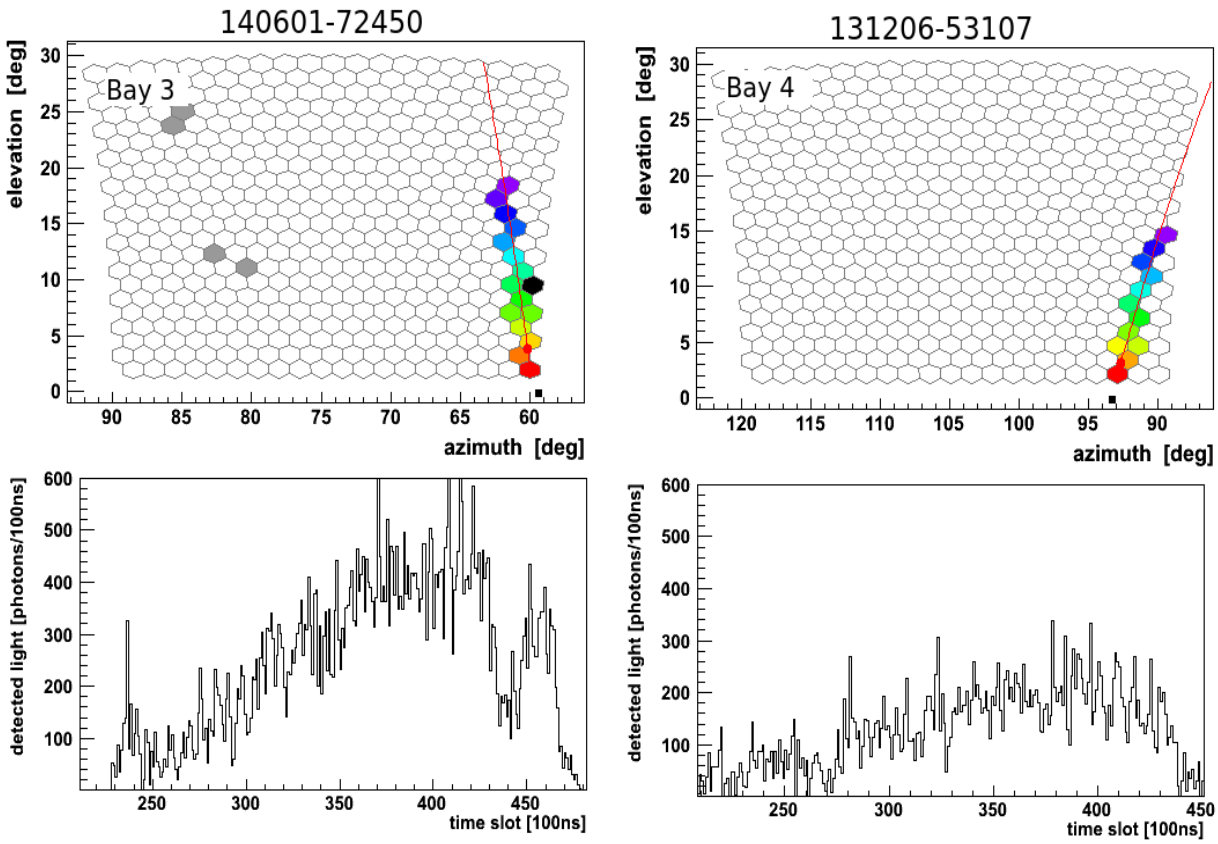

Figure 5.17: Top: Pixels triggered in FD LL camera for events 140601-072450 (left) and 131206-053107 (right). The pixels with a gray color are noisy pixels. Bottom: Sum of photon traces for the same event.

Figure 5.18 presents two FD light profiles created by a CLF laser shots fired within minutes of detection of the two shower events under study. The two laser shots have time stamps of 140601-072120 (left) and 131206-053629 (Right) (in YYMMDD-HHMMSS format). The measured energies are 5.0 ± 0.05 J and 4.6 ± 0.05 J respectively. The laser photon traces are an absolute scale and they have not been normalized to laser energy. The shower light

profiles are superimposed on top of the laser light profiles in Figure 5.18. In order to compare events that travel in opposite directions, the shower events were inverted and translated in time such that the start of the laser detection coincides with the end of the shower event detection.

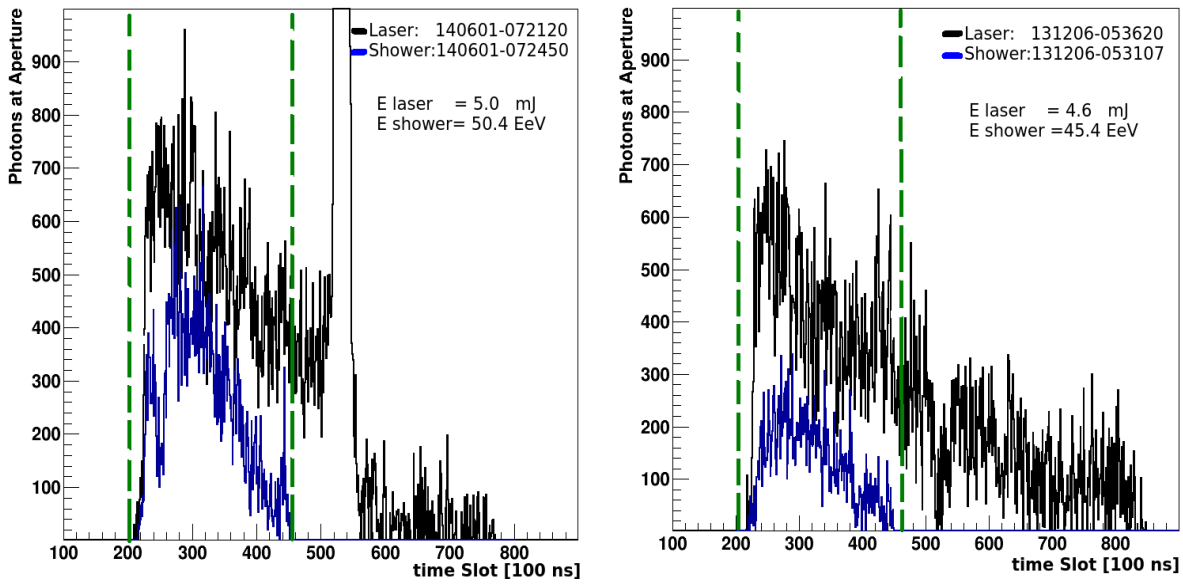

Figure 5.18: The superimposed FD traces of the shower and laser for event 140601-072450 (left) and 131206-053107 (right). The shower light profile is inverted and translated in time. The laser light profile with a spike in intensity indicates a cloud presence over the CLF. Regions of interest are between the dashed lines.

The laser light profile on 140601-072120 (left) indicates cloud presence above the CLF. The cloud is located at high altitude, in a region that is uninteresting for this particular comparison because it is above the development of the shower.

A systematic comparison of the light profiles is performed to the events presented in Table 5.4. Only the laser profile region that superimposes the shower profile (region of interest) is considered in this study. The laser profile beyond the region of interest is truncated since it does not contributes to the comparison and its contents are set to zero. The integral of the shower light profile and the truncated laser light-profile are calculated. The ratio of the two integral values is also calculated for each event. A summary of the 10 events is presented in Table 5.4.

Table 5.4: Summary of the light profile integrals and ratio for the 10 candidate shower and laser events.

Event	YYMMDD-HHMMSS	E Shower (EeV)	E laser (mJ)	Int Shower	Int Laser	Ratio Int	Ratio E
1	130603-002219	12.5	4.9	16830.0	94938.3	5.64	0.39
2	130827-014323	20.0	5.2	18739.2	61424.5	3.27	0.26
3	131206-053107	35.4	4.6	31414.7	106825.0	3.40	0.13
4	140203-013637	17.8	4.7	13129.7	89295.8	6.80	0.26
5	140601-072450	50.4	5.0	64186.9	129551.0	2.01	0.10
6	140726-012152	41.4	4.7	33028.4	86424.8	2.61	0.11
7	141022-055858	14.9	5.0	14318.7	79695.1	5.56	0.34
8	150417-032532	11.4	4.7	14778.7	69444.8	4.73	0.41
9	150612-053912	11.7	4.9	11432.1	83575.4	7.75	0.42
10	150721-085505	20.4	4.8	17422.9	107297.0	6.15	0.23

The integrals and ratios for the laser and shower profiles can be visualized in picture Figure 5.19, while the ratios of the integrals vs the energy of the showers are presented in the scatter plot in Figure 5.20

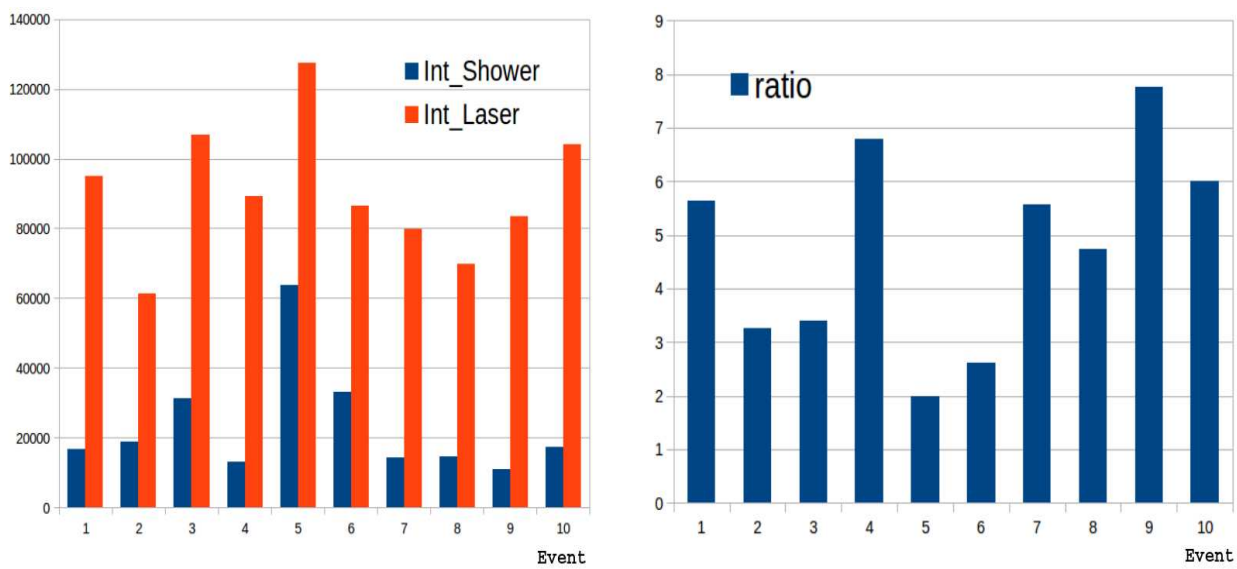

Figure 5.19: Left: The integral of the selected shower events next to the integral of the truncated laser profile. Right: The ratio of the integrals.

A possible linear behavior can be seen in Figure 5.19. Some outliers are also present. A line was drawn for reference purposes. Unfortunately more statistics are necessary in order

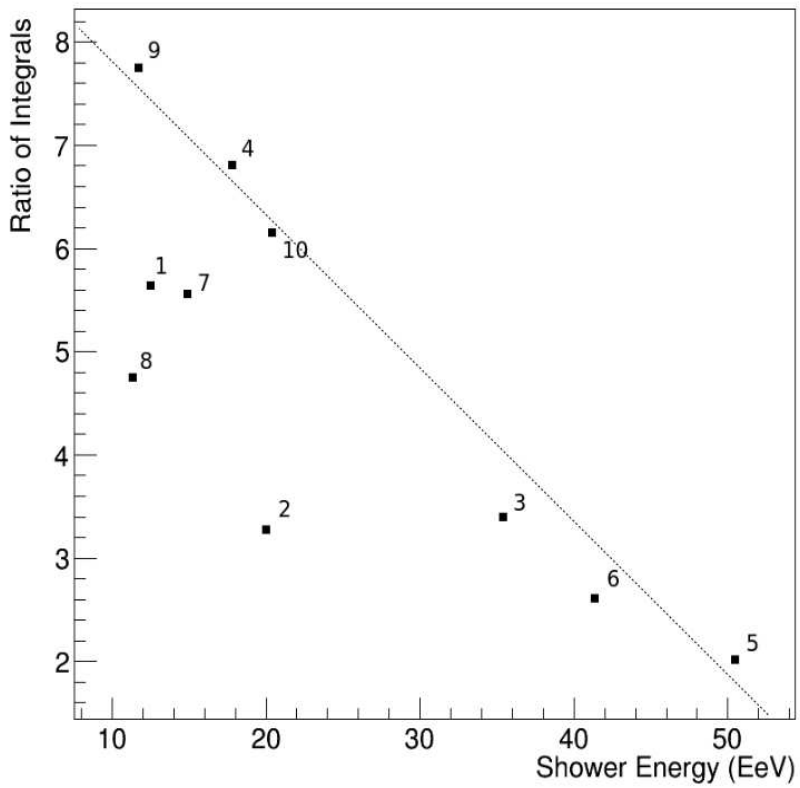

Figure 5.20: The ratio of the integral vs shower energy. A line has been drawn to indicate a possible linear behavior, although more statistics will be needed to determined if this linearity is real.

to provide any conclusions. But an initial explanation for the presence of outliers include local atmospheric effects, loose geometrical cuts, uncertainties in the FD reconstructions, and differences between FD bays calibrations. If a linearity is present with the addition of more candidates from other years and eyes then a qualification of the energy equivalence can be easily calculated in terms of MeV per mJ of laser energy. If a linearity is not found it will be an indication of the intrinsic differences in the physics of an EAS or laser shot.

CHAPTER 6

AEROSOL MEASUREMENTS AND THE DATA NORMALIZED ANALYSIS

Aerosol measurements of $\tau(z)$ at the Pierre Auger observatory are derived from FD measurements of side scattered light out of the CLF and XLF laser beams. Two methods, the Laser Simulation (LS) and the Data Normalized (DN) are used to obtain $\tau(z)$ measurements from the laser tracks. This chapter will describe both with a focus on the DN method.

6.1 Detection of Laser Light by the FD

An example of a CLF laser event as seen by four FD sites (stereo event) using the $\overline{Off}\underline{line}$ software is presented in Figure 6.1.

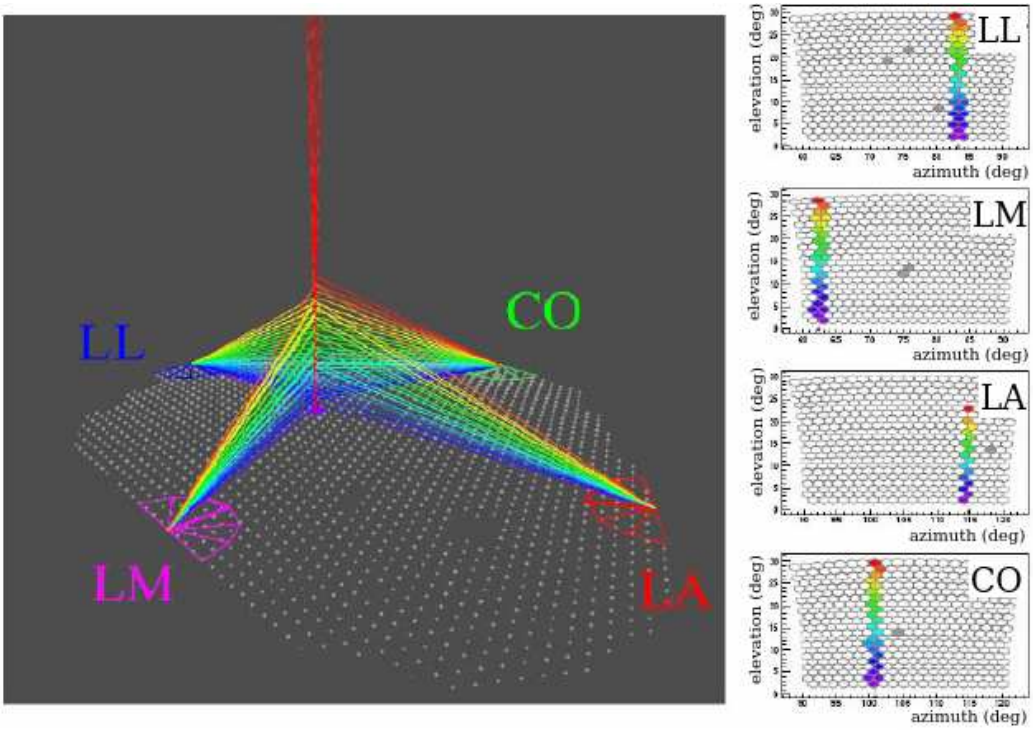

Figure 6.1: Left: A representation of a CLF laser event recorded by 4 FD sites. The lines represent the scattered light traveling towards the cameras, they are color coded to represent time of detection. Right: The light track produced in each FD camera. The pixels are color coded to represent time of detection (purple is earlier time and red is later time).

All FD laser tracks are detected with time offsets of 250 ms and 500 ms (CLF and XLF) after the second. They are separated from all other events using this time signature and later used in the atmospheric analysis. A typical CLF track seen by the FD site LL (bay 3) is presented in Figure 6.2 (left). Each hexagon represents one pixel of the FD camera. The colors on the pixels represent time of detection. Several pixels are marked with a dot and their corresponding ADC signal vs time is presented in Figure 6.2 (left). The ADC maximum signal decreases for pixels overlooking higher altitudes (pixels located on the upper part of the camera). This effect is explained by the increase in the total path length traveled by the light scattered at higher elevations (larger attenuation effects). Cosmic rays have an inverted time signature, where photons emitted in the upper atmosphere are detected earlier than those emitted in the lower part of the atmosphere . Negative counts are present due to noise pedestal subtraction.

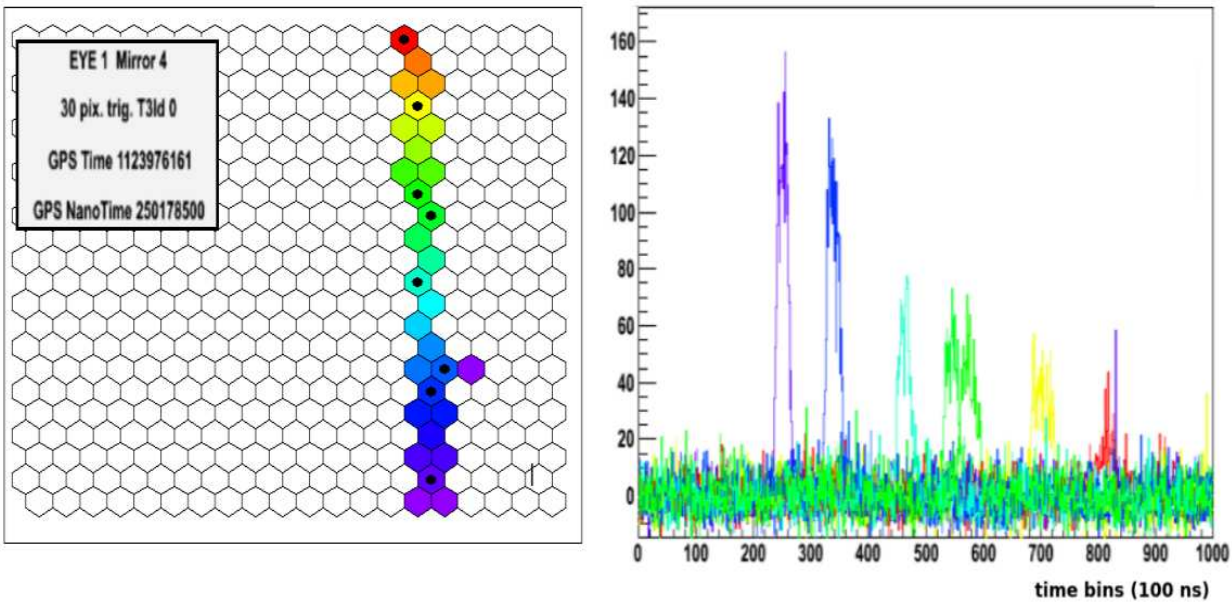

Figure 6.2: Left: A laser track detected in FD LL. The track can be identified to be produced by the CLF due to is 250 ms offset (GPS nanosecond signature). The pixels are color coded to represent time of detection. Right: The ADC counts vs time, of several pixels (marked with a dot) from this laser track are superimposed. Negative counts are the product of a noise pedestal subtraction.

A measurement of $\tau(z)$ begins with the generation of a laser light profile (number of photons at aperture vs altitude) from the ADC signal vs time bin of pixels containing the laser track. These pixels are always located within three consecutive columns in the FD camera. The group of pixel columns is selected to be the closest to the laser track axis. The selection is different for each FD eye and laser source and it depends on the FD-laser position. Table 6.1 presents the bays and columns selected.

Table 6.1: Summary of the pixels columns and bays used in the DN analysis.

FD site	Los Leones		Los Morados		Loma Amarilla		Coihueco	
	bay	pixel columns	bay	pixel columns	bay	pixel columns	bay	pixel columns
CLF	4	14,15,16	3	1,2,3	4	15,16,17	3	6,7,8
XLF	4	14,15,16	3	15,16,17	4	14,15,16	3	12,13,14

The ADC counts vs time bins from the pixels belonging to the three selected columns are added bin by bin. This signal addition also includes all atmospheric laser tracks detected during a quarter of hour time window (normally 50 laser shots). The electronic signal is then converted into photons at aperture at each time bin (100 ns). This conversion involves a photometric calibration of the FD cameras with a calibrated 2.5 m diameter light source known as the "drum". This calibration is performed once per year and it is of extreme importance not only in the production of the laser light profile but especially for the reconstruction of EASs. Specifics of this calibration are found in [46]. The resulting profile is known as either a trace profile or a light profile. An example of a trace profile is presented in Figure 6.3 (left). The repeating peaks and valleys of intensity are an effect of spot sweeping across the small gaps between pixels in the camera.

The next step normalizes the trace profiles to 1 mJ energy laser shots to make them independent of the initial laser energy. The normalization is performed by scaling the light profile to the corresponding calibration factor (CF) as described in Chapter 5. The corresponding CF is found by matching the GPS times. The time bins of the normalized light profiles are converted into altitude bins (100 m each) using equation 6.1 and FD-laser geometry

introduced in Chapter 4:

$$H_{bin} = (-D) * tan\left(\phi_0 - 2 * atan\left[\frac{c}{D * (t_{bin} - t_0)}\right]\right) + H_0; \tag{6.1}$$

where D is the distance between the laser facility and the FD, ϕ_0 is the laser vertical inclination angle (90° for fixed vertical mode), c is the speed of light, t_{bin} and t_0 are the bin and initial time of detection, H_0 is the altitude correction which includes the altitude difference between the laser facility and the FD, plus an altitude corrections due to the curvature of the Earth (nearly 50 m for distance of 30 km). The resulting profile is known as the light profile. An example of the light profile obtained is presented in Figure 6.3 (right).

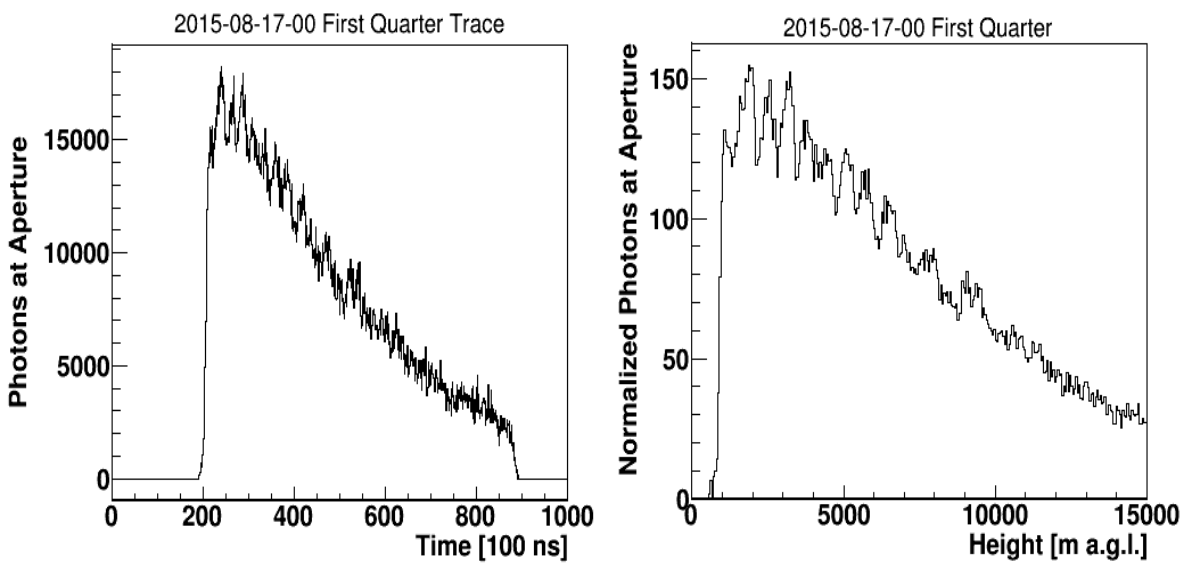

Figure 6.3: Left: The light profile obtained by the FD from the side scattered light from 50 laser shots (nominal for a quarter of hour) from the CLF. Right: The light profile for the same quarter hour period when normalized by the laser energy. The repeating peaks and valleys of intensity are an effect of spot sweeping across the small gaps between pixels in the camera.

An hourly light profile is obtained by averaging four quarter-hour laser profiles. Ideally, under a clear atmosphere and equal telescope performance, the shape of all hourly profiles (from the same laser source and FD site) will be practically identical to one another. In reality, the light profiles change due to the different atmospheric conditions present at the time of detection such as aerosol content and cloud coverage. Figure 6.4 (left) presents three

hourly CLF light profiles measured by the FD LM, under low, average and high aerosol content. The light profiles are different because the aerosol particles attenuate the number of photons reaching the detector as well as scatter more light from the initial beam. Observing the scattering produced at an altitude 4 km above ground level, low aerosol concentration reduces the observed signal by 29%. Similarly, high aerosol concentration would reduce the same signal by roughly 70%.

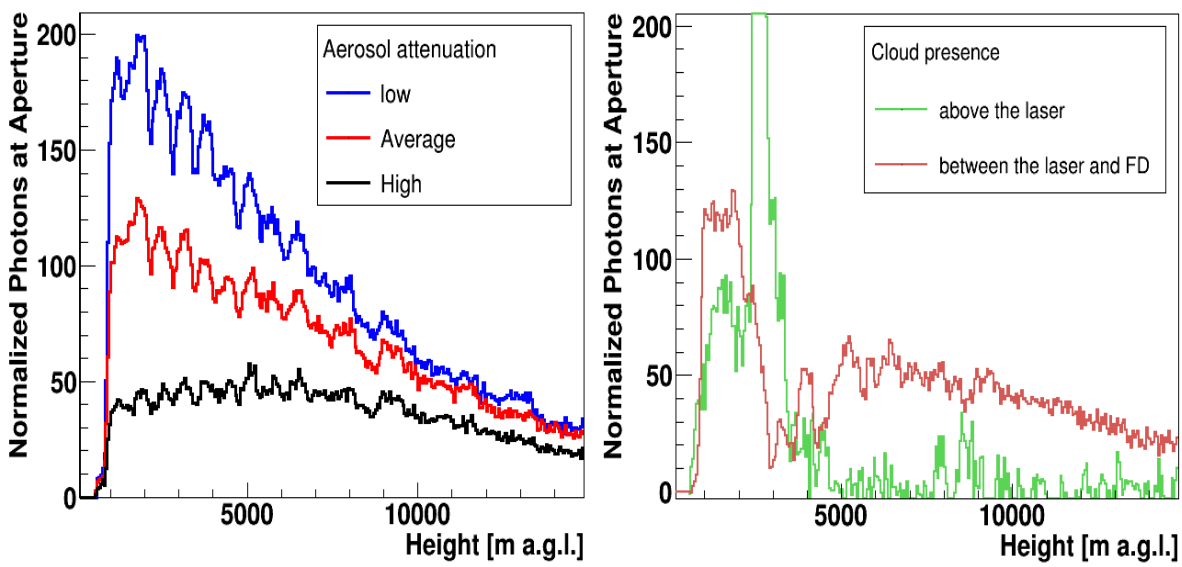

Figure 6.4: Left: Three hourly light profiles seen by the FD Los Morados during 2015 for three different aerosol attenuation levels: high (04/10 at 01 UTC), average (05/16 at 00 UTC) and low(06/16/ at 23 UTC). Right: A cloud above the laser (08/21 at 09 UTC) and cloud between the laser and the FD (05/27 at 04 UTC) affect the amount of laser light reaching the detector.

Figure 6.4 (right) presents two light profiles affected by clouds. If the cloud is directly above the laser beam, the amount of scattered light increases at the altitude where the cloud is present and it prevents scattered light at higher altitudes from reaching the telescope. Cloud presence between the FD and the laser will attenuate the scatter light traveling towards the FD creating a deficit of detected photons in some regions of the profile. The fraction of hourly profiles that are affected by clouds per year is nearly 35% as averaged over all FD eyes.

6.2 The Data Normalized Analysis Formulation

The Data Normalized formulation was developed at the HIRES experiment [83] and adopted by the Pierre Auger Observatory [84]. It is based on the light propagation theory described in Chapter 3 and the laser-FD geometry illustrated in Figure 6.5.

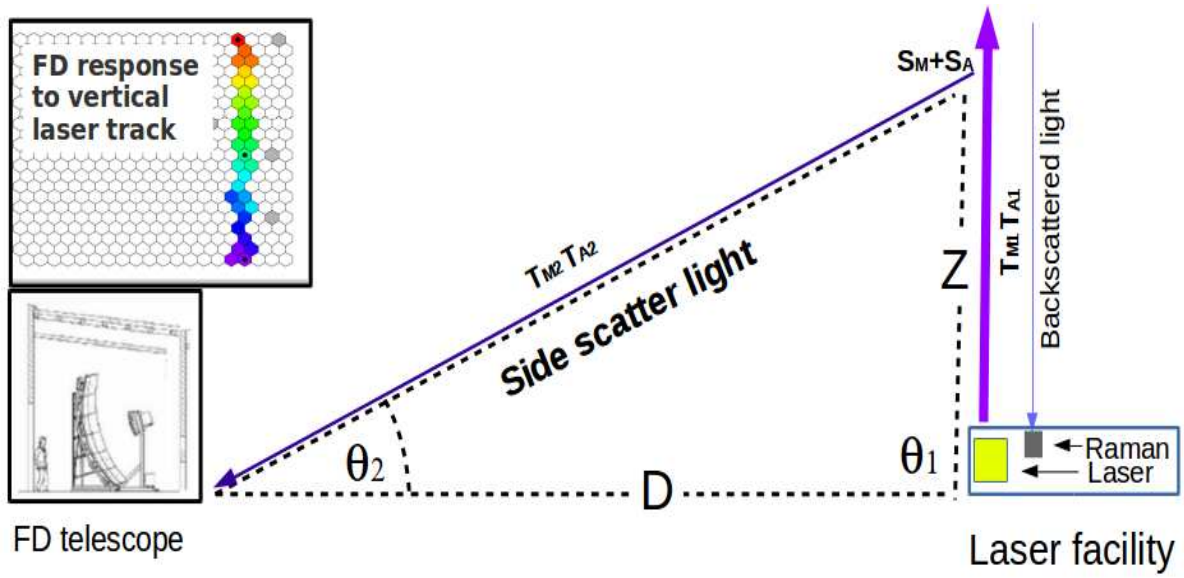

Figure 6.5: Layout of the laser-FD geometry, where D is the distance between the laser and the FD site, Z is the scattering point altitude (a.g.l) and θ is the elevation angle of the scattered light detected by the FD. T_M, T_A, S_M and S_A are the atmospheric, aerosol transmission and scattering factors. The backscattered light is only detected by the Raman LIDAR.

The number of laser scattered photons arriving at any FD telescope is (N_{obs}) is given by:

$$N_{OBS} = N_{LASER} \cdot (T_{M1}T_{A1}) \cdot (S_M + S_A) \cdot (T_{M2}T_{A2}) \tag{6.2}$$

where N_{LASER} is the number of photons coming out of the laser facility, T_{M1} and T_{A1} are the molecular and aerosol transmission factors from the laser output to the scattering point, S_M and S_A are the molecular and aerosol scattering factors and T_{M2} and T_{A2} are the molecular and aerosol transmission factors from the scattering point to the FD aperture.

Under purely molecular atmospheric conditions equation 6.2 becomes:

$$N_{MOL} = N_{LASER} \cdot T_{M1} \cdot S_M \cdot T_{M2} \tag{6.3}$$

the ratio of 6.2 and 6.3 is:

$$\frac{N_{OBS}}{N_{MOL}} = T_{A1}T_{A2} \cdot \left(\frac{S_A}{S_M} + 1\right) \tag{6.4}$$

using equation 3.3, equation 6.4 can be expressed in term of τ and θ

$$\frac{N_{OBS}}{N_{MOL}} = exp\left(\frac{-\tau_{A1}}{sin\theta_1}\right) exp\left(\frac{-\tau_{A2}}{sin\theta_2}\right)\left(\frac{S_A}{S_M} + 1\right). \tag{6.5}$$

Under the assumption of horizontal atmospheric homogeneity $\tau_{A1} = \tau_{A2} = \tau_A$ and taking the natural logarithm on both sides, equation 6.6 reads

$$ln\left(\frac{N_{OBS}}{N_{MOL}}\right) = \frac{-\tau_A(sin\theta_1 + sin\theta_2)}{sin\theta_1 sin\theta_2} + ln\left(\frac{S_A}{S_M} + 1\right) \tag{6.6}$$

for vertical laser shots $sin\theta_1 = 1$, solving for τ_A ones get

$$\tau_A = \frac{sin\theta_2}{(sin\theta_2 + 1)} \cdot \left(-ln\left(\frac{N_{OBS}}{N_{MOL}}\right) + ln\left(\frac{S_A}{S_M} + 1\right)\right). \tag{6.7}$$

As explained in chapter 3, the scattering factors S_A and S_M depend on the phase function but unfortunately, they cannot be easily incorporated into equation 6.7. Fortunately, in most cases the amount of light molecularity scattered greatly exceeds the amount scattered by aerosols and the ratio S_A/S_M can be assumed to be very close to zero and equation 6.7 simplifies to

$$\tau_A = \frac{sin\theta_2}{(sin\theta_2 + 1)} \cdot ln\left(\frac{-N_{OBS}}{N_{MOL}}\right). \tag{6.8}$$

When the last expression is applied to different scattering point along the beam path, a $\tau_A(z)$ profile can be written as

$$\tau_A(z) = ln\left(\frac{NPA(z)_{REF}}{NPA(z)_{OBS}}\right)\left(\frac{z}{z + \sqrt{z^2 + D^2}}\right) \tag{6.9}$$

where $NPA(z)_{OBS}$ and $NPA(z)_{REF}$ are the number of photos at aperture (the light profiles) from an observed hour and a reference molecular hour respectively. Equation 6.9 is the heart of the Data Normalized analysis since it allows the calculation of $\tau_A(z)$ in terms of known quantities, such as the altitude (z), the distance (D) from the laser to the FD, and the amount of photons recorded by the camera.

6.3 The Reference Profiles

The selection of the reference light profile is a crucial piece in the DN analysis. The reference hourly light profile is assumed to be measured during a night of pure atmospheric conditions with negligible levels of aerosol. If this condition is not achieved, the calculated $\tau_A(z)$ measurements can decrease by more than 20% (see chapter 8). Consequently, it is helpful to have an independent $\tau_A(z)$ measurement as the one provided by the Raman LIDAR to benchmark the DN analysis by direct comparison of the two independent methods.

Before the CLF upgrade in 2013, one reference profile was selected per "epoch" (each epoch ranging from several weeks to several months). After the CLF upgrade, epochs were no longer necessary (as explained in chapter 4) because of the new automatic calibration system. Instead, the use of one reference profile per year is now implemented. The XLF has been working under this scheme since it was built.

The process to build a reference light profile is quite simple. A list of hourly light profiles for the year of interest (nearly 2500 profiles per FD per year) is produced. From the produced set of light profiles one can select the profiles with regular shape, similar to the one presented in Figure 6.3. Profiles with cloud presence or discontinuities should not be taken into consideration. After this first selection one can hand pick the light profiles with the largest signal (largest NPA(z)) at most altitude bins. Generally for each year, there is only one night (or two) with hourly profiles that are obvious candidates. The final reference light profile is obtained by averaging three or more hourly light profiles during this clearest night.

Table 6.2: Dates when the reference hours were found for each FD site, year and laser facility.

FD site	Los Leones		Los Morados		Loma Amarilla		Coihueco	
year	CLF	XLF	CLF	XLF	CLF	XLF	CLF	XLF
2013	Jul 15	Jul 15	Jul 15	Jul 15	Jul 15	Jul 15	Jul 15	Jul 15
2014	Jul 07	Jul 07	May 5	May 5	Jul 15	Jul 15	Jul 15	Jul 15
2015	Aug 18	Aug 18	Aug 18	Aug 18	Aug 18	Aug 18	Aug 18	Aug 18

The reference nights are generally found during austral winter nights. One reference profile is needed per FD site and laser facility. The list of the day and hours found used to build reference profiles after the CLF upgrade is presented in Table 6.2.

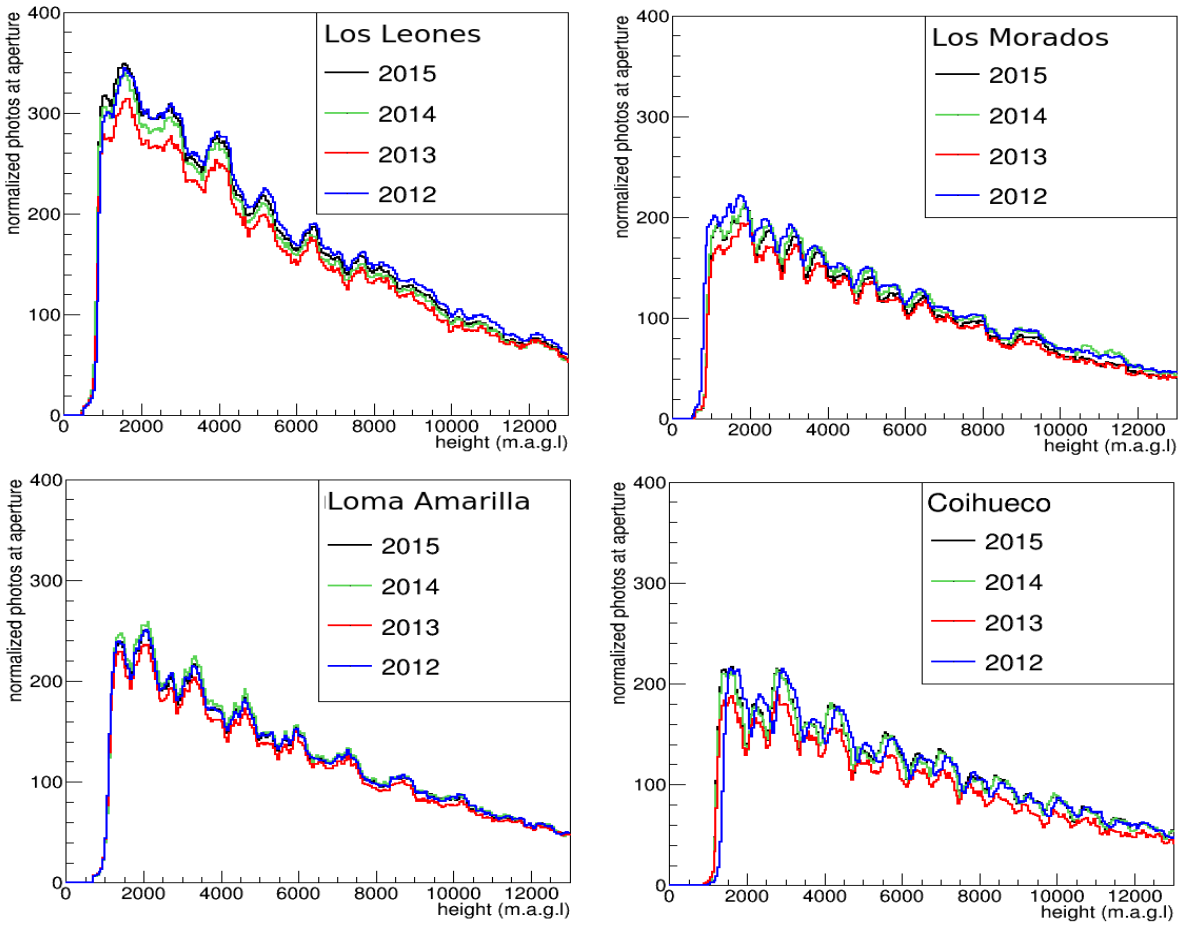

Figure 6.6: The reference light profiles used found from 2012 to 2015 in all FD sites. The light profiles obtained with the FD site LL, LM and CO use the CLF, while the profile from FD site LA uses the XLF. The intensity of each FD site light profile varies accordingly to its distance to the laser. Differences in the profiles up to 10% suggest that not all yearly reference profile are of a purely molecular nature and free of aerosols.

Figure 6.6 superimpose the reference light profiles used in the DN analysis after the CLF Upgrade. The profiles from 2012 (with the old CLF laser) have been included for reference purposes and they demonstrate that the normalization method is independent of the laser energy. The intensity of the profiles is proportional to the distance to the laser. The overall

shape of the profiles is similar but there are differences up to 20% on the NPA(z) . These differences are presented in Figure 6.7 where the light profiles are scaled by the average of the four years selected.

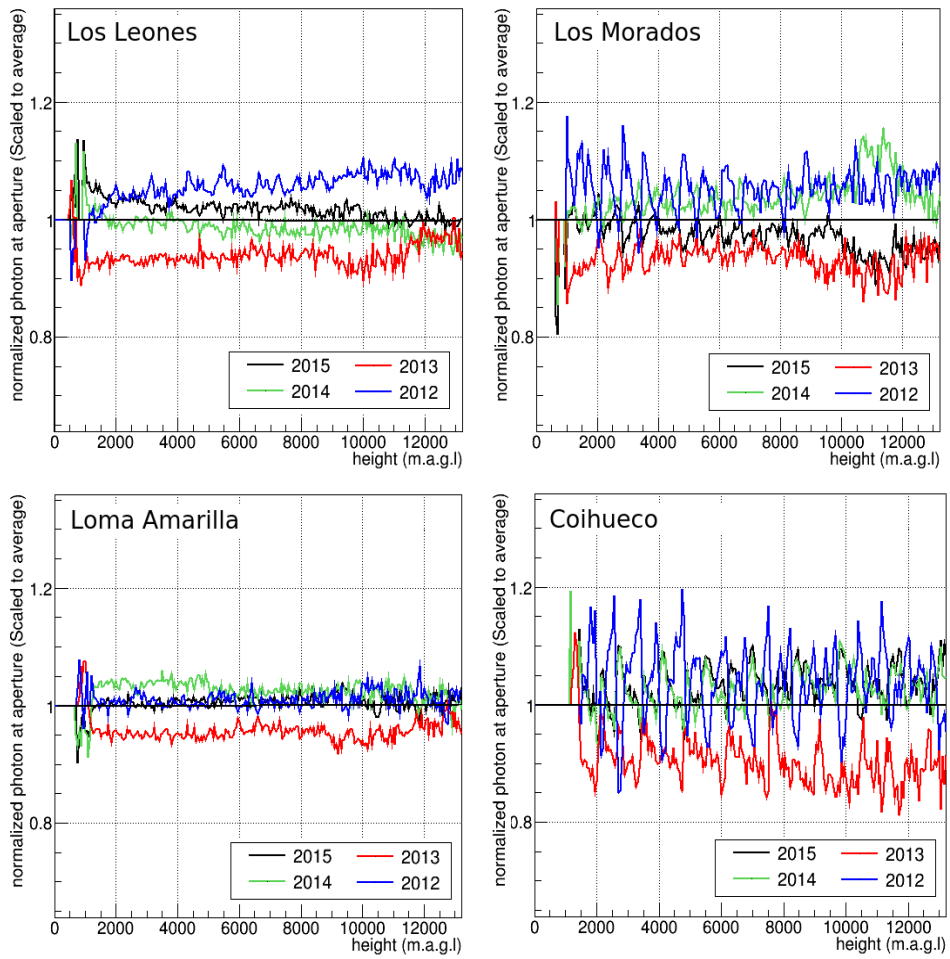

Figure 6.7: The reference light profiles used found from 2012 to 2015 in all FD sites.

The relative larger variations in CO and LM compared with LL and LA is produced by a small offset in the height bins of the 2012 profile. This offset may be produced by a change in the telescopes alignment, FD absolute calibration issues, or the use of an incorrect FD-laser distance in the DN algorithm. The fact that this effect is more pronounced in some FD sites eliminates the possibility of a laser alignment problem of the upgraded laser. This offset have no consequence in the calculation of τ_z as explained in the following sections. One possible contribution to the difference on the reference profiles is that the aerosol concentration

during the reference nights changes year by year (for example, 2013 had an averaged higher aerosol content). If this is the case, the reference hours are not completely free of aerosols. Conclusive evidence is still not available, and the Auger atmospheric group (including the work in this thesis) is currently investigating this situation.

6.4 Building a $\tau(z)$ Profile

A detailed explanation about this process is found in [84]. This section summarizes the major steps. Once the reference hour is selected, a profile of the ratio $NPA(z)_{REF}/NPA(z)_{OBS}$ is calculated bin by bin for each laser shot. Ratio profiles are grouped based on the quarter of hour that the laser shot was fired. Then, they are averaged to produce 4 quarter hour ratio profiles. The averaged-ratio profiles include considerations about the cloud presence. A 30% excess of the ratio at a particular height suggest the beginning of cloud presence over the laser at that height. A 90% deficit of the ratio suggest that the light is being obscured by one or more clouds located between the laser and the FD site. If a cloud is identified under the previous criteria, the ratio profile above that height is not used in τ_{meas} calculations. Instead, it is used to provide a cloud base layer (if any) per hour.

The following step is to apply equation 6.9 to each quarter of hour ratio profile. A first estimation of an hourly τ_{meas} is obtained after averaging the four quarter of hour profiles. The first estimation of τ_{meas} may produce negative slopes in some altitude regions (which is unphysical). This behavior is corrected later after the aerosol extinction (α_{aer}) coefficient is calculated. An α_{aer} profile is calculated by taking the first derivative of the first estimation of τ_{meas} profile. This α_{aer} profile is fitted using two functions, one linear and one exponential. Both fits are done at each altitude bin (50 m). Only the higher altitude region of the profile after the bin selected is taken into account. The α_{aer} profiled is then built bin by bin by taking the first derivative of the fit function with the lower χ^2 value. Negative α_{aer} are set to zero and a more refined estimation of τ_{fit} profile is created by numerical integration of α_{aer}. The process makes τ_{fit} slightly larger than τ_{meas}, especially in regions with a low aerosol level. To correct this, τ_{fit} is normalized to the integral of τ_{meas}. The final profile is

called the central profile and it does not include any consideration on the uncertainties. Two different kind of uncertainties are considered, uncorrelated and correlated. The uncertainties are treated separately and propagated through every step previously described.

Correlated uncertainties are identified as those affecting the individual shape of a laser light profile. They include:

- the relative laser energy (2%)
- the relative FD calibration (2%)
- the atmospheric fluctuation within an hour (3%).

Uncorrelated uncertainties affect the overall observation. They were identified as:

- the correct choice of a reference night (3%),
- the absolute laser energy calibration (1%)

This last uncertainty used to be 2.5%, and it was reduced due to the better energy calibration available in the upgraded CLF. A more detailed explanation of the identification of the uncertainties can be found in [84]. A total uncertainty of 5.20% is obtained when all individual uncertainties are added in quadrature.

Four additional τ profiles are created in addition to the central profile: lower and upper correlated profiles and lower and upper uncorrelated profiles. An example of FD response between the 2014 reference hour for the FD LL and a typical aerosol-content-hour profile is shown in Figure 6.8. The resulting τ_{meas} and τ_{fit} outputs and its associated uncertainties $\tau \pm \sigma_{corre+uncorre}$ are also presented. All five profiles of $\tau_{fit}(z)$ plus $\alpha_{aer}(z)$ are stored in binary files. The altitude of cloud detection is also included. In the case of no cloud presence, that altitude is set to the maximum FD field of view. The binary files are separated by date, FD and laser facility. These files are later translated into MySQL DB files and used in the reconstruction of EASs. The DN analysis uses the CLF for FD sites Los Leones, Los

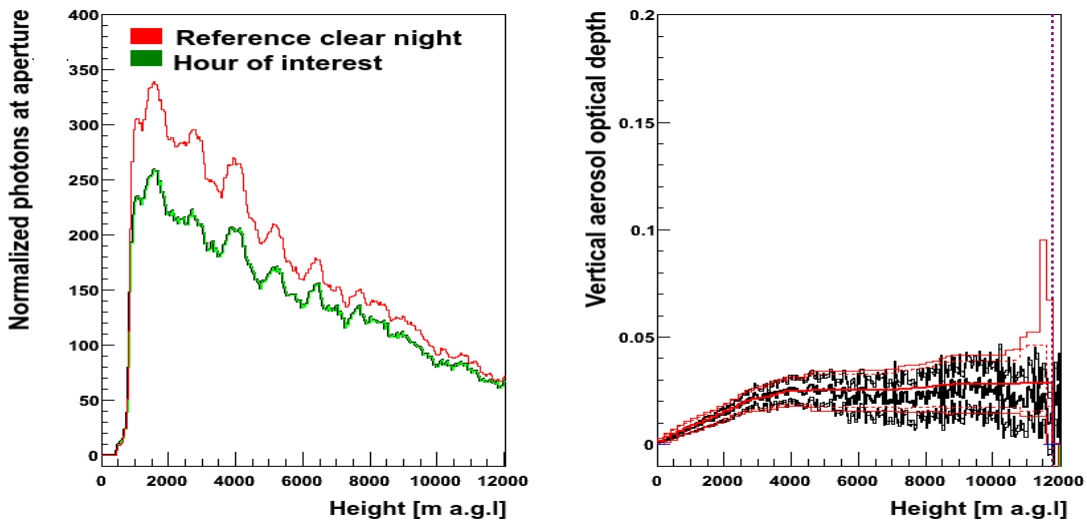

Figure 6.8: Left: Example of the light profiles for an hour with typical aerosol content at the FD Los Leones. The green line represents the reference profile and the red line represents the observed profile. Right: Corresponding $\tau(z)$ profiles after being proceeded with the DN analysis. The black traces represent τ_{meas} and its uncertainties (correlated and uncorrelated). The red traces represents the fitted profiles (τ_{fit}).

Morados and Coihueco, and it uses the XLF for the FD site Loma Amarilla. This schema was developped by the observatory atmospheric group to ensure that the scattered photons travel similar distances from the laser source to the FD sites and atmosphere above the observatory in four regions.

6.5 The Laser Simulation Analysis

A parallel analysis to measure $\tau_A(z)$ using the FD light profiles was developed by the Napoli University. The method is detailed in [85]. It is based on the comparison of the FD laser light profiles with a grid of simulated laser light profiles under different aerosol conditions. The analysis uses an advanced algorithm to select the set of atmospheric parameters that simulate a profile that is the closest in shape and scale to the observed profile. This analysis is called the Laser Simulation (LS) Analysis and is included in the $\overline{Off}\underline{line}$ software.

The LS analysis assumes that $\tau_{aerosol}$ can be simplified to:

$$\tau_{aer}(z) = \frac{H_{mie}}{L_{mie}} \left[1 - exp\left(\frac{-z}{H_{mie}} \right) \right] \tag{6.10}$$

where H_{mie} is the aerosol scale height that accounts for the aerosol dependence as height increases and L_{mie} is the aerosol horizontal attenuation length, describing the attenuation of light at ground level.

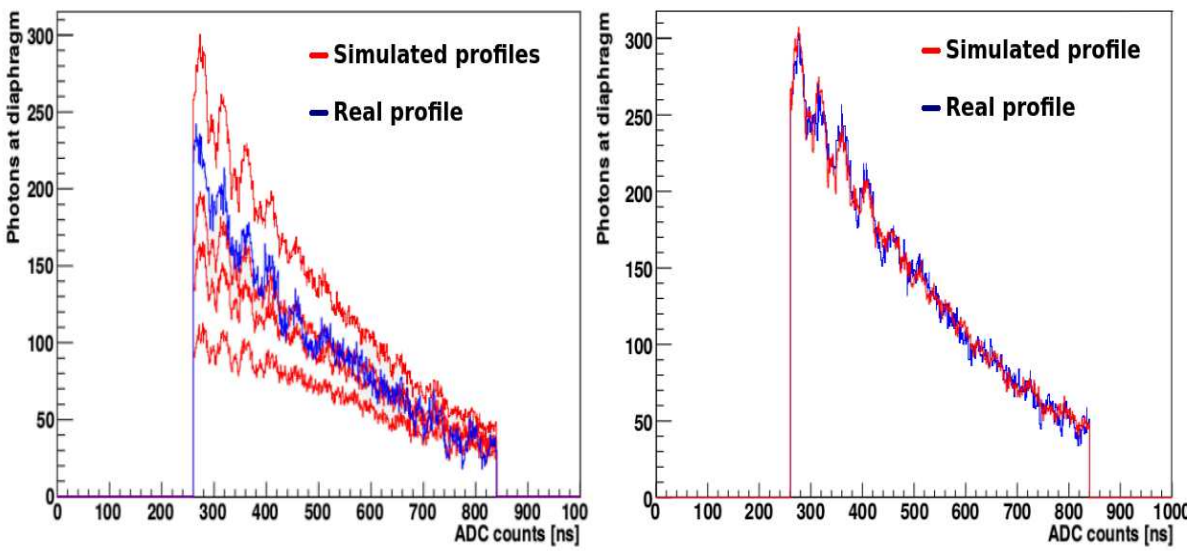

Figure 6.9: Left: a comparison between a real (blue) and a simulated (red) light profile. Right: the simulated profile presented has been selected among a group of profiles simulated under different atmospheric conditions to be the most similar in shape and in scale to the real profile.

The simulated grid uses a L_{mie} range from 5 to 150 km in steps of 2.5 km and a H_{mie} range from 0.5 km to 5 km in steps of 0.25 km. The laser energy used in the simulations is 6.5 mJ. An example of a comparison between a real light profiles and 4 (out of 1121) simulated profiles is presented in Figure 6.9 [85].

The LS analysis is unfortunately not entirely independent of the DN analysis because both analyses use the same CF and, the same FD calibration database and the same reference nights until the CLF was upgraded. The LS analysis is however still important because it provides redundancy in the aerosol database production process. In fact, the LS τ values

are used as a complement of the DN analysis. Before delivering an aerosol database to the collaboration, the LS values are used to fill up any hour where DN measurements are not produced. The amount of hours belonging to the LS analysis in the final aerosol DB is nearly 16%.

6.6 Post Upgrade Results

The data set period used in this analysis includes data after completion of the CLF upgrade (June 2013) through the end of 2015. The number of hourly τ profiles obtained with the DN analysis is summarized in Table 6.3 and it includes measurements with both the CLF and the XLF.

Table 6.3: Number of hourly profiles obtained using the DN analysis after the CLF upgrade

FD site	Los Leones		Los Morados		Loma Amarilla		Coihueco	
Year	CLF	XLF	CLF	XLF	CLF	XLF	CLF	XLF
2013	260	676	244	715	239	751	247	721
2014	907	887	876	898	805	892	885	847
2015	867	787	803	859	720	802	883	865

The average monthly τ profiles measured with different FD eyes after the CLF upgrade is presented Figure 6.10. The average is calculated selecting all the τ(z) hourly values available during a particular month. The error bars are not statistical errors. They represent the averaged value of the individual uncertainties.

The results show a yearly seasonal tendency with lower aerosol levels during the austral winter and higher levels during the first months of the year (Figure 6.10). January presents the largest concentration of aerosol and July the lowest concentration. The yearly combined average τ for 2014 and 2015 is 0.0401 and it is consistent with the historical measurements of the observatory [84].

The yearly averaged τ profiles is presented in Figure 6.11. The averaged profiles have an altitude binning of 200 m. The altitude is presented in m.a.s.l (meters above sea level) to provide a common reference to FD sites which are located at different altitudes. The plot

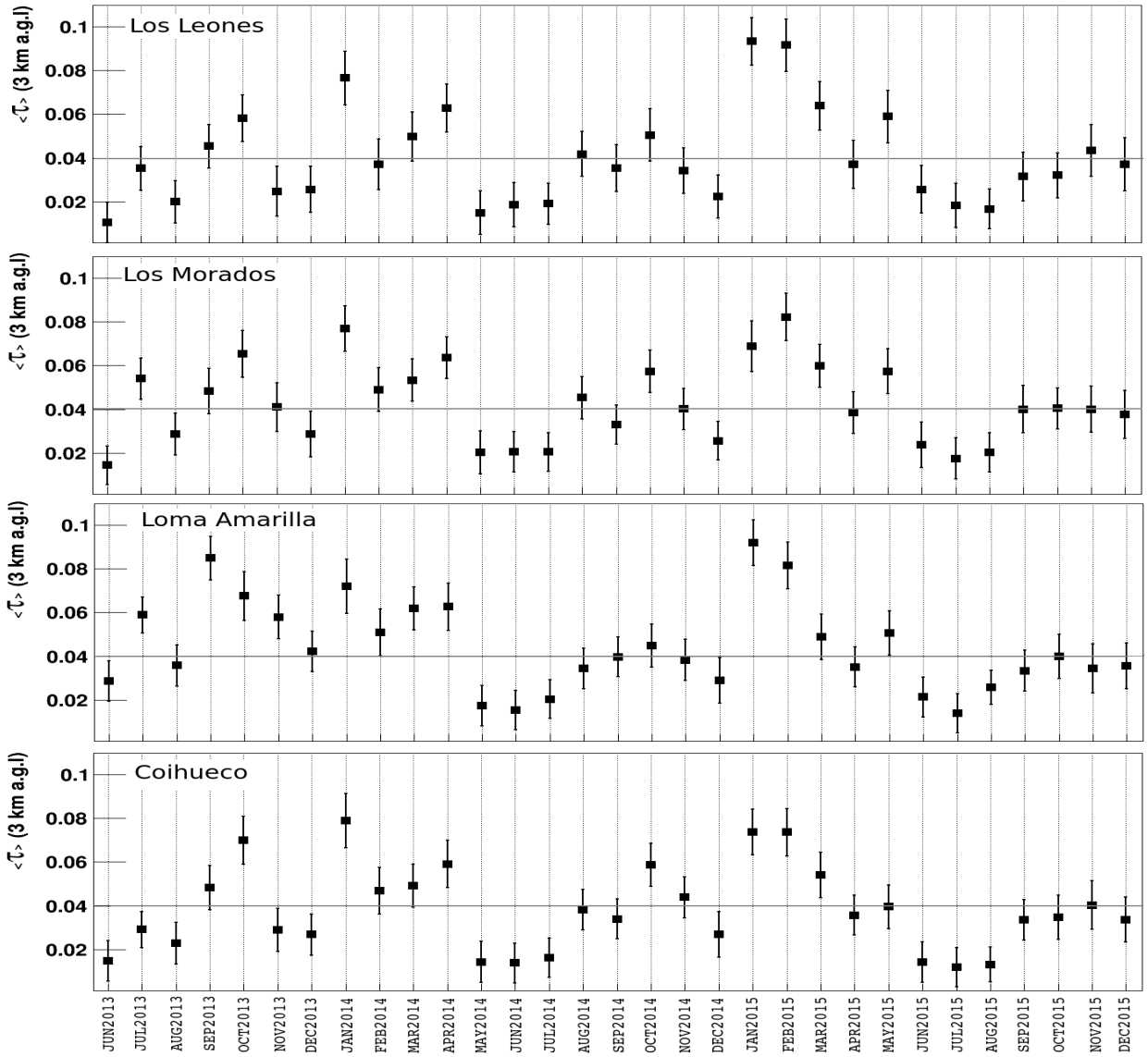

Figure 6.10: Average monthly τ measurements using the CLF after the upgrade (June 2013) shows a seasonal dependency. The yearly average (represented with the gray horizontal line) is consistent with the historical averages.

reflects the strategy adopted by the atmospheric group, where the FD Loma Amarilla uses the XLF as a laser source and all others use the CLF.

The profiles exhibit similar tendencies except for 2013 where some of the average τ profiles are significantly lower than the average. This behavior is explained by the fact that the CLF was decommissioned for the most part of the first 6 months in 2013, where the

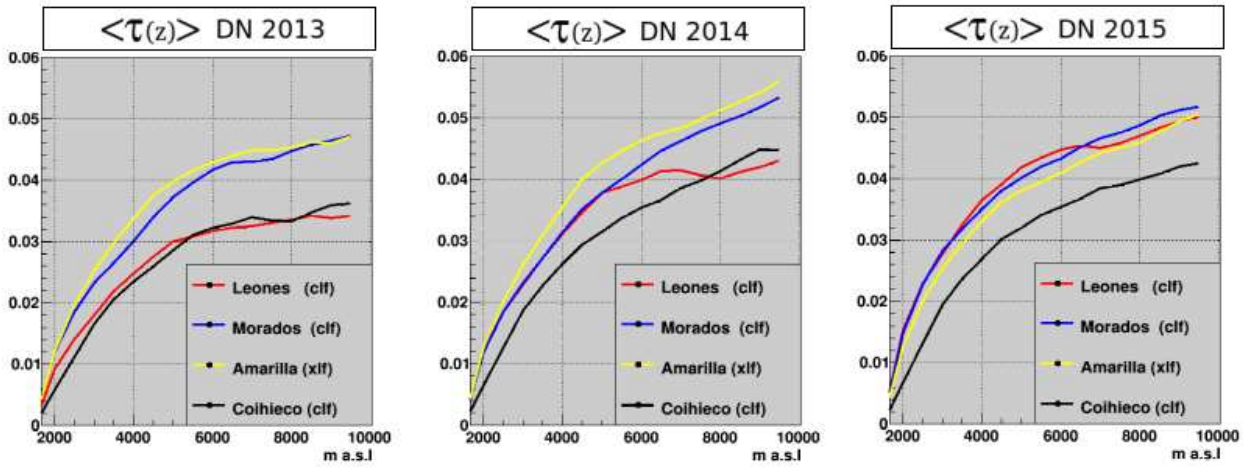

Figure 6.11: Average yearly τ profiles after the CLF upgrade. The FD site CO presents consistently lower values (see text).

aerosol concentration tend to be higher.

6.6.1 Comparison Between Laser Facilities

Since 2013, the DN code allows for each FD camera to measure τ using the light from either laser facility. Two τ profiles per FD eye were obtained by averaging τ values from 2003 to 2015 that were obtained using either the CLF or the XLF. The profiles are superimposed in Figure 6.12. The τ profiles are calculated using 250 m height bins. The profiles have heights above sea level to account for the differences in altitude among the FD sites.

The superimposed profiles are compatible with each other within the uncertainties. LL and LA are not nearly equidistant to the laser sources and they presents the largest profile differences. The FD-laser distances are found in Table 3.2. Some differences on τ in LA are near to 10% at 6 km. This suggest a limitations in the DN analysis at large distances, polarization issues in the laser facilities beam, problems in the calculation of altitudes, or it may also indicate a non homogeneity of the upper atmosphere.

The relationship between τ measurements using both laser facilities can be better understood by looking at the correlation in the scatter plots of the measurements (see Figure 6.13) Each point in the scattered plots is a measurement of τ taken during the same hour by the

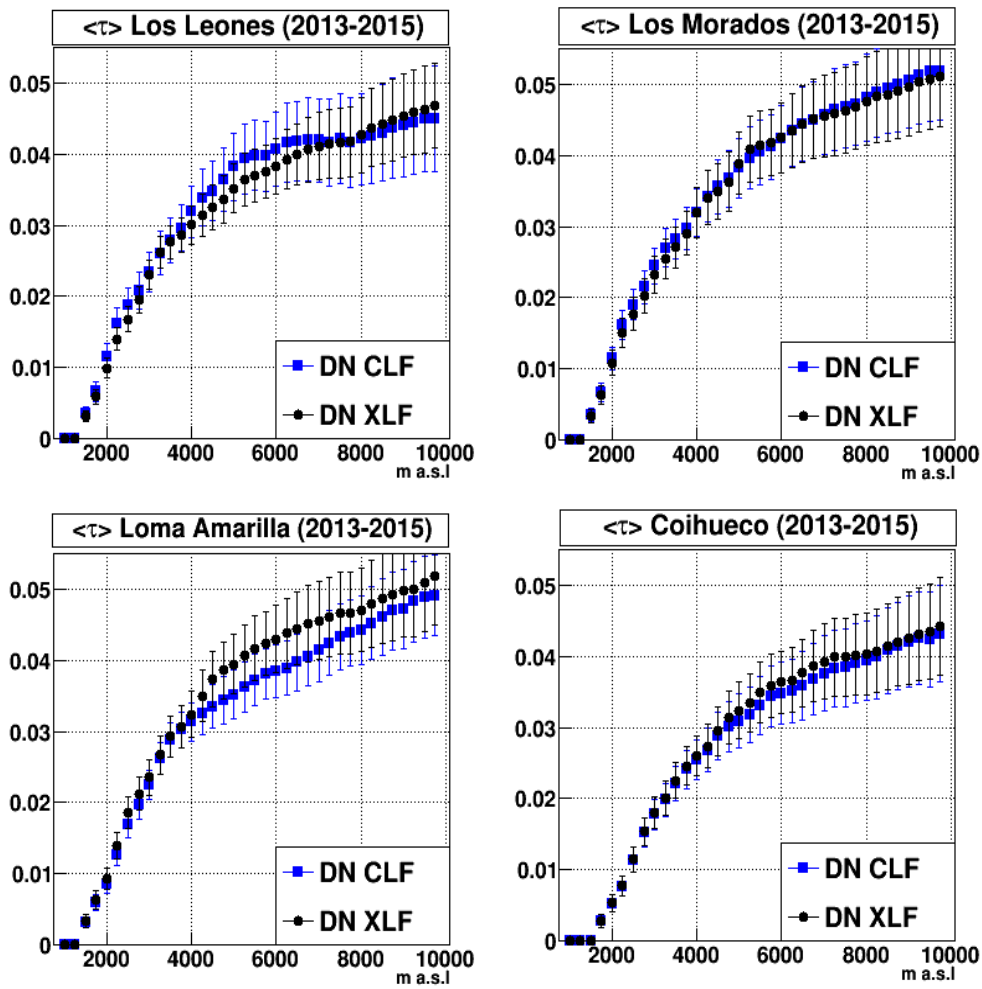

Figure 6.12: Average τ profiles after the CLF upgrade for all FD sites and laser facilities. All profiles agree within the uncertainties. The two FD eyes (LL and LA) that are not nearly equidistant to the laser sources presents the largest profile differences.

same telescope but with different laser sources. The plots are well described by a linear fit(red line). For example, correlation plots at 3.0 km a.g.l have slopes values equal to 1.067 for LL, 0.980 for LM, 0.897 for LA and 0.955 for CO. The fitted slope parameter tends to be closer to 1 for higher altitudes.

The number of common hours (dots in the scatter plot) varies slightly between FD-sites and altitudes. The τ differences at 3.0 km a.g.l are normalized by the average of the measurements according to: $\left(2 \cdot \left(\tau_{(CLF)} - \tau_{(XLF)}\right) / \left(\tau_{(CLF)} + \tau_{(XLF)}\right)\right)$. these differences

were plotted in Figure 6.14 for each FD site.

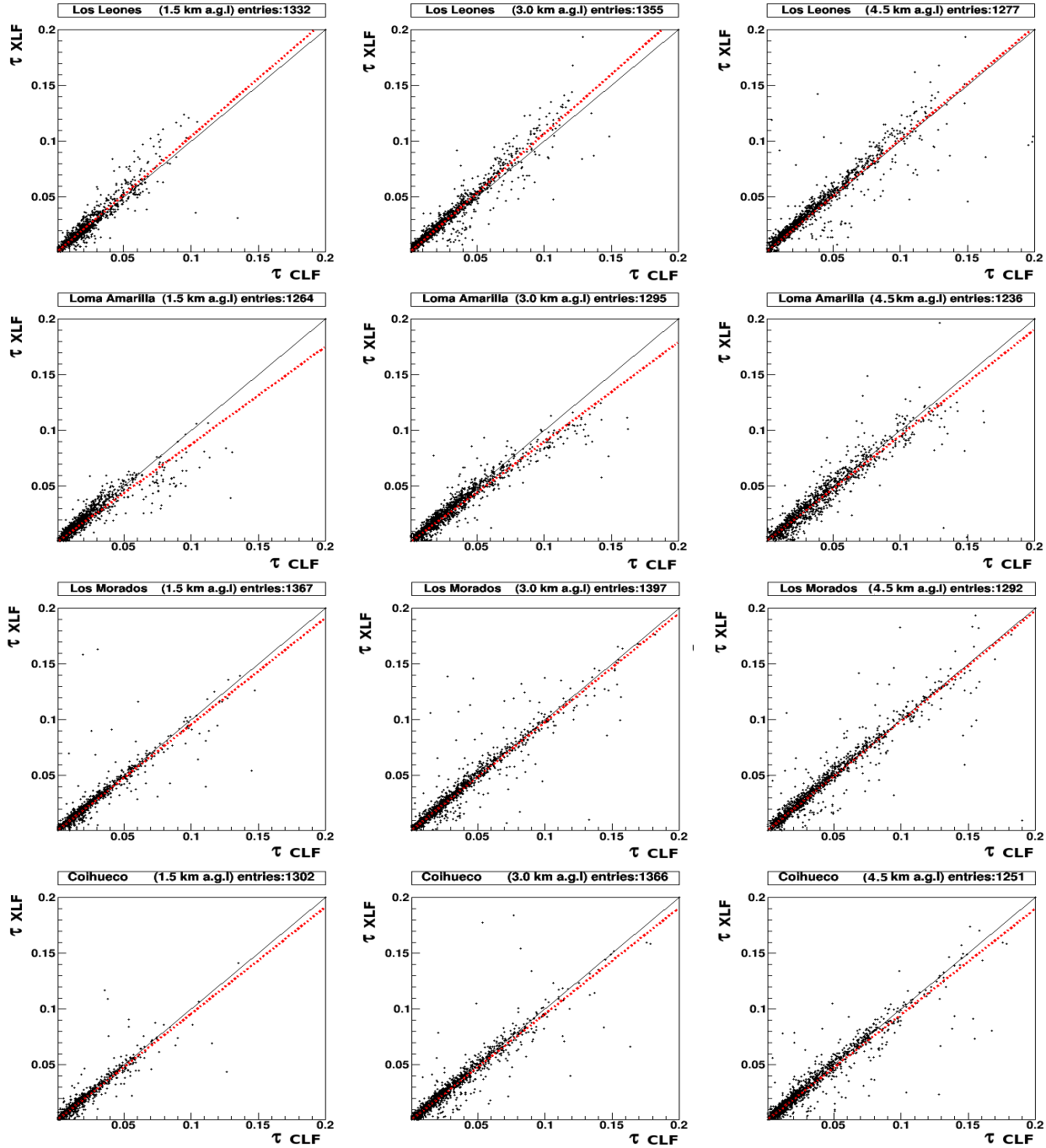

Figure 6.13: τ at z=1.4 km (left), z=3.0 km (center), and z=4.5 km (right) a.g.l, correlations between the CLF and XLF using the DN analysis data available after the CLF upgrade. The red dashed line represents a linear fit passing by the origin. The black line is the unitary line. The total number of common hours found is presented in the top right corner of each plot.

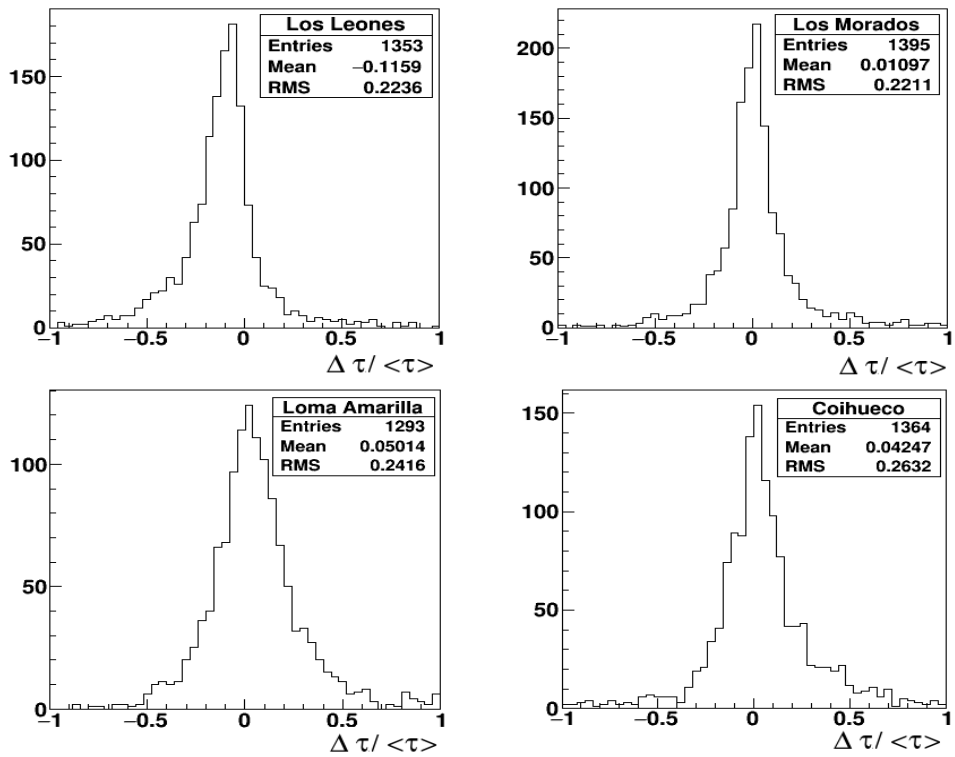

Figure 6.14: τ(z=3 km) normalized differences for common XLF-CLF hours. LL presents the highest differences ($\sim$ 10%) , while LA and CO presents $\sim$ 5% and a $\sim$ 1% average difference for LM

6.6.2 Comparison Between FD Telescopes

A similar approach can be followed by comparing τ measurements using the same laser source but different FD telescope. Six different combinations of two telescopes can be achieved with 4 FD sites and one laser (see Figure 6.15). It is important to recognize that this approach compares τ at the same height but at different regions of the atmosphere, since the path traveled by the XLF and CLF scattered light to the FD is not the same. Therefore the correlation is expected to broaden in comparison to the ones in Figure 6.13. All the points in these scatter plots are measurements of τ(z=3 km) using the CLF from 2013 to 2015.

The correlation presented in Figure 6.15 are not as well defined as the correlations in Figure 6.13. A much larger spread is noticeable. Again, a possible explanation is the non-

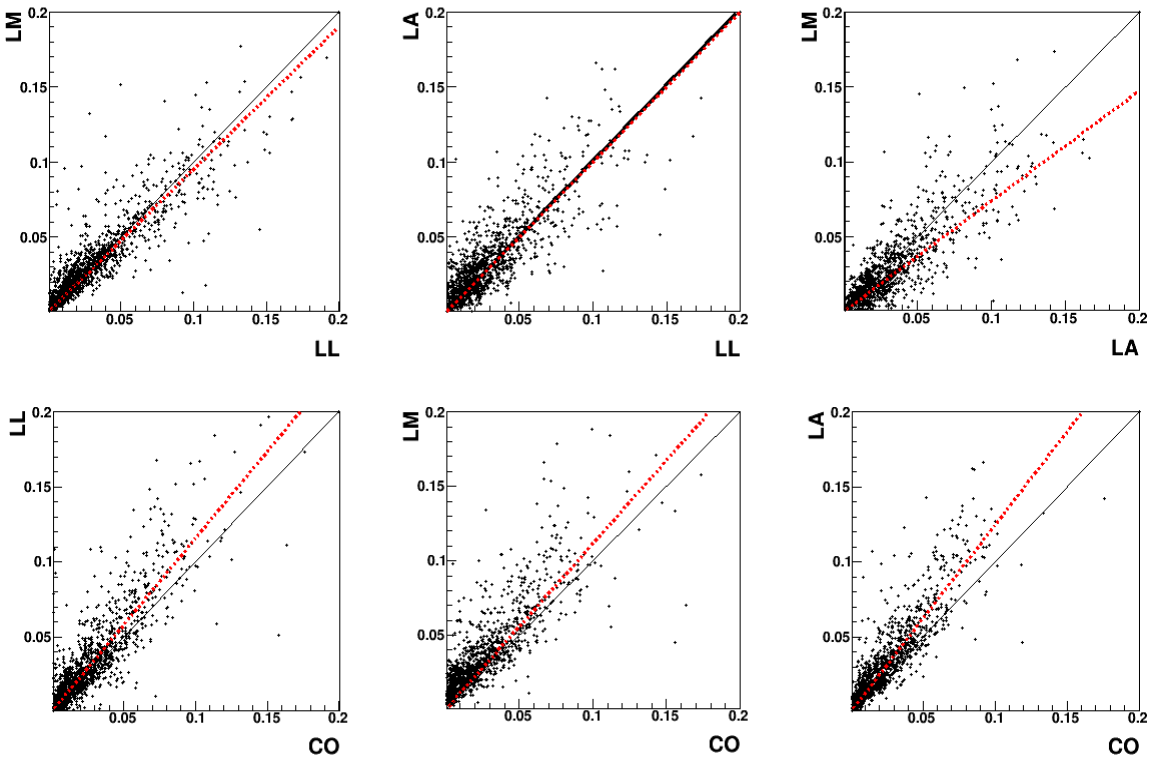

Figure 6.15: τ(z=3 km) correlations between FD sites looking at the CLF. The dashed red line represent a linear fit passing by the origin. The solid black line is the unitary line.

uniformity of the aerosol distribution in the atmosphere. Also, altitude differences in the FD site Coihueco (nearly 200 m with respect of other sites) could cause the light to travel through a less thick atmosphere. One more possible explanation, not yet studied, is the mis-calibration of the FD cameras.

The difference between τ(z=3 km) measurements are presented in Figure 6.16. These differences are normalized to average of the two measurements $\left(2\left(\tau_{(FD1)} - \tau_{(FD2)}\right) / \left(\tau_{(FD1} + \tau_{(FD2)}\right)\right)$. The averaged RMS for the six FD combinations is nearly 0.38. An increase of 0.2 in RMS compared to those in Figure 6.14. The 3 FD combinations involving CO have the largest averaged deviations from zero (nearly 1.83), while the others have a deviation average, ranging from zero to 0.70. This can explained by the overall lower τ(z) measurements in CO. The analysis in this work did not find a conclusive explanation about these issues. They have been addressed to the atmospheric group for further investigation and analysis.

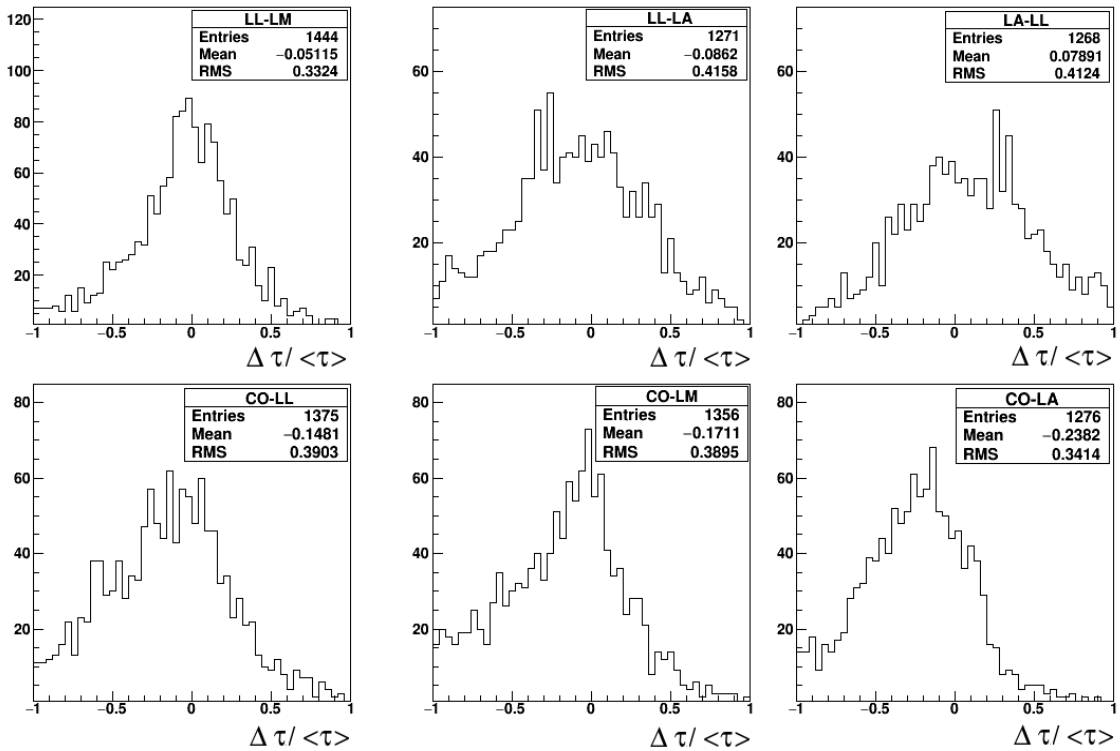

Figure 6.16: τ(z=3 km) difference normalized to the average between different combinations of two FD sites using the CLF as a light source. The widths of the distribution increased compared to the ones in Figure 6.14 which may suggest a large non-uniformity in the atmosphere aerosol concentration.

6.6.3 Comparison Between Analyses

The LS can be used as an alternative aerosol database to validate the DN analysis results. Comparisons between the LS and the DN analysis are presented for the years 2014 and 2015. The number of hourly τ profiles available for these years with the LS analysis are summarized in Table 6.4.

Table 6.4: Number of LS hourly profiles available

FD site	Los Leones		Los Morados		Loma Amarilla		Coihueco	
Year	CLF	XLF	CLF	XLF	CLF	XLF	CLF	XLF
2014	787	331	830	630	457	598	780	546
2015	771	487	734	395	643	488	829	487

A comparison between the laser simulation and the data normalized analysis is presented in 6.6.3 for profiles obtained using the CLF

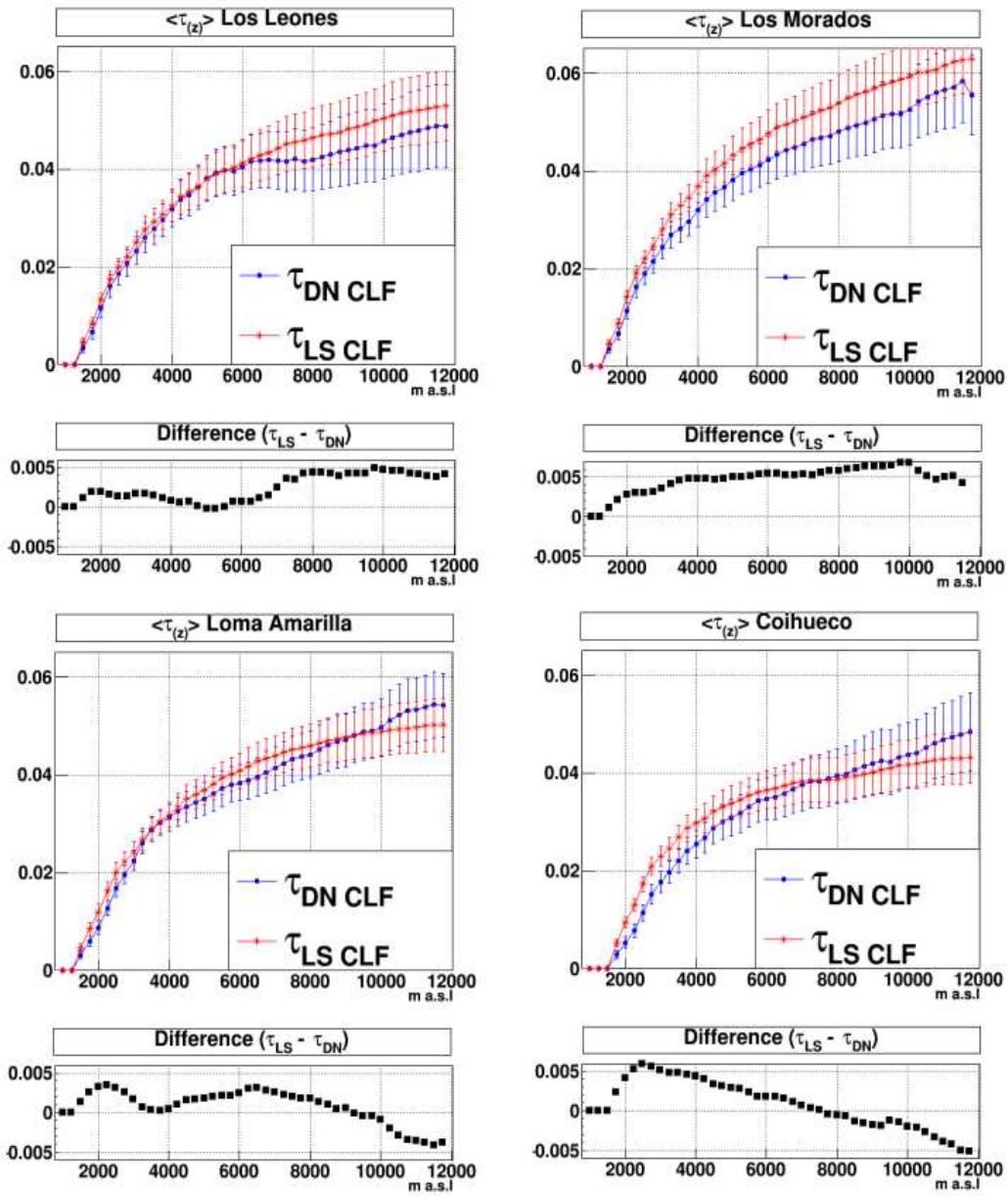

Figure 6.17: τ(z=3 km) correlations between the LS and the DN analysis for the CLF data after the upgrade. Both analysis are consistent within the uncertainties.

In a similar way, the comparisons for profiles obtained using the XLF are presented in Figure 6.18.

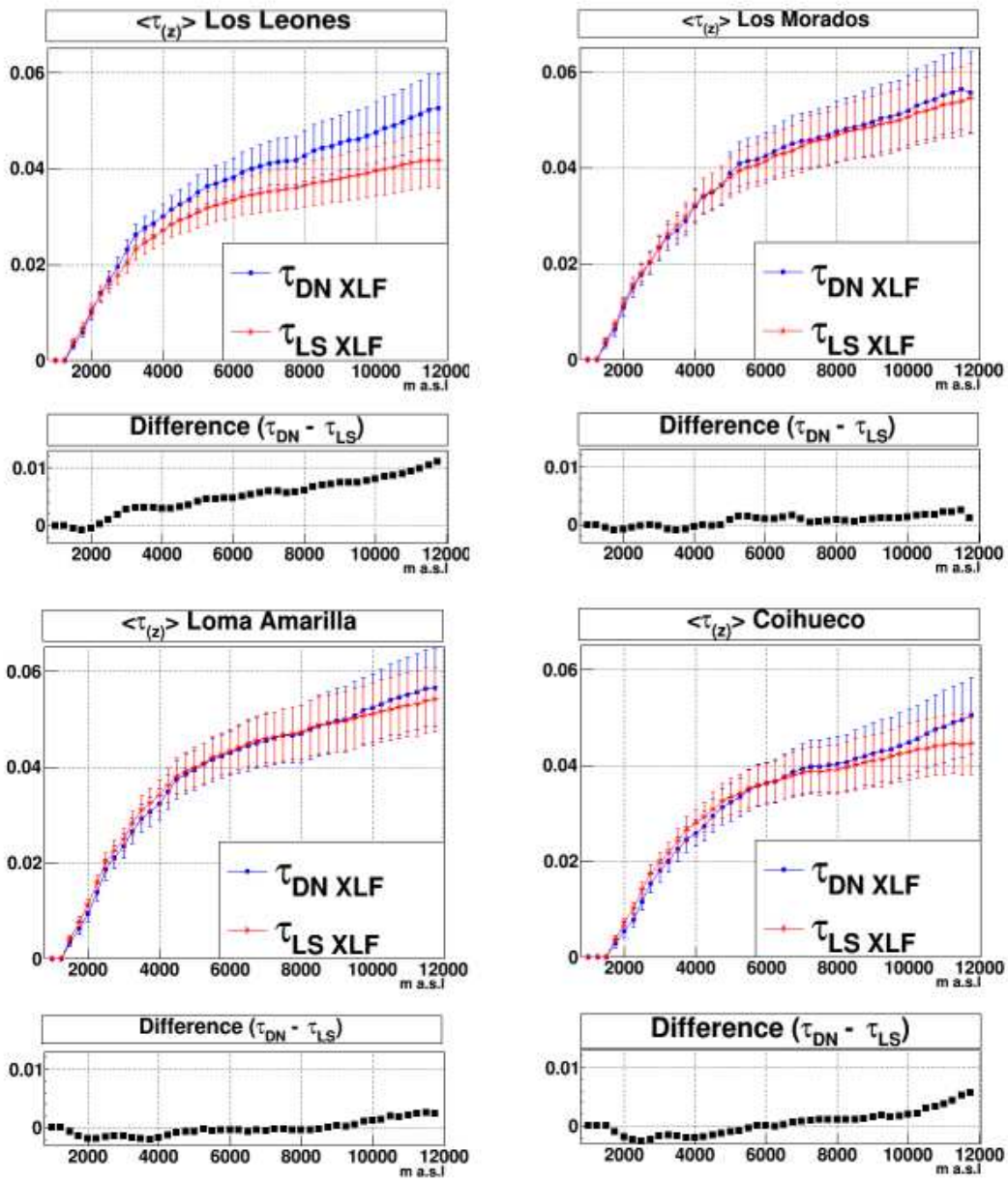

Figure 6.18: τ(z=3 km) correlations between the LS and the DN analysis for the XLF data after the upgrade. Both analysis are consistent within the uncertainties.

The data normalized analysis has been independently processed by our colleges in Naples University and presented as a standard DB binary file. Before comparing results, The Napoli's database needed to be converted into the same file structure as the DN analysis database. The results agree within the uncertainties with a maximum $\Delta\tau < 0.01$ for all eyes.

Figure 6.19 correlation plot compares the τ(z=3 km) common hours between LS analysis and the DN analisys.

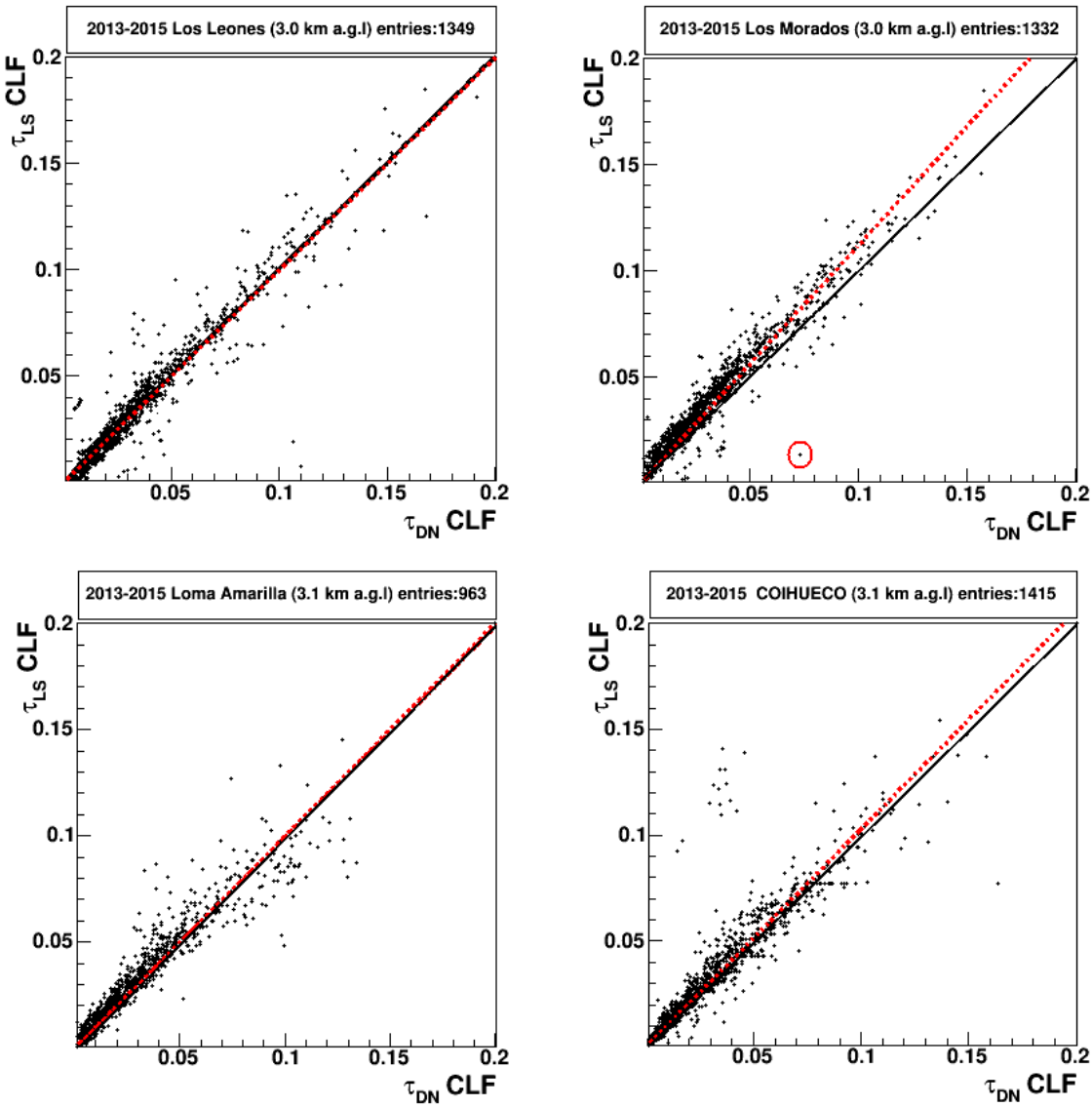

Figure 6.19: Common measurements of τ(z=3 km) between the LS and the DN analysis for the CLF from 2013 to 2015. Red dashed lines are lines are linear fit passing through the origin. The number of common hours found are presented on the top right corner. One outlier in LM has been marked with a red circle an its $\tau(z)$ profile is presented in Figure 6.21.

A linear fit passing through the origin has been applied for all FD eyes. The values are 1.00 ± 0.005 for LL, 1.11 ± 0.004 for LM, 0.99 ± 0.006 for LA and 1.03 ± 0.007 for CO. A good agreement is found between the two methods. The largest difference (still within the

quoted uncertainties) is found in Los Morados. This can be explained by the use of different reference night between the two analyses in this specific FD eye.

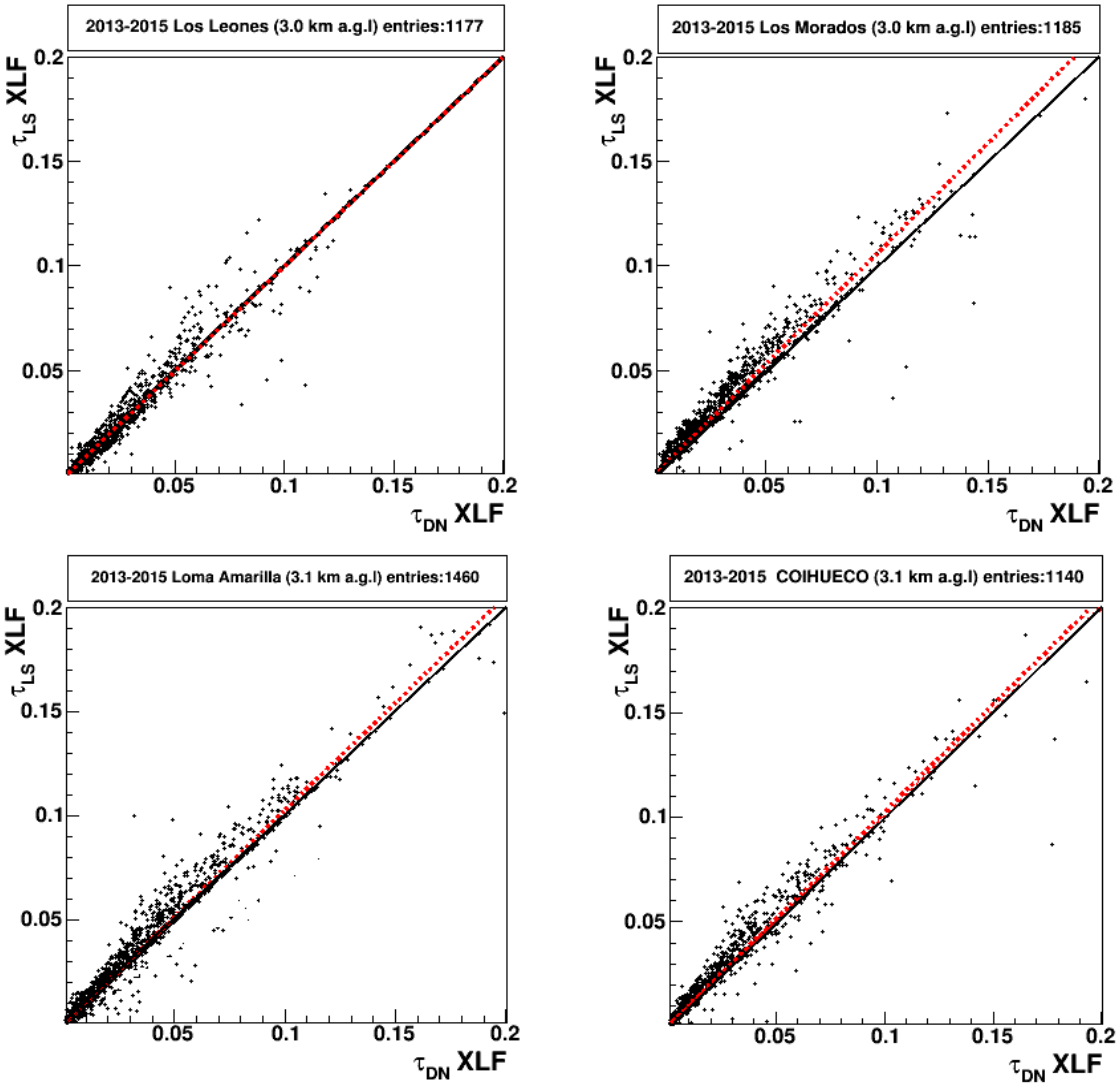

Figure 6.20: Common measurements of τ(z=3 km) between the LS and the DN analysis for the XLF from 2013 to 2015. Red dashed lines are linear fit passing through the origin. The number of common hours found are presented on the top right corner.

The same exercise can be done on the XLF and the results are presented in figure Figure 6.20 The slope values for the linear fit are: 1.00 ± 0.004 for LL, 1.05 ± 0.005 for LM, 1.03 ± 0.004 for LA and 1.02 ± 0.005 for CO. The correlation shows a good agreement between

the two analyses.

In the correlation plot for LM in Figure 6.19 one outlier has been clearly marked with a red circle. This hour presents a strange behavior in the DN $\tau(z)$ profile (Figure 6.21 (left)) where suddenly the profile rises dramatically. An inspection of the light profile (Figure 6.21 (right) reveals a spike on the number of photons at aperture around 4 km a.s.l (2.6 km.a.g.l) and then a drop at higher altitudes. This behavior agrees with the presence of the cloud. Many times the DN analysis fails to detect a cloud and consequently it provides a higher estimation of $\tau(z)$. On the other hand, the LS analysis in many occasions forces the fit of the profile shape as a smooth function when is not the case. Fortunately this discrepancies between the two analyses are very rare (less than 2% of the total hours have a difference larger than 10%).

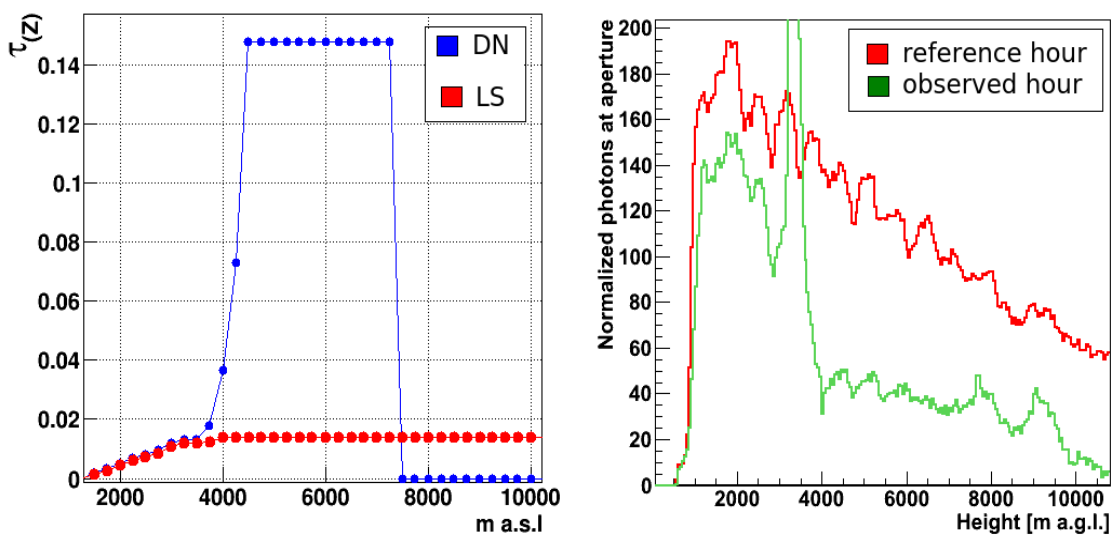

Figure 6.21: Left: $\tau(z)$ profile for the measurement marked in red in Figure 6.13. Right: The light profile in the camera revels a cloud presence near 3km a.g.l

The differences between $\tau(z = 3km)$ measurements from Figure 6.19 and normalized to the average are presented in Figure 6.22.

The width of the differences increases compared to those in Figure 6.16. The largest RMS is found in LM, where an offset in the $\tau(z)$ profile was clearly visible in . This offset

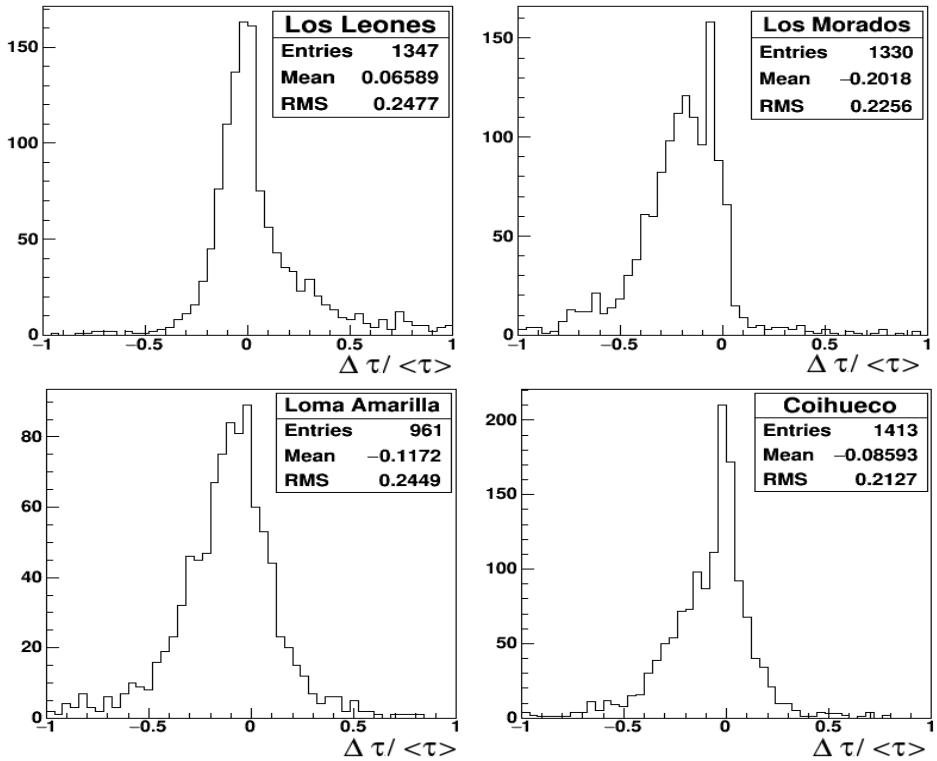

Figure 6.22: τ(z=3 km) difference normalized to the average for the data points presented in Figure 6.19. The RMS are comparable to those from Figure 6.16 exept for LM where a clear offset is observable.

can be due to the use of a different reference night between analysis in 2013. All other RMS are compatible with the quoted uncertainties.

6.7 Comparison to the Raman LIDAR

This section compares τ measurements obtained with the DN analysis and the Raman LIDAR during 2014 and 2015. The total number of hourly τ measurements produced by the Raman LIDAR are 536 in 2014 and 624 in 2015. 2015 have more hours due the addition of the "middle of the shift Raman run" after November 2014. A major difference between the DN and the Raman analyses is that they measure different region of the atmosphere, and these measurements are not simultaneous. A mono-static configuration approach is achieved with the Raman LIDAR because the laser source and the detector are co-located. A bi-static configuration approach using the FD sites located several kilometers away from the

laser source.

The comparison presented considers hourly measurements of τ within a 3 hour maximum difference. Figure 6.23 presents the τ(z=3 km) correlation plots the Raman values and the DN values for each FD eyes during the years 2014 and 2015.

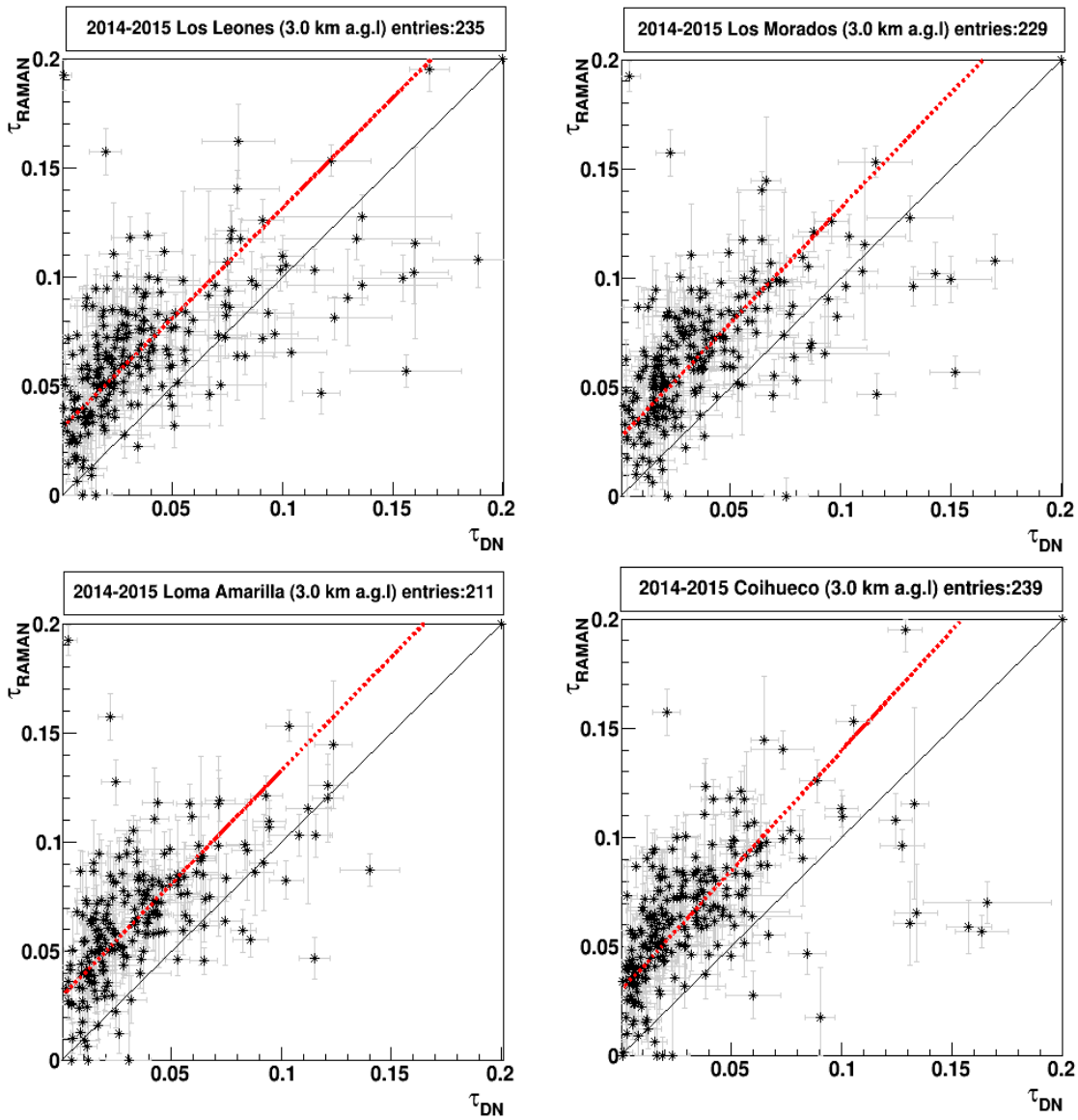

Figure 6.23: τ(z=3 km) correlations between the Raman and the DN analysis. Red dashed lines are linear fits

The fit parameters found are listed in Table 6.5. The plots are linearly fitted according to $f(x) = P_0 * X + P_1$.

Table 6.5: Summary of the linear fit of the scattered plots presented in Figure 6.23.

eye	parameter	values	error	parameter	values	error
LL	p0	1.00 e+00	3.91 e-02	p1	3.11 e-02	1.28 e-03
LM	p0	1.05 e+00	4.05 e-02	p1	2.69 e-02	1.44 e-03
LA	p0	1.03 e+00	4.24 e-02	p1	2.92 e-02	1.42 e-03
CO	p0	1.09 e+00	3.60 e-02	p1	2.97 e-02	1.18 e-03

The fit parameters (p1) reveal an offset of 2.92 for all the eyes, which suggest a systematic effect not identified yet.

The normalized differences of $\tau(z = 3km)$ between the side scattering and the Raman method are presented in Figure 6.24 for all FD sites.

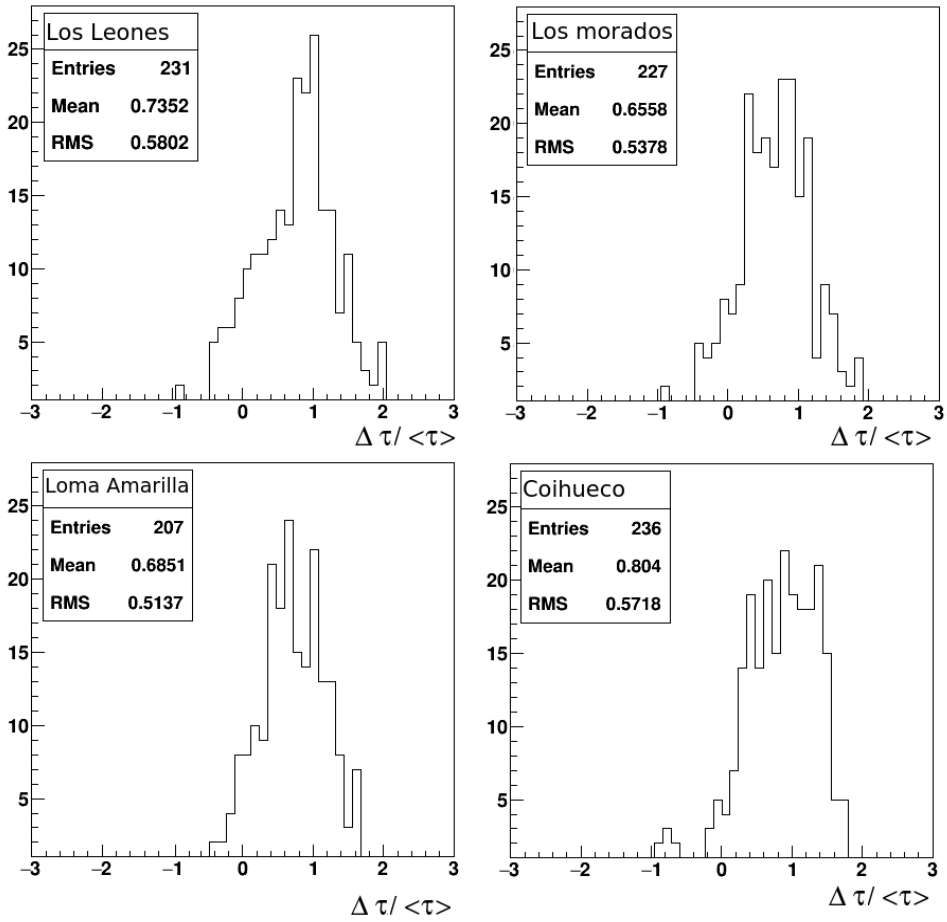

Figure 6.24: τ(z=3 km) normalized difference to the average for the data points presented in Figure 6.23. The scale of the X axis was increased to illustrate the larger RMS values.

But these plots still provide compelling evidence that indicates a clear difference of the aerosol contents measured by the two analyses, where the Raman LIDAR measures systematically higher values of τ in almost every single hour and altitude than the DN analyses. Figure 6.25 presents the average τ profile between the two atmospheric databases. The altitude is presented above sea level to provide a common reference between all the FD sites and the Raman LIDAR located at the CLF. Finally, the monthly average τ(z=3 km) contents measured by the 2 analysis during 2014 and 2015 (see Figure 6.26) also confirm this behavior. It presents an average difference of 0.043 for two years in consideration.

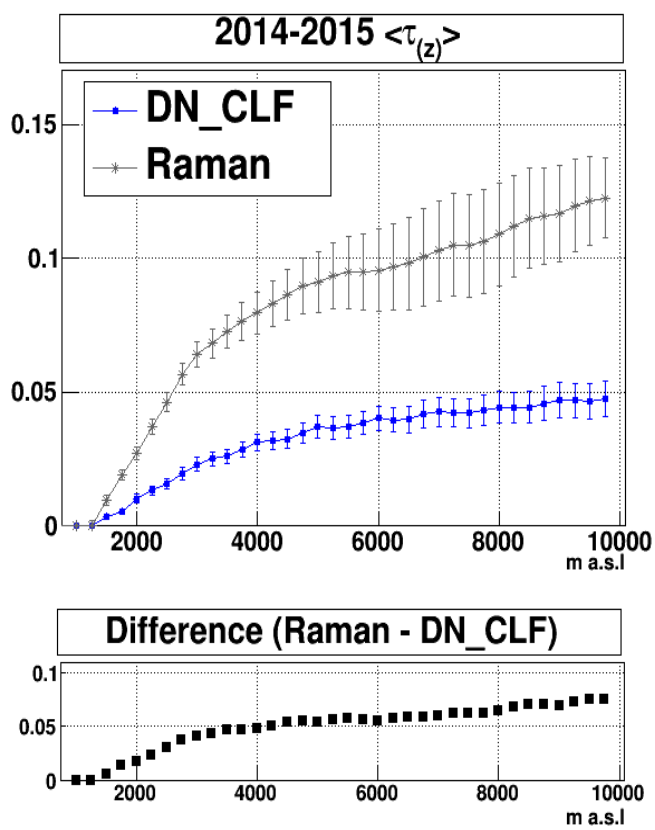

Figure 6.25: τ profile comparison between the Raman and the DB analyses. All the FD site τ values presented here were measured using the CLF and they were averaged.

All the previous results suggest that the DN analysis (and therefore the LS analysis) is under-estimating the τ values measured. Among some contributions to the Raman-DN

differences are:

- the effects on the aerosol profile of multiple scattering and the aerosol phase function,
- the systematic effects of a lack of a cloud identification algorithm in the Raman analysis,
- the large uncertainties in the Raman analysis due to the limited acquisition time.

Under the current conditions, it is difficult to quantify the mis-calculation since there is still no evidence that proves that the Raman analysis provides the true τ measurements. But this study has motivated several efforts within the atmospheric group and in particular the L'Aquila group to better understand the Raman method. This group is working towards a newer and more refined Raman analysis.

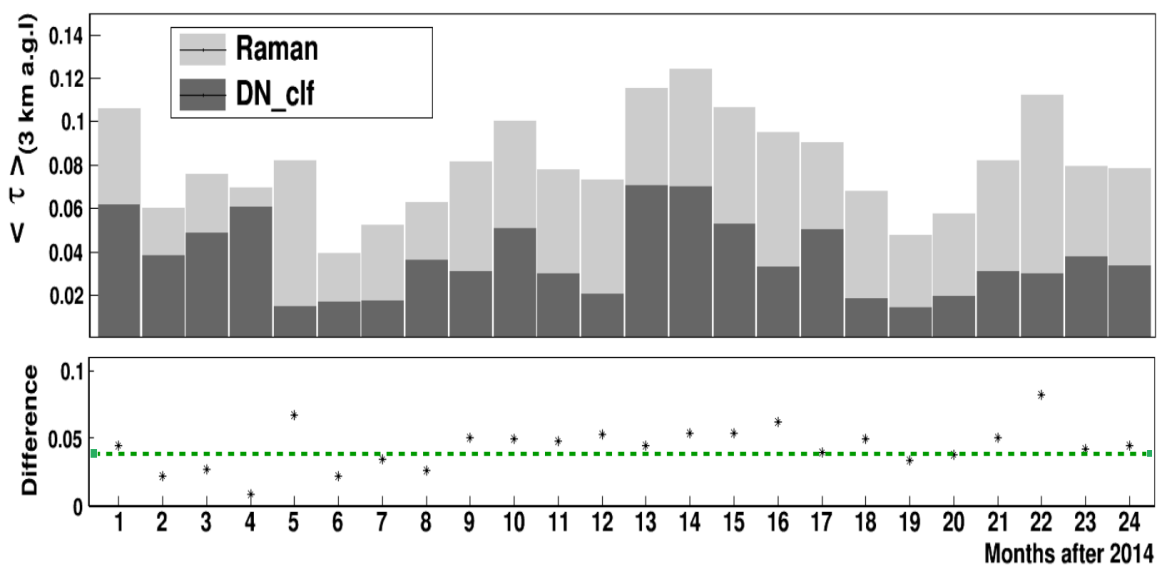

Figure 6.26: τ(z=3 km) average monthly. The DN values for all FD sites have been included in the average. The green dashed line represents the average difference.

6.8 Summary of τ(z=3 km) Differences

The last 4 sections presented analysis of the histograms representing the difference in τ measurements. This section summarizes all the histograms per section (Figure 6.14, Figure 6.16, Figure 6.22, and Figure 6.24), by adding them together, scaling them to the

maximum entry, and superimposing them (see Figure 6.27). The histograms are labeled: "XLF-CLF" for the difference between laser facilities, "LS-DN" for the difference between analysis using the CLF laser, "FD1-FD2" for difference between FD telescopes using the CLF laser and "Raman-DN" for the difference between the Raman and the DN analysis using the CLF laser. The RMS of the histogram between laser facilities and analysis is similar (approximately 0.3). The RMS of the histogram between FD telescopes increases by 60% and the RMS of the Raman by almost 120%. These large difference were addressed in the previous sections.

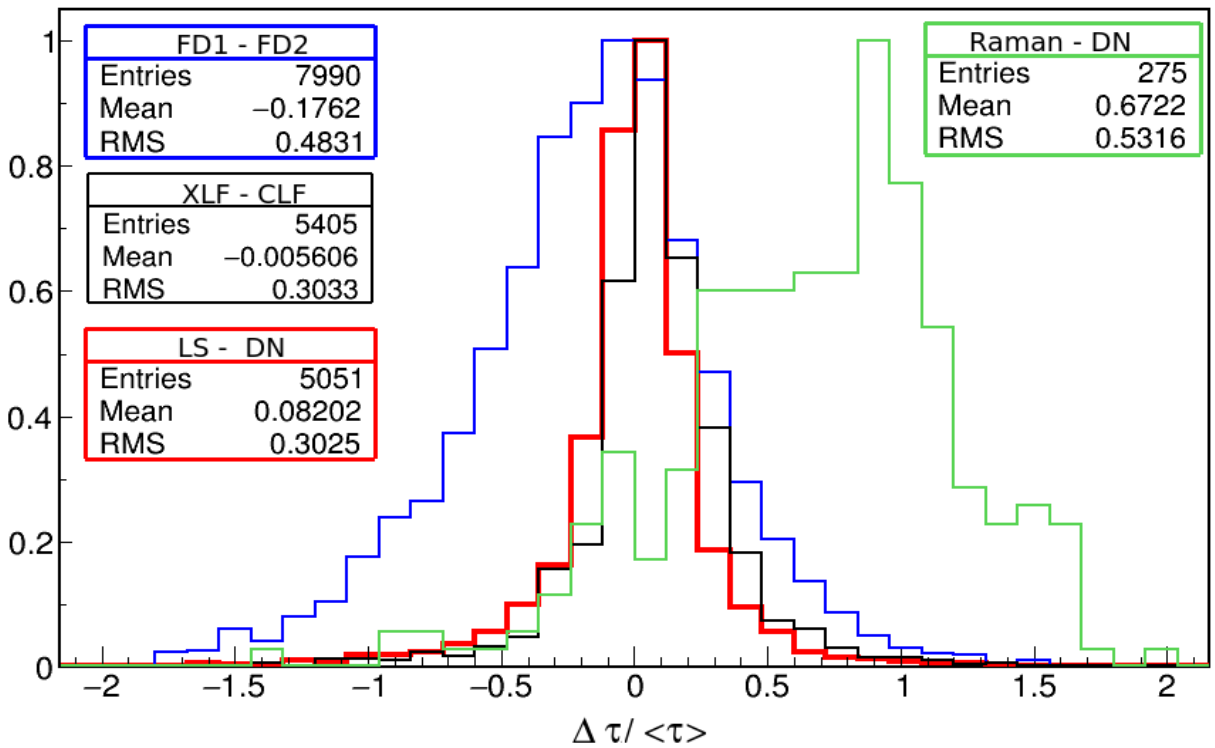

Figure 6.27: A summary of the τ(z=3 km) differences (Normalized to average) for the different analyses described in this chapter (see text for labeling description).

The DN and the LS present similar behavior. They have been used for several years by the atmospheric group to benchmark each other's method. Unfortunately this may have created a false sense of security about the measurements. But now, with the introduction of the Raman LIDAR analysis, there is a concern that the τ measurements provided to the

collaboration may be under-estimated. The quantification of this under-estimation is important because it may be larger than the quoted uncertainties. If this is the case, the energy reconstruction of the FD would be affected and this will be propagated to the measurement of the Auger spectrum (see Chapter 7). Therefore, it is essential to continue the efforts to improve all type of analysis. In addition to my work described in this thesis, these efforts include:

- the newer version of the Raman analysis by the L'Aquila group.
- a preliminary work by the Chicago group that includes the effects of the aerosol scattering and multiple scattering in the DN analysis (see Chapter 7).
- the Napoli group is working towards a LS analysis that avoids the use of the reference hour.
- the Adelaide group is currently re-writing the DN code to develop a more modern version.
- the Roma group is creating a grid of reconstructed FD events with artificial aerosol databases with different $\tau(z)$ offsets to study the effects in the cosmic ray physics.
- a general efforts to estimate how large is the error in the assumption of a reference hour free of aerosol.

CHAPTER 7

EFFECTS OF DIFFERENT AEROSOL DATABASES ON THE UHECR SPECTRUM

This study presents possible impacts to the Auger spectrum at the highest energies when different aerosol databases are used. The full spectrum analysis is described in [75].

7.1 Alternative Aerosol Databases

Four aerosol alternative databases created by the aerosol group are used to test the effects on the spectrum. The aerosol databases are available as Advance Data Summary Trees (ADST) files. All aerosol databases were created using τ measurements during in 2014 and 2015.

7.1.1 Bi-modality Corrections

In 2010, the DN analysis source code was modified to allow simultaneous runs of the DN analysis using both laser facilities [51]. This modification was implemented to save some computational time. Unfortunately it also introduced a bug that altered the results of the DN analysis.

The bug was discovered during this research and compromised the way that the analysis, distinguished between the GPS time stamp signature of the CLF and XLF. As a result some CLF reconstructed hours were calculated using the XLF geometrical information and vice versa. For example in the case of FD LL, the FD-laser distance used for some calculation was nearly 40 km instead of 26 km. This makes those hourly τ calculations consistently lower than expected. Figure 7.1 presents an example of the bi-modality results in FD LL. The bi-modality behavior was discovered in the scattered plot between the LS and the DN analysis. This behavior is present in all FD eyes but it is more apparent in FD site LL and LA, since the difference between the FD-CLF and FD-XLF distance is the largest. The red

point in Figure 7.1(left) was selected as an example and its profiles are shown in the right plot.

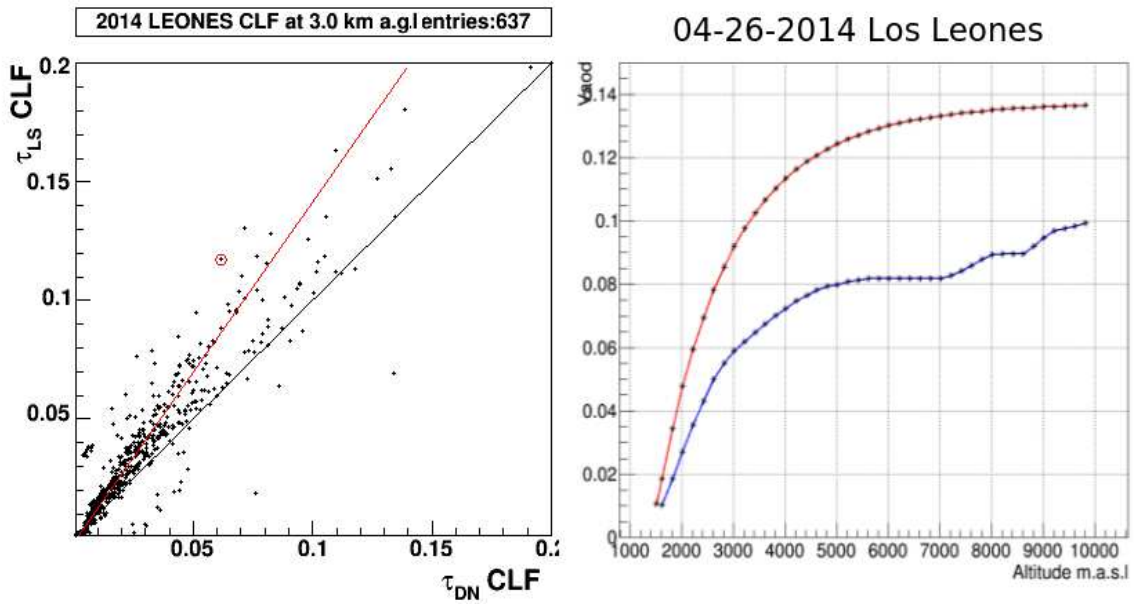

Figure 7.1: Left: A Bi-modality behavior was noticed in the scattered plots of the DN analysis vs the LS analysis. The τ profiles corresponding to the point circled in red are presented on the right. Right: This hour presents a clear discrepancy between the two analyses.

The bi-modality behavior was corrected with the use of a XML card that permits the process of the data using the CLF and the XLF independently. The bi-modality behavior is more clear in the scatter plot presented in Figure 7.2. This plot compares two versions of the DN analysis. DN.v0 is the compromised version created using the DN code before the bug was detected. DN.v1 is a later version where the XML card was used. DN.v1 is the version presented in Chapter 7. The bi-modality behavior has clearly disappeared as presented in Figure 6.19. Version DN.v0 has been archived and version DN.v1 will be referred simply as the DN database or DN (original).

7.1.2 Aerosol Scattering and Multiple Scattering

A preliminary upgraded version of the Data Normalized analysis was developed by Max Malacari, at University of Chicago. This version includes the effects of Multiple Scattering

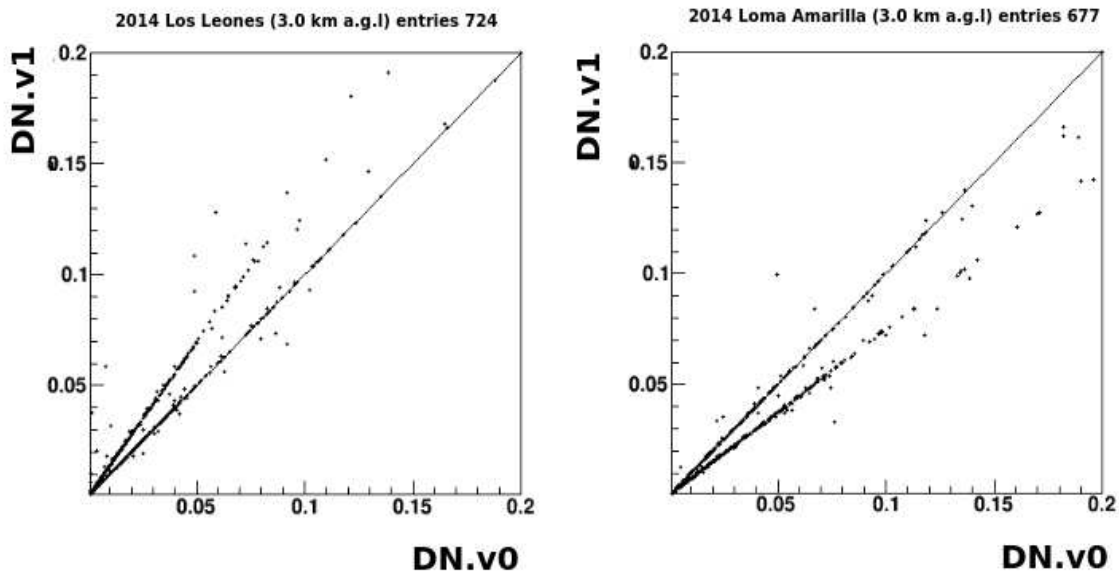

Figure 7.2: Scatter plots of τ(z=3 km) for two FD eyes between a compromised version of the DN (DN.v0) and a later version (DN.v1) that corrects for effects of the bug discovered. The bi-modality behavior is evident.

(MS) and Aerosol Scattering (AS) in the amount of light arriving to the FD cameras, as explained Chapter 3. Figure 7.3 presents a comparison between this upgraded DN analysis (MS +AS) and the original analysis. An small increase of nearly 0.006 in τ for altitudes larger than 3 km is observed in the aerosol profiles.

7.1.3 Raman LIDAR

An alternative aerosol database was created by the Roma University group. This database uses exclusively the τ measurements provided by the Raman LIDAR during 2014 and 2015. This Raman database used to produce this ADST has been altered from the one presented in Chapter 6 by the Roma group. The Raman profiles were fitted to an exponential function and profiles with obvious cloud were removed. Since the Raman only produces three τ profiles per night, the $\overline{Off\underline{line}}$ algorithm uses the nearest in time profiles available to the shower to be reconstructed.

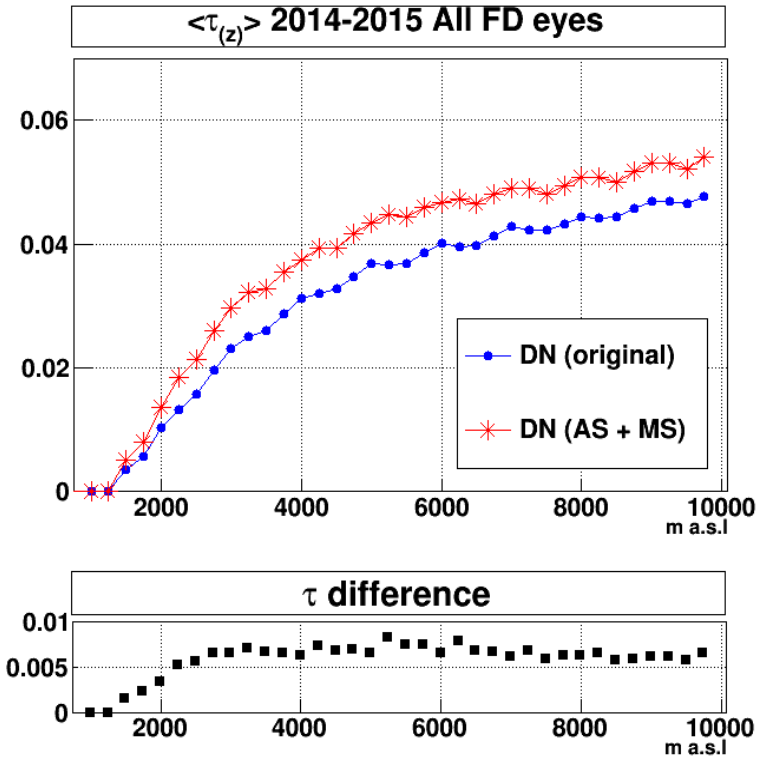

Figure 7.3: Difference on the τ(z) profiles (2014 and 2015 average) due to the introduction of aerosol scattering and multiple scattering effects.

7.1.4 Raman Biased DN Database

An additional database has been created using the DN analysis with some modifications based on the Raman LIDAR τ(z) results. This modification recognizes the differences between the DN and Raman analysis and assumes that the true aerosol contents are higher than the DN analysis claims. Under this assumption the clearest hour of the year (reference hours) already found in the DN analysis are not 100% molecular, and the number of photons arriving to the FD camera is reduced because of aerosol attenuation. To correct for this attenuation the light profiles of the reference hours need to be scaled by a factor. This factor is based on the τ(z) measurements provided by the Raman analysis. The method to calculate this factor is described below: A group of hourly τ(z) measurements from the DN analysis was selected under the following criteria:

- τ at infinite should not be larger than 0.03.
- τ(z) profiles must be smooth and continues and without cloud presence.
- The τ measurements during the hours before and after, must be also smooth and continue, to avoid a night of changing aerosol conditions.
- A Raman measurement within $\pm$ 3 hours needs to exist. Its profile should be smooth and continuous.

Table 7.1 presents the 34 hours that meet the criteria listed above. For each of these hours there are two τ(z) profiles. One created at that hour by the DN analysis and the other from a nearby time using the Raman LIDAR. The τ(z) profile of this 34 hours is averaged and presented in Figure 7.4 (left) for both the DN and the Raman. Figure 7.4 (right) shows the difference between the two averaged profiles and a linear approximation that simplifies the resulting function. The uncertainties above 7000 m a.s.l of the Raman are too high to be considered [79] in this analysis. The difference is assumed to be constant after this altitude.

Table 7.1: List of dates and hours identified as a clean hour according to the DN analysis.

year	month	days	hour	year	month	days	hour	year	month	days	hour
2014	05	24	07	2014	07	07	09	2015	07	15	09
2014	05	25	07	2014	07	18	03	2015	07	17	09
2014	05	26	09	2014	07	19	06	2015	07	23	09
2014	06	03	09	2014	07	20	07	2015	07	26	09
2014	06	05	09	2014	07	24	02	2015	08	18	08
2014	06	20	05	2014	07	29	09	2015	09	08	05
2014	06	21	05	2014	08	03	09	2015	09	10	08
2014	06	22	04	2014	08	04	09	2015	09	11	08
2014	06	27	09	2014	08	17	05	2015	10	20	07
2014	06	28	09	2015	06	11	08	2015	11	17	07
2014	07	04	09	2015	06	20	09				
2014	07	06	09	2015	07	08	04				

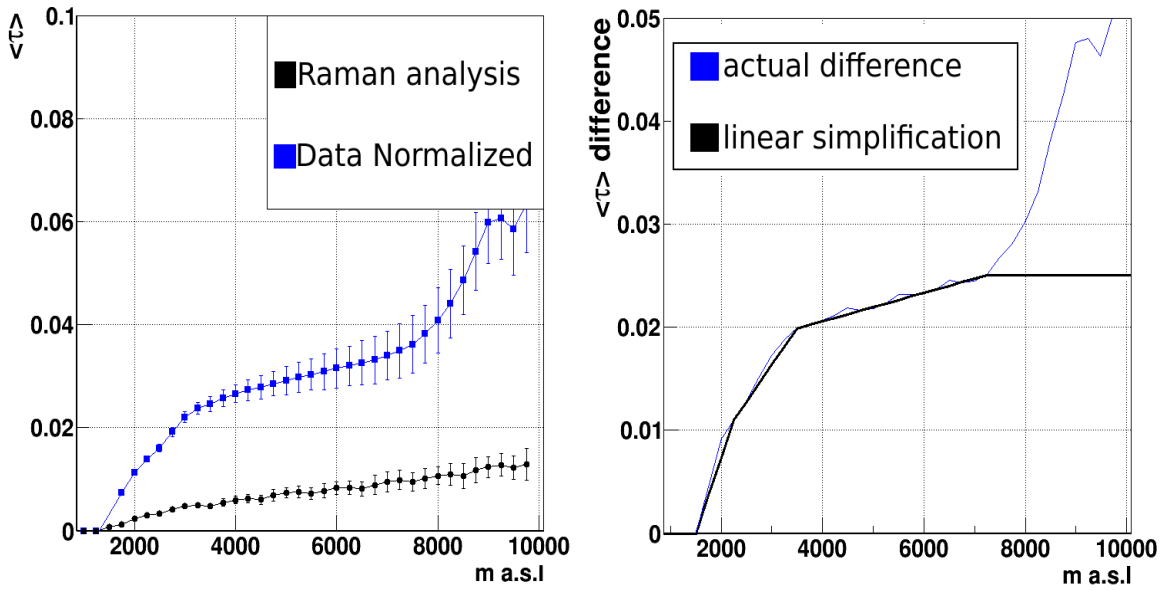

Figure 7.4: Left: Average τ(z) profiles for the 34 hours found in Table 7.1 as seen for the Raman analysis and the DN analysis Right: The difference between the two profiles was simplified to a linear function.

The τ(z) profile difference (simplified function) in Figure 7.4 can be placed in terms of optical transmission using equation 7.1. This expression was introduced in Chapter 3.

$$\tau(z) = ln\left(\frac{1}{T(z)}\right)\left(\frac{z}{z+\sqrt{z^2+D^2}}\right) \tag{7.1}$$

where z is the altitude (a.g.l), D is the distance between FD and the laser and T is the optical transmission. After the appropriate geometric corrections (z and D), for each FD eye, the inverse of the transmission T profile can be calculated (see Figure 7.5). This profile is used to scale (bin by bin) the reference hour used in the DN analysis in 2014 and 2015 and to create a modified DN aerosol database for the same years.

The modified Database such has an increase of 10% in the ratio signal for the cloud rejection cut. It also has an increase of 10% on the uncertainty of the selection of the reference profile. The new database is called "DN Raman biased". The number of hourly profiles obtained during 2014 and 2015 is presented in Table 7.2.

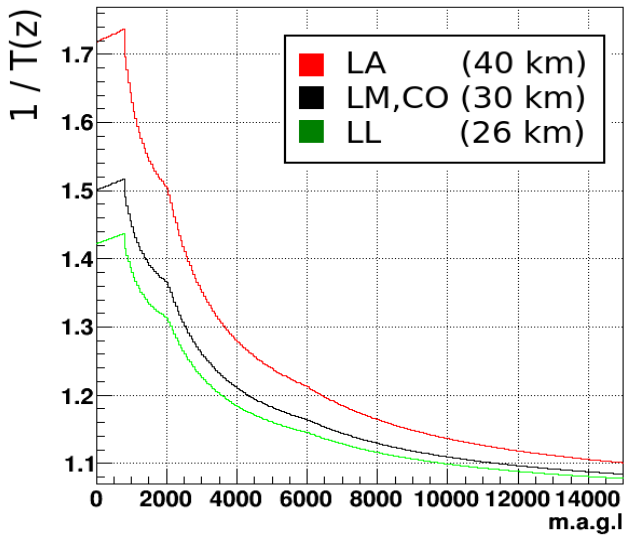

Figure 7.5: The inverted transmission function based in the difference for selected hour between the DN and the Raman analysis. This function is used to scale the reference light profiles used in the DN database to create a "DN(Raman biased)" database.

Table 7.2: list of hours produced in the DN (Raman biased) aerosol database

FD site	Los Leones		Los Morados		Loma Amarilla		Coihueco	
Year	CLF	XLF	CLF	XLF	CLF	XLF	CLF	XLF
2014	849	898	791	942	732	924	791	901
2015	790	832	744	927	575	863	775	924

A comparison between the DN(Raman biased) and the original DN databases is presented in Figure 7.6(left) for the FD LL. As a cross check, this comparison only uses the selected days from Table 7.1 to create the averaged τ(z) profiles . The difference between the two profiles in the left clearly overlaps the simplified function in red presented in Figure 7.4. The new levels of τ for the DN(Raman biased) during clear days are nearly 0.03 at 3 km, a value that is closer to the average aerosol concentration during the year. Large differences (exceeding 0.02) on τ are present after 3 km. All other FD eyes present similar results.

The averaged τ profile using all available hours in 2014 and 2015 and all FD eyes is presented in Figure 7.7. The profiles are superimposed with the profiles from the original DN database and their differences are calculated.

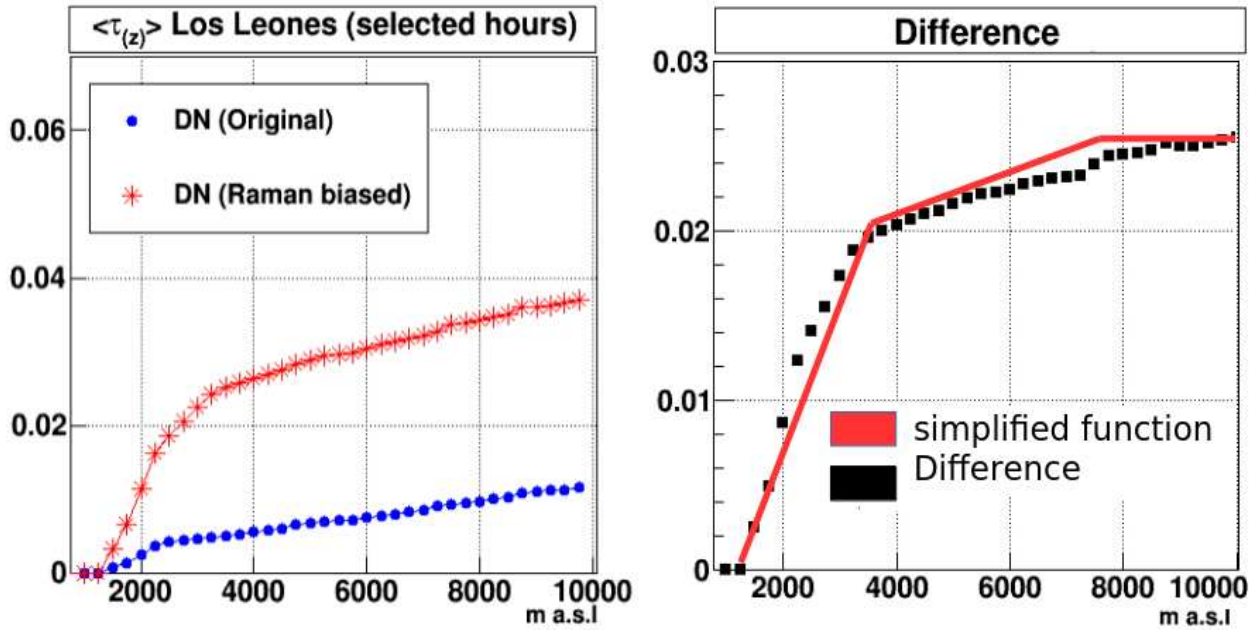

Figure 7.6: Left: A comparison between the DN(Raman biased) and the original DN databases for the averaged τ(z) profiles using only the selected days from Table 7.1. Right: The difference between the two profiles presented on the left (black dots) agrees with the linear function presented in Figure 7.4 (right).

The DN(Raman biased) database presents a rather extreme scenario, where the cleanest hours found during the year have higher levels of aerosol content and the overall τ average is 0.02 higher for most heights. An extreme scenario like this is very unlikely to be real at the observatory site. The study of the consequence of such scenarios in the reconstruction of cosmic events by the FD is still important.

7.2 The FD-SD Energy Fit

As explained in Chapter 3 the first step towards an energy spectrum is the production of the SD-FD energy fits. The SD-FD energy fits provide the necessary energy calibration for the SD, which is able to detect more events than the FD due to its nearly 100% duty cycle. Four different fits were performed, each using the ADST's created with the alternative aerosol databases introduced in the previous sections. The method used to obtain the energy calibration function is known as the "simplified likelihood method" and it is a standard

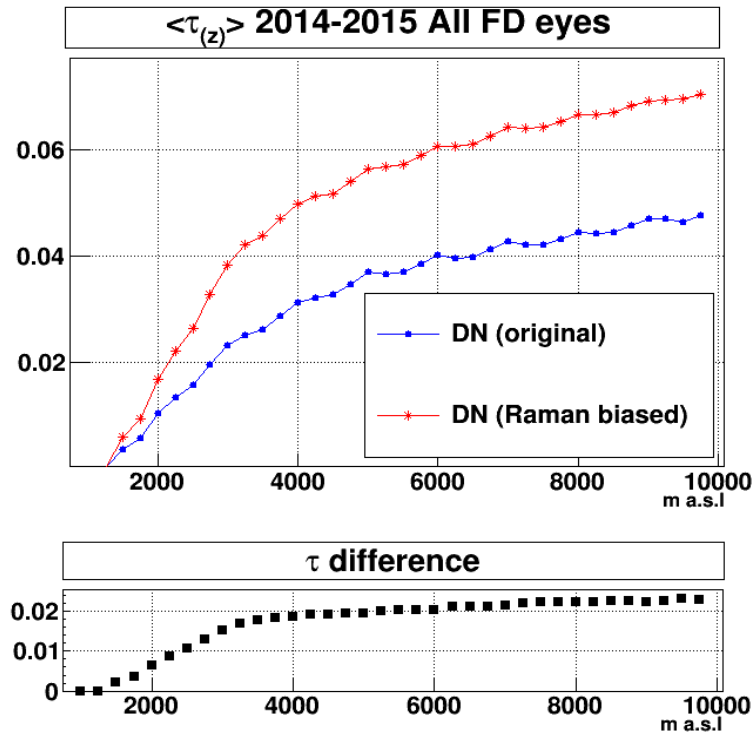

Figure 7.7: A comparison of the average τ(z) profiles of the DN(Raman biased) and the original DN databases using all the average produced in all FD eyes. The DN(Raman biased) presents differences larger than 0.02 after 3 km a.g.l.

method used by Auger. The description of this method and the selection cuts used to fit the SD energy are explained in [74]. The reconstructed energy using the FD and the SD S_{38} signal for the same cosmic event is presented in the scatter plot in Figure 7.8 for each of the alternative aerosol databases.

The scatter plot in Figure 7.8 is fitted to an exponential function: $E_{FD} = A \cdot E_{38}^{B}$ where A and B are two free parameters (See Chapter 3 for details). The fits are represented with the red line and the resulting fir parameter are visible in the corner of each plot, and they are summarized on Table 7.3.

To visualize the differences of the FD-SD calibration functions, they are superimposed in Figure 7.9 (left) using a logarithmic scale. Events with similar S_{38} signal have different FD energies that depend on the aerosol database. For databases with relatively lower val-

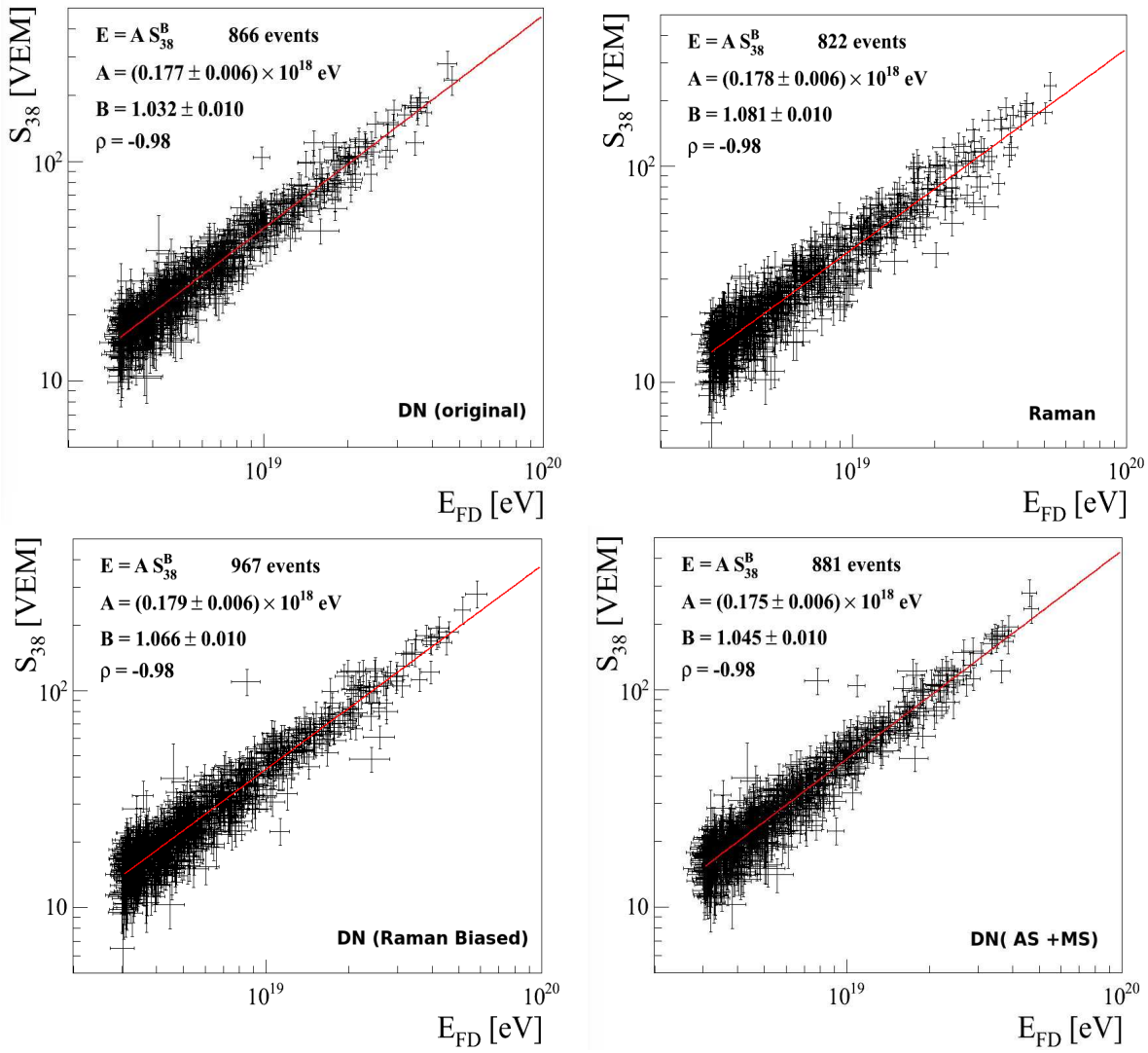

Figure 7.8: Different energy fits are found when using four alternative aerosol databases.

Table 7.3: The FD-SD calibration parameters for each aerosol databases used.

Database	Data Normalized	Raman	DN(Raman biased)	DN(AS+MS)
Parameter A	0.177±0.006	0.178±0.006	0.179±0.006	0.175±0.006
Parameter B	1.032±0.001	1.081±0.001	1.066±0.001	1.045±0.006

ues of τ such as the DN the reconstructed FD Energy values are lower than those using aerosol databases with relatively higher values of τ such as the Raman database and the DN(Raman biased). This effect can also be seen in the higher number of events used in the DN(Raman biased) fit, since more events are able to pass the lowest energy threshold

required as presented in Figure 7.9 (right).

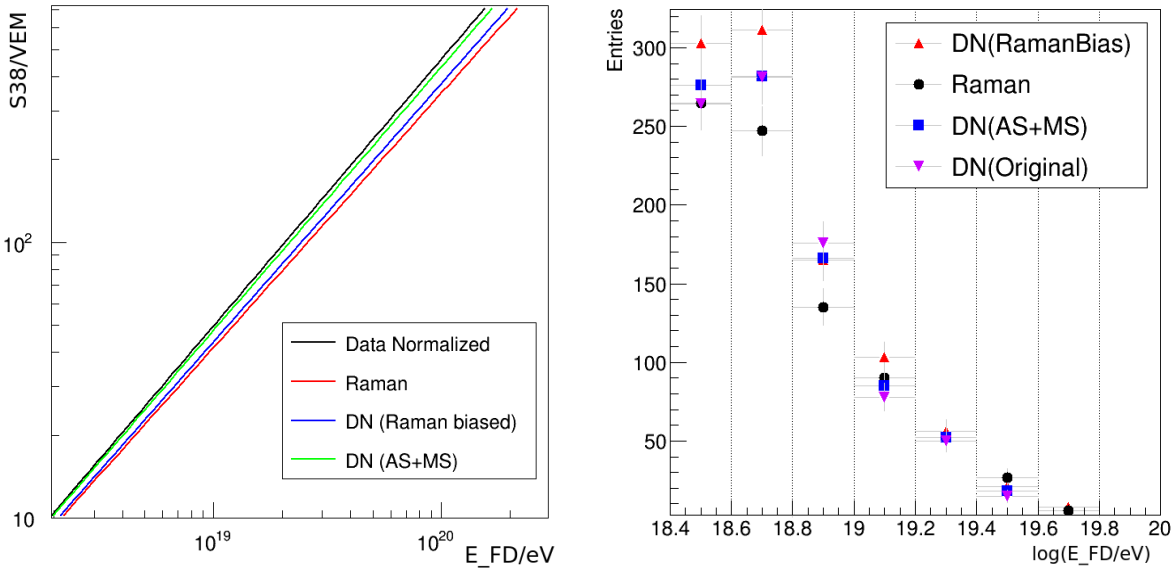

Figure 7.9: Left: The FD-SD energy calibration functions using alternative aerosol databases are superimpose to illustrate the change on the relationship between E_{FD} and S_{38}. Right: The use of different aerosol databases affects the reconstructed FD energies; therefore, the number of events passing the lower energy cut changes.

7.3 The Energy Spectrum

The full description and details of the UHECR spectrum can be found at [76]. The analysis of the spectrum is rather complicated and depends on many careful calculations, such as the FD-SD exposure, Montecarlo modeling and fiducial cuts. The simplifications include the use of the SD array on energies where the SD becomes fully efficient (3×10^{18} eV) [86]. The SD events used, belong to a selected group of events passing a criteria determined by the Energy Spectrum Analysis group. This criteria is known as "6T5 fiducial cut", which requires SD events to trigger all six SD stations neighboring the most active one (hot tank). It also includes the SD reconstructed inclination angle (zenith angle) to be less than 60°. This events are known as vertical events. The criteria also excludes all events from a list of bad periods explained in [76].

The energy spectrum of UHECR is defined as the number of events (cosmic ray intensity) per bin of energy per exposure time:

$$J_E = \frac{dN}{dEd\varepsilon} \tag{7.2}$$

where ε is the exposure of the detector defined as:

$$d\varepsilon = dt \cdot dA \cdot d\Omega \tag{7.3}$$

Ω is the solid angle and A the projected element of surface.

For the SD only, the exposure is rather simple and it is determined based on pure geometrical models and operation times. The determination of the SD exposure is well explained in [87]. Updates of the exposure are regularly presented at every collaboration meeting and their values are found in [88].

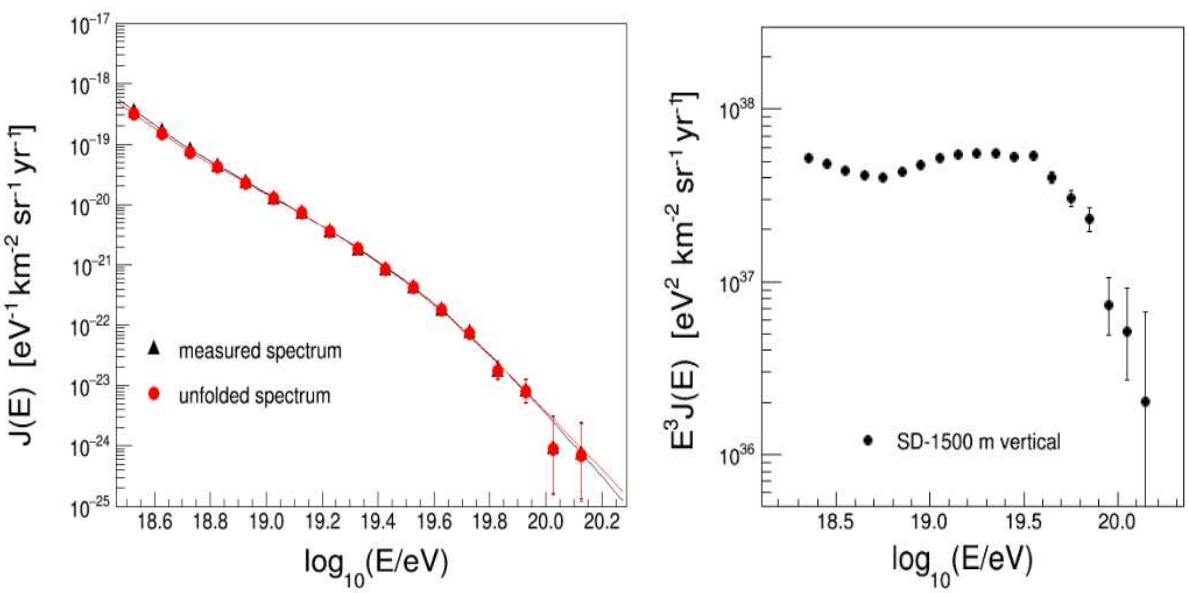

Figure 7.10: Left: spectrum plots created with the toolkit (ICRC 2015) reproduced the results published in [76] Right: To enhance the spectral features, each point is scaled by a factor of E^3.

The flux is recovered using a standard tool available by the spectrum group and used to calculate the spectrum presented in the International Cosmic Ray Conference (ICRC) in 2015. It takes into account the exposure correction and the migration effects due to the

finite detector resolution and fluctuations in the shower development [76]. The spectrum plots created with the toolkit and same selection criteria and data as the one used in the ICRC 2015 paper [76] is presented in Figure 7.10. The same toolkit was used with the same selection criteria on the same data, but the SD-FD calibration parameters were replaced by the ones on Table 7.3 for the different databases. The results are presented on Figure 7.11.

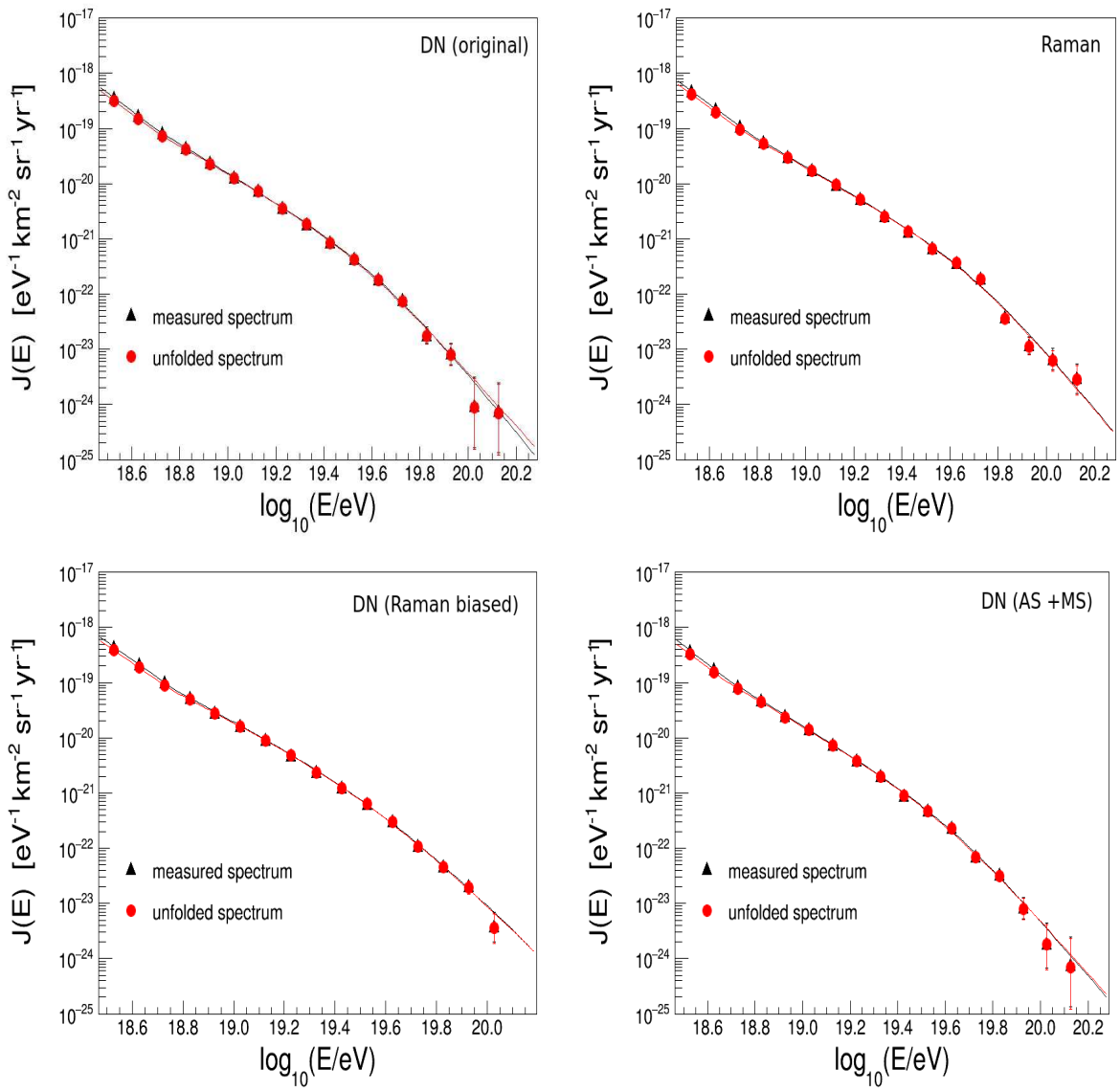

Figure 7.11: The particle flux achieved using different aerosol databases. Each plot includes the flux as measured and the correction due to migration effects (unfolded spectrum).

The relative differences between the entries per energy bin of the raw spectrum obtained with the different databases and the one obtained for the ICRC 2015 is presented in Figure 7.12. The largest differences are presented at the highest values of energies for the Raman and DN(Raman biased) databases. The original DN presents the smallest differences. This difference is not expected to be zero since the FD-SD energy calibration fit produced for this study with the original DN database, uses data only from 2014 and 2015. The FD-SD energy calibration fit used in the ICRC 2015 uses data from 2004 to 2013.

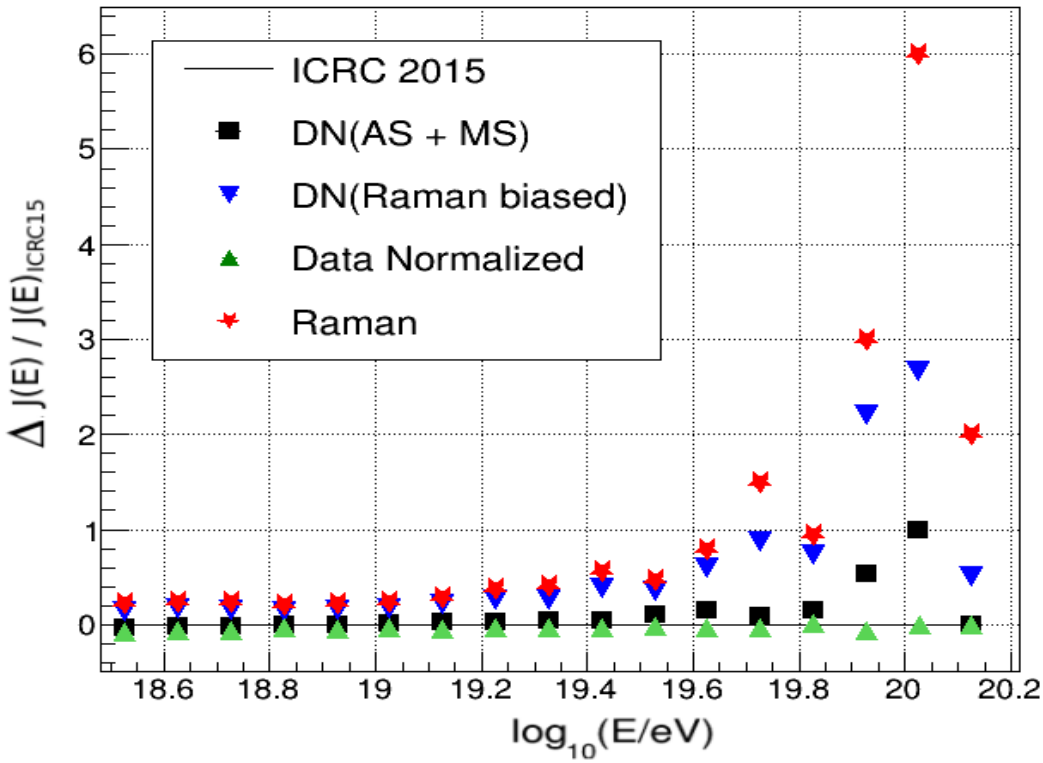

Figure 7.12: Relative differences in the number of entries per energy bin between the flux obtained with different aerosol databases and the flux reported in the ICRC 2015.

The spectrum plots were superimposed after they were scaled by a factor of E^3 (Figure 7.13). The energy spectrum features an increase on the scaled flux for aerosol databases that present larger overall values of $\tau(z)$, such as the Raman and the DN (Raman biased) databases. The increase on scaled flux is more noticeable for regions at the end of the spectrum.

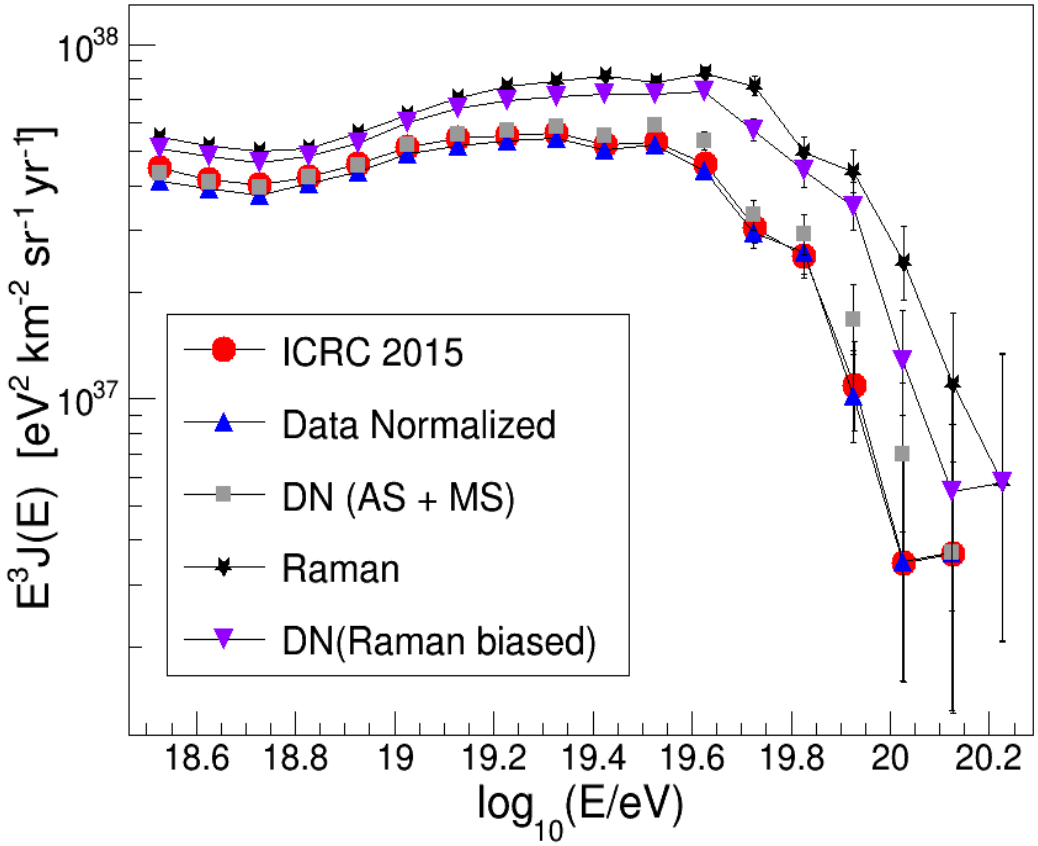

Figure 7.13: Energy Spectrum for different aerosol databases features an increase in the scaled flux for databases with average larger values of τ(z).

If the Raman database is correct, and the reference nights have levels of aerosol with offsets up to 0.02 as presented in this chapter, it may have consequences on the cosmic ray science delivered by Auger. However the Raman LIDAR may be overestimating the aerosol levels. Some of the concern about the Raman LIDAR measurements includes the large uncertainties a heights larger than 6 km. Raman LIDARs are most commonly used to measure aerosol contents in polluted environments. Theτ measurements at the Observatory site using a Raman LIDAR are pioneering. Measurements at these lower aerosol levels are not yet been bench-marked. A large number of profiles present a suspicious continuous increase of τ level at high altitudes, which contradicts the established idea of a τ profile that flattens at high altitudes. The relative large distance between the Raman LIDAR and the

FD eyes introduces an uncertainty about the atmosphere uniformity. Aerosol fluctuations over these large distances may introduce a large energy shift on the sparse number of events at the highest energies.

A more refined Raman analysis is currently under development by our colleges from the University of L'Aquila. This includes the use of GDAS hourly molecular atmosphere profiles from 2014 to 2016. A different fit model based on Mie scattering theory will replace the simplistic exponential fit currently in use. A better Raman aerosol database will be crucial to enhance the current understanding of the atmospheric aerosol uncertainties.

CHAPTER 8

SUMMARY AND CONCLUSIONS

In the introduction, some discrepancies between the flux of cosmic rays measured by different experiments were presented. The most recent example is the discrepancy at the highest energy of the spectrum, between the Pierre Auger Observatory and the Telescope Array. The central purpose of this thesis was to determine if this discrepancy could be attributed to the uncertainties in the calibration of the instrument. Specifically, could these differences be understood by applying alternative atmospheric databases to the energy spectrum analysis?

The increased interest in alternative aerosol databases appeared after the upgrade of the CLF. My participation in this upgrade represents my most important contributions to the Observatory science.

The upgraded CLF has now been running for almost 4 years. Two major benefits of this upgrade include:

- A more stable and better understood laser that reduced some uncertainties in the τ measurements used by the DN method.
- An independent measurement $\tau(z)$ by the Raman LIDAR that was installed as part of the upgrade.

This thesis described the details of the upgrade and it presented for the first time the comparisons between the DN analysis and a preliminary analysis of the Raman measurements using data from 2014 to 2015. The comparisons revealed differences in the average τ measurements as large as 0.04 above 3 km. These differences are larger than the quoted uncertainties and they suggest that the measurement of aerosol content at the Observatory site is not completely understood. In particular, it is likely possible that the reference profiles used in the DN and LS are not free of aerosols. The following contributions are considered to explain the Raman-DN differences:

- the Raman method measures $\tau(z)$ above the CLF, while the DN method measures $\tau(z)$ in the region between the CLF and a FD site.
- the Raman and the DN measurements are not simultaneous,
- the effects of the light scattered by aerosols out of the laser beam and the effects of multiple scattering are not implemented in the DN analysis,
- the Raman analysis lacks a cloud identification algorithm,
- the relative large uncertainties in $\tau(z)$ in the Raman analysis introduced by the limited acquisition time.

This thesis studied one scenario where the reference hours (used in the DN analysis) have a $\tau(z)$ larger than zero. The results of the Raman measurements, during low aerosol content hours according to the DN analysis, were used to create an alternative aerosol database called the DN(Raman biased). This database has an average τ 0.02 larger than the original DN database at most heights. This "worst case scenario" database is unlikely to be found with correct $\tau(z)$ measurements for Auger. But the use of this alternative database is still beneficial for a better understanding of the aerosol corrections on the flux measurement.

Two other alternative databases were additionally provided by our colleagues in the atmospheric group: a preliminary Raman database, and a DN preliminary version that includes the effects of the aerosol scattering and the multiple scattering. For an accurate comparison between databases, only data from 2014 and 2015 (the only data available for the Raman database) have been included. A set of Golden-hybrid cosmic events were used to establish the FD-SD energy calibration fit parameters for each alternative aerosol database. It was verified that the Auger energy spectrum plot (presented in ICRC 2015) using vertical events from 2004 to 2013 observed by the SD (1.5 km) array was correctly reproduced. Then, the parameters obtained by the FD-SD energy fit using the alternative aerosol databases were used to produce the energy spectrum plots, and to study differences in the resulting measured particle flux.

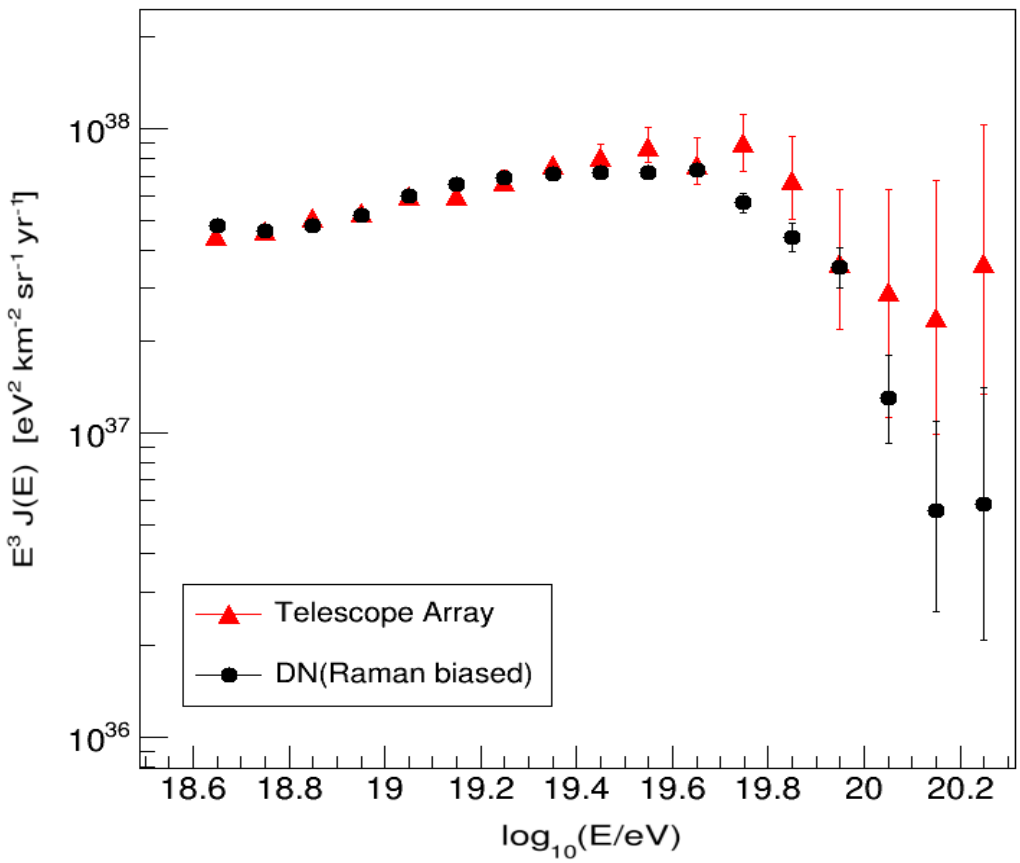

Figure 8.1: The cosmic ray spectrum measured by TA is compared with the spectrum obtained using the DN(Raman biased) database. The discrepancies (particularly at high energies) are reduced compared to those in Figure 1.3. The comparison reveals that the fluxes are within the uncertainty bars at the highest part of the spectrum.

The energy spectrum obtained with the DN (Raman biased) compared to the energy spectrum reported by TA is presented in Figure 8.1. The TA data used to create the energy spectrum plot in Figure 1.3 is not of public domain. In order to superimpose the two plots, the TA energy spectrum plot reported in [4] was digitized using software from [89]. The differences in the flux measurements are lower than the differences in Figure 1.3 for most energy bins. Above 8×10^{19} eV (where the largest Auger-TA discrepancies were present) the flux measurements are now within the error bars. These error bars are purely statistical. Both experiments have additional systematic energy uncertainties that are not shown. The result is interesting because it demonstrate that it is possible to have a better agreement

between the Auger and TA energy spectrum, by using an alternative aerosol database for Auger. The better agreement does not lead to conclude that Auger $\tau(z)$ measurements are incorrect. TA uses a similar method as the DN analysis for their aerosol measurements, and by using a similar logic it is possible that TA obtains relative higher primary energies by over-estimating their $\tau(z)$ corrections. In addition, the results presented here do not indicate that a mis-measurement of τ is the only explanation for a better agreement. It is possible that there are other effects that have not been studied yet that can cause similar results.

The Auger atmospheric group is collaborating on a more complex study with similar goals. A grid of alternative aerosol databases will be created where the DN has an offset derived from simulated τ profiles with different H_{mie} and L_{mie}. This grid of databases will be used to study the systematic effects on the FD-SD energy calibration, the X_{max} reconstruction and the energy reconstruction. These efforts together with the newer release of the Raman data, will provide a better estimation of the aerosol contents at the observatory site, in addition to the possible effects that the aerosol databases will have on the flux measurements. Once these effects are quantified, a final assessment about the Auger-TA differences in the energy spectrum is expected.

APPENDIX A - THE AUTOLOGS FILES

The autologs files are text files produced during CLF or XLF operations. the file naming convention uses the date as the prefix, for example yy2000mm07dd04 represent July 4th of 2000, followed by the name of the facility and finally the file extension ".autolog". The autologs records information for individual laser shots and the summary of a set of laser shots. The individual laser shots will be identify with the prefix "DATA:FIRE" and it will write one line per shot.

Table A.1: This table describes the information in any line of the autologs that stars with the Prefix DATA:FIRE:

column	name	type	description
1	prefix	%s	Prefix for individual shots, one per row.
2	setID	%d	unique identifier
3	n	%d	number of current shot in the set.
4	emon	%e	energy reading from the monitor (pick up) probe.
5	ecal	%e	energy reading from the calibration probe during energy calibrations, otherwise a negative number is written.
6	dpw	%d	energy mode
7	mode	%d	1: fixed vertical, 2: steering, 3:calibration.
8	azi	%f	azimuth angle of the beam, CCW from north.
9	elv	%f	elevation angle (90° at the zenith, 0° at the horizon)
10	year	%d	year of the laser shot.
11	month	%d	month of the laser shot.
12	day	%d	day of the laser shot.
13	hour	%d	the hour is in 24 hour format and in UTC time.
14	minute	%d	minute of the laser shot.
14	second	%d	second of the laser shot.
15	ns	%d	nanosecond time stamp.
16	gps	%d	GPS second

The summary information for a set of shots will be identified with a prefix , and there is one line per set of shots. There is also a special line " which present summary information every 25 shots with the same formating. A unique identifier categorizes the laser shot type: for example, "0" for fixed vertical and steered shots, "2000" for energy calibration shots,

“3000” for polarization calibration shots, 10** for AGN shots where the last two digits correspond to a list of object of interest.

The information of the atmospheric laser shots written in the autolog files is described in Table A.1. The information necessary in the DN analysis (as the calibration factors CF) is extracted from this autologs.

APPENDIX B - CLF CONNECTION SUMMARY

The hardware integration in the CLF is presented in Figure B.1.

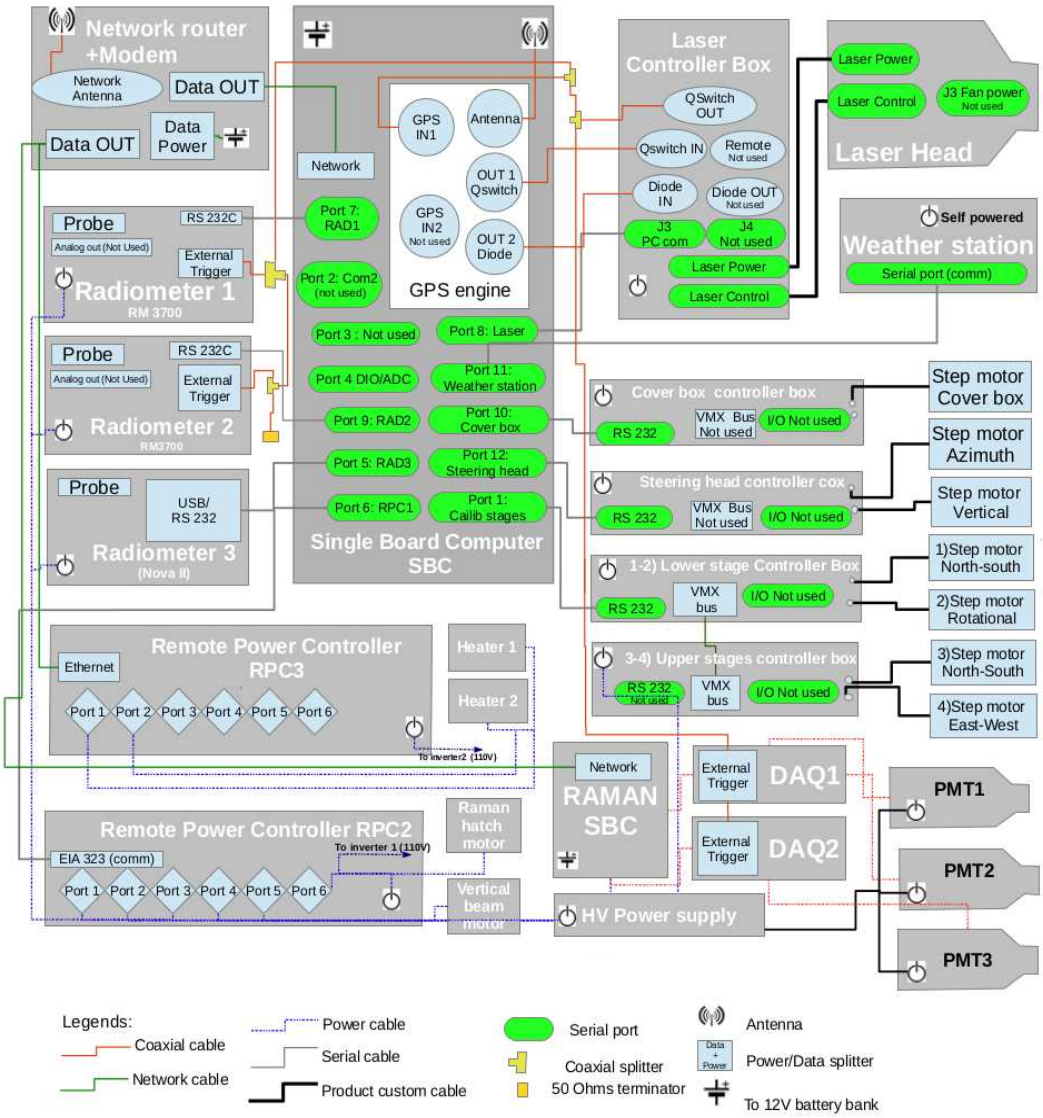

Figure B.1: CLF hardware integration.

REFERENCES CITED

[1] P. Abreu et al. The Pierre Auger Observatory I: The Cosmic Ray Energy spectrum and Related Measurements. In *Proceedings, 32nd International Cosmic Ray Conference (ICRC 2011): Beijing, China, August 11-18, 2011*, 2011.

[2] R. U. Abbasi et al. First observation of the Greisen-Zatsepin-Kuzmin suppression. *Phys. Rev. Lett.*, 100:101101, 2008. doi: 10.1103/PhysRevLett.100.101101.

[3] Alexander Aab et al. The Pierre Auger Cosmic Ray Observatory. *Nucl. Instrum. Meth.*, A798:172–213, 2015. doi: 10.1016/j.nima.2015.06.058.

[4] The Pierre Auger collaboration. Measurement of the cosmic ray spectrum above 4 eev using inclined events detected with the pierre auger observatory. *Journal of Cosmology and Astroparticle Physics*, 2015(08):049, 2015.

[5] V. F. Hess. Über Beobachtungen der durchdringenden Strahlung bei sieben Freiballonfahrten. *Physikalische Zeitschrift*, 13:1084–1091, November 1912.

[6] Robert a. millikan - biographical. URL `http://www.nobelprize.org/nobel_prizes/physics/laureates/1923/millikan-bio.html`.

[7] Arthur H. Compton. A geographic study of cosmic rays. *Phys. Rev.*, 43:387–403, Mar 1933. doi: 10.1103/PhysRev.43.387. URL `http://link.aps.org/doi/10.1103/PhysRev.43.387`.

[8] Georgi Zatsepin and Georgi Khristiansen. Dmitri v. skobeltsyn. *Physics Today*, 45(5): 74–76, 1992. doi: 10.1063/1.2809672. URL `http://dx.doi.org/10.1063/1.2809672`.

[9] Pierre Auger, P. Ehrenfest, R. Maze, J. Daudin, and Robley A. Fréon. Extensive cosmic-ray showers. *Rev. Mod. Phys.*, 11:288–291, Jul 1939. doi: 10.1103/RevModPhys.11.288. URL `http://link.aps.org/doi/10.1103/RevModPhys.11.288`.

[10] W. Heitler. *The quantum theory of radiation / by W. Heitler*. Clarendon Press Oxford, 3rd ed. edition, 1954.

[11] Penzias A.A. and Wilson R.W. A Measurement of Excess Antenna Temperature at 4080 Mc/s. *APJ.*, 142:419–421, jul 1965. doi: 10.1086/148307.

[12] K. Greisen. End to the Cosmic-Ray Spectrum? *Physical Review Letters*, 16:748–750, April 1966. doi: 10.1103/PhysRevLett.16.748.

[13] John Linsley. Evidence for a primary cosmic-ray particle with energy 10^{20} ev. *Phys. Rev. Lett.*, 10:146–148, Feb 1963. doi: 10.1103/PhysRevLett.10.146. URL `http://link.aps.org/doi/10.1103/PhysRevLett.10.146`.

[14] D. M. Edge et al. The cosmic ray spectrum at energies above 10-to-the-17 ev. *J. Phys.*, A6:1612–1634, 1973. doi: 10.1088/0305-4470/6/10/019.

[15] A. N Bunner. Cosmic ray detection by atmospheric fluorescence. *Sky and Telescope*, 10:201–208, 1967. URL `http://archive.org/details/Sky_and_Telescope_1967-10-cbr`.

[16] A. N Bunner. *Cosmic Ray Detection by Atmospheric Fluorescence*. PhD thesis, 1967. Cornell University.

[17] The fly's eye observatory (1981-1993). URL `http://www.physics.adelaide.edu.au/astrophysics/hires/flyseye.html`.

[18] M. Takeda et al. Energy determination in the akeno giant air shower array experiment. *Astroparticle Physics*, 19(4):447 – 462, 2003. ISSN 0927-6505. doi: http://dx.doi.org/10.1016/S0927-6505(02)00243-8. URL `http://www.sciencedirect.com/science/article/pii/S0927650502002438`.

[19] W. D. Apel et al. KASCADE-Grande measurements of energy spectra for elemental groups of cosmic rays. *Astropart. Phys.*, 47:54–66, 2013. doi: 10.1016/j.astropartphys.2013.06.004.

[20] Karl-Heinz Kampert. Cosmic Rays from the Knee to the Ankle: Status and Prospects. *Nucl. Phys. Proc. Suppl.*, 165:294–306, 2007. doi: 10.1016/j.nuclphysbps.2006.11.048. [,294(2006)].

[21] E. Kido and O. E. Kalashev. Constraining UHECR source models by the TA SD energy spectrum. In *Proceedings, 33rd International Cosmic Ray Conference (ICRC2013): Rio de Janeiro, Brazil, July 2-9, 2013*, page 0136, 2013. URL `https://inspirehep.net/record/1261846/files/arXiv:1310.6093.pdf`.

[22] Karl-Heinz Kampert and Peter Tinyakov. Cosmic rays from the ankle to the cutoff. *Comptes Rendus Physique*, 15:318–328, 2014. doi: 10.1016/j.crhy.2014.04.006.

[23] Schueesles F. *Measurements of the Energy Spectrum of Ultra-High Energy Cosmic Rays using Hybrid Data of the Pierre Auger Observatory*. PhD thesis, 2008. Karlsruhe, KIT, Diss., 2008.

[24] F. W. Stecker and M. H. Salamon. Photodisintegration of ultra-high-energy cosmic rays: A new determination. *The Astrophysical Journal*, 512(2):521, 1999.

[25] ENRICO Fermi. On the origin of the cosmic radiation. *Phys. Rev.*, 75:1169–1174, Apr 1949. doi: 10.1103/PhysRev.75.1169. URL `http://link.aps.org/doi/10.1103/PhysRev.75.1169`.

[26] E.G. Berezhko. Maximum energy of cosmic rays accelerated by supernova shocks. *Astroparticle Physics*, 5(3):367 – 378, 1996. ISSN 0927-6505. doi: http://dx.doi.org/10.1016/0927-6505(96)00037-0. URL `http://www.sciencedirect.com/science/article/pii/0927650596000370`.

[27] A. M. Hillas. The origin of ultra-high-energy cosmic rays. *Annual Review of Astronomy and Astrophysics*, 22(1):425–444, 1984. doi: 10.1146/annurev.aa.22.090184.002233.

[28] Wolfgang Rhode. *Introduction*, pages 1–16. Springer Netherlands, Dordrecht, 2012. ISBN 978-94-007-5422-5. doi: 10.1007/978-94-007-5422-5_1. URL `http://dx.doi.org/10.1007/978-94-007-5422-5_1`.

[29] Claus Grupen. *Astroparticle Physics*. Springer, July 2005. ISBN 3540253122.

[30] Pedro Abreu et al. Interpretation of the Depths of Maximum of Extensive Air Showers Measured by the Pierre Auger Observatory. *JCAP*, 1302:026, 2013. doi: 10.1088/1475-7516/2013/02/026.

[31] J. Matthews. A heitler model of extensive air showers. *Astroparticle Physics*, 22(56):387 – 397, 2005. ISSN 0927-6505. doi: http://dx.doi.org/10.1016/j.astropartphys.2004.09.003. URL `http://www.sciencedirect.com/science/article/pii/S0927650504001598`.

[32] C. C. Thakuria and K. Boruah. Comparison of EPOS and QGSJET-II in EAS Simulation using CORSIKA. *ArXiv e-prints*, February 2012.

[33] R. S. Fletcher, T. K. Gaisser, Paolo Lipari, and Todor Stanev. s. *Phys. Rev. D*, 50:5710–5731, Nov 1994. doi: 10.1103/PhysRevD.50.5710. URL `http://link.aps.org/doi/10.1103/PhysRevD.50.5710`.

[34] D. Heck, J. Knapp, J. N. Capdevielle, G. Schatz, and T. Thouw. *CORSIKA: a Monte Carlo code to simulate extensive air showers.* 1998.

[35] Ralph Engel, Dieter Heck, and Tanguy Pierog. Extensive air showers and hadronic interactions at high energy. *Ann. Rev. Nucl. Part. Sci.*, 61:467–489, 2011. doi: 10.1146/annurev.nucl.012809.104544.

[36] P. Davoudifar and K. Rowshan Tabari. Statistical study of extensive air showers and the question of mass composition. *Astronomy Letters*, 40(12):821–828, 2014. ISSN 1562-6873. doi: 10.1134/S1063773714120032. URL `http://dx.doi.org/10.1134/S1063773714120032`.

[37] J et al. Abraham. Measurement of the depth of maximum of extensive air showers above 10^{18} eV. *Phys. Rev. Lett.*, 104:091101, Mar 2010. doi: 10.1103/PhysRevLett.104.091101. URL `http://link.aps.org/doi/10.1103/PhysRevLett.104.091101`.

[38] K.-H. Kampert and M. Unger. Measurements of the cosmic ray composition with air shower experiments. *Astroparticle Physics*, 35:660–678, May 2012. doi: 10.1016/j.astropartphys.2012.02.004.

[39] R. U. Abbasi et al. Study of Ultra-High Energy Cosmic Ray composition using Telescope Arrays Middle Drum detector and surface array in hybrid mode. *Astropart. Phys.*, 64: 49–62, 2015. doi: 10.1016/j.astropartphys.2014.11.004.

[40] Alexander Aab et al. The Pierre Auger Cosmic Ray Observatory. *Nucl. Instrum. Meth.*, A798:172–213, 2015. doi: 10.1016/j.nima.2015.06.058.

[41] The futures bright for the Pierre Auger Observatory. Jul 2006. URL `http://cds.cern.ch/record/1733941`.

[42] The Pierre Auger Collaboration. The pierre auger project design report. *FERMILAB-PUB-96-024*, 1996.

[43] J. Abraham and et al. Properties and performance of the prototype instrument for the pierre auger observatory.

[44] The Pierre Auger Collaboration. The pierre auger collaboration, 2010. URL `https://www.auger.org/index.php/about-us`.

[45] I. Allekotte et al. The Surface Detector System of the Pierre Auger Observatory. *Nucl. Instrum. Meth.*, A586:409–420, 2008. doi: 10.1016/j.nima.2007.12.016.

[46] The Pierre Auger Collaboration, J. Abraham, P. Abreu, M. Aglietta, C. Aguirre, E. J. Ahn, D. Allard, I. Allekotte, J. Allen, P. Allison, and et al. The Fluorescence Detector of the Pierre Auger Observatory. *ArXiv e-prints*, July 2009.

[47] Alexander Aab et al. The Pierre Auger Observatory: Contributions to the 33rd International Cosmic Ray Conference (ICRC 2013). In *Proceedings, 33rd International Cosmic Ray Conference (ICRC2013): Rio de Janeiro, Brazil, July 2-9, 2013*, 2013.

[48] J.T. Brack, R. Meyhandan, G.J. Hofman, and J. Matthews. Absolute photometric calibration of large aperture optical systems. *Astroparticle Physics*, 20(6):653 – 659, 2004. ISSN 0927-6505. doi: http://dx.doi.org/10.1016/j.astropartphys.2003.09.004.

[49] R. Knapik et al. The Absolute, Relative and Multi-Wavelength Calibration of the Pierre Auger Observatory Fluorescence Detectors. In *Proceedings, 30th International Cosmic Ray Conference (ICRC 2007): Merida, Yucatan, Mexico, July 3-11, 2007*, volume 4, pages 343–346, 2007. [4,343(2007)].

[50] W. Apel et al. Thunderstorm observations by air-shower radio antenna arrays. *Advances in Space Research*, 48(7):1295 – 1303, 2011. ISSN 0273-1177. doi: http://dx.doi.org/10.1016/j.asr.2011.06.003.

[51] C. Martin Will. *Atmospheric Monitoring for Ground-Based Cosmic Ray Detectors*. PhD thesis, 2012. URL `http://digbib.ubka.uni-karlsruhe.de/volltexte/1000028831`. Karlsruhe, KIT, Diss., 2012.

[52] Thunderstorm observations by air-shower radio antenna arrays. URL `http://badc.nerc.ac.uk/`.

[53] S. Y. BenZvi, B. M. Connolly, J. A. J. Matthews, M. Prouza, E. F. Visbal, and Stefan Westerhoff. Measurement of the Aerosol Phase Function at the Pierre Auger Observatory. *Astropart. Phys.*, 28:312–320, 2007. doi: 10.1016/j.astropartphys.2007.06.005.

[54] P. Abreu et al. The Rapid Atmospheric Monitoring System of the Pierre Auger Observatory. *JINST*, 7:P09001, 2012. doi: 10.1088/1748-0221/7/09/P09001.

[55] Barbara Wilczynska, D. Gora, P. Homola, J. Pekala, M. Risse, and H. Wilczynski. Variation of atmospheric depth profile on different time scales. *Astropart. Phys.*, 25: 106–117, 2006. doi: 10.1016/j.astropartphys.2005.12.007.

[56] ARGENSIG Soluciones Cartogrficas. Medicion de fd buildings and laser stations, 2007. URL `http://www.auger.org.ar/survey/CoordenadasFD.pdf`.

[57] B. Fick, M. Malek, J. A. J. Matthews, J. Matthews, R. Meyhandan, M. Mostaf, M. Roberts, P. Sommers, and L. Wiencke. The Central Laser Facility at the Pierre Auger Observatory. *JINST*, 1(11):P11003–P11003, 2006. doi: 10.1088/1748-0221/1/11/P11003.

[58] M. Ave et al. Spectrally resolved pressure dependence measurements of air fluorescence emission with {AIRFLY}. *Nuclear Instruments and Methods in Physics Research Section A: Accelerators, Spectrometers, Detectors and Associated Equipment*, 597(1): 41 – 45, 2008. ISSN 0168-9002. doi: http://dx.doi.org/10.1016/j.nima.2008.08.052. Proceedings of the 5th Fluorescence Workshop.

[59] Vázquez et al. The effect of the fluorescence yield selection on the energy scales of Auger, HiRes and TA. In *European Physical Journal Web of Conferences*, volume 53 of *European Physical Journal Web of Conferences*, page 10002, June 2013. doi: 10.1051/epjconf/20135310002.

[60] Claudio Tomasi, Vito Vitale, Boyan Petkov, Angelo Lupi, and Alessandra Cacciari. Improved algorithm for calculations of rayleigh-scattering optical depth in standard atmospheres. *Appl. Opt.*, 44(16):3320–3341, Jun 2005. doi: 10.1364/AO.44.003320. URL `http://ao.osa.org/abstract.cfm?URI=ao-44-16-3320`.

[61] A. Aab et al. Origin of atmospheric aerosols at the pierre auger observatory using studies of air mass trajectories in south america. *Atmospheric Research*, 149:120 – 135, 2014. ISSN 0169-8095. doi: http://dx.doi.org/10.1016/j.atmosres.2014.05.021.

[62] M.I. Micheletti et al. Elemental analysis of aerosols collected at the pierre auger cosmic ray observatory with {PIXE} technique complemented with sem/edx. *Nuclear Instruments and Methods in Physics Research Section B: Beam Interactions with Materials and Atoms*, 288:10 – 17, 2012. ISSN 0168-583X. doi: http://dx.doi.org/10.1016/j.nimb.2012.07.022.

[63] Anthony Bucholtz. Rayleigh-scattering calculations for the terrestrial atmosphere. *Appl. Opt.*, 34(15):2765–2773, May 1995. doi: 10.1364/AO.34.002765. URL `http://ao.osa.org/abstract.cfm?URI=ao-34-15-2765`.

[64] Tadeusz Wibig and Arnold W Wolfendale. At what particle energy do extragalactic cosmic rays start to predominate? *Journal of Physics G: Nuclear and Particle Physics*, 31(3):255, 2005. URL `http://stacks.iop.org/0954-3899/31/i=3/a=005`.

[65] J. Abraham and et al. A study of the effect of molecular and aerosol conditions in the atmosphere on air fluorescence measurements at the Pierre Auger Observatory. *Astroparticle Physics*, 33:108–129, March 2010. doi: 10.1016/j.astropartphys.2009.12.005.

[66] S. Argiro, S. L. C. Barroso, J. Gonzalez, L. Nellen, Thomas Cantzon Paul, T. A. Porter, L. Prado, Jr., M. Roth, R. Ulrich, and D. Veberic. The Offline Software Framework of the Pierre Auger Observatory. *Nucl. Instrum. Meth.*, A580:1485–1496, 2007. doi: 10.1016/j.nima.2007.07.010.

[67] Alexander Aab et al. Reconstruction of inclined air showers detected with the Pierre Auger Observatory. *JCAP*, 1408(08):019, 2014. doi: 10.1088/1475-7516/2014/08/019.

[68] H.M.J. Barbosa, F. Catalani, J.A. Chinellato, and C. Dobrigkeit. Determination of the calorimetric energy in extensive air showers. *Astroparticle Physics*, 22(2):159 – 166, 2004. ISSN 0927-6505. doi: http://dx.doi.org/10.1016/j.astropartphys.2004.06.007. URL `http://www.sciencedirect.com/science/article/pii/S0927650504001239`.

[69] Ulrich R. *Measurements of the proton-air cross section using hybrid data from the Pierre Auger Observatory*. PhD thesis, 2008. Karlsruhe, KIT, Diss., 2008.

[70] S. Ostapchenko. Qgsjet-ii: towards reliable description of very high energy hadronic interactions. *Nuclear Physics B - Proceedings Supplements*, 151(1):143 – 146, 2006. ISSN 0920-5632. doi: http://dx.doi.org/10.1016/j.nuclphysbps.2005.07.026.

[71] D. Heck S. Ostapchenko T. Pierog, R. Engel and K. Werner. In *Proceedings, 30th International Cosmic Ray Conference (ICRC 2007): Merida, Yucatan, Mexico, July 3-11, 2007*, volume 4, 2007.

[72] Abraham and et al. Measurement of the Depth of Maximum of Extensive Air Showers above 10^{18}eV. *Physical Review Letters*, 104(9):091101, March 2010. doi: 10.1103/PhysRevLett.104.091101.

[73] Alexander Schulz. *Measurement of the Ultra High Energy Cosmic Ray Flux using Data of the Pierre Auger Observatory*. PhD thesis, 2009. Karlsruhe, KIT, Diss., 2008.

[74] MARIS I. C. *Measurement of the Energy Spectrum and Mass Composition of Ultra-high Energy Cosmic Rays*. PhD thesis, 2016. Karlsruhe, KIT, Diss., 2016.

[75] P. Abreu et al. The flux of ultra-high energy cosmic rays after ten years of operation of the Pierre Auger Observatory. In *Proceedings, 34nd International Cosmic Ray Conference (ICRC 2015): The Hague, The Netherlands, 2015*, 2015.

[76] Ines Valino. The flux of ultra-high energy cosmic rays after ten years of operation of the Pierre Auger Observatory. *PoS*, ICRC2015:271, 2016.

[77] L Wiencke et al. Atmospheric super test beam for the pierre auger observator. *PoS*, ICRC2011, 2011.

[78] HIRES Collaboration. Absolute GPS Time Event Generation and Capture for Remote Locations. *International Cosmic Ray Conference*, 2:825, 2001.

[79] V. Rizi, A. Tonachini, M. Iarlori, and G. Visconti. Atmospheric monitoring with lidars at the pierre auger observatory. *The European Physical Journal Plus*, 127(8):92, 2012. ISSN 2190-5444. doi: 10.1140/epjp/i2012-12092-0.

[80] Pierre Auger Collaboration. Official web page of the acceptance group of the pierre auger collaboration, 2015. URL http://www.auger.org.ar/FD/documents/fd_shift_manual_en_2015.pdf.

[81] M. Fitzgibbon, A. W.and Pilu and R. B. Fisher. Direct least-squares fitting of ellipses. 21(5):476–480, May 1999.

[82] R. Caruso on beh. of the P. Auger Collaboration. General overview of recent results from the pierre auger observatory. *Astrophysics and Space Sciences Transactions*, 7(4): 445–451, 2011. doi: 10.5194/astra-7-445-2011.

[83] R. Abbasi et al. Techniques for measuring atmospheric aerosols at the high resolution flys eye experiment. *Astroparticle Physics*, 25(1):74 – 83, 2006. ISSN 0927-6505. doi: http://dx.doi.org/10.1016/j.astropartphys.2005.11.006.

[84] Pedro Abreu et al. Techniques for Measuring Aerosol Attenuation using the Central Laser Facility at the Pierre Auger Observatory. *JINST*, 8:P04009, 2013. doi: 10.1088/1748-0221/8/04/P04009.

[85] Laura Valore. Atmospheric aerosol characterization using the central laser facility at the pierre auger observatory. *Nuclear Instruments and Methods in Physics Research Section A: Accelerators, Spectrometers, Detectors and Associated Equipment*, 630(1):246 – 250, 2011. ISSN 0168-9002. doi: http://dx.doi.org/10.1016/j.nima.2010.06.077.

[86] P. Abreu et al. The exposure of the hybrid detector of the pierre auger observatory. *Astroparticle Physics*, 34(6):368 – 381, 2011. ISSN 0927-6505. doi: http://dx.doi.org/10.1016/j.astropartphys.2010.10.001. URL http://www.sciencedirect.com/science/article/pii/S0927650510001829.

[87] J. Abraham et al. Trigger and aperture of the surface detector array of the pierre auger observatory. *Nuclear Instruments and Methods in Physics Research Section A: Accelerators, Spectrometers, Detectors and Associated Equipment*, 613(1):29 – 39, 2010. ISSN 0168-9002. doi: http://dx.doi.org/10.1016/j.nima.2009.11.018.

[88] Pierre Auger Collaboration. Official web page of the acceptance group of the pierre auger collaboration, 2010. URL http://ipnwww.in2p3.fr/~augers/AugerProtected/AcceptMain.html.

[89] Copyright 2010-2017 Ankit Rohatgi. Webplotdigitizer, web based tool to extract data from plots, images, and map. URL http://arohatgi.info/WebPlotDigitizer/app/.